A Phenomenological Model for Particle Dispersion and Clustering

Kyriakoulis L. Resvanis, MSc, MEng

submitted in partial fulfillment

of the requirements for the

degree of Doctor of Philosophy

Imperial College London

Department of Mechanical Engineering

Thermofluids Division

Abstract

The objective of this thesis is to propose a new model for particle dispersion and clustering for use within an (unsteady)-Reynolds Averaged Navier-Stokes ((u)RANS) computational framework. The need for an improved model stems from industrial requirements to address certain limitations of the currently used models. Namely, low predicted particle entrance into recirculation zones for particles with large *Stokes* numbers and unrealistically spatial and temporal uniform predicted particle concentrations.

The literature review presented within this thesis examines the various computational tools available for modeling the Lagrangian phase and identifies Kinematic Simulations (KS) as potentially capable of reproducing accurate Lagrangian statistics and particle clustering across a range of physical scales while at the same time requiring a modest increase of computational resources relative to the presently used methods.

The thesis proposes a combination of (u)RANS and KS in a coupled Eulerian-Lagrangian framework.The (u)RANS calculations will be responsible for modeling the large coherent motions while the KS will be employed to model the effects of all the other scales, that are represented statistically in the (u)RANS context, on particle motion. In other words, the representation of the velocity field within the 'eddies' will be simulated by tracking a particle through an isotropic turbulent field constructed with the aid of KS. The extent of scales and the energy content of the isotropic field modeled by KS at every instance is determined by the local properties of the under-resolved 'eddy' as determined by the Eulerian framework.

The proposed model is evaluated on an axisymmetric sudden expansion test case through comparisons with experimental results, LES calculations as well as RANS simulations employing the current industry standard dispersion model. Improved overall performance was observed with significant differences between the particle trajectories computed with the proposed model and those with a model widely used in industry. This last point is of particular significance as one of the limitations of the currently used models was the high degree of spatial uniformity in the predicted particle distribution.

I hereby declare that the work presented throughout this thesis is my own unless explicitly stated otherwise.

"Believe me, my young friend, there is *nothing* –absolute nothing– half so much worth doing as simply messing about in boats."

said the Water Rat to the Mole
The Wind in the Willows

Acknowledgments

First and foremost, I would like to express my gratitude to the European Union for funding this work through the FP7 Project for Fuel Injector Research for Sustainable Transport (FIRST-Grant Agreement no. 265848) and to Drs. Daren Luff and Marco Zedda from Rolls-Royce plc for managing the research consortium successfully. Additional acknowledgments are due to Drs. Simon Stowe and Marco Zedda for implementing the dispersion model proposed in this thesis within their proprietary code and for performing the calculations on the industrial geometry presented within the Appendices.

I am very grateful to my thesis advisers Profs. Yannis Hardalupas and Alex Taylor for their continuous encouragement, insight and guidance over the past few years and for their unique combination of direction and freedom in pursuing this research. I would also like to express my gratitude to my thesis co-adviser Prof. Nick Cumpsty for his counseling that was paramount in ensuring this work was completed in a timely manner.

I am also indebted to my colleagues in rooms 760 & 761 of the City & Guilds Building and especially Nick, George & Kostas for their assistance over the course of this work. My thanks also go out to my flatmates Alex, Ares & George who over the years ensured that there was never a mundane moment.

Last but not least I would like to thank my family for their continuous support, especially my sister Elli for putting up with me during my stay in London and my brother Themis for his assistance in proof-reading this manuscript but above all for the long and fruitful discussions without which this work would not have been possible.

Contents

1 Introduction **23**

1.1 Overview . . . 24
1.2 Multiphase flows in CFD . . . 25
1.3 Eulerian-Lagrangian interaction & the need for dispersion models. . . . 27
1.4 Review of Lagrangian Methods . . . 31
1.4.1 Lagrangian Overview . . . 32
1.4.2 Lagrangian Dynamics . . . 32
1.4.3 The added complexity of inertial particles . . . 43
1.4.4 Dispersion Experiments . . . 45
1.4.5 The closure problem . . . 46
1.4.6 Models for Relative Dispersion . . . 47
1.5 Review of Kinematic Simulations . . . 54
1.6 The need for a new Dispersion Model - Present Contribution . . . 59
1.7 Scope of this work . . . 61
1.8 Outline of this thesis . . . 62

2 CFD Basics and Eulerian-Lagrangian Solver Development **63**

2.1 Computational methods for fluid dynamics . . . 63
2.1.1 Direct Numerical Simulations . . . 64
2.1.2 Large Eddy Simulations . . . 64
2.1.3 Reynolds Averaged Navier Stokes . . . 68
2.1.4 Governing Equations . . . 71
2.1.5 Discretization . . . 72
2.1.6 Convective and diffusive operators . . . 73
2.1.7 Boundary-Conditions Discretization . . . 75
2.1.8 Temporal Discretization . . . 77
2.1.9 Higher Order Schemes, Errors and Stability of Solution . . . 80
2.1.10 Linear Algebra . . . 81
2.1.11 Navier-Stokes and Pressure Equations Discretization . . . 82
2.1.12 Coupling of Pressure and Momentum . . . 84
2.2 Development of the Eulerian-Lagrangian solver . . . 86
2.2.1 Necessary modifications to openFOAM solvers . . . 86
2.3 Summary . . . 87

3 Large Eddy Simulations of an Axisymmetric Sudden Expansion **89**

3.1 The sudden expansion test case . . . 89
3.2 Experimental Details - Operating Conditions . . . 90
3.3 Large Eddy Simulations - Eulerian Phase . . . 92
3.3.1 Discretization & SGS . . . 94
3.3.2 Boundary Conditions . . . 94
3.3.3 Measurement Locations And Normalizing Quantities . . . 95

3.3.4 Mesh Sensitivity Analysis . . . 99
3.3.5 y^+ Analysis . . . 102
3.3.6 Instantaneous Values . . . 102
3.3.7 Comparisons With Experiments-Time Averaged Results . . . 108
3.3.8 Sub-Grid-Scale Viscosity Comparison . . . 112
3.3.9 Velocity fluctuations . . . 116
3.3.10 Recirculation Zone *Loci* . . . 116
3.3.11 Eulerian Phase Summary . . . 116
3.4 Large Eddy Simulations - Lagrangian Phase . . . 120
3.5 Turbulent structures . . . 127
3.5.1 *Stokes* Numbers . . . 139
3.5.2 Large scale oscillations of the jet . . . 142
3.5.3 *Voronoi* Analysis . . . 148
3.6 Summary . . . 157

4 Implementation of Kinematic Simulations within openFOAM 158
4.1 Particle Pair Evolution In Isotropic Turbulent Fields by Stochastic Motion . . . 159
4.2 Kinematic Simulations implementation within openFOAM . . . 163
4.2.1 Version A . . . 171
4.2.2 Version B . . . 171
4.3 Particle Pair Dispersion in Isotropic Turbulent Fields . . . 174
4.3.1 Kinematic Simulations implemented as a Dispersion Model - Coupling with openFOAM . . . 174
4.4 Summary . . . 182

5 KS in sudden expansion 183
5.1 Selection of k-Epsilon closure model . . . 183
5.2 Qualitative Comparisons . . . 184
5.3 KS-model Evaluation . . . 190
5.3.1 Evaluation of particle concentration . . . 198
5.3.2 Quantitative comparison of fluctuating velocity components . . . 206
5.4 Summary . . . 209

6 Future work & Conclusions 216
6.1 Summary . . . 216
6.2 Recommendations for Future Work . . . 217
6.3 Conclusions . . . 218

A Spectral Methods 231

B Time Averaging for LES 241

C Industrial Geometry 245

List of Figures

1 Flow chart for the developed two-way coupled Eulerian-Lagrangian solver within openFOAM. For details regarding the implementation of the KS dispersion model see Chapter 4 88

2 Perspective view of the D/d=5 sudden expansion computational domain. Viewed from the inlet tube at the bottom right of the figure to the expansion tube at the upper right corner. Characteristic dimensions for the inlet and expansion tubes are $15mm$ & $75mm$ diameters and $500mm$ and $600mm$ length respectively. . . . 91

3 Slices through the RANS simulation used to initialize the LES calculation. Visible at the bottom is the $15mm$ inlet tube and the whole domain of the expansion tube of $75mm$ diameter and $600mm$ length. Flow is from the bottom of the page to the top. Depicted from left to right; velocity magnitudes colored for a range [0, $18m/s$]; dissipation rate of specific turbulent kinetic energy colored between [0, $1000m^2/s^3$] and specific turbulent kinetic energy colored between [0, $10m^2/s^2$] . 93

4 Spanwise and streamwise sections through the inlet tube with the step in place. Detail on the right hand side shows the zero thickness step of $3mm$ introduced into the inlet pipe to trip the flow. Coloring is by normalized velocity magnitude (U/U_o)and range of scale is [0, 2.5].Characteristic dimensions for the inlet tube diameter and length are $15mm$ and $500mm$ respectively. Flow direction is from the bottom of the page to the top. 96

5 Section through LES domain showing an improved prediction of the position of the recirculation zone. Colored by the axial velocity component with a range [-3, $3m/s$]. Flow direction is from the bottom of the page to the top. Blue colors indicate flow reversal. 97

6 Computational mesh of the expansion tube with the measurement locations indicated by the black lines. Also shown is a slice depicting the normalized axial velocity colored by the normalized axial velocity (U_z/U_o) with a range [-5, 35]. Expansion tube dimensions are $75mm$ and $600mm$ for the diameter and length respectively. Flow direction is from the bottom of the page to the top. 98

7 Representation of the 3 meshes depicting the mesh at the step from a perspective view, from left to right; the coarse (800k cells), the standard (1,300k cells) and the fine grid (8,800k cells). Inlet and expansion tube diameters are $15mm$ and $75mm$ respectively. 99

8 Representation of an axisymmetric portion of the 3 meshes depicting the mesh at the step. Shown from left to right; the coarse, the standard and the fine grid. The cells are all hexa-hedral despite appearing to be prisms due to an issue with the rendering process of the post-processing software. 100

9 Representation of the 3 meshes depicting details of the mesh at the step location Shown from left to right; the coarse, the standard and the fine grid. 100

10 Representation of the 3 meshes depicting details of the mesh at the inlet, diameter is $15mm$, from left to right; the coarse, the standard and the fine grid. 101

11 Representation of the 3 meshes depicting details of the mesh at the outlet, diameter is $75mm$, from left to right; the coarse, the standard and the fine grid. . . . 101
12 From left to right details of; the coarse, the standard and the fine meshes, respectively, depicting on the left the y^+ values plotted on the surface of the domain as calculated within openFOAM, with a range [0,10] and the magnitude of velocity on the right of each pane, with a range [0, $15m/s$]. Flow direction is from the bottom of the page to the top. 103
13 Variation of y^+ with u^+ in the inlet pipe at at location $z/D = -0.33$ upstream of the step for the three mesh densities along with the theoretical predictions. Note that the coarse gird makes use of wall functions. 104
14 Streamwise variation of the instantaneous axial velocity along the centreline ($y/D = 0$) 105
15 Streamwise variation of the instantaneous axial velocity along the wall ($y/D = 0.5$) 105
16 Spanwise variation of the instantaneous axial velocity at $z/D = 0.08$ 106
17 Spanwise variation of the instantaneous axial velocity at $z/D = 2.67$ 106
18 Spanwise variation of the instantaneous axial velocity at $z/D = 5.33$ 107
19 Streamwise (y/D) variation of the instantaneous axial velocity at 1, 1.5 & 2mm from the wall 108
20 Streamwise variation of the time-averaged axial velocity along the centreline (y/D=0) 109
21 Streamwise variation of the time-averaged axial velocity at the wall (y/D=0.5) . 109
22 Spanwise variation of the time-averaged axial velocity at z/D=0.08 110
23 Spanwise variation of the time-averaged axial velocity at z/D=2.67 110
24 Spanwise variation of the time-averaged axial velocity at z/D=5.33 111
25 Comparison between the instantaneous and *Reynolds averaged* axial velocities, colored between [0, $20m/s$] on the left and right respectively for the coarse, standard and fine meshes; from left to right. Flow direction is from the bottom of the page to the top. 112
26 Comparison between the 'instantaneous' and *Reynolds-Averaged* radial velocities, colored betwen [-1, $+1m$], on the left and right respectively for the coarse, standard and fine meshes; from left to right. The orientation of the schematics is such that the x- component is normal to the page. Flow direction is from the bottom of the page to the top. 113
27 Streamwise variation of the *Reynolds Averaged* Axial Velocity along the centreline ($y/D = 0$) 113
28 Streamwise variation of the *Reynolds Averaged* Axial Velocity along the wall ($y/D = 0.5$) 114
29 Spanwise variation of the *Reynolds Averaged* Axial Velocity at z/D=0.08 114
30 Spanwise variation of the *Reynolds Averaged* Axial Velocity at z/D=2.67 115
31 Spanwise variation of the *Reynolds Averaged* Axial Velocity at z/D=5.33. 115
32 Variation of the ratio of **instantaneous** turbulent to physical viscosity 117
33 Variation of the ratio of **time averaged** turbulent to physical viscosity 118

34 Spanwise profile of the instantaneous axial velocity fluctuations at time instants A & B separated by $0.1s$ . . . 119
35 Spanwise profile of the time averaged axial velocity fluctuations. . . . 120
36 Spanwise instantaneous variation of the axial velocity fluctuations. . . . 121
37 Representation of Lagrangian particles within the expansion tube for the ML1 case from left to right at an early, intermediate and fully developed time instant. Flow direction is from the bottom to the top of the page similarly for the direction of gravity. Sub-Figure (a) shows the $40\,\mu m$ and Sub-Figure (b) the $80\,\mu m$ particles. 123
38 Extracted instantaneous data at measurement locations for Lagrangian phases at ML1 conditions; spanwise at z/D=0.08, 2.67 & 5.33 from the bottom of the image to the top, and for the streamwise direction at y/D=0 & 0.5, from the centreline and the wall, respectively. Flow direction is from the bottom to the top of the page. Of note is the limited number of particles away from the centreline for the larger particle size class. Sub-Figure (a) shows the $40\,\mu m$ and Sub-Figure (b) the $80\,\mu m$ particles. . . . 124
39 Qualitative representation of the instantaneous Lagrangian axial velocity at the three spanwise measurement locations at ML1 conditions, from top to bottom, z/D=0.08,2.67 & 5.33, for the two particle size classes. Particles are colored by their normalized axial velocity, (U_z/U_o) for a range between [-0.239, +2.32]. Sub-Figure (a) shows the $40\,\mu m$ and Sub-Figure (b) the $80\,\mu m$ particles. . . . 125
40 Discrepancy between Eulerian and the Lagrangian velocities at the step. Histograms for the Lagrangian data generated from all particles within that domain section for a given instant in time. Similarly, the Eulerian data extracted from the cells lying within that same section of the domain with zeros values corresponding to cells by the walls and the no slip condition imposed. At $z/D = -0.05$ upstream of the step. . . . 127
41 Lagrangian instantaneous axial velocity for the $40\,\mu m$ particles along the centreline ($y/D = 0$) . . . 128
42 Lagrangian instantaneous axial velocity for the $40\,\mu m$ particles along the wall ($y/D = 0.5$) . . . 129
43 Lagrangian instantaneous axial velocity for the $40\,\mu m$ particles at z/D=0.08 . . 130
44 Lagrangian instantaneous axial velocity for the $40\,\mu m$ particles at z/D=2.67 . . 131
45 Lagrangian instantaneous axial velocity for the $40\,\mu m$ particles at z/D=5.33 . . . 132
46 Lagrangian instantaneous axial velocity for the $80\,\mu m$ particles at z/D=0.08 . . . 133
47 Lagrangian instantaneous axial velocity for the $80\,\mu m$ particles at z/D=2.67 . . 134
48 Lagrangian instantaneous axial velocity for the $80\,\mu m$ particles at z/D=5.33 . . 135
49 Spatial non-uniformity of $40\,\mu m$ particles at ML1 conditions at four distinct time instances for the three spanwise measurement stations at z/D=0.08, 2.67 & 5.33, from top to bottom respectively . . . 136
50 Spatial non-uniformity of $80\,\mu m$ particles at ML1 conditions at four distinct time instances for the three spanwise measurement stations at z/D=0.08, 2.67 & 5.33, from top to bottom respectively . . . 137

51 Sample sections though the LES domain for 40 μm ML1 case, near the expansion tube outlet, showing only the clusters of particles that lie close to the slices through the domain depicting from left to right; enstrophy colored by a range [0, $10^4 s^{-2}$]; Q, the second invariant of the velocity gradient tensor colored by a range [100, 2x$10^3 s^{-2}$] and the magnitude of vorticity colored by a range [0, $250 s^{-1}$] 140
52 Sample sections though the LES domain of the expansion tube outlet for the 40 μm ML1 case , viewed from the step towards the expansion tube outlet. the view shows, in black, only the particles that lie close to slices through the domain. The left panel shows enstrophy colored by a range [0, 2x$10^5 s^{-2}$] and a contour of Q at 2.5x$10^4 s^{-2}$. The middle pane shows a plane colored by the magnitude of Q for a range [0, 5x$10^4 s^{-2}$] along with contours of the magnitude of vorticity at $10^3 s^{-1}$. The right hand pane shows a plane colored by the magnitude of vorticity for a range [0, 5x$10^3 s^{-1}$] along with contours of enstrophy at $10^5 s^{-2}$. 141
53 Large scale oscillations of coarse mesh jet, showing the normalized axial velocity (U_z/U_o) colored for a range [-5,35]. Flow direction is from the bottom of the page to the top. 143
54 Large scale oscillations of the standard mesh jet , showing the normalized axial velocity (U_z/U_o) colored for a range [-5,35]. Flow direction is from the bottom of the page to the top. 144
55 Large scale oscillations of the fine mesh jet, showing the normalized axial velocity (U_z/U_o) colored for a range [-5,35]. Flow direction is from the bottom of the page to the top. 145
56 Detailed view of the large scale oscillations of the coarse mesh jet, showing the normalized axial velocity (U_z/U_o) colored for a range [-5, 35]. Flow direction is from the bottom of the page to the top. 146
57 Detailed view of the large scale oscillations of the standard mesh jet, showing the normalized axial velocity (U_z/U_o) colored for a range [-5, 35]. Flow direction is from the bottom of the page to the top. 146
58 Detailed view of the large scale oscillations of the fine mesh jet, showing the normalized axial velocity (U_z/U_o) colored for a range [-5, 35]. Flow direction is from the bottom of the page to the top. 147
59 Probe Location and sample time trace 148
60 Effect of jet flapping on particle spatial distribution at an early, intermediate and fully developed time instance , from left to right. Flow direction is from the bottom to the top of the page. 149
61 Details of the instantaneous 40 μm particle spatial distribution viewed as a slice of the Lagrangian domain at 0, 30, 60 90, 120 & 150 degrees from the normal of the xy-plane. Flow direction is from the bottom of the page to the top. 150
62 Voronoi plots for the 40 μm particles at z/D=0.08 for 6 instances in time 151
63 Voronoi plots for the 40 μm particles at z/D=2.67 for 6 instances in time 152
64 Voronoi plots for the 40 μm particles at z/D=5.33 for 6 instances in time 153
65 Voronoi plots for the 80 μm particles at z/D=0.08 for 6 instances in time 154

66 Voronoi plots for the 80 μm particles at z/D=2.67 for 6 instances in time 155
67 Voronoi plots for the 80 μm particles at z/D=5.33 for 6 instances in time 156
68 Domain details 163
69 Particle pair trajectories by 'G&I-like' motion and KS in blue and red respectively, for $Ea = 10\,m^2/s^2$ 164
70 Particle pair trajectories by 'G&I-like' motion and KS in blue and red respectively, for $Ea = 20\,m^2/s^2$ 165
71 XY-plane 166
72 Particle pair trajectories by 'G&I-like' motion and KS in blue and red respectively, for $Ea = 30\,m^2/s^2$ 166
73 Evolution of the magnitude of the particle pair separation vector by 'G&I-like' and KS models 167
74 Evolution of the magnitude of the particle pair separation vector with an increasing number of realizations for the KS model 168
75 Averaged particle pair trajectories from KS for $Ea = 30\,m^2/s^2$ after 1,2,5,10 & 50 realizations 169
76 Flowchart for KS version A (descriptive) 172
77 Flowchart for KS version A (mathematical definitions) 173
78 Flowchart for KS version B (descriptive) 175
79 Flowchart for KS version B (mathematical definitions) 176
80 From left to right the continuous domains for the G&I, KS & no-dispersion dispersion models; depicting the magnitude of velocity on the periodic boundary face, at several instants in time confirming that the 3 domains are almost identical. 178
81 Streamlines within the isotropic turbulence domain 179
82 Particle pair trajectories for 80μm diameter particles with a release time smaller than the *Kolmogorov* timescale. Black trajectories indicate the no dispersion model, red indicate the KS dispersion model and blue the G&I dispersion model particle pair respectively. 180
83 Particle pair trajectories for 80μm diameter particles with a release time larger than the *Kolmogorov* timescale. Black trajectories indicate the no dispersion model, red indicate the KS dispersion model and blue the G&I dispersion model particle pair respectively. 181
84 Slices through an equatorial plane of the RANS simulation. Visible at the bottom is the 15mm inlet tube and the whole domain of the expansion tube of 75mm diameter and 600mm length. Flow is from the bottom of the page to the top. Depicted from left to right; continuous phase mean velocity magnitudes colored for a range [0, 18m/s]; dissipation rate of turbulent kinetic energy colored between [0, 1000m^2/s^3] and turbulent kinetic energy colored between [0, 10m^2/s^2] 185
85 Comparison between LES-RANS inhomogeneity of 80μm particle spatial distributions shown on an equatorial plane through the domain colored by the continuous phase velocity magnitude [0, 15m/s]. 186

86 From top to bottom; LES, KS & GI. Depicting the instantaneous particle positions and the equatorial plane depicting the particle concentration before normalization. 188
87 $80\mu m$ particles positions, collapsed onto a single azimuthal plane, depicted within the expansion tube, equatorial planes through the Eulerian domain shows the continuous phase axial velocity, blue regions indicate negative velocities and the extend of the recirculation zone. G&I on the left and KS2 on the right. (Note: The particles that appear to lie outside the domain are a result of the rendering process and are actually within the domain. The concentration has not been normalized here) 189
88 Magnitude of fluctuating velocity vector, u', for $80\mu m$ particles as calculated by the GI on the left and the KS2 models on the right. Note that the domain is restricted to show only the particles lying close to an equatorial plane. 191
89 x-component of fluctuating velocity for $80\mu m$ particles as calculated by the G&I on the left and the KS2 models on the right 192
90 y-component of fluctuating velocity for $80\mu m$ particles as calculated by the G&I on the left and the KS2 models on the right 193
91 z-component of fluctuating velocity for $80\mu m$ particles as calculated by the G&I on the left and the KS2 models on the right 194
92 x-component of fluctuating velocity for $80\mu m$ particles as calculated by the G&I on the left and the KS2 models on the right. Note that the domain is restricted to show only the particles lying close to an equatorial plane. 195
93 y-component of fluctuating velocity for $80\mu m$ particles as calculated by the G&I on the left and the KS2 models on the right. Note that the domain is restricted to show only the particles lying close to an equatorial plane. 196
94 z-component of fluctuating velocity for $80\mu m$ particles as calculated by the G&I on the left and the KS2 models on the right. Note that the domain is restricted to show only the particles lying close to an equatorial plane. 197
95 Schematic indicating the particle number density evaluation problem; For the two boxes on the top the number density evaluated at the measurement location will be the same, while for those at the bottom of the figure, the result will be completely different. 198
96 Sample instantaneous $40\mu m$ particle concentration representation of the concentration evaluation annuli of the domain. (Note: the concentration here has not been normalized) 199
97 Sample instantaneous $80\mu m$ particle concentration representation of the concentration evaluation annuli of the domain. (Note: the concentration here has not been normalized) 199
98 Schematic depiction the three spanwise stations in the pipe at z/D=0.08-1.33-2.66 200
99 Eulerian representation of instantaneous particle concentrations - $40\mu m$ particles, section through a plane of symmetry. Flow direction is from the bottom to the top of the page. (Note: the concentration here has not been normalized) 201

100 Eulerian representation of instantaneous particle concentrations - 80μm particles, section through a plane of symmetry. Flow direction is from the bottom to the top of the page. (Note: the concentration here has not been normalized) 202
101 40μm-ML1 condition 204
102 80μm-ML1 condition 205
103 40μm-ML2 condition 207
104 80μm-ML2 condition 208
105 Comparison of the probability of occurrence of the particle fluctuating velocity component, $\mathrm{UTurb_x}$, calculated from the dispersion models restricted to those particles lying within the recirculation zone. 210
106 Comparison of the probability of occurrence of the fluctuating velocity component, $\mathrm{UTurb_y}$, calculated from the dispersion models restricted to those particles lying within the recirculation zone. 211
107 Comparison of the probability of occurrence of the particle fluctuating velocity component, $\mathrm{UTurb_z}$, calculated from the dispersion models restricted to those particles lying within the recirculation zone. 212
108 Comparison of the probability of occurrence of the particle fluctuating velocity components, calculated from the dispersion models restricted to those particles lying within the recirculation zone. 213
109 Comparison of the probability of occurrence of the particle velocity components, calculated from the dispersion models, and restricted to those particles lying within the recirculation zone. 214
110 Instantaneous axial velocity profiles for bootstrap method 242
111 Averaged axial velocity profiles for bootstrap method using different number of samples 243
112 Detailed view of averaged axial velocity profiles for bootstrap method using different number of samples 244
113 Particle Dispersion in the gas turbine combustor, from left to right, no dispersion model, GI dispersion model and finally the KS2 dispersion model. Coloring is by Sauter Mean Diameter 246
114 Liquid mixture fraction and temperature shown on the top and bottom respectively in the gas turbine combustor employing no dispersion, GI dispersion and the KS2 dispersion models from left to right respectively. 247

List of Tables

1 Operating conditions and characteristic dimensions for the sudden expansion test case of Hardalupas *et al.* (1992) 92
2 Mesh details for the three grids tested.... 100
3 Lagrangian Phase Characteristic Dimensions and Properties 122
4 Information on the Isotropic Turbulence Domain 162

Nomenclature

List of abbreviations

CFD	Computational Fluid Dynamics
DDDM	Deterministic Direct Discrete Models
DNS	Direct Numerical Simulations
FVM	Finite Volume Method
FFT	Fast Fourier Transform
GI	Gosman & Ioannides (1981) paper
K41	Kolmogorov's (1941) paper
KS	Kinematic Simulations
KSIM	Kinematic Simulations Inertial Model
KSSM	Kinematic Simulations Sweeping Model
LDV	Laser Doppler Velocimetry
LES	Large Eddy Simulations
LHDI	Lagrangian History Direct Interaction model
LHF	Locally Homogeneous Flow
ML	Mass Loading condition
NO_X	Nitrogen Oxides
PISO	Pressure Implicit with Splitting of Operator algorithm
PIMPLE	merged PISO-SIMPLE algorithm
RANS	Reynolds Averaged Navier-Stokes
RF	Relaxation Factor
RMS	Root Mean Square
RSM	Reynolds Stress Model
openFOAM	open-source CFD software (Field Operation And Manipulation)
SDDM	Stochastic Direct Discrete Models
SIMPLE	Semi-Implicit Method for Pressure Linked Equations algorithm
SGS	Sub Grid Scale

TCT	Turbulence Correlation Time
TI	Turbulence Intensity
VoF	Volume of Fluid method

List of Latin symbols

$\mathbf{a}$	Lagrangian location of particle/fluid element
A_{ij}	velocity gradient tensor
$\mathbf{A}$	coefficient matrix in linear algebra
$\mathbf{a}_{mnp}$ & $\mathbf{b}_{mnp}$	random vectors used in the construction of KS fields
$\mathbf{A}_n$ & $\mathbf{B}_n$	random vectors used in the construction of KS fields
$\mathbf{B}_{FC}$	vector in the FVM
C_B	coefficient of Basset force
C_D	coefficient of drag force
C_I	coefficient of virtual mass force
Co	*Courant* number
d_p	particle diameter
d	inlet tube diameter
D	expansion tube diameter
D/d	sudden expansion ratio
$E(k)$	energy spectrum
Ea	initial specific energy of an isotropic field
f	body forces
f	When used as a subscript this refers to the carrier, or continuous, phase
$\bar{f}$	mean component of a variable
f'	filtered or fluctuating component of a variable
F_{11}	longitudinal energy spectrum
F_{22}	transverse energy spectrum
g_0	Richardson's constant
g_b	normal gradient on the cell boundary

$G(x,x)$	filtering kernel
h	step height
$\mathbf{H}$	vector including contributions of all neighboring matrix coefficients
k	turbulent kinetic energy
k_c	cut-off wavenumber
k_{max}	largest wavenumber
k_{min}	smallest wavenumber
$\mathbf{k}$	wavenumber vector
K	scale dependent eddy diffusivity
l	integral length scale
l_e	eddy characteristic length scale
p	pressure
p	when used as a subscript indicates the discrete phase
Pe	*Peclet* number
Ps	persistence parameter
$P_t^{(1)}$	one-particle probability distribution
$P_t^{(2)}$	two-particle probability distribution
Q	second invariant of the velocity gradient tensor A_{ij}
$\mathbf{r}$	distance $\mathbf{x}$ from the origin or separation vector
R	third invariant of the velocity gradient tensor A_{ij}
$R^{1/2}$	Eulerian velocity structure function
R_{ij}	*Reynolds* stress tensor
$R_{ij}(r)$	spatial correlation tensor
$R_{ij}(\tau)$	temporal correlation tensor
Re	*Reynolds* number
St	*Stokes* number
S_{ij}	strain rate tensor
$\mathbf{S}$	area vector in the FVM

$d\mathbf{S}$	infinitesimal surface element in the FVM
t	time instant indicator
t_c	particle crossing time
t_e	eddy turnover time
T	energy exchange rate per unit mass
T_L	Lagrangian time scale
u_i'	fluctuating velocity in the literature review
u_t	friction velocity
$\mathbf{U}'$	fluctuating velocity in the computational framework review
$\mathbf{U}$	velocity vector
$\mathbf{U}_p^T$	particle terminal velocity
$\mathbf{V}$	Lagrangian velocity vector
$\mathbf{X}_{\mathrm{t_0}}^{\mathrm{t}}(\mathbf{a})$	location of Lagrangian particle with an initial location $\mathbf{a}$ at time $\mathrm{t_0}$ to its new location at time t
y/D	normalized distance from the centreline in the sudden expansion
z/D	normalized distance from the axial station containing the step in the sudden expansion

List of Greek symbols

γ	dimensionless drift velocity
Γ	diffusivity
$\Delta^{(2)}(t)$	distance between two particles at time t
$\left\langle \Delta^{(2)}(t) \right\rangle$	mean square displacement of two particle at time t
ε	dissipation rate of turbulent kinetic energy
ζ	value selected from a randomly sampled Gaussian distribution
$\zeta(t)$	an *Uhlenbeck-Ornstein* process
η	*Kolmogorov* length scale
ϑ	a passive scalar in the Lagrangian framework
κ	modulus of the wavenumber vector $\mathbf{k}$
λ	*Taylor* micro-scale length

Λ	a constant proportional to the integral length scale, l
μ	dynamic viscosity
ν	kinematic viscosity
ν_τ	effective turbulent viscosity or eddy viscosity
ρ_f	carrier phase density
ρ_p	particle density
σ_w	shear stress at the wall
τ_p	particle relaxation time
τ	sub-grid scale stress
φ	an arbitrary scalar or a surrogate variable
ϕ_{ii}	spectrum tensor
$\phi_{ij}(r)$	spectrum tensor of the *Fourier* transform corresponding to the spatial correlation tensor
$\phi_{ij}(\tau)$	spectrum tensor of the *Fourier* transform corresponding to the temporal correlation tensor
ω	vorticity or the specific rate of dissipation (k/ν_τ)
$\omega_{0,1,2,\ldots n}$	'eddy' turnover time at wavenumber $\mathbf{k}_n$
$\boldsymbol{\Omega}$	*Cauchy* invariant

1 Introduction

Turbulent multiphase flows are present many engineering and environmental flows. At their heart lie the interactions between the dispersed phase and the carrier flow, whether one is talking about either particles or droplets in a gas stream or bubbles in a liquid. The original impetus for investigations into the subject a century ago, at the peak of the steam age, was coal combustion. The problems being addressed at the time were to increase efficiency in the burner and boiler as well as looking into the exhaust plume and the effects that pollution had on the surrounding inhabitants.

More than a century later two-phase flow is still just as relevant, whether the focus is on designing a better gas-turbine combustor with a uniform fuel droplet distribution in order to increase energy efficiency, reduced pollutant formation and avoid premature wear and tear through hot-spot induced combustor liner damage or whether one is investigating the optimal positioning of a flue-stack to minimize pollution to surrounding inhabitants. The applications though are not limited to man made interference, the same physics govern the evolution and the colonization of coral reefs as well as the formation of cloud structures through the successive interactions of smaller water droplets. Computational modeling techniques can play a central role in improving existing energy systems and in our understanding of environmental flows. They can aid in identifying revolutionary energy conversion strategies replacing Edisonian design approaches with simulation based optimization. Similarly, modeling can provide insight to meteorologists and oceanographers about weather phenomena. They can explain to marine biologists how a particular coral species is found unexpectedly 5000 miles away on the other side of an ocean, where it had never been noticed before, and they can aid the engineer in positioning a sewage outlet for minimal environmental impact.

The **purpose** of this study is to develop a novel droplet and particle dispersion model within the framework of Reynolds Averaged Navier Stokes (RANS) simulations capable of predicting the spatial and temporal distributions of dispersed particles and droplets in engineering flows with a greater accuracy than is currently feasible with RANS but without the computational cost associated with Large Eddy Simulations (LES). The currently available dispersion models leave room for improvement and the main reason for this is that they contain very little physical information regarding the turbulent eddies of the flow and their effects on particles. **The novelty of the proposed model is to improve the present dispersion models through the introduction of Kinematic Simulations (KS) for the tracking of the Lagrangian phase through the scales of the Eulerian phase that have been time-averaged and represented only in a statistical sense in the (u)RANS context.**

The proposed phenomenological dispersion model is based on KS; these have recently been shown capable of reproducing particle preferential concentration phenomena. The underlying idea is to better approximate the structures and physics of eddies of the RANS simulations by creating a KS turbulent flow for the particle to interact with. The developed model will be integrated within openFOAM, an open-source Computational Fluid Dynamics (CFD) software package and will be compared to LES calculations (of the same test case). The test case selected is an axisymmetric sudden expansion flow at high Reynolds numbers for which detailed experimental measurements are available. After the LES is validated against the experimental results,

it is proposed to probe the LES model to identify regions of variation in the discrete phase's spatial distribution and relate these to surrounding turbulent flow structures. Such insight might prove useful for further development of the proposed phenomenological model.

This study proposes the adoption of an Eulerian approach for the continuous phase and a Lagrangian one for the dispersed phase. The study of dispersion phenomena can be done in either Eulerian or Lagrangian frameworks. In the former case, the frame of reference is fixed with respect to the fluid and the dispersed phase is treated like another continuum with its own set of governing equations. In the Lagrangian case, the frame of reference is fixed to the particle (or a group of particles' center of mass) and is tracked in time. For the Lagrangian particles that interact with inadequately resolved eddies of the RANS simulation, a KS will be constructed to model an isotropic turbulent field in order to generate more realistic fluctuating velocity components of the carrier phase for interaction with the particles. The CFD software will be responsible for the book-keeping of the two phases and implementing the KS model developed within the RANS framework.

A literature survey will be presented on turbulent particle dispersion, Lagrangian statistics and models available for simulating particle dispersion in order to identify the advantages and limitations of the reviewed methods. This is followed by a overview of spectral methods for turbulent flows and of Kinematic Simulations. The final section of the literature survey will review how the governing equations of fluid mechanics are discretized and solved in the subsequent sections. This will be followed by a section describing the development of a coupled Eulerian-Lagrangian solver and the introduction of the test case. Subsequently, a LES is performed on the chosen test case to validate the developed solver and to establish a computational benchmark for the subsequent calculations. Flow structures, that have important effects on the particle trajectories within the LES, will be identified and the findings used to improve the developed phenomenological model. The following section describes the implementation of the Kinematic Simulation model within the openFOAM package. Afterward, the proposed model is validated on the test case and compared to experimental measurements and the LES calculations. Finally, the proposed model is tested on an industrial geometry of an aviation gas-turbine combustor currently in flight.

1.1 Overview

The field of fluid mechanics has been revolutionized over the past decades through the use of computers for the solution of the Navier-Stokes equations; the partial differential equations that govern fluid flow. Although several approaches are possible, the most popular over the past several decades has been to use the Finite Volume Method (FVM) to discretize the Navier-Stokes equations. The FVM requires the decomposition of the flow domain into small volumes, small in relation to the overall physical domain sizes but significantly larger than the microscopic level, permitting the treatment of the flow as a continuum. Across these small volumes the principles of conservation of momentum and mass may be applied, in a similar manner as that used to derive the Navier-Stokes equations in the first place, and through the use of matrix algebra the equations over all the small volumes may be solved simultaneously. What is immediately clear is that the computational requirements must be proportional to the number of equations being

solved and the number of finite volumes into which the domain has been discretized, and herein lies the fundamental problem of CFD. In an ideal world without computational restrictions the method could be applied to provide a solution, with a relatively small error, to the most complicated fluid flow problems imaginable provided a fine enough grid is used. That is, given a small enough size for each finite volume, the method can provide accurate descriptions of highly turbulent fluid flow through very complicated geometries. Turbulence scaling arguments may be used to provide an estimate for the size of the smallest scales, thus providing an indication for the size of the finite volume required. Such an approach is employed by Direct Numerical Simulations (DNS) where even the smallest turbulent scales are resolved.

Today after more than 50 years of use of CFD, the most expensive DNS can only be used to describe isotropic turbulent flows with a Reynolds number of the order of less than 10^3 while channel flows in the 10^4 have just recently been performed. Early on, it was realized that the computational resources were not available, nor would they be there in the foreseeable future, to allow DNS of engineering or environmental flows. If the field of CFD was to be of any use to the engineer, a different approach would have to be adopted. The solution came, first, in the form of the Reynolds Averaged Navier-Stokes (RANS) and later on with Large Eddy Simulations (LES). In the case of the former, *Reynolds Averaging* is used to describe the mean components of the turbulent flow and a statistical approach is adopted to treat the smaller fluctuating scales, much in the same manner as that used by early researchers for investigations into the field of turbulence. In a similar manner LES employs filtering of all the fluctuations smaller than a certain size and approximates those through the use of a model while solving the Navier-Stokes equations directly for all scales larger than the filter width. Computational requirements are smaller for RANS simulations, increase substantially for LES and become prohibitively expensive for DNS. LES are capable of describing many of the interesting features of turbulence associated with the larger scales and might appear to be an ideal compromise but even today are sparingly used in industry due to their cost. This is but a very brief introduction into the field of CFD in order to set the stage for the remainder of this chapter and Chapter 2 will deal in greater detail with the specifics of the FVM and the various options available to the researcher and engineer for CFD modeling. In either case what is evident is that, despite the impressive improvements in computational resources available today, RANS and LES modeling are still very relevant and active fields of research, respectively, and there is a requirement for improved models for turbulence, dispersion, atomization etc.

1.2 Multiphase flows in CFD

The treatment of multiple phases in the Finite Volume Method poses some difficulties. Not because of lack of research, as it has been an active field of research for several decades, as Unverdi and Tryggvason (1992) point out. The earliest methods, using front/surface tracking methods, were inspired and developed from the earliest compressible flow methods of von Neumann and Richtmyer (1950) where the prediction of the shock front was of paramount importance. Similar schemes where employed to add artificial viscosity near the front/surface in order to avoid numerical instabilities that arise across sharp interfaces. Because the shear number of different methods proposed over the years does not make their review practical within the extent of this

thesis, we will restrict the discussion to the two most commonly used today in the context of multiphase flows; the level-set and the volume of fluid methods. For a review of earlier methods used to treat multiphase flows the reader is directed to Floryan & Rasmussen (1989).

The simplest of the two is the Volume of Fluid (VoF) method, where the volumetric fraction of each fluid phase is stored for every mesh cell. This is achieved through the introduction of an additional transport equation for a scalar, a, bounded between 0 and 1[1]. Near the front/surface the scalar value within the cell take on values between 0 and 1 ($0<a<1$) whilst far away from the interface they are either 0 or 1 ($a=0$ or $a=1$) depending on which side of the surface they lie on. It is important to note that the surface itself is not physically present and advected with the flow, rather it must be implicitly reconstructed according to some algorithm. The consequence of this approach is that the interface is rather diffuse since it depends on the computational grid size. However, as Gueyffiers *et al.* (1999) show, with careful combination of interface reconstruction algorithm (in this case the piecewise linear interface construction (PLIC)) and grid size the method is capable of remarkably good agreement between experimental and computational results on coarse grids albeit for fairly simple flows.

Level-Set methods are the other popular family of methods available, defined by Tanguy *et al.* (2005) as those that rely on a continuous function, φ, typically, a linear algebraic relation between any grid point and the surface, to characterize the interface. A zero value describes the location of the interface. An additional convection equation is needed for the function but care is needed as low order discretization schemes tend to result in discontinuities. Level-Set methods typically have a sharper interface compared to the VoF method for the same computational domains, however they suffer from mass loss in the conservation equations. Tanguy & Berlemont (2005) quantify the level of mass loss and for simple problems (droplet collision) this is of the order of less than 1%. However, applying the method to more complicated flows requires caution. Menard *et al.* (2007) describe how the VoF may be combined with the Level-Set method to address this issue and show very promising results for a liquid jet breakup, as they achieve the sharper interface of the latter with the mass conservation of the former.

The Eulerian approaches described above may be well suited to academic flows, such as liquid film and jet breakup, single droplet impingement, droplet pair collisions but they are of limited use for industrial applications. This is due to the extremely fine mesh sizes required to resolve the physics along the interface in order to make accurate predictions. In order to predict accurate film or jet breakup one must be able to resolve the small scales of turbulence that give rise to the interfacial instabilities, whether these are *Rayleigh-Taylor* or *Kelvin-Helmholtz*. Hence, the grid size must be several times smaller than the smallest instability wavelength and amplitude predicted by the analytical solutions. Alternatively, if it is a droplet or bubble transport problem, the mesh size will be dictated by the smallest sized droplet one wants to resolve, since several cells are required to adequately reproduce the curvature of a sphere. This results in meshes numbering hundreds of millions, even billions of cells. Requiring months of computational time on thousands of computer nodes just to resolve problems at relatively low Reynolds numbers of the order of a couple of hundred. Their application to industrial sized

[1] If there are three distinct fluids/phases yet another scalar, b, also bounded between 0 and 1, must be tracked and so forth for every additional phase.

problems and flow conditions is not expected to happen any time soon. Present day hardware limitations seem to suggest that for industrial problems, an alternative approach is required. By no means does this imply that the methods just described are of limited use to industry. On the contrary, although, they cannot be used for modeling complete industrial geometries, they provide invaluable information for the development of the individual sub-models. These sub-models typically attempt to replicate the actual physical processes through a statistical model or a phenomenological description.

1.3 Eulerian-Lagrangian interaction & the need for dispersion models.

So far we have seen how the finite volume method may be used to discretize the Navier-Stokes equations, that completely describe the continuous carrier phase in an Eulerian framework, and how they may be solved simultaneously through the use of matrix algebra to provide a solution to the partial differential equations. On the other hand, the solution of the Lagrangian phase is somewhat more straightforward as the ordinary differential equations describing the motion of the particles (or spheres) may be solved with a range of quick and easy to implement methods such as multi-step linear, Runge-Kutta, Euler, etc. The issue that still remains to be covered is how the two methods may be connected.

In a one-way coupled Eulerian-Lagrangian framework the presence of the dispersed phase does not affect the carrier phase (*i.e.* there is no effect of mass loading nor is there, e.g., a force acting on the continuous phase due to drag from the discrete phase), hence, it is should be used when the Eulerian phase is steady and the evolution of the particle or dispersed phase trajectory is mainly dependent on the particular geometry of the domain. It is to be kept in mind that such an approach will be satisfactory only if the mass loading of the dispersed phase is small.

If, on the other hand, the mass loading is large or if the geometry and flow conditions are such that instabilities arise causing oscillations in the defining flow structures, then a two-way coupled approach should be adopted. In the first case, the implication of large mass loading is that the momentum of the dispersed phase will have a significant effect on the development of the surrounding flow field. If, on the other hand, the Eulerian phase is unsteady then, even at low mass loadings the contribution of the dispersed phase may be important and should be accounted for in the Eulerian phase. This is because even small changes in the nature of the perturbation upstream can significantly change the shape of flow-field at a downstream location. Mostafa (1992) mentions the experimental and computational observations of particle effects on the turbulent structures making two-way coupling of paramount importance in flow fields where said structures play a defining role in the shape of the field.

The way the interaction of the dispersed phase is accounted for on the carrier phase is through the inclusion of additional source terms in the partial differential equations that describe the Eulerian phase. The exact nature of the source terms will depend on the problem being modeled and on the format in which the equations are cast. If one is solely interested in the evolution of particle trajectories then it may be adequate to account for the particle's momentum as an additional contribution to the momentum of the Eulerian phase, evaluated across the computational cell within which it lies. If, on the other hand, the case being investigated involves reacting or non-isothermal flows, an additional contribution from the dispersed phase

is required in the scalar transport equation. Whether one chooses to model all contributions or only a subset of them will depend on the accuracy desired and the computational resources available. On the other hand there are instances where trying to describe all physical phenomena accurately is meaningless as there are large uncertainties in the formulations themselves. For example, the estimation of drag coefficients for small spheres is still an active field of research with large discrepancies in the quoted values. It may be argued that there is little point in trying to account for the contribution of the Basset forces, when estimating the forces on a solid sphere in a gaseous continuous phase since their contribution is at least an order of magnitude smaller than that of the drag force. In any case, the forces are evaluated and the particle trajectory is updated by solving the equation of motion and adjusting or correcting the Eulerian field through the addition or removal of momentum and energy or source terms. At the next time step, the process is repeated for the updated particle position taking into account the updated local parameters. The problem that arises, and is of particular interest, is how particle dispersion is treated when the fluctuating components of the Eulerian field are not modeled. For a well resolved LES or DNS Eulerian-Lagrangian calculation there is sufficient instantaneous velocity information to ensure adequate dispersion of the Lagrangian particles with time. In both cases a substantial range of length scales are modeled resulting in realistic turbulent flow-fields, which in turn will ensure that two particles that start next to each other will eventually exhibit a turbulent-like relative dispersion. The adjective 'turbulent-like' is needed because, in the case of LES, the dissipative scales are modeled while even the latest DNS will not resolve the larger energy containing scales (at least not at high *Reynolds* numbers).

However, in RANS simulations, the 'raw' fluctuating velocity components of the carrier phase are not present and a mechanism or model is needed to represent turbulent dispersion. The early work in this field, namely Locally Homogeneous Flow (LHF) models, assumed that the dispersed phase was in dynamic and thermodynamic equilibrium with the carrier phase. This required that the density of the dispersed matter be very close to that of the carrier phase as well as the diameter of the dispersed matter be extremely small. When these two requirements are taken to their limits, this results in gaseous flow with dispersed gaseous particles. Versions of LHF models were constructed to include the effects of turbulent fluctuations. Nonetheless its applicability was limited by the aforementioned limitations, namely density ratios and disregard for relative velocity slip. Faeth (1983) points out that the LHF methods, when applied to atomizers/injectors with sprays consisting of uniform and very small particles (10 μm) may provided a good estimate for the extent of the spray boundaries.

Later on, Deterministic Direct Discrete Models (DDDM) focused on modeling evaporating or combusting dilute sprays for several particle sizes and extending the result to the whole spray. Unlike LHF models they address the relative velocity difference between particle and surrounding fluid and are not limited to small density ratios between dispersed and carrier phases. DDDM were primarily concerned with increasing the accuracy of droplet size evolution predictions or species concentrations within the vapor cloud surrounding the particle, than with modeling the dispersion due to turbulence. Faeth (1983) reviewed the various implementations of available DDDM and their effectiveness however, Kuo & Acharya (2012) summarize their limitation as requiring a high degree of calibration for each specific case in order to obtain reliable predictions.

This, in turn, is possible only for flows where detailed experimental measurements have been performed and even then the model, with its tuned parameters, is applicable only under very similar operating conditions and geometries. To address the limitations of the previous models Yuu *et al.* (1978) developed one of the first Stochastic Direct Discrete Models (SDDM) where they prescribed fluctuating velocity components to the dispersed phase. The model simulated the dispersion of dust particles in a round jet and was compared against experimental measurements. The fluctuating velocity components of the particles were prescribed depending on their location within the jet from the turbulence intensity measurements of Corrsin & Uberoi (1943,1949,1951), Liepman & Laufer (1947) and Laurence (1956) quoted therein. For the mixing layer region, in the axial and radial directions respectively:

$$\left\langle u_z^{'2} \right\rangle = 0.0217 U_o^2 e^{(-200\eta_1^2)} \;\&\; \left\langle u_r^{'2} \right\rangle = 0.0103 U_o^2 e^{(-217\eta_1^2)}$$

and for the main regions:

$$\left\langle u_z^{'2} \right\rangle = \frac{1.91 U_o^2 e^{(-154\eta^2)}}{\bar{z}^2} \;\&\; \left\langle u_r^{'2} \right\rangle = \frac{2.26 U_o^2 e^{(-178\eta^2)}}{\bar{z}^2}$$

where U_o is the bulk velocity, $\bar{r} = r/D$, $\bar{z} = z/D$, $\eta = \bar{r}/\bar{z}$ $\eta_1 = (\bar{r}-0.5)/\bar{z}$.

The agreement with experimental results was good, however the method is heavily dependent on these empirical relationships for the fluctuating components. In the absence of detailed experimental measurements for specific geometries –in order to generate such tailored empirical relationships– the model breaks down. Although its application was limited, the model served to establish the principle of prescribing a fluctuating velocity component to every particle, thereby mimicking the interaction between a single eddy and a perturbed particle. The breakthrough, however, in SDDM models came when Gosman & Ioannides (1981) (hereafter G&I) established a criterion for determining the eddy-particle interaction and prescribed fluctuating velocity components that were Gaussian in nature. The latter came about as a result of the experimental measurements of Hetsroni & Sokolov (1971) and Ribero & Whitelaw (1975) in turbulent round jets. In the G&I model, the fluctuating velocity component of the eddy, $\mathbf{U_p'}$, is assumed to be constant and is randomly sampled from a probability density function. The velocity is typically calculated by randomly sampling a *Gaussian* probability distribution of zero mean and a standard deviation estimated from the local value of the turbulent kinetic energy, k, according to:

$$u_{rms,i} = \sqrt{2/3k}$$

where u_{rms} is the root mean square of the continuous phase fluctuating velocity components and the above relationship with the specific turbulent kinetic energy is valid when these fluctuations are isotropic. Each fluctuating velocity component is calculated independently of the others as well as independently of the choices at the previous instance in time. In this model the particle is assumed to interact with an eddy for a time equal to the interaction time, which is also sometimes referred to as the Turbulence Correlation Time (TCT), $t_{interaction}$. This is defined as

the minimum of the eddy lifetime, t_e or the particle transit time/crossing time, t_c:

$$t_{interaction} = min(t_e, t_c)$$

where t_e is calculated from:

$$t_e = \frac{l_e}{\sqrt{2k/3}}$$

and l_e is the characteristic dimension of the eddy given by a dissipation length scale assuming isotropic fluctuating velocities:

$$l_e = \frac{C^{3/4}k^{3/2}}{\varepsilon}$$

where ε is the dissipation rate of the turbulent kinetic energy. The term *dissipation* is a confusing one although it is the one used in the literature. Because this estimate is not the dissipation length scale but rather a quantity much closer to the integral length scale in size. It has retained this name since in the RANS framework the energy is dissipated across all the scales unlike LES where there is a clear distinction between resolved and unresolved scales. **For the remainder of this thesis, wherever there is a mention of particles interacting with 'eddies' in a RANS context, it is this length scale, l_e that is being referred to.** The particle crossing time[2] is defined as follows:

$$t_c = -\tau_p \ln\left(1 - \frac{l_e}{\tau_p \left|\mathbf{U_f} - \mathbf{U_p}\right|}\right)$$

where τ_p is the particle relaxation time:

$$\tau_p = \frac{4\rho_p d_p}{3\rho C_D \left|\mathbf{U_f} - \mathbf{U_p}\right|}$$

The purpose of selecting the smaller of the two quantities is to ensure that a particle interacts with an eddy for as long as its displacement (along its computed trajectory) is smaller than the characteristic dimension of the eddy, that is, for a time equal to t_e. If t_c is very large, the implication is that the particle is moving slowly, with very little inertia and becomes 'trapped' within the eddy, so that the interaction time between the particle and eddy should again be at most equal to the eddy lifetime, t_e.

The Gosman & Ioannides (1981) approach remains to date the most widely used method although a few researchers (Shuen *et al.* (2003)) have proposed small improvements, calculating slightly different values for the constants. Although a range of constants is available in the literature, it should not be assumed that these are arbitrarily selected. Rather, through multiple realizations of simulated particle dispersion, the turbulence statistics of the model are compared to those of the experimental setup and the value of the constants are selected in order to improve the agreement. However, it should be noted, that depending on the unique characteristics of each test case there can be a need for a significant amount of adjustment to these constants.

Furthermore, Yeoh & Tu (2009) note that the Lagrangian and Eulerian autocorrelations are

[2]Note that sometimes the natural logarithm is omitted from the expression, in which case the definition bears remarkable similarity to the minimum crossing time definition, $t_c = \frac{l_e}{\left|\mathbf{U_f} - \mathbf{U_p}\right|}$. This is done because the particle –eddy relative velocity is not actually known and must be approximated by its value at the beginning of the interaction as noted by Yeoh & Tu (2009).

dependent on the choice of definition for the eddy lifetime and eddy size respectively. In these simple SDDM the desired effect, that is a linear decrease, on the Lagrangian autocorrelation is achieved implicitly through the repeated selection of random velocities. Thus the time correlation is treated in a very simple manner and no endeavor is made to address the spatial correlations and account for the anisotropy of the carrier phase. Accounting for anisotropy requires knowledge of how fluid elements are evolving around the discrete particle and relating the two. This approach was extended by Berlemont *et al.* (1990) and Burry & Bergeles (1993) with predicted particle velocities and fluxes that agreed closer with the experimental measurements of Shuen *et al.* (1983). However, it required construction of spatial and temporal correlations function tensors which are computationally expensive to both construct and store. Most important though is that, in order to construct these tensors, experimental measurements are required in order to determine the constants for the correlation functions. In the absence of this information the benefits of modeling the spatial anisotropy limit the applicability of the model to geometries where detailed measurements have been made.

1.4 Review of Lagrangian Methods

The purpose of this section is to review the modeling approaches capable of predicting the relative particle dispersion and to extensively discuss their limitations. This is a necessary exercise if a novel approach is to be identified that will permit the development of a new dispersion model for RANS with improved particle dispersion. The need for a new RANS model stems from the inability of the currently used models, namely the G&I derived models, to predict accurate levels of particle dispersion as well as particle preferential concentrations. The G&I models were introduced earlier in this chapter and their shortcomings may be primarily attributed to the limited description of turbulence, they employ for the dispersion of particles. The available models will be reviewed in an effort to identify those capable of allowing us to introduce the required physics (even in a phenomenological sense) in order to provide a means for predicting more realistic particle dispersion as well as forming a basis for a model capable of predicting particle preferential concentration.

The starting point in the development of an improved model for particle dispersion model is a review of the theory of Lagrangian Dynamics. Since we are interested in turbulent flows, covering the theory of one-particle diffusion and then two-particle diffusion is instructive. The latter is especially interesting if a dispersion model is to be developed that is capable of predicting particle preferential concentration; Apart from the immediate relevance to the problem at hand (*i.e.* the development of a new dispersion model) the following review is also useful for the literature review on spectral methods and KS. A substantial amount of the early work done in an attempt to understand and characterize turbulence was done in a Lagrangian framework, and as will be shown, several of the concepts introduced in these sections concerning the particle diffusion are relevant and useful for the comprehension of concepts introduced later on during the review of spectral methods.

1.4.1 Lagrangian Overview

Turbulent transport is responsible for the large amount of mixing observed in real flows, which is of both practical and theoretical importance and interest. Practical, as mentioned already, because most real flows lie in the turbulent regime, whether we are dealing with combustion processes or polyp transport in oceans resulting in new coral reef formations –as well as everything in between–. Theoretical, because turbulence to this day remains one of the great unsolved problems in physics.

As a turbulent flow evolves and moves through space it carries with it packets of fluid. This packet or parcel of fluid is small compared to the Kolmogorov microscale but much larger than the molecular scale, in order that it may still be treated as a continuum. Turbulent diffusion, is this movement of fluid packets from one region of the flow into another, resulting in the transport of momentum, kinetic energy and contaminants or passive tracers. For the majority of flows one of the general attributes of turbulence and more specifically of the *Reynolds Stress* is its ability to drive spatial inhomogeneities towards uniformity.

Despite recent advances in computational capabilities it is still not feasible to precisely model the overwhelming majority of flows of engineering or practical importance, as will be discussed in subsequent sections on current modeling practices and capabilities. The limitation arises because the higher the Reynolds number of the flow in question the smaller the scale that must be resolved. The smaller the scale, the greater the number of locations, for a given size flow, where the partial differential equations must be solved, thus significantly increasing the computational cost.

1.4.2 Lagrangian Dynamics

Historically, the distinction between an Eulerian and a Lagrangian frame of reference can be made by analogy to trains passing through a station. In the Eulerian case, the passenger or observer is standing on the platform observing the trains arriving and departing from the station platform whereas, in the Lagrangian case, the observer would be aboard one of the carriages observing the world move past him, occasionally coming to a stop in a station.

While the above statement definitely holds, Holmes *et al.* (1996) explain how in the realm of Fluid Mechanics a further point should be made. This is closely related to the laboratory experiments that were used (and still are) to study flows over the last century, namely channel flows and wind tunnels. These have an inlet and an outlet, prescribed to be on the left and right sides, respectively, in order to match our mental construct of the situation. These flows are typically on average steady, but instantaneously unsteady. They tend to vary slowly in the flow direction and suddenly in the spanwise directions[3], with the use of simple dimensional arguments the cross-sectional structures at different locations appear similar (the Eulerian viewpoint). However, one may also think of time as flowing from the left to the right due to western convention of righting from left to right. That is, the initial state of the fluid parcel is taken to be the state when it passed the inlet of the apparatus and its evolution is tracked -and drawn- from left to right until it exits the domain. In other words parcels of fluid or material elements are found in

[3]For the remainder of this thesis, the spanwise direction will refer to the cross-stream direction, one that is perpendicular to the streamwise direction, the principal direction of the flow.

their youth next to the inlet, traced through their lifetime along the length of the channel/tunnel until they pass the exit boundary in their old age (the Lagrangian viewpoint). The two points of view are ultimately equivalent, as it is presumed that small statistical inhomogeneities are dynamically irrelevant and so far this is supported by the literature.

The equations that govern viscous fluid flow are the Navier-Stokes Equation and the continuity equation, cast here in an Eulerian framework for an incompressible fluid:

$$\frac{\partial \mathbf{u}\left(\mathbf{r},\mathrm{t}\right)}{\partial t}+\left(\mathbf{u}\cdot\boldsymbol{\nabla}\right)\mathbf{u}+\frac{\boldsymbol{\nabla}\mathrm{p}}{\rho}+\nu\nabla^{2}\mathbf{u}=\mathbf{f}$$

$$\nabla\cdot\mathbf{u}=0$$

where $\mathbf{u}\left(\mathbf{r},\mathrm{t}\right)$ and $\mathrm{p}\left(\mathbf{r},\mathrm{t}\right)$ are the Eulerian velocity and the pressure fields field respectively at location $\mathbf{r}$ and time t, ν is the kinematic viscosity of the fluid, and $\mathbf{f}$ are the sum of body forces acting on the packet. Adopting a Lagrangian approach can be very beneficial as Lagrangian Dynamics are well suited to studies of small scale phenomena or many point correlations functions, like particle dispersion or coalescence. Eyink (2012) posits that Lagrangian Dynamics are closely related to the mechanism of mixing while in the recent work of Lucci *et al.* (2013) the authors identify that they are especially important in calculations of the turbulent kinetic energy spectrum of inertial particle laden flows where an Eulerian approach results in a corrupted energy spectrum[4]. In the Lagrangian frame of reference the Navier-Stokes Equation is:

$$\frac{d\mathbf{u_L}\left(\mathbf{r}_0,\mathrm{t}\right)}{dt}+\left[\nabla\mathrm{p}-\nu\nabla^{2}\mathbf{u}\right]_{L}\left(\mathbf{r}_0\mid t\right)=\mathbf{f_L}\left(\mathbf{r}_0\mid t\right)$$

where the subscript L indicates Lagrangian properties and the terms in brackets imply that the function is taken at $\mathbf{r}=\mathbf{r_L}\left(\mathbf{r_0}\mid t\right)$.

Fundamentals of Lagrangian Dynamics

Before reviewing one-particle and two-particle turbulent diffusion it necessary to start with the fundamental concepts of Lagrangian Dynamics. The approach outlined here follows closely that of Tennekes and Lumley (1972) and Eyink (2012). The central idea behind Lagrangian dynamics is the notion of a Lagrangian flow which traces the location $\mathbf{a}$ of a particle at time t_0 to its new location $\mathbf{X_{t_0}^{t}}\left(\mathbf{a}\right)=\mathbf{x}$ at a time t after a short time interval dt. It should be noted here that $t<t_0$ just as easily as $t>t_0$. Lagrangian traces are one-to-one mappings[5]of the flow domain and given the smooth nature of the flow field ($\mathbf{u}(\mathbf{x},t)$) this means that they too in turn are invertible, that is: $\mathbf{a}=\left(\mathbf{X_{t_0}^{t}}\right)^{-1}\left(\mathbf{x}\right)$. The Lagrangian flow satisfies the following equation:

$$\frac{d}{dt}\mathbf{X_{t_0}^{t}}(\mathbf{a})=\mathbf{u}\left(\mathbf{X_{t_0}^{t}}(\mathbf{a}),t\right)\ \mathbf{X_{t_0}^{t_0}}(\mathbf{a})=\mathbf{a}$$

A further property of Lagrangian mapping is that two successive mappings from time $t_0\rightarrow t_1$ and $t_1\rightarrow t_2$ are identical to a single mapping from $t_1\rightarrow t_2$: $\mathbf{X_{t_1}^{t_0}}\cdot\mathbf{X_{t_2}^{t_1}}=\mathbf{X_{t_2}^{t_0}}$ and the trivial

[4]However, it should be noted that due to dependance of the Lagrangian kinetic Energy Spectrum $\frac{\partial}{\partial t}E_L(t,\omega)$ on the flow history (time non-locality) this cannot be computed directly in a Lagrangian framework and the authors adopted a quasi-Lagrangian framework and the derivation of Eulerian-Lagrangian bridges.

[5]Strictly speaking they are diffeomorphisms (isomorphisms of a smooth manifold); a space where one can perform calculus and that locally resembles Euclidean space, Chicone (1999) & V.I.Arnold (1988)

case of $\mathbf{X_t^t} = \mathbf{I}$

The Jacobian determinant is unity: $|^{\partial \mathbf{X_{t_0}^t(a)}}/_{\partial \mathbf{a}}| = 1$ for incompressible flows (solenoidal velocity field, $\nabla \cdot \mathbf{u} = 0$). Let us now define the inverse Lagrangian map which traces the location $\mathbf{x}$ of the particle at time t back to its label $\mathbf{A_{t_0}^t(x)} = \mathbf{a}$ at the initial time t_0: $\mathbf{A_{t_0}^t} = \left(\mathbf{X_{t_0}^t}\right)^{-1}$which arises from the group property $\mathbf{A_{t_0}^t} = \mathbf{X_t^{t_0}}$ resulting from the aforementioned property regarding successive mappings. For an incompressible flow, we expect the Jacobian determinant to be equal to unity:

$$\left|\frac{\partial \mathbf{A_{t_0}^t(x)}}{\partial \mathbf{x}}\right| = \left|\frac{\partial \mathbf{X_{t_0}^t(a)}}{\partial \mathbf{a}}\right| = 1$$

Finally, the fact that the labels $\mathbf{a}$ are Lagrangian invariants and constant with respect to time along their corresponding particle trajectories can be arrived at by employing the chain rule whilst differentiating the following relation:

$$\mathbf{A_{t_0}^t}\left(\mathbf{X_{t_0}^t}\left(\mathbf{a}\right)\right) = \mathbf{a}$$

$$\partial_t \mathbf{A_{t_0}^t}\left(\mathbf{X_{t_0}^t}\left(\mathbf{a}\right)\right) + \mathbf{u}\left(\mathbf{X_{t_0}^t}\left(\mathbf{a}\right),t\right) \cdot \nabla_{\mathbf{x}} \mathbf{A_{t_0}^t}(\mathbf{X_{t_0}^t}(\mathbf{a}) = 0$$

or [6]

$$D_t \mathbf{A_{t_0}^t}\left(\mathbf{x}\right) = \left[\partial_t + \mathbf{u}\left(\mathbf{x},t\right) \cdot \nabla_{\mathbf{x}}\right] \mathbf{A_{t_0}^t}(\mathbf{x}) = 0$$

Lagrangian dynamics are intrinsically linked to the advection of an *ideal* passive scalar:

$$\partial_t \theta(\mathbf{x},t) + \mathbf{u}(\mathbf{x},t) \cdot \nabla_{\mathbf{x}} \theta(\mathbf{x},t) = 0$$

reducing to when solved using the method of characteristics:

$$\theta(\mathbf{x},t) = \theta(\mathbf{A_{t_0}^t}(\mathbf{x}), t_0)$$

$$\theta(\mathbf{X_{t_0}^t}(\mathbf{a}), t_0) = \theta(\mathbf{a}, t_0)$$

In the case that the scalar is *non-ideal,* diffusion must be included in the equation as well resulting in:

$$\partial_t \theta(\mathbf{x},t) + \mathbf{u}(\mathbf{x},t) \cdot \nabla_{\mathbf{x}} \theta(\mathbf{x},t) = \kappa \bigtriangledown^2 \theta(\mathbf{x},t)$$

Solving this stochastic ordinary differential equation for an n-dimensional Brownian motion $(\mathbf{W}(t') = (W_1(t'), ..., W_n(t')))$:[7]

$$d\widetilde{\mathbf{X}}_{\mathbf{t}}^{\mathbf{t}'}(\mathbf{x}) = \mathbf{u}(\widetilde{\mathbf{X}}_{\mathbf{t}}^{\mathbf{t}'}(\mathbf{x}), t') + \sqrt{2\kappa} d\mathbf{W}(t')$$

Finally, setting $\widetilde{\mathbf{A}}_{\mathbf{t_0}}^{\mathbf{t}}(\mathbf{x}) \equiv \widetilde{\mathbf{X}}_{\mathbf{t}}^{\mathbf{t_0}}(\mathbf{x})$ one obtains : $\theta(\mathbf{x},t) = E\left[\theta(\mathbf{A_{t_0}^t}(\mathbf{x}), t_0)\right]$ where E denotes averaging over the successive Brownian motion realizations.

We can now use these concepts relating to an advecting velocity ($\mathbf{u}$(x,t)) to formulate a solution of the equations governing fluid mechanics, namely the Navier-Stokes equation. Here

[6] The subscript t_0 is often omitted to simplify or de-clutter the functions $\mathbf{A_{t_0}^t}(\mathbf{x})\&\mathbf{X_{t_0}^t}(\mathbf{a})$ to $\mathbf{A}(\mathbf{x},t)\&\mathbf{X}(\mathbf{a},t)$ respectively.

[7] For details see Sawford (2001)

it will be cast in terms of the Lagrangian flow map $\mathbf{X}_{\mathbf{t_0}}^{\mathbf{t}}(\mathbf{a})$ and its derivatives:

$$\frac{d}{dt}\mathbf{X}_{\mathbf{t_0}}^{\mathbf{t}}(\mathbf{a}) = \mathbf{u}\left(\mathbf{X}_{\mathbf{t_0}}^{\mathbf{t}}(\mathbf{a}), t\right) = \mathbf{v}_{\mathbf{t_0}}^{\mathbf{t}}(\mathbf{a})$$

$$\frac{d^2}{dt^2}\mathbf{X}_{\mathbf{t_0}}^{\mathbf{t}}(\mathbf{a}) = \frac{d}{dt}\mathbf{v}_{\mathbf{t_0}}^{\mathbf{t}}(\mathbf{a}) = (D_t\mathbf{u})\left(\mathbf{X}_{\mathbf{t_0}}^{\mathbf{t}}(\mathbf{a}), t\right)$$

Employing the Navier-Stokes equation for the Eulerian field and using $D_t = \partial_t + \mathbf{u}(\mathbf{x}, t) \cdot \bigtriangledown_{\mathbf{x}}$[8] result in:

$$\frac{d^2}{dt^2}\mathbf{X}_{\mathbf{t_0}}^{\mathbf{t}}(\mathbf{a}) = -\nabla p\left(\mathbf{X}_{\mathbf{t_0}}^{\mathbf{t}}(\mathbf{a}), t\right) + \nu\triangle\mathbf{u}\left(\mathbf{X}_{\mathbf{t_0}}^{\mathbf{t}}(\mathbf{a}), t\right)$$

Despite the basis for this equation being Newton's 2^{nd} law, the Laplacian operator introduces a substantial degree of complexity.

Eyink (2012) points out an interesting result arising from Salmon (1988) in the inviscid case where the equation reduces to Euler's equation and the Lagrangian equation of motion follows from a least-action principle where the particle trajectories minimize the action S for every fluid element $\mathbf{a}$:[9]

$$S_{t_0}^{t}[\mathbf{x}, \mathbf{a}] = \int_{t_0}^{t}\left[\left|\dot{\mathbf{X}}(\mathbf{a}, \tau\right|^2 - p(\mathbf{X}(\mathbf{a}, t))\right] d\tau$$

Several important results arise when the equations of motion are cast in such a manner. Perhaps the most important one is the Cauchy Vorticity Equation or the Cauchy Form of the Vorticity Equation which describes the rate of vortex stretching and rotation: [10]

$$\boldsymbol{\omega}(\mathbf{x}(\mathbf{a}, t)) = \boldsymbol{\Omega}(\mathbf{a}) \cdot \nabla_{\mathbf{a}}\mathbf{X}(\mathbf{a}, t)$$

Durbin & Petterson-Reif (2001) relate the evolution of the vorticity to the infinitesimal deformation of a line element, $\delta\mathbf{a}$ between two neighboring fluid particles $\mathbf{a}$ and $\mathbf{a} + \delta\mathbf{a}$. Two neighboring particles will initially follow very similar paths but eventually the trajectories will begin to deviate from each other.

$$\delta\mathbf{X}(\mathbf{a}, t) = \mathbf{X}(\mathbf{a} + \delta\mathbf{a}, t) - \mathbf{X}(\mathbf{a}, t)) = \delta\mathbf{a} \cdot \nabla_{\mathbf{a}}\mathbf{X}(\mathbf{a}, t)$$

The physical interpretation of the Cauchy formula is that the evolution of the vorticity vector is like an infinitesimal material line element. An important point to be made is that this elegant relationship between the mean flow and the vorticity is applicable solely in the case of irrotational mean flow (*i.e.* $\nabla\times\mathbf{U} = 0$). P.G. Saffman (1992), in his classical monograph provides alternative relationships for the cases of more complicated flows. The separation between two particles formed the basis of the initial research into the field of turbulence at the beginning of the 20^{th} century by G.I Taylor (1921) and L.F. Richardson (1926) and the results are still relevant today in that these provide not only a quantitative answer to the behavior of separation with time

[8] This is the definition of the total (material) derivative, $^{D}/_{Dt} = {}^{\partial}/_{\partial t} + \mathbf{u} \cdot \bigtriangledown$ and is the relationship linking the time derivatives in the Eulerian and Lagrangian frames; the unsteady time derivative at a fixed point in space, ${}^{\partial}/_{\partial t}$ and the material derivative, ${}^{D}/_{Dt}$ evaluated along the trajectory of the fluid particle, respectively.

[9] The action is a functional, defined as the integral of the Lagrangian between two times and uses the trajectory or path as an argument and results in a Real number with units of Joule*Seconds.

[10] This is a direct result of the Cauchy invariant, $\boldsymbol{\Omega} = (\boldsymbol{\omega}\cdot\nabla_{\mathbf{x}})\mathbf{A}$, $D_t\boldsymbol{\Omega} = 0$ & $D_t\mathbf{A} = 0$

under some assumptions but also a framework for describing separation in the absence of these assumptions.

One-particle diffusion & statistics

The prediction of transport phenomena in all but the simplest cases is nearly impossible and, even when an analytical solution is possible as is the case of a stationary, zero mean flow with homogeneous turbulence the physical validity of the solution is questionable[11].

One particle diffusion in turbulent flows was first studied by G.I. Taylor (1921). As Chronopoulos (2005) explains, G.I Taylor's reasoning was that the description of turbulent diffusion must be similar to the statistical description of fluid element motion. Taylor was able to show that the fluctuating components of successive fluid elements were correlated to the fluctuating velocity components parallel to the same direction after some later time interval. The main focus of interest is the mean square dispersion of particles: $\left\langle |\delta \mathbf{X}(\mathbf{a}, t_0; t)|^2 \right\rangle$ where the displacement of the particle between times is:

$$\delta \mathbf{X}(\mathbf{a}, t) \equiv \mathbf{X}(\mathbf{a}, t_0 + t) - \mathbf{X}(\mathbf{a}, t_0)$$

and the averaging operation $\langle\rangle$ may be spatial, temporal or both. One may even perform ensemble averaging of velocities. When the mean square is independent of $\mathbf{a}$ and t_0, *i.e.* the flow is stationary and homogeneous, it may be reduced to[12]:

$$\delta \mathbf{X}(\mathbf{a}, t) = \mathbf{X}(\mathbf{a}, t) - \mathbf{a} = \int_0^t ds \mathbf{v}(\mathbf{a}, s)$$

where $\mathbf{v}(\mathbf{a},s)$ denotes a Lagrangian velocity. In turn the mean square dispersion of particles will become:

$$\left\langle |\delta \mathbf{X}(\mathbf{a}, t_0; t)|^2 \right\rangle = \int_0^t ds \int_0^t ds' \left\langle \mathbf{v}(s') \cdot \mathbf{v}(s) \right\rangle$$

If the turbulence is stationary and homogeneous, then the Lagrangian velocity process is stationary in time and the statistics are independent of both space and time, resulting in:

$$\left\langle \mathbf{v}(s') \cdot \mathbf{v}(s) \right\rangle = \left\langle \mathbf{v}(s' - s) \cdot \mathbf{v}(0) \right\rangle$$

which along with employing the following substitutions for the evaluation of the integrands:

[11] Bird *et al.* (1960)) explain on the following physical ground; first the energy being dissipated to the smaller scales will eventually decay and die out in the absence of a mean velocity gradient so in turn this is no longer a stationary flow; secondly and more important as Tennekes & Lumley (1972) point out, the characteristic time scale of a fluid parcel is of the order of the decay time. The implication is that no real flow with decaying energy can appear to be stationary to a wandering point.

[12] For the sake of simplicity $t_0 = 0$ in the equations with no loss of universality.

$\tau = s' - s$ & $T = 1/2\,(s' + s)$, results in : [13]

$$\left\langle |\delta \mathbf{X}(t)|^2 \right\rangle = 2 \int_0^t d\tau\, (t - \tau)\, \langle \mathbf{v}(\tau) \cdot \mathbf{v}(0) \rangle$$

As the time, t, approaches infinity, the following result is obtained:

$$\lim_{t\to\infty} \left\langle |\delta \mathbf{X}(t)|^2 \right\rangle = 2 \int_0^\infty d\tau\, (t)\, \langle \mathbf{v}(\tau) \cdot \mathbf{v}(0) \rangle \leftrightarrow \lim_{t\to\infty} \frac{\left\langle |\delta \mathbf{X}(t)|^2 \right\rangle}{2t} = D$$

where

$$D = \int_0^\infty d\tau\, \langle \mathbf{v}(\tau) \cdot \mathbf{v}(0) \rangle \; < +\infty$$

Provided the stated condition (stationary & homogeneous turbulence) remains true particle dispersion in the limit is diffusive:

$$\left\langle |\delta \mathbf{X}(t)|^2 \right\rangle \propto 2tD$$

This is the main result at which G.I. Taylor arrived at in 1921[14]. An implication of the aforementioned conditional statement is that the time-correlations of the Lagrangian velocity ($\mathbf{v}(\mathbf{a},t)$) must decay rapidly, resulting in the relevant characteristic time:

$$T_L = \frac{1}{\langle |\mathbf{v}(0)|^2 \rangle} \int_0^\infty \mathbf{v}(\tau) \cdot \mathbf{v}(0) d\tau = \frac{D}{\langle |\mathbf{v}(0)|^2 \rangle}$$

This result is known as the Lagrangian integral time-scale and $\delta \mathbf{X}(t)$ operates diffusively whilst $t \gg T_L$, known as the Markov limit. Following, Tennekes' & Lumley's (1972) dimensional reasoning, the Lagrangian time scale T_L must be of the same order as the ratio of the integral length scale to the fluctuating velocity:

$$T_L \sim {}^{l}/_{u}$$

A similar result may be arrived at by using a mixing length approach; the eddy viscosity or turbulent viscosity must be of the order of the product of the square of the RMS velocity and the characteristic time-scale:

$$\nu_T \sim u^2 T_L$$

Hence one may think of D as an effective turbulent viscosity in the flow, ν_T, since :

$$T_L \sim {}^{l}/_{u} \sim {}^{\nu_T}/_{u^2}$$

[13] Where use has been made of $\langle \mathbf{v}(\tau) \cdot \mathbf{v}(0) \rangle = \langle \mathbf{v}(0) \cdot \mathbf{v}(-\tau) \rangle$ and that the Jacobian of the transformation is ${}^{\partial(\tau,T)}/_{\partial(s,s')} = 1$

[14] The resultant equation is quite similar to that governing Brownian motion and one could cast this in a more general form for d-dimensional Brownian motion, $\mathbf{W}(t)$: $\lim_{e\to 0} \frac{\left\langle |\delta \mathbf{X}(t/e)|^2 \right\rangle}{\sqrt{2D/e}} = \mathbf{W}(t)$

This is, quite similar to the way CFD closure models introduce an effective viscosity for the modeling of the unresolved scales. Durbin & Petterson-Reif (2001) call this an eddy diffusivity, defined as one-half of the rate of the mean square dispersion of trajectories, originating from a common point. However, the eddy diffusivity should not be interpreted as an instantaneous metric of dispersion rather as the averaged effect of the turbulence. More formally, while the Markov limit still holds, eddy diffusion should be thought of as a Markovian approximation for the random trajectory of fluid elements. Conversely, when $t \ll T_L$, according to Taylor (1921), the standard deviation of the particle from its initial position will be proportional to t. Which is to say that no substantial change in velocity is expected along the path/trajectory during the very short time span. At this point may be necessary to introduce the statistical representations that are pertinent to the matter at hand and to point out that, for single point statistics, Eulerian $\mathbf{u}(\mathbf{x},t)$ are identical to the Lagrangian velocity statistics $\mathbf{v}(\mathbf{a},t)$ provided the flow is incompressible and homogeneous in the direction of interest[15]:

$$\left\langle |\mathbf{v}(0)|^2 \right\rangle = \left\langle |u(0)|^2 \right\rangle = u_{rms}^2$$

The next paragraph will aim to summarize the single-point Lagrangian statistics. The one-particle probability distribution, $P_t^{(1)}$, with the aid of the Dirac delta function provides a more elegant representation of one-particle diffusion than the mean dispersion:

$$P_t^{(1)}(\mathbf{x}|\mathbf{a}) = \langle \delta \left(\mathbf{X} \left(\mathbf{a}, \mathbf{t} \right) - \mathbf{x} \right) \rangle$$

For homogeneous flows and the corresponding statistics the conditional statement is redundant and may be omitted:

$$P_t^{(1)}(\mathbf{x} - \mathbf{a}) = P^{(1)}(\mathbf{x} - \mathbf{a}|0)$$

And as time approaches infinity ($t \to \infty$) this becomes:

$$P_t^{(1)}(\mathbf{x} - \mathbf{a}) \propto \exp(\frac{-|\mathbf{x}-\mathbf{a}|^2/4Dt}{(4\pi Dt)^{d/2}})$$

This result is of interest when evaluating mean scalar evolution: $\bar{\theta}\left(\mathbf{x},t\right) = \langle \theta \left(\mathbf{x},t\right) \rangle$, where the instantaneous scalar is defined as a function of the initial value of the scalar, θ_0, and the initial position as follows:

$$\theta\left(\mathbf{x},t\right) = \theta_0\left(\mathbf{A}\left(\mathbf{x},t\right)\right) = \int d^d a \theta_0(\mathbf{a}) \delta\left(\mathbf{A}\left(\mathbf{x},t\right) - \mathbf{a}\right)$$

[15] In the non-homogeneous case, the variance of the Lagrangian velocity will receive one contribution from the Eulerian velocity variance and another one from the square of the difference between the bulk velocity and Eulerian mean velocity. In other words, a Lagrangian point's velocity will fluctuate due to both the fluctuating velocity at the Eulerian point and also because of the difference between the mean Eulerian velocity at that point and the bulk velocity of the flow.

with the aid of the Dirac delta function and incompressibility this becomes[16]:

$$\theta(\mathbf{x},t) = \int d^d a \theta_0(\mathbf{a}) \delta(\mathbf{X}(\mathbf{a},t) - \mathbf{x})$$

For an initial scalar field that is statistically independent of the velocity, applying the averaging operation reduces the equation to:

$$\bar{\theta}(\mathbf{x},t) = \int d^d a \left\langle \theta_0(\mathbf{a}) \delta(\mathbf{X}(\mathbf{a},t) - \mathbf{x}) \right\rangle = \int d^d a \left\langle \theta_0(\mathbf{a}) \right\rangle \left\langle \delta(\mathbf{X}(\mathbf{a},t) - \mathbf{x}) \right\rangle =$$

$$= \int d^d a \bar{\theta_0}(\mathbf{a}) P_t^{(1)}(\mathbf{x}|\mathbf{a})$$

Hence, the mean concentration at a point is the concentration carried by the particle multiplied by the probability of the particle being at the point, integrated over the total population of particles that may be found there. As Tennekes & Lumley (1972) point out, the profound implication of this result is that the probability density may be measured by inserting a contaminant at some initial location and measuring the mean concentration field at a later instant. It should now be clear how and why non-diffusive contaminants or minute-sized particles may be used to mark the evolution of Lagrangian points. However, these results are only true for stationary flows. Batchelor (1957) describes the process of treating non-stationary flows by transforming the particle velocity into a suitable random function, with the provision that the particles/elements do not move from the turbulent shear layers into regions of laminar flow[17]. This was achieved through the adjustment, at downstream locations, of the length and velocity scales as functions of the distance from the originating point raised to some positive and negative exponent respectively. Meanwhile the corresponding variation of the timescale was raised to an exponent equal to the sum of the velocity and length scale exponents. This was achieved through the formulation of a similarity hypothesis in the Lagrangian frame, in a similar manner to the Eulerian similarity hypothesis.

Two-particle relative diffusion & statistics

The following section will address two-particle turbulent diffusion. Two-particle statistics are paramount to describing the evolution of particle clouds and clusters as the same equations presented may be applied between a particle and every other particle within the cloud to completely describe its evolution. The problem was first tackled by Richardson (1926) in an effort to derive an equation to describe the phenomenon with an equation similar to Fick's law but capable of accounting for the significant eddying motion present in the atmosphere. This was accomplished whilst observing various dispersion problems, ranging from volcanic ash plumes and primitive anemometer data to balloon pairs drifting in the atmosphere. Here we outline the results in a similar manner to the one-particle diffusion and we will arrive at Richardson results once a prob-

[16] The implication of incompressibility is $|\partial \mathbf{A}/\partial \mathbf{x}| = 1$, the Dirac delta is:

$$\delta(\mathbf{A}(\mathbf{x},t) - \mathbf{a}) = \frac{\delta(\mathbf{X}(\mathbf{a},t) - \mathbf{x})}{|\partial \mathbf{A}/\partial \mathbf{x}|} = \delta(\mathbf{X}(\mathbf{a},t) - \mathbf{x})$$

and $d^d a$ refers to d-dimensional space

[17] Observed experimentally three years earlier by Corrsin & Kistler (1954)

abilistic approach is adopted. Similar to the previous section, we are interested in the distance $\Delta^{(2)}(t)$ separating two particles at some instant in time, t, which were initially separated by a distance $\Delta_0^{(2)} = |\Delta \mathbf{a}_0|$, that is: $\Delta^{(2)}(t) = |\mathbf{X}(\mathbf{a}', t) - \mathbf{X}(\mathbf{a}, t)|$ where $\mathbf{a}' = \mathbf{a} + \Delta \mathbf{a_0}$. The starting point is to make the switch into the Hoelder space[18] with an exponent of yet unknown value h,

$$|\mathbf{u}(\mathbf{x}', t) - \mathbf{u}(\mathbf{x}, t)| \leq A|\mathbf{x}' - \mathbf{x}|^h$$

and through the use of the triangle inequality[19]:

$$^{d}/_{dt}|\mathbf{X}(\mathbf{a}', t) - \mathbf{X}(\mathbf{a}, t)| \leq |^{d}/_{dt}\left[\mathbf{X}(\mathbf{a}', t) - \mathbf{X}(\mathbf{a}, t)\right]|$$

Resulting in,

$$^{d}/_{dt}\Delta^{(2)}(t) \leq |\mathbf{u}(\mathbf{X}(\mathbf{a}', t), t) - \mathbf{u}(\mathbf{X}(\mathbf{a}, t), t)|$$

since $^{d}/_{dt}(\mathbf{X}(\mathbf{a}, t) = \mathbf{u}(\mathbf{X}(\mathbf{a}, t), t)$. Again through the Hoelder continuity we obtain:

$$^{d}/_{dt}\Delta^{(2)}(t) \leq A|\mathbf{X}(\mathbf{a}', t) - \mathbf{X}(\mathbf{a}, t)|^h = A\left[\Delta^{(2)}(t)\right]^h$$

The integration of this inequality is now straightforward yielding:

$$\Delta^{(2)}(t) \leq \left[\Delta_0^{(1-h)} + (1-h)A(t-t_0)\right]^{\frac{1}{1-h}}$$

It is now necessary to distinguish between the case where the Hoelder exponent, $h \to 1$ and $0 < h < 1$. In the first case where the exponent tends to unity we obtain:

$$\Delta^{(2)}(t) \leq \Delta_0 \left[1 + \frac{(1-h)A(t-t_0)}{\Delta_0^{1-h}}\right]^{\frac{1}{1-h}}$$

and taking the limit, $\lim_{n\to\infty}(1 + {}^{x}/_{n})^n = e^x$ resulting in:

$$\Delta^{(2)}(t) \leq \Delta_0 e^{A(t-t_0)}$$

Meanwhile if the exponent is bounded between 0 and 1 the following result is obtained:

$$\Delta^{(2)}(t) \leq [(1-h)A(t-t_0)]^{\frac{1}{1-h}}$$

It is also possible to cast the original Hoelder inequality into an approximate equality, that is: $|\mathbf{u}(\mathbf{x}', t) - \mathbf{u}(\mathbf{x}, t)| \cong A|\mathbf{x}' - \mathbf{x}|^h$ which will respectively yield as the time limit approaches infinity:

$$\Delta^{(2)}(t) \cong \begin{cases} \Delta_0 e^{A(t-t_0)} & while\ h \to 1\ \&\ t \to \infty \\ [(1-h)A(t-t_0)]^{\frac{1}{1-h}} & while\ 0 < h < 1\ \&\ t \to \infty \end{cases}$$

[18] The assumption that the advecting velocity field is Holder continuous is quite logical given the parabolic-elliptical nature of incompressible-viscous flow, see Tannhill *et al.* (1997)

[19] Here we are using the reverse triangle inequality to provide an estimate for the lower bound, $||x|-|y|| \leq |x-y|$

The interesting result is that in the first case the initial separation, Δ_0 is never forgotten while in the latter case it is lost as time tends to infinity. From "K41 theory" (Kolmogorov (1941)) the exponent h is determined to be equal to $1/3$ for the inertial range, $\eta \ll \Delta^{(2)}(t) \ll L$ (between the *Kolmogorov* and the Integral length scales):

$$\Delta^{(2)}(t) \propto A(t-t_0)^{\frac{3}{2}}$$

Casting this in the correct dimensional format yields:

$$\left[\Delta^{(2)}(t)\right]^2 \propto \langle\varepsilon\rangle\,(t-t_0)^3$$

Compared to the rate of growth of the diffusive case, here we notice that the separation distance grows much faster $\propto t^3$ and this exponential dependence is attributed to the fact that, as the two particles separate, they will start experiencing progressively greater relative velocities[20]. This is the famous result to which Richardson (1926) arrived at by considering the two-particle separation statistics: $\left\langle\left[\Delta^{(2)}(t)\right]^2\right\rangle \propto g_0\,\langle\varepsilon\rangle\,(t-t_0)^3$ where g_0 is known as the Richardson constant. We will derive this in a similar fashion shortly. Later on, Batchelor (1950) used dimensional arguments to validate the use of the similarity hypothesis for the derivation of a relationship relating the time derivative of the mean square separation distance $\left(\left\langle\Delta^2\right\rangle\right)$ between two particles to their initial separation distance (Δ_0), for a limited range of separations lying in the inertial sub-range region.

The two-particle probability distribution is :

$$P_t^{(2)}\left(\mathbf{x},\mathbf{x}'|\mathbf{a},\mathbf{a}'\right) = \left\langle\delta\left(\mathbf{X}\left(\mathbf{a},t\right)-\mathbf{x}\right)\delta\left(\mathbf{X}\left(\mathbf{a}',t\right)-\mathbf{x}'\right)\right\rangle$$

which for a spatially homogeneous field may be rewritten as[21]:

$$P_t^{(2)}\left(\mathbf{x},\mathbf{x}'|\mathbf{a},\mathbf{a}'\right) = P_t^{(2)}\left(\mathbf{x},\mathbf{x}+\Delta\mathbf{x}|\mathbf{a},\mathbf{a}+\Delta\mathbf{a}\right) = P_t^{(2)}\left(\mathbf{x}-\mathbf{a},\mathbf{x}-\mathbf{a}+\boldsymbol{\Delta}\mathbf{x}|\mathbf{0},\boldsymbol{\Delta}\mathbf{a}\right)$$

The probability density function in turn becomes:

$$\bar{P}_t^{(2)}\left(\boldsymbol{\Delta}\mathbf{x}|\boldsymbol{\Delta}\mathbf{a}\right) = \int d^d\mathbf{x} P_t^{(2)}(\mathbf{x},\mathbf{x}+\boldsymbol{\Delta}\mathbf{x}|\mathbf{0},\boldsymbol{\Delta}\mathbf{a})$$

and since knowledge of $\Delta\mathbf{a}$ is lost as $t \gg t_0$ we may write

$$\bar{P}_t^{(2)}\left(\boldsymbol{\Delta}\mathbf{x}|\boldsymbol{\Delta}\mathbf{a}\right) = \lim_{\boldsymbol{\Delta}\mathbf{a}\to 0} \bar{P}_t^{(2)}(\boldsymbol{\Delta}\mathbf{x}|\boldsymbol{\Delta}\mathbf{a})$$

Meanwhile the probability density function will depend solely on $|\boldsymbol{\Delta}\mathbf{x}|$, for an isotropic velocity field, or perhaps more accurately a field whose velocity statistics are isotropic, as knowledge of the magnitude and orientation of $|\Delta\mathbf{a}|$ is lost. Setting $|\boldsymbol{\Delta}\mathbf{x}| = l$ and in turn $\bar{P}_t^{(2)}\left(\boldsymbol{\Delta}\mathbf{x}\right) = \bar{P}_t^{(2)}\left(l\right)$

[20] This is evident in the Hoelder eq. above, *i.e.* $|\mathbf{u}\left(\mathbf{x}',t\right)-\mathbf{u}\left(\mathbf{x},t\right)| \propto |\mathbf{x}'-\mathbf{x}|^{1/3}$

[21] since $\mathbf{x}' = \mathbf{x}+\boldsymbol{\Delta}\mathbf{x}$ & $\mathbf{a}' = \mathbf{a}+\boldsymbol{\Delta}\mathbf{a}$

permits comparison to the results of Richardson (1926):

$$\frac{\partial}{\partial t}\bar{P}_t^{(2)}(l) = \frac{1}{l^{d-1}}\frac{\partial}{\partial t}\left[l^{d-1}K(l)\frac{\partial \bar{P}_t^{(2)}(l)}{\partial l}\right]$$

where $K(l) \cong k\langle\varepsilon\rangle^{1/3} l^{4/3}$, is the scale dependent eddy diffusivity[22]. An analytical solution exists, initially derived by Richardson, but here we give the more elegant formulation of Eyink (2012):

$$\bar{P}_t^{(2)}(l) = \frac{A\,l}{\left(k_0\langle\varepsilon\rangle^{1/3} t\right)^{9/2}} \exp\left[-\frac{9l^{2/3}}{4k_0\langle\varepsilon\rangle^{1/3} t}\right]$$

where the constant A is independent of the initial concentration and the elapsed time[23] for the initial condition: $\bar{P}_{t=0}^{(2)}(l) = \delta(l)$, which corresponds the initial condition of all neighbors being indefinitely close. The importance of the analytical solution is evident once higher order moments are derived, specifically for the variance, the t^3 dependance is obtained:

$$\left\langle\left[\Delta^{(2)}(t)\right]^2\right\rangle = \left\langle l^2\right\rangle = g_0\langle\varepsilon\rangle t^3$$

where the Richardson constant mentioned earlier is: $g_0 = {}^{1144k_0^3}/_{81}$. However the absolute values of this constant constitute an active field of research and a source of much debate to this present day and will be discussed in following sections. Perhaps the most astonishing result of Richardson's work though, was the inference of the scale dependent eddy-diffusivity, $K \propto l^{4/3}$. Monin & Yaglom (1971) elucidate that the effective eddy diffusivity for the admixture cloud is proportional to the effective cloud radius raised to the power 4/3 emphasizing that we now understand this scaling as a direct consequence of the second Kolmogorov similarity hypothesis (Kolmogorov (1941)); however, Richardson managed to deduce this result 15 years earlier than Kolmogorov and more than 2 decades before K41 was widely known and accepted in occidental Europe. As mentioned already, Batchelor (1950) and (1952) re-derives the Probability Density Functions and Richardson's scaling laws and Batchelor & Townsend (1956) & Batchelor (1957) extend this analysis into free shear flows. An interesting result is the note of quasi-asymptotic motion for particles pairs whose initial separation distance, or conversely time release, is smaller than the corresponding *Kolmogorov* scales. Monin & Yaglom (1971) acknowledge that Obukhov and Landau derived similar results independent of the Cambridge school as published in an early Russian version of the classic textbook Landau & Lifshitz (1963).

Perhaps one of the most insightful remarks that Monin & Yaglom(1971) make is the fact that identical results may be obtained without employing the similarity hypothesis or dimensional arguments. Citing the work of Corrsin (1962), Lin (1960) and Lin & Reid (1963) they show how

[22]For molecular diffusion $K = 0.17cm^2s^{-1}$ and Richardson estimated values of K ranging from $3.2\times10^3 cm^2s^{-1}$ to $10^{11}cm^2s^{-1}$ for l ranging from $1.5\times10^3 cm$ to $10^8 cm$, respectively, through observation of atmospheric phenomena ranging from closely spaced anemometer readings to atmospheric cyclone diffusion measurements. Where the estimates were obtained through evaluation of the standard deviation from the mean of the thickness of the lamina, according to $\sigma^2 = \sqrt{2Kt}$ and t is the time ellapsed since indefinite thinness. Meanwhile the product $k\langle\varepsilon\rangle^{1/3}$was found to be 0.2.

[23]for the sake of completion $A = \frac{(3/2)^8}{\Gamma(9/2)}$

the only assumptions necessary are that the state of the fluid particle be governed by a Markov process and that the correlation function for the acceleration be independent and decreases sufficiently rapidly at infinity.

1.4.3 The added complexity of inertial particles

Up until this point we have treated particles and parcels as if they were continua of finiteless dimensions and effectively we were investigating fluid element evolution. Accounting for the effect of different densities and finite dimensions of droplets and real particles, whether traces or larger contaminants, is by no means a trivial task. The earliest work in the field may be traced back to the middle of the 19th century when Stokes (1850), the namesake of the dimensionless number that will be introduced shortly, investigated the effects of drag on a ball pendulum. The latter, was a field of research which had found a new lease of life after the mathematical developments of Coulomb, Maxwell and Lord Kelvin as mentioned by Stokes (1850). Later, Oseen (1927) improved Stokes solution; which had accounted solely for the drag in a creeping flow, attributing a third to the pressure distribution and the other two-thirds to the existence of shear, through the inclusion of the effects of the inertial terms of the Navier-Stokes equations. The form widely accepted today (Fan & Zhu (1998)) is the Basset-Boussinesq-Oseen equation (often abbreviated to BBO), named after the early researchers Basset (1888), Boussinesq (1903) and Oseen (1927). For spherical particles heavier than the carrier phase[24], the elegant form derived by Tchen (1947); achieved by casting the velocities in a relative sense ($\mathbf{U}_f - \mathbf{U}_p$) and then bestowing the whole system with the far field carrier velocity, is as follows:

$$\frac{\pi d_p^3 \rho_p}{6}\frac{d\mathbf{U}_p}{dt} = 3\pi\mu d_p\left(\mathbf{U}_f - \mathbf{U}_p\right) - \frac{\pi d_p^3}{6}\nabla p + \frac{\pi d_p^3 \rho_f}{12}\frac{d}{dt}\left(\mathbf{U}_f - \mathbf{U}_p\right) + ...$$
$$... + \frac{3d_p^2\sqrt{\pi\mu\rho_f}}{2}\int_{t_0}^{t}\frac{\frac{d}{d\tau}\left(\mathbf{U}_f - \mathbf{U}_p\right)}{\sqrt{t-\tau}}d\tau + \sum_i \mathrm{f_i}$$

Here the subscripts p & f indicate the particle and the undisturbed far-field carrier phase properties, respectively. This is an expanded version of Newton's equation of motion; the left hand side of the equation is the volume of the particle multiplied by its density and its acceleration, while on the right hand side the first term is the force due to *Stokesian* drag, the second term is the pressure gradient force, the third is the force due to inertia of the added mass (sometimes called virtual mass), the fourth is the viscous drag due to unsteady relative accelerations, known as the *Basset history term* and finally the summation is there to account for body forces arising from gravitational and electromagnetic fields or even inter-particle forces. Corrsin & Lumley (1956) proposed that the static pressure gradient term be replaced with the full Navier-Stokes equation:

$$-\nabla p = \rho\frac{D\mathbf{U}_f}{Dt} - \mu\nabla^2\mathbf{U}_f$$

Combining the two, leads to an expression for the acceleration of a solid particle:

[24]The buoyancy force, (2nd term on RHS) has been replaced by the pressure gradient force

$$\frac{d\mathbf{U}_p}{dt} = \frac{3\rho_f}{2\rho_p + \rho_f}\left(\frac{d\mathbf{U}_\mathrm{f}}{dt} - \frac{2}{3}\nu\nabla^2\mathbf{U}_f\right) - \frac{2}{2\rho_p + \rho_f}\left[\frac{18\mu}{d_p^2}\left(\mathbf{U}_f - \mathbf{U}_p\right) + \rho_f\left(\mathbf{U}_f - \mathbf{U}_p\right)\cdot\nabla\mathbf{U}_f\right] + ...$$

$$... + \sqrt{\frac{\mu\rho_f}{\pi}}\frac{18}{d_p\left(2\rho_p + \rho_f\right)}\int_{t_0}^{t}\frac{\frac{d}{d\tau}\left(\mathbf{U}_f - \mathbf{U}_p\right)}{\sqrt{t-\tau}}d\tau + \frac{12}{\pi d_p^3\left(2\rho_p + \rho_f\right)}\sum_i \mathrm{f_i}$$

This equation is valid in the small particle limit, that is for small particle Reynolds numbers, small shear numbers[25] and when the particle diameter is smaller than, or comparable to, the *Kolmogorov* scale, η, measured at the far field. Another way of determining whether the particles will closely follow the carrier phase is by comparing the *Stokes* number, which is the name given to the ratio of the particle relaxation time, $\tau_p = \rho_p d_p^2/18\mu$ to the characteristic time scale of the flow:

$$St = \tau_p/\tau_c$$

where the subscript, c, indicates the relevant characteristic scale. For laminar flow the latter will be the ratio of the characteristic dimension (integral length) over the bulk velocity while for turbulent flows one may cast the comparison between *Stokes* number and either the inertial, or Taylor, or *Kolmogorov* timescales to determine to what extent the particles will follow the smaller eddies. Additionally, it is important to take into account the effects of gravity on an inertial particle. This is usually characterized by a dimensionless drift velocity, γ, defined as the ratio of the particle terminal velocity to the RMS velocity of the flow:

$$\gamma = \frac{\mathbf{U}_p^T}{u'}$$

Chronopoulos (2005) states that particles with high drift velocity tend to pass through structures relatively unaffected, dispersing by a smaller amount than their lower drift velocity counterparts.

Whilst reviewing the work of Csanady(1963) on the atmospheric dispersion of particles, he notes that it was determined that the inertia of the particles did not play a substantial role in dispersion. Rather, it was the particle's terminal velocity that contributed significantly to dispersion. The dispersion in the direction normal to the drift was found to be half as much as that parallel to the direction of drift.

Voth (2000) shows how the equation is still valid for near neutrally buoyant particles that have *Stokes* numbers, based on *Kolmogorov* timescales, greater than unity and this equation is the basis for comparing the measured trajectories in experiments with the computed ones, that will be discussed in the following section. However, once the ratio is much greater than unity it is necessary to amend this equation, this is usually achieved through the inclusion of coefficients in front of the terms to make them applicable to much greater range. The form given here is from Fan & Zhu (1998) who in turn attribute it to Hansell *et al.* (1992):

$$\frac{d\mathbf{U}_p}{dt} = \frac{3\rho_f C_D}{4\rho_p d_p}\left(\mathbf{U}_f - \mathbf{U}_p\right)\left|\mathbf{U}_f - \mathbf{U}_p\right| + \frac{\rho_f C_I}{2\rho_p + \rho_f}\left[\frac{d}{dt}\left(\mathbf{U}_f - \mathbf{U}_p\right)\right] + ...$$

[25] $Re_p = (\mathbf{U}_f - \mathbf{U}_p)d_p/\nu \ll 1$ & $Re_s = d_p^2/\nu\tau_\eta \ll 1$

$$... + \frac{\rho_f}{\rho_p}\frac{D\mathbf{U}_f}{Dt}d\tau + \frac{9\rho_f}{d_p\rho_p}\left(\frac{\nu}{\pi}\right)^{1/2} C_B \int_{t_0}^{t} \frac{\frac{d}{d\tau}\left(\mathbf{U}_f - \mathbf{U}_p\right)}{\sqrt{t-\tau}}d\tau + \left(\frac{\rho_f}{\rho_p} - 1\right)\mathbf{g}$$

These coefficients C_D, C_I & C_B are the drag, the virtual mass and the Basset coefficient, respectively, which are functions of the particle Reynolds number and the particle acceleration number[26]. For the drag coefficient alone, there are several possible expressions each covering a limited range and flow condition, one has only to look at the sinuous form of a drag curve to appreciate the complexities involved in deriving a universal expression and this is before one takes into account further forces that become important such as induced lift on the particle from the spatial velocity gradients or rotation, the Saffman and the Magnus effects, respectively. For further details the reader should consult the seminal monograph by Schlichting (1968). Boffetta *et al.* (2004) summarize the behavior of particles based on their *Stokes* number as follows, as $St \to 0$ the inertial particle will tend to completely recover the motion of the carrier fluid while as $St \to \infty$ the particles tend to respond reluctantly to the spatial and temporal gradients of the carrier phase. However, several interesting phenomena are observed at the intermediate values and these will be discussed in the following sections.

1.4.4 Dispersion Experiments

The previous section mentioned in passing the difficulty in estimating Richardson's constant and the discrepancies amongst the measurements. At the same time it touched upon how the various pioneers in the field tackled the theoretical side of the problem and despite often starting from different assumptions or following varied approaches were able to arrive at very similar results. The question however still remains as to which of all the derivations is the most rigorous and whose estimate of measured quantities or constants is the most exact.

The problem is not an easy one to answer and despite the theoretical progress in the field over the last century the experimental investigations have not always been as convincing. One reason behind this has been that the theoretical analysis is usually cast in an idealized homogeneous and isotropic framework that is quite hard to achieve in the laboratory, giving rise for the need for experimental computational investigations. Another, is the difficulty of extrapolating results from two dimensional flows to three dimensional ones; accounting for factors of dimensions in the determination of constants to the problem of the inverse energy cascade arising close to walls in planar flows. Another complexity is added by the experimental tools available, most of the early experimental validation work was performed through the observation of plumes or the analysis of anemometer data and some work even extended to astronomical observations like those of Tatarski (1960). But it is only very recently that progress of experimental apparatus has permitted direct measurements of Lagrangian dynamics with high fidelity.

Voth (2000) pioneered the use of silicon strip detectors, borrowed from the high energy particle physics community, for the measurement of particles in high Taylor micro-scale Reynolds

[26] $An_p = \frac{\left|d\left(\mathbf{U}_f - \mathbf{U}_p\right)/dt\right|}{\left(\mathbf{U}_f - \mathbf{U}_p\right)^2} d_p$ & typical expressions for the coefficients are:

$$C_I = 2.1 - {}^{0.132An_p^2}/_{1+An_p^2} \;\&\; C_B = 0.48 - {}^{0.52An_p^3}/_{\left(1+An_p\right)^3}$$

number[27] flow between two counter rotating discs. The experimental findings comprise the first validation that at high Reynolds number the Lagrangian accelerations can be described by K41 scaling. However this was done without providing conclusive remarks regarding intermittency corrections to Kolmogorov scaling. Meanwhile, Virant & Dracos (1997) and Ott & Mann (2000) used Particle Tracking Velocimetry to investigate Lagrangian dynamics in flows of $Re \sim 100$. The latter studied a two-grid generated turbulent flow and observed a good agreement with the Richardson-Obukhov law for particle separations up to the integral length scale. The former examine an open channel flow and their results show better agreement with Batchelor's law[28], however the initial separation of particles in their case is greater than the integral length scale and perhaps the findings cannot be extrapolated within the inertial-sub range. In both cases though, the Kraichnan models (for details on the Kraichnan model see the following section) do not provide good agreement, but perhaps that is to be expected since the nature of the model is not diffusion specific but rather an all-encompassing description of turbulence. Meanwhile, Chronopoulos (2005) performed an experimental investigation of the relative dispersion between two particles in a vertical tube flow at high Re ($\mathcal{O} \sim 15 - 20 \cdot 10^3$), where the effect of gravity on the particle separation, $\left\langle \Delta^2 \right\rangle$, was found to be significant and varied with time in a range between, $t^{0.6} \rightarrow t^{0.75}$, depending on the initial separation, Δ_0^2.

Sawford (2001) discusses the difficulty in making reliable dispersion measurements under conditions where isotropy applies for an adequate range of scales and even more so when measurements of Richardson constant are being performed due to the requirement to simultaneously measure the dissipation rate of turbulent energy. The difficulties inherent in performing satisfactory experimental measurements are the impetus behind the development of many of the Lagrangian models and these will be introduced in the following section.

1.4.5 The closure problem

The famous closure problem of turbulence arises while attempting to solve the averaged conservation equations as it contains two unknown terms, namely the scalar concentration and a second-moment term, the turbulent flux density. As Brodkey (1967) explains any number of equations may be generated however there will always be one more unknown than there are equations. That is, the non-linear nature of the equations implies that second order moments will give rise to third order terms and third order moments will give rise to fourth order terms and so forth. The solution is to either parametrize the turbulent flux covariance in the form of a diffusion process or try solving additional second moment rate equations for the Reynolds

[27] $Re_\lambda \sim [140 - 900]$ where the *Taylor* micro-scale Reynolds number is given by $Re_\lambda = \frac{\lambda^2}{15^{1/2}\eta^2}$, and the *Taylor* micro-scale is give by $\lambda = \left(\frac{15v\sigma^2}{\varepsilon}\right)^{1/2}$, $\eta = \left(\frac{\nu^3}{\varepsilon}\right)^{1/4}$ & $\tau_\eta = \left(\frac{\nu}{\varepsilon}\right)^{1/2}$are the *Kolmogorov* length and timescales respectively and the variance of one component's velocity is given by: $\frac{3}{2}\sigma^2 = \int_0^\infty E(k)dk$ where $E(k) = \alpha\varepsilon^{2/3}k^{-5/3}$ is the von Karman energy spectrum, k is the wavenumber and α is the spectral Kolmogorov constant (from Hinze (1975) and Monin & Yaglom (1971))

[28] The distance-neighbor function for both cases is given as : $q(l,t) = \frac{1}{N\left\langle l^2 \right\rangle^{3/2}} exp\left[-H(l/\left\langle l^2 \right\rangle^{1/2})\right]$. Richardson's expression behaves like $e^{-|l|^{2/3}}$with a pronounced cusp at l=0: $N = \frac{35}{3}\left(\frac{2\pi}{143}\right)^{3/2}$ & $H(\rho) = \left(\frac{1287\rho^2}{8}\right)^{1/3}$. Batchelor's is smoothly Gaussian: $N = \left(\frac{2\pi}{3}\right)^{3/2}$ & $H(\rho) = \frac{3\rho^2}{2}$ whilst Kraichnan's is very similar to Richardson's for small separations but the tails behave more like $e^{-|l|^{4/3}}$.

stresses, the turbulent kinetic energy or the turbulent flux covariance again. Such an approach does not result in the desired universal description of turbulence along with an equally ecumenical applicability. Baldocchi (1992) notes that first order Eulerian closure schemes fail in flows where counter-gradient transport is present whilst higher-order moment models will in-turn rely on gradient transfer schemes to obtain closure. As explained by Deardoff (1978) this is a result of the inherent dependence of gradient transfer schemes on time-independent turbulent diffusivities.

The assumption of time-independence, however, is far from accurate in regions of far and near field diffusion, such as sinks and sources. Kraichnan (1965) provides an explanation as follows: The Eulerian velocity covariance cannot discriminate between the small-scale time dependence measured at a fixed point, that arise, from internal distortion, and the time dependence of small scale features being swept along by the larger scales, nearly undistorted. In the former case, the measured time fluctuations are pertinent to the calculation of the energy transfer between scales, whereas in the later they are not. In a Lagrangian framework it is straightforward to distinguish between the two circumstances as one can cast the equations in such a way that a quasi-Lagrangian velocity, $\mathbf{u}_L(\Delta\mathbf{x})$ is used for the second particle located at a position $\Delta\mathbf{x}$ that is moving in a frame of reference fixed to the first particle with velocity $\mathbf{u}_L(0,t)$:

$$\frac{d}{dt}\Delta\mathbf{x} = \mathbf{u}_L(\Delta\mathbf{x}) = \mathbf{u}(\Delta\mathbf{x},t) - \mathbf{u}(0,\mathbf{t})$$

1.4.6 Models for Relative Dispersion

Many Lagrangian models have been proposed over the last half-century. The following description will attempt to adhere to the structure of the review paper of Sawford (2001). We will aim to review the Lagrangian Stochastic Models, which were first historically, followed by spectral and two-point closure models, then Direct Numerical Simulations (in the Lagrangian context) and finally introduce Kinematic Simulations.

Lagrangian Stochastic Models

In the previous sections it was mentioned how one could arrive at the equations for the probability density function through the assumption that the position and velocity of a fluid particle is a Markovian process[29], this assumption forms the starting point for most stochastic models. Sawford (2001), explains how a continuous Markov process may be expressed either as a stochastic differential equation or as a diffusion equation in phase space, *i.e.* with the Fokker-Planck equation (citing Gardiner (1983)). The two representations are analogous. In the first case differential equations for velocity and position are respectively:

$$dU_i = a_i\left(\mathbf{U},\mathbf{X},t\right)dt + b_{ij}\left(\mathbf{U},\mathbf{X},t\right)dW_j\left(t\right) \;\&\; dX_i = U_i dt$$

where $d\mathbf{W}\left(t\right)$ is the incremental Wiener function [30]. The above equation can be used to represent, without loss of generality, particle pair motions by doubling the length of the vectors $\mathbf{U}$

[29] Durbin (1980) notes that if $t \gg T_L$ the 'velocity memory' of the particle diminishes to the point where it may be assumed that the motion of the particle is through a series of uncorrelated jumps .

[30] with a corresponding correlation $\overline{dW_i(t)dW_j(t+\tau)} = \delta_{ij}\delta(\tau)dtd(t+\tau)$

and $\mathbf{X}$, the first three components corresponding to the first particle and the last three to the second particle. The equivalent diffusion equation for the joint velocity-displacement probability density function $p_L(\mathbf{u},\mathbf{x},t;\mathbf{v},\mathbf{y},s)$[31] is:

$$\frac{\partial p_L}{\partial t}+\frac{\partial u_i p_L}{\partial x_i}=-\frac{\partial a_i p_L}{\partial u_i}+\frac{\partial^2 B_{ij} p_L}{\partial u_i \partial u_j}\ \&\ B_{ij}=\frac{1}{2}b_{ik}b_{kj}$$

The second formulation provided the starting point for the very first models, along with the additional requirements of incompressibility and that the equation be Galilean invariant, as Monin & Yaglom (1971) mention citing Obukhov (1959)). These requirement simplify the equation, since $a_i=0\ \&\ B_{ij}=B\delta_{ij}$ resulting in: $\frac{\partial p_L}{\partial t}+u_i\frac{\partial p_L}{\partial x_i}=\frac{\partial^2 p_L}{\partial u_i \partial u_i}$.

Sawford (2001) notes that within the inertial sub-range, as a direct result of Kolmogorov's 2^{nd} hypothesis (Kolmogorov (1941)) $B=0.5C_0\bar{\varepsilon}$ and the diffusion equation yields for the one-particle one-time velocity covariance (also known as the Lagrangian Velocity Structure function), $\left\langle U_i^2\right\rangle=3C_0\left\langle\varepsilon\right\rangle t$ and for the two-time velocity covariance: $\left\langle X_i^2\right\rangle=C_0\left\langle\varepsilon\right\rangle t^3$. These results should not come as a surprise given the fact that Taylor (1921) started from similar assumptions and employed similarity arguments to arrive at his equations. It is usually of greatest interest to study the relative motion between particle pairs.

Another model was introduced by Novikov (1963), as explained by Monin & Yaglom (1975), where linearized versions of the Markovian equation (effectively Langevin equations) were employed. The relative velocity of the two particles was determined by the difference of the Langevin equation for each particle. Though, in doing so, he neglected the correlation between the two particle accelerations resulting in an explicit connection between the one particle dispersion and two-particle relative dispersion.

One of the first models to attempt to tackle this last issue was proposed by Durbin (1980) where again Langevin equations are employed along with a non trivial correlation between particle pair velocities and in turn a non trivial correlation for the accelerations[32]. Sawford (2001) explains that this is achieved through the inclusion of a Uhlenbeck & Ornstein (1930) process[33], $\zeta(t)$, relating the rate of each Cartesian component of the particle-pair separation, Δ_x, to the corresponding Eulerian velocity structure function, $R^{1/2}(\Delta_x)$:

$$\frac{d\Delta_x}{dt}=\frac{d\left(x^{(1)}-x^{(2)}\right)}{dt}=R^{1/2}(\Delta_x)\,\zeta(t)$$

where $R(\Delta_x)=\left[\Delta_x^2/(\Delta_x^2+\Lambda^2)\right]^{1/3}$and Λ is proportional to the integral length scale. The model was successful in reproducing the Richardson t^3 law for the mean-square separation, however it did so at the cost of modeling accuracy within the dissipative scales since the inertial scales extend to arbitrarily small scales. The implication is that, for all but the smallest time and space scales, the particle displacement statistics for high Re flows will be identical to those for high $Peclet$ number, Pe.

[31] Where the subscript L is for Lagrangian statistics. The need for distinguishing will become apparent when the "well mixed" hypothesis is introduced

[32] Discretizing the Markov equations with a time increment $\Delta T\to 0$ the equations describing the acceleration of the particle become continuous Langevin equations (Durbin (1980)).

[33] A stochastic process that is simultaneously Stationary, Gaussian and Markovian and mean-reverting.

Sawford (1983) proposed an improvement to Durbin's model by relating the particle-pair separation to the RMS separation:

$$\frac{d\Delta_x}{dt} = R^{1/2}\left(\overline{\Delta_x^2}^{1/2}\right)\zeta\left(t\right)$$

The resulting model obtained Richardson' s law but predicted a probability density function for particle separation that was more *Gaussian*. Chronopoulos (2005) points out that this resulted in diminished relative fluctuations at larger times and in turn 'smoother' structures for the plumes. The main issue regarding this model, as Baldocchi (1992) points out, citing Thompson (1987), is the violation of the well-mixed constraint. This is the thermodynamically imposed constraint that an initially uniform distribution of material remains so. In other words we do not expect turbulence give rise to mean concentrations gradients in what was initially a uniform field.

Thompson (1987) & (1990) set out to develop a model that did not violate the the well-mixed constraint. This was achieved by not constraining the diffusion equation (*Fick's* first law) to be incompressible and invariant under Galilean transformations. The implication is that $a_i \neq 0$[34] and the diffusion term equal to $B_{ij} = 1/2C_0\left\langle\varepsilon\right\rangle\delta$ for compliance with Kolmogorov's similarity theory for times smaller than $t_0 = \left(\Delta_0^2/\left\langle\varepsilon\right\rangle\right)^{1/3}$, which is the time for which the initial separation is important[35]. These modifications had the desired effect of reproducing the classic inertial sub-range behavior for isotropic turbulence; roughly Gaussian separation probability density functions for large times but non-Gaussian for small initial separations and small times.

Ermak & Nasstrom (2000) proposed a stochastic model that would employ higher order moments, by taking into account the skewness of the particle position distribution. This approach was shown to have very good agreement with the analytical solution for a case where the eddy diffusivity is inhomogeneous and varied as a function of position (in this a case a linear variation with distance from a boundary). The problem with these types of models, as Borgas & Sawford (1994) identify, is the selection of a different expression for a_i in the diffusion equation, that may well still satisfy the well-mixed condition, but will result in entirely different Lagrangian statistics. Meanwhile, their attempts to impose additional constraints on the diffusion equation did not have the desired results of increasing the reproducibility of the statistics. These drawbacks along with the increase in required computational resources paved the way for the DNS models that will be introduced in the following section.

This introduction to early Lagrangian models would be incomplete if we did not mention the Lagrangian-History Direct-Interaction (LHDI) model proposed by Kraichnan (1966). We have already mentioned how Kraichnan (1965) identified the problem that arises in an Eulerian framework with the sweeping of the small scale from the larger ones and the resulting bias of

[34] Thompson (1987) states that in its simplest form this is of the following form: $a_i = -\frac{C_0\left\langle\varepsilon\right\rangle}{2\sigma^2}\lambda_{ij}U_j + \frac{1}{2}\lambda_{lj}\frac{\partial\lambda_{il}^{-1}}{\partial t}U + \frac{1}{2}\lambda_{lj}\frac{\partial\lambda_{il}^{-1}}{\partial x_k}U_jU_k$ where σ^2 & $\sigma^2\lambda_{ij}^{-1}$ are the velocity variance and the six-dimensional velocity correlation tensor respectively.

[35] This is important within the inertial sub-range where two particle statistics show a dual nature i.e:

$$\left\langle\tilde{U_i^{(r)}}\right\rangle \approx \begin{cases} 6C_0\left\langle\varepsilon\right\rangle t & t_\eta \ll t \ll t_0 \\ \left(6C_0 - 4C_1\right)\left\langle\varepsilon\right\rangle t & t_0 \ll t \ll t_L \end{cases}$$

which is consistent with Batchelor's (1950) results discussed earlier.

Eulerian statistics. The implication of this is that the Eulerian moments are not sufficient to correctly represent the energy transfer of the smaller scales as these are being convected by the larger ones. In mathematical terms this means that invariance under Galilean transformations is not preserved. Kraichnan's solution was to preserve the existing formulation for the moments but to measure the relaxation distances and/or times in a coordinate systems that was being convected with the flow. According to the author, the conversion to the Lagrangian framework was heuristic in an effort to find a way of preserving the invariance. However there is no arbitrary use or introduction of constants, functions and cut-offs in his model. The only caveat was that the Lagrangian equations, unlike the Eulerian ones do not preclude negative spectra.

The success of the early LHDI model was in producing identical results to Taylor's for dispersion in flow with homogeneous turbulence whilst also reproducing Richardson's law for particle pair separation within the Kolmogorov inertial sub-range. Kraichnan (1965) argued that LHDI consistency with K41 is a logical outcome, since it shares the approach of treating the dynamics of shearing flows and energy transfer between scales in a mobile coordinate system. Furthermore, in Kraichnan (1966b), a case is made for further consistency due to the localness of energy transfer between the neighboring wavenumbers[36], much in the same way that K41 explains energy transfer between the adjacent spatial scales. However, for the purpose of this study Kraichnan's work is of particular significance since he was one of the first (Kraichnan 1970) to use Fourier series to represent velocity fields for his numerical experiments which will form the basis of Kinematic Simulations.

Direct Numerical Simulations

Direct Numerical Simulations (DNS) attempt to solve the Navier-Stokes equations explicitly for all spatial scales. In doing so, uncertainties introduced through the application of modeling or filtering operations are avoided entirely. The fluid parcel's Lagrangian velocity is determined by the instantaneous value of the Eulerian velocity field at that specific location. The main disadvantage of such an approach is the computational cost associated with solving the equations and the massive storage requirement. For the former, the implication is that most simulations of isotropic turbulence must be limited to small Re numbers, initially these were in the order of a few double digits to perhaps a hundred and more recently several hundred, which in turn means that the calculations were performed on cubical computational domains ranging from 128-512 grid points in each direction. The latter limitation implies that it is very costly to do 'backwards dispersion' investigations, where individual parcel pathlines are compared to identified pairs that originated close to one another. Yeung (2002) notes one more implications arising from the limited number of grid points available, that is the introduction of numerical noise from the differentiation of the interpolated Eulerian field when computing Lagrangian accelerations. The solution is to employ higher order schemes (*circa* 4^{th} order and higher) that are computationally expensive. Yet one more limitation, is the need to have a sufficient number of statistically independent samples.

In DNS the cost is such that it typically precludes the repetition of the simulation several

[36] In LHDI neighboring wavenumbers are not necessarily those that lie adjacent in wavespace rather those that satisfy the following vector addition: $\mathbf{k} = \mathbf{p} + \mathbf{q}$ where $\mathbf{k}$, $\mathbf{p}$ & $\mathbf{q}$ are three wavenumbers. For a succinct review of Kraichnan's early work, see Brodkey (1967).

times. Rather the usual method is to track several particles through the domain whilst ensuring the initial separation is such that it would imply that the initial velocities were uncorrelated. These limitations have been mentioned, not in order to reduce the importance nor the contribution of the DNS results, but rather that they should always be interpreted bearing this in mind. Provided there exists sufficient simulation time to ensure statistical independence, DNS provide valuable insight to a range of flow conditions that would otherwise be very hard to achieve under laboratory conditions.

One of the earliest studies in this field, was performed by Yeung (1994) where he investigated two-particle relative dispersion for stationary isotropic non-decaying flow. It should be noted here, that the stationary attribute applies to the Eulerian field as the inter-particle distances on average will tend to increase due to the accelerating nature of diffusion. The energy was supplied through forcing of the larger scales and several initial separations were examined ranging from: $\Delta_0/\eta = 1/4 \rightarrow 64$. The mean-square relative displacement, $\left\langle \Delta^2(t) \right\rangle - \Delta_0^2$, was found to increase with t^2 for the short times investigated. The absence of the t^3 in this investigation is attributed, by Sawford (2001), to the low Taylor scale $Re \sim 90$. Another interesting result that arises from the analysis is that the correlation coefficient for the particle-pair velocity components falls much more abruptly than the correlation coefficient for the particle-pair displacement; the author attributes this to the fact that the displacement, being the integral of the velocity, carries a longer memory.

In subsequent work on homogeneous turbulent shear flow, Shen & Yeung (1997) increased the range of Taylor scale Reynolds number being investigated to $Re \sim 140$ and this time the domain was instead of cubic was rather twice as large in the direction of mean shear. They continued the investigation started by Yeung (1994) and again do not observe t^3 behavior. They noticed a marked difference in the behavior of the separation vector orientation, with the particle pair velocity correlation coefficient decreasing faster when the initial vector orientation is aligned with the direction of the mean shear.

Meanwhile, Borgas & Yeung (1998) extended the investigations to yet higher Taylor scale Reynolds number ($Re \sim 240$) and even though part of the inertial range[37] was now being modeled it is not recommended that their findings be extrapolated to larger Re pertinent to engineering or atmospheric flows. Their work is more applicable to the development of stochastic models as they investigated the importance of evaluating higher order moments for the Eulerian phase in order to introduce better closure approximations for the stochastic modeling.

Yeung (2002), briefly reviews the ongoing work in DNS calculations of stratified flows in the work of Kimura & Herring (1996) and Yeung & Zhou (1998), pointing out the two main observations; reduced energy transfer from the larger to the smaller scales and significantly reduced single particle displacement and particle-pair separation between the strata for both planar stratification and in rotating turbulence, respectively. Boffetta & Sokolov (2002), in a two dimensional investigation of isotropic and homogeneous turbulence at Reynolds numbers of a couple of hundred, were able to reproduce Richardson's law for the most part with some deviation towards the tail ends, attributed to crossover effects produced by the limited Reynolds

[37] Recall that an alternative formulation for the Reynolds number is through the ratio of the integral to dissipative scale, or outer to inner scale as they are called in such cases: $Re = \left(L_{outer}/L_{inner}\right)^{4/3} = \left(l/\eta\right)^{4/3}$

number in the calculations. In addition they estimate a value for the persistence parameter, Ps. A measure of whether the dispersion is diffusive or ballistic, $Ps \ll 1$ & $Ps \gg 1$, respectively. Whilst also noting that the behavior is also relatively ballistic for values of $Ps \sim 1$.

A difficulty arises, as the calculations shift to progressively greater Reynolds numbers, from the intermittency of the energy transfer between scales. Biferale *et al.* (2005), in their study of 3D isotropic and homogeneous turbulence, investigated the effects effects of intermittency further. They provide a method for quantitatively correcting for these for the relative particle-pair separation but were unable to do so for the velocity correlations. They do however observe that the Lagrangian higher order velocity moments scale in a similar manner to the Eulerian one's.

Both Sawford (1985) and Yeung (2002) make it clear that the available models capable of predicting pollutant transport in the atmosphere, whose closest laboratory equivalent would be a boundary layer flow over a flat plate, are relatively simple, still largely untested with a striking scarcity of data available in literature for establishing meaningful comparisons. Once atmospheric Reynolds numbers (of the order of at least several hundred to a few thousands) can be achieved, DNS calculations will be very useful in this field as this will allow the comparison of the stochastic models with the DNS data. It would then be relatively straightforward to investigate the effects of introducing particle pairs or plumes at various locations (both from the leading edge and height from the plate) on the subsequent dispersion in the inner & outer boundary layers.

Perhaps one of the most important investigations of particle preferential concentrations are the DNS particle laden calculations of Squire & Eaton (1991) as they were the first to identify that particles accumulate in regions of low vorticity[38] and high strain and dispelled the common perception, believed up until that point, that turbulence enhances mixing . Zones were identified where the particle number density was 25 times greater than the mean value. Subsequent work has mainly been focused on confirming these results and increasing the grid refinement of the numerical simulations in order to extend the findings to large Re and an exhaustive list is provided by Mashayek & Pandya (2003). That DNS are capable of modeling such complex phenomena should come as no surprise since all the physical information required is present in the calculation. In a similar fashion to DNS, so too must LES be capable of predicting particle preferential concentration at least at the larger scales. As all the physics are modeled only for the scales greater than the filter width, any preferential concentration extant on scales smaller than the filter width cannot possibly be predicted. The implication is that even an LES would require a dispersion model, similar to the sub-grid-scale models used for the Eulerian phases, if additional dispersion and preferential concentrations prediction is desirable.

Kinematic Simulations

Kinematic Simulations (KS) is the name given to a Lagrangian model of turbulent dispersion constructed on a gridless flow field from spectral methods. Rather than relying on a dynamical equation to develop a random field, this is generated according to a prescribed formula. According to Sawford (2001) and Fung *et al.* (1992), its origins may be traced back to the early

[38] The definition of a vortical region therein is that of a region of strong rotational motions and low pressures.

work of Lumley & Corrsin (1959) and Kraichnan (1970). Lumley and Corrsin were the first to propose a random walk based on Markov processes rather than the more traditional Brownian motion in an effort to determine relationships between the Eulerian and Lagrangian statistics. They constructed an Eulerian lattice for space and time where for every given point of time and space the temporal and spatial instructions respectively follow a simple Markov chain. These sets of rules determine the Eulerian statistics while the Lagrangian statistics were obtained by allowing a particle to 'walk' along the lattice. Davidson *et al.* (2011) mention how the set of instructions was later made more complex by Patterson & Corrsin (1966) but that they were unable to determine a single Eulerian two-point correlation function that could approximate satisfactorily the corresponding Lagrangian one. However, it was Kraichnan (1970) who extended the method to three dimensions made it gridless, casting the velocity field in wave-space as a combination of random Fourier components/modes whose spectrum conformed to a prescribed value and synthesizing only the computed particle trajectories in physical space.

Fung *et al.* (2002) performed the first combined study of inertial particle movement within KS fields and confirmed some interesting results predicted from theory. First and foremost they observe the correct response of inertial particles within the constructed turbulent-like random flow fields. Ballistic trajectories are noted for larger *Stokes* numbers while at the smaller *Stokes* numbers particles follow closely the fluid element trajectories. An interesting result the authors note is that even at the smaller end of the *Stokes* number range the inertial particle trajectories and fluid element trajectories eventually differentiate. An investigation is carried out wherein the higher wavenumber range of the KS field is systematically filtered out to remove the effects of progressively smaller scales and they note that the change in diffusivity between the two trajectories is attributed to the compounding effect of many small scale differences.

In a similar manner Goto & Vassilicos (2006) study inertial particle preferential concentration in isotropic turbulence. The authors arrive at two especially noteworthy results. First, they extend the Stokes number criterion for particle fluid interaction to a scale dependent one:

$$St(l) = \frac{\tau_p}{\tau_c(l)} \;\&\; \tau_c(l) \sim \frac{l}{\sqrt{E(1/l)/l}} \sim \epsilon^{-1/3} l^{2/3}$$

and for an isotropic turbulent field with an energy spectrum, $E(k) \sim \epsilon^{2/3} k^{-5/3}$, the constant of proportionality was found to be $\tau_c(l) = 0.11\epsilon^{-1/3} l^{2/3}$. As before, if $St(l) \ll 1$ the particles follow the fluid flow of l-sized eddies so closely that no clustering is observed. Similarly when $St(l) \gg 1$ no clustering is observed since particles traverse the l-sized eddies ballistically without responding to the surrounding eddies. By investigating different spatial distributions of particles across turbulent fields of different *Kolmogorov Stokes* numbers, $St_\eta = \tau_p/\tau_\eta$ (*i.e.* where the timescale in the denominator is the *Kolmogorov* timescale), they were able to observe particle clustering across a range of different scales and to confirm the self-similar nature of particle clustering across those scales. From this observation the authors propose that particle clustering is actually determined by a resonance between l-sized eddies and the relaxation timescale of the particles. The criterion proposed is that particles exhibit clustering between $\alpha < St(l) < \beta$ where α and β are constants determined to be approximately 0.6 and 6 respectively, resulting

in a resonant eddy band within the inertial range responsible for particle clustering:

$$l_{min} = \beta^{-3/2} St_\eta \eta \;\&\; l_{max} = \alpha^{-3/2} St_\eta \eta$$

The implication of this lead the authors to note their second significant result, that vortical regions are not convenient for the identification of clusters. Instead they propose that zero-acceleration points within the flow domain should be identified since their location seems to correlate with particle cluster regions much better. The misconception until now regarding particle clustering about vortical regions is attributed to the limited *Re* investigated by others researchers which limited the extent of large eddies sweeping the smaller ones.

Readers unfamiliar with the mathematical underpinnings of spectral methods and their suitability for investigating turbulence in a statistical sense will find Appendix A constructive. Those familiar with the material should proceed directly to the next section.

1.5 Review of Kinematic Simulations

The impetus for Kraichnan's (1970) work was the evaluation of the direct-interaction approximations; which are statistical models for describing Lagrangian velocity covariance, effective eddy diffusivity and dispersion amongst others and comparison against computational experiments. The computations were performed with Kinematic Simulations (KS) and are included here as this early form of KS formed the foundation for further investigations with this method. The simulations in general agreed with G.I.Taylor's description of fluid element diffusion for long times compared to the eddy-turnover period except for the cases where the fluid elements were evolved through a two dimensional frozen velocity field as in this case there were instances where the elements could be 'trapped' within certain recirculation regions resulting in the relative dispersion tending to finite values despite the time approaching infinite. However the author stated that this was to be expected in two dimensional random fields as there should exist several locations where the streamlines are closed.

Kraichnan adopted a gridless approach for the computations, choosing instead to store the wavenumber vectors and reconstructing the physical field solely along the particle pathline or trajectory. The fluid element's starting position was placed at the origin of the Cartesian and temporal coordinates ($\mathbf{x} = 0,\ t = 0$) and the pathline at any given instant in time was determined by integrating:

$$\frac{d\mathbf{y}(t)}{dt} = \mathbf{v}(t)\,,\ \mathbf{v}(t) = \mathbf{u}(\mathbf{y}, t)\,,\ \mathbf{y}(0) = 0$$

While the velocity field was realized in the following form:

$$\mathbf{u}(\mathbf{x}, t) = \sum_{n=1}^{N} \left[\mathbf{v}(\mathbf{k}_n) \cos\left(\mathbf{k}_n \cdot \mathbf{x} + \omega_n t\right) + \mathbf{w}(\mathbf{k}_n) \sin\left(\mathbf{k}_n \cdot \mathbf{x} + \omega_n t\right)\right]$$

where

$$\mathbf{v}(\mathbf{k}_n) = \overrightarrow{\zeta_n} \wedge \mathbf{k}_n \;\&\; \mathbf{w}(\mathbf{k}_n) = \overrightarrow{\xi_n} \wedge \mathbf{k}_n$$

in order to satisfy incompressibility. Vectors $\overrightarrow{\zeta_n} \& \overrightarrow{\xi_n}$ were chosen independently from 2 or 3 dimensional Gaussian distributions. Meanwhile ω_n was also chosen at random from a Gaussian

distribution with a standard deviation of ω_0 prescribed from the time correlation function: $D(t-t') = e^{-1/2\omega_0^2(t-t')^2}$. The selection of ω_0 is a somewhat arbitrary process, with the reciprocal of the eddy turnover time being a good estimate, defined as $\omega_0 \sim {}^{u_0}/_{l}$. An important part of this analysis was the investigation of whether the statistical models remain valid when the field is frozen which required setting $\omega_0 = 0$. Finally, the wavenumber vectors $\mathbf{k}_n$ were picked from a statistically isotropic distribution such that the prescribed energy spectrum $E(k)$ was satisfied as the number of modes, N, approached infinity. The implication is that $\mathbf{k}_n$ is isotropically distributed on the surface of a sphere of radius k_0 or each component of $\mathbf{k}_n$ is picked from a Gaussian distribution of standard deviation ${}^{k_0}/_{\sqrt{3}}$ for the respective energy spectrum

$$E(k) = {}^{3}/_{2} u_0^2 \delta(k - k_0)$$

and

$$E(k) = 16({}^{2}/_{\pi})^{1/2} u_0^2 k^4 k_0^{-5} e^{-\frac{3}{2}k^2/k_0^2}$$

k_0 is the wavenumber at the peak of the energy spectrum. The author reported that most of the calculations were performed with $N = 100$ however the statistics were shown to remain unchanged for half the number of modes.

The pathline was reconstructed by integrating the equation of motion forward in time and evaluating the fluid element velocity at each updated location. A Newton-Rhapson method was employed for determination of the starting values for the first three time steps while the remaining locations of the pathline were determined with the use of a Hamming predictor-corrector scheme.

In its present form, KS are the result of the work of Fung *et al.* (1992), who extended the model, to include the inertial-sub-range, and were the first to study relative diffusion of fluid element pairs using KS. At the time, it was the only simulation capable of investigating turbulence within the inertial range as the computational resources were not excessive in contrast to the alternative computational methods. The success of the study was determined through confirmation of the form of the Eulerian frequency spectrum,

$$\phi_{11}^E = C\varepsilon^{2/3} U_{rms}^{2/3} \omega^{-5/3}$$

where C was calculated to be 0.82 which is very close to the measured value of 0.78. In addition the form of the Lagrangian spectrum was found to be,

$$\phi_{11}^L = C\varepsilon\omega^{-2}$$

with the constant found to be equal to 0.8 which coincides with atmospheric measurements. A further success of the study was the measurement of the relative mean square separation of particle pairs over several decades of the energy spectrum. This was found to conform to Richardson's and Obukhov's form,

$$\left\langle \Delta^2 \right\rangle = G_\Delta \varepsilon t^3$$

and the constant $G_\Delta$was estimated to be 0.1 in close agreement with Tatarski's (1960) mea-

surement of 0.06. The stationary (over a time period T) velocity field which was represented through the sum of Fourier series as $N, P_\omega \to \infty$ over a bounded region of space $|x_i| < X_i$ was realized according to:

$$\mathbf{u}(\mathbf{x},t) = \sum_{n_i=-N_k}^{N_k} \sum_{p=-P_\omega}^{P_\omega} \mathbf{S}_{n_i p} e^{\left[\mathrm{i}\left(k_{n_i} x_i + \omega_p t\right)\right]} \; for \; i = (1,2,3)$$

where

$$k_{n_i} = {}^{2\pi n_i}/_{X_i} \, , \; \omega_p = {}^{2\pi p}/_{T}$$

and with the random vector Fourier coefficients $\mathbf{S}_{n_i p}$. This form is the universal velocity field definition and may be simplified and cast into the more familiar form by replacing the Cartesian wavenumber coordinates with a spherical coordinate system. Where there are N_k shells and the modulus of the wavenumber vector, $\kappa = |\mathbf{k}|$ and the angle M_θ define each mode. The implication is that any variable dependent on n^{th} mode must now be cast as an mn^{th} mode. The vector Fourier coefficients $\mathbf{S}_{n_i p}$ may now be re-written as

$$\mathbf{S}_{n_i p} = \hat{\mathbf{S}}_{mnp} \wedge \hat{\kappa}_{mn}$$

where

$$\hat{\kappa}_{mn} = {}^{\vec{\kappa}_{mn}}/_{|\kappa_{mn}|} \text{ for all } m \text{ and } \hat{\mathbf{S}}_{mnp} = {}^1/_2 \left(\mathbf{a}_{mnp} \pm \mathrm{i}\, \mathbf{b}_{mnp}\right) \text{ for all } n$$

and $\mathbf{a}_{mnp}\&\mathbf{b}_{mnp}$ are random vectors uniformly distributed over all directions and are statistically independent such that:

$$\langle \mathbf{a}_{m_1 n_1 p_1} \mathbf{a}_{m_2 n_2 p_2} \rangle = 0 \; for \; m_1 \neq m_2, \; n_1 \neq n_2 \, or \, p_1 \neq p_2$$

Finally, if the number of frequency modes p are limited for each spatial mode n, that is $\omega_p = fn(|\mathbf{k}_n|)$, ω_p may be rewritten as ω_{np}, resulting in:

$$\mathbf{u}(\mathbf{x},t) = \sum_{m=1}^{M_\theta} \sum_{n=1}^{N_k} \sum_{p=1}^{P_\omega} \left[\left(\mathbf{a}_{mnp} \wedge \hat{\kappa}_{mn}\right) \cos\left(\vec{\kappa}_{mn} \cdot \mathbf{x} + \omega_{np} t\right) + \left(\mathbf{b}_{mnp} \wedge \hat{\kappa}_{mn}\right) \sin\left(\vec{\kappa}_{mn} \cdot \mathbf{x} + \omega_{np} t\right) \right]$$

When compared to Kraichnan's (1970) equation this is a slightly more complicated form of the velocity equation as ω_{np} and $\hat{\kappa}_{mn}$ are not strictly defined. The rational behind this, as the authors explain, is that the nonlinear interactions between different modes and the non-uniform advection of the vorticity field by the larger scales are what actually determine the time dependence of turbulence. This could be investigated through their careful selection.

Based on this equation for the velocity field and through the introduction of a cut-off wavenumber, k_c, for the separation of the larger scales from the smaller ones, two separate models were created. The Kinematic Simulation Sweeping Model (KSSM) and the Kinematic Simulation Inertial Model (KSIM). In the first case the integral scales are included as part of the simulation while the second, as the name suggests, is limited to the inertial part of the spectrum and relative motion at smaller scales. KSSM is, effectively, a KS nested within another KS, where, with the appropriate selection of the wavenumber range and the energy spectrum expo-

nent the large scale KS sweeps the smaller KS along. The following problems arise in KSSM: first a discontinuity is created right at the cutoff wavenumber while, more importantly, the continuity equation is not explicitly satisfied because of the sweeping motion (the error though was quantified by Fung (1990) and the effect on the second order statistics found to be about 10%). The cut-off frequency was determined to be of the order of a decade or less and the exponent of the energy spectrum for the large scales and inertial scales was set to be equal to 4 and -5/3, respectively. The largest wavenumber was varied from several decades to several hundred decades of the wavespace. However as the time-step of the KS should be equal to the inverse of the largest wavenumber, caution is needed as to not increase the computational requirements without reason. These two models were capable of reproducing many of the experimentally measured turbulence statistics, however they fell short in reproducing the high-order turbulence statistics which in turn are known to depend on the intermittency of turbulence which cannot be modeled by KS due to their dynamic nature.

Perkins *et al.* (1993), in a similar manner, created the Cloud Dispersion Model, but now rather than reconstructing the trajectory of a single fluid element, a whole cloud is evolved through the turbulent field with a further KS evolving the boundary of the cloud as it is advected through the field. The model was used to estimate the transport of a plume of contaminant in the deep ocean as well as in a tidal region. The CDM was compared to a standard steady state gradient-diffusion model[39] and the agreement was found to be good except for locations near the source of contaminant and at the plumes tip. However the gradient diffusion model is not really applicable at those two locations due to the magnitude of the gradient and the lack of stationarity respectively. The main problem however remains (and is common to most spectral methods) one is limited to very simple square or spherical geometries for the simulation's domain. Meanwhile it is only recently that a spectral method has been performed with a blunt obstacle in the middle of the domain as the mathematics required for the generation of the Fourier modes are very complicated.

More recently, Mallik & Vassilicos (1999) investigated two-particle dispersion statistics with KS in an isotropic turbulent flow with a $Re \sim 91$ and were able to obtain higher order statistics, namely skewness and kurtosis, that compared remarkably, with those that Yeung (1994) calculated with a DNS. This close agreement is contrasted with other stochastic models where the relative particle velocities are generated from Langevin equations. The difference is attributed to the latter's dependence on Wiener processes resulting in a very gradual separation between the particles. On the other hand, in KS the particle pair might spend a long time traveling very close to each other until it encounters what the authors call a 'violent event', that is some strong straining region in the flow, where the separation distance will then increase dramatically. To summarize, in Wiener processes particle separation is by slow continuous motion whereas in KS it is by sudden bursts.

The particle trajectories were obtained by integrating the equation of motion, similarly to Kraichnan (1970) mentioned earlier:

$$\frac{d\mathbf{y}(t)}{dt} = \mathbf{v}(t)\,,\ \mathbf{v}(t) = \mathbf{u}(\mathbf{y},t)\,,\ \mathbf{y}(0) = 0$$

[39]The reader is directed to Hunt (1985) for further details on diffusion models

However, there are some differences in the definitions of some of the constants in the equation for constructing the velocity field which will be detailed here as this is the version of KS that is used for the remainder of this thesis:

$$\mathbf{u}(\mathbf{x},t) = \sum_{n=1}^{N_k} \left[\left(\mathbf{A}_n \times \hat{\mathbf{k}}_n \right) \cos\left(\mathbf{k}_n \cdot \mathbf{x} + \omega_n t \right) + \left(\mathbf{B}_n \times \hat{\mathbf{k}}_n \right) \sin\left(\mathbf{k}_n \cdot \mathbf{x} + \omega_n t \right) \right]$$

Here, N_k, is the number of modes, ranging between $50 \sim 250$; $\hat{\mathbf{k}}_n$ the random unit vector $\hat{\mathbf{k}}_n = \mathbf{k}_n / k_n$ and the orientations of $\mathbf{A}_n$ and $\mathbf{B}_n$ are chosen randomly with the sole constraint that they be orthogonal[40] to $\hat{\mathbf{k}}_n$ and the choice is independent for each wave mode. Their magnitude is determined according to:

$$\mathbf{A}_n \wedge \hat{\mathbf{k}}_n \;\&\; \mathbf{B}_n \wedge \hat{\mathbf{k}}_n \;\&\; A_n^2 = B_n^2 = \frac{2}{3} E(k_n) \Delta k_n$$

where

$$\Delta k_n = \begin{cases} {}^{(k_2 - k_1)}/_2 & for\, n = 1 \\ {}^{(k_{n+1} - k_{n-1})}/_2 & for\, 1 < n < N_k \\ {}^{\left(k_{N_k} - k_{N_{k-1}}\right)}/_2 & for\, n = N_k \end{cases}$$

The unsteadiness of the KS field was chosen to be proportional to the eddy-turnover time of each wave mode:

$$\omega_n = \lambda \sqrt{k_n^3 E(k_n)}$$

where λ is a dimensionless constant of the order of unity. Setting $\lambda \sim 0$ would result in a frozen field whereas values much larger than 1 correspond to the field flapping too fast for the turbulent structures to have meaningful contribution on the particle trajectory. In their investigation the authors tested a variety of different energy spectra. For this thesis we will adopt a energy spectrum with a ${}^{-5}/_3$ slope within the inertial range, prescribed according to:

$$E(k) \sim \varepsilon^{2/3} k^{-5/3}$$

Finally, the minimum and maximum wavenumbers are determined from the prescribed spectrum and those in between are generated from a geometric distribution according to $k_n = k_1 a^{n-1}$ and a may be determined from $a = \left({}^{k_{N_k}}/_{k1} \right)^{1/(N_k - 1)}$.

The main advantages of Kinematic Simulations are twofold. First, by construction they require significantly fewer computational resources compared to DNS. Fung *et al.* (2002) have determined empirically that in KS the required computational power scales with $Re^{3/4}$ whereas in DNS the scaling is $Re^{9/4}$. The scaling factor of less than unity seems implausible and further investigations are probably required to validate this. However, the mathematical underpinnings of spectral methods suggest that the computational requirements for the investigation of higher Re flows should require the wavespace extent, $k_{min} \& k_{max}$, to increase but that is not associated with an increase in computational cost. Rather, it is the associated increase in the number of modes, k_N, into which the wavespace will be decomposed that will incur greater computa-

[40] $\mathbf{A}_n \wedge \hat{\mathbf{k}}_n \;\&\; \mathbf{B}_n \wedge \hat{\mathbf{k}}_n$

tional resources. This in turn means that the more interesting phenomena that occur at higher Reynolds numbers may be studied with the currently available hardware if KS is employed. Secondly, despite this marked difference in computational costs, KS are still capable of representing the major kinematic features of the flow. As Fung *et al.* (1991) explain, many interesting concepts of turbulence may be investigated with KS models despite lacking the accuracy of DNS as most of these concepts are subject to dimensional scaling arguments which are equally applicable to sums of Fourier modes as they are to non-linear physical flow-fields.

Being constructed by random superposition of Fourier modes, there will be regions within the domain where two waves of different frequency but similar direction will interfere constructively and result in high local energy, whereas two waves that are orthogonal will form a vortex, with its associated spiraling streamlines and helical motion. The instantaneous streamlines of a KS velocity field have well defined regions of eddying, straining and streaming flow structures which, as Mallik & Vassilicos (1999) point out, are partially responsible for the good agreement of the statistics predicted by KS with those of DNS. The importance of being able to capture and model such features may be understood when studying chemical reactions, particle trajectories or particle and bubble concentrations, as noted by Fung *et al.* (1992) citing the work of Broadwell & Breidenthal (1982), Maxey (1987) and Hunt *et al.* (1988), respectively.

A statistical approach cannot always provide the insight required for many phenomena. The non-linear nature of combustion means that using averaged quantities for the stoichiometry significantly under predicts local pollutant emissions and temperatures. Similarly, for droplets, particles or bubbles the use of averaged trajectories may result in component designs that will eventually suffer from premature wear from pitting or cavitation, respectively, to name just a few. Therefore even though KS is not entirely successful in predicting the dynamical evolution of vortex tubes and horseshoes, it does permit the investigation of various interesting structures inherent in turbulent fields, such as zero-acceleration and zero-strain points and, at least on an instantaneous level vortex tubes which in turn are paramount to the accurate calculations of Lagrangian statistics.

1.6 The need for a new Dispersion Model - Present Contribution

The finite volume method may be used to discretize the continuous carrier phase and in turn the Navier-Stokes equations that completely characterize the Eulerian phase may be solved simultaneously through the use of matrix algebra. On the other hand the solution of the Lagrangian phase is somewhat more straightforward as the ordinary differential equations describing the motion of the particles may be solved with a range of easy to implement methods such as multi-step linear, Runge-Kutta, Euler, etc.

The problem that still remains to be treated is how the two methods are connected. In one way coupled Eulerian-Lagrangian frameworks, the dispersed phase does not have feedback on the carrier phase, hence it should be used when the Eulerian phase is steady and the evolution of the particle/dispersed phase trajectory is mainly dependent on the particular geometry of the domain. Such an approach will be satisfactory if the mass loading of the dispersed phase is small. If the mass loadings are large or if the geometry and/or flow conditions are such that instabilities arise causing variations in the defining characteristic structures of the flow, then a

two-way coupled approach should be adopted. In the first case, the implication of large mass loading is that the momentum of dispersed phase will have a significant contribution on the shape of the surrounding flow field. If however, the Eulerian phase is unsteady then, even at low mass loadings the contribution of the dispersed phase is important and should be accounted for in the Eulerian phase since even small changes in the nature of the perturbation upstream can significantly change the flow field downstream.

Mostafa (1992) mentions the experimental and computational observations of particle effects on turbulent structures, making two-way coupling of paramount importance in flow fields where the said structures play a defining role. The way the interaction of the dispersed phase is accounted for on the carrier phase is through the inclusion of additional source terms in the partial differential equations describing the Eulerian phase. The exact nature of the source terms will depend on the problem being modeled and on the format in which the equations are cast.

If one is interested in the evolution solely of particle trajectories, then it is enough to include the derivative of the particle's momentum as a force on the computational cell in which it lies. If on the other hand, the case is investigating non-isothermal flows an additional contribution from the dispersed phase is required in the scalar transport equation. Whether one chooses to model all contributions or only a subset of them will depend on the accuracy desired and the computational resources available. However, there are instances where trying to describe all physical phenomena accurately is meaningless, since there are large uncertainties in some of the formulations. For example, the estimation of drag coefficients for small spheres is still an active field of research with large discrepancies in the quoted values. It may be argued that there is little point in trying to account for the contribution of the Basset force when estimating the forces on a sphere since its contribution is at least an order of magnitude smaller than that of the drag forces.

In any case, the forces are evaluated and the particle trajectory is updated by solving the equation of motion and correcting the Eulerian field through the addition or removal of momentum and energy source or sink terms. At the next time step, the process is repeated for the updated particle location taking into account the updated local parameters.

The problem that arises, and is of particular interest, is how particle dispersion is treated when the fluctuating components of the Eulerian field are not modeled. For a well-resolved LES or DNS Eulerian-Lagrangian calculation, there is sufficient instantaneous velocity information to ensure adequate dispersion of the Lagrangian particles with time. In both cases, a substantial range of length scales are modeled resulting in realistic turbulent flow-fields, which in turn will ensure that two particles that start next to each other will eventually exhibit a turbulent-like relative dispersion. The adjective, turbulent-like, is needed because in the case of LES the dissipative scales are modeled. However, in Reynolds Averaged Navier-Stokes simulations, the fluctuating velocity components of the carrier phase are not present and a mechanism is needed to account for the lack of turbulent dispersion. The purpose of the presented model is to propose an alternative dispersion model that simulates the effect of those scales of the turbulent energy spectrum that contribute to particle dispersion with a spectral method.

Within the context of the Fuel Injector Research for Sustainable Transport (FIRST) project[41], the source of funding for the present work, the investigation of the temporal and spatial clustering of sprays is of particular importance. In such a context clustering manifests itself as a non-homogeneous distribution of the air-fuel mixture within a combustor that leads to locally leaner or richer pockets of mixture. Once combustion takes place, these hot-spots become areas of increased NO_x and soot emissions reducing the effectiveness of the lean burn injectors as well as having detrimental effects on the combustor liner life expectancy due to increased thermal fatigue.

The most important operational goal, though, is the ability to ensure that the next generation of combustors operating in the lean regime are capable of in-flight re-light under all operating conditions. Even if it were possible to design, simulate and build the most effective of atomizers, it would not be sufficient. Without an improved representation of the underlying physics behind droplet clustering even a perfectly uniform spatial distribution of droplets emanating from an atomizer would eventually form clusters downstream. Hence, the need for further research in the field in order to understand the phenomenon and be able to design taking it into consideration.

At the same time it is important to recall that the industrial community requires improved modeling tools that can make use of the presently available computational hardware rather than what is thought will be widely available in the coming years. It is this very requirement that motivates this research project and will be presented in the following chapters. The FIRST consortium comprised the major European manufacturers and several research centers and the primary goal was to develop novel computational methods for improving the design of the next generation of aviation gas-turbine fuel injectors and combustors.

Within the FIRST consortium the task of describing the physics of primary and secondary atomization, where an Euler-Euler approach is necessary to capture the originating interfacial instabilities, lay with other project partners. The present contribution was tasked with dealing with the downstream temporal and spatial evolution of the spray from the fuel injector, further justifying the choice of an Eulerian-Lagrangian framework. The spray emanating from aero fuel injector results in highly uniform droplet size distributions thanks to the very high Reynolds numbers and Momentum ratios. This means that resources can be focused on characterizing the carrier flow field and trying to identify those features that have the largest effect on the evolution of the Lagrangian particles rather than focusing on how the individuals came to have their current size.

1.7 Scope of this work

The discussion up to this point had served to identify the requirement for a new dispersion model. The literature review showed that there exist computational tools to accurately describe particle dispersion and preferential concentrations. However the cost associated with such calculations remains prohibitively expensive. The implication is that there is a need within the community, especially the industrial one, for a model that is capable of producing improved particle dispersion characteristics without the costs associated with the more expensive methods. The proposed model will not aspire to describe all the physics accurately, rather it will

[41] http://www.first-fp7project.eu

introduce in a phenomenological sense some of the characteristics of the more costly methods in an effort to allow industrial codes to predict spatial and temporal non-uniformities of particle concentrations and realistic dispersion properties.

What is proposed within this thesis is the combination of the well established and inexpensive RANS, and unsteady-RANS, methods with Kinematic Simulations for more realistic modeling of the dispersed phase. The RANS approach will be responsible for the modeling of the larger features and the mean velocity component of the flow of the continuous phase, while KS will be introduced to improve the representation of the dispersion of particles by an improved representation of smaller 'unresolved' scales of the continuous phase. In a sense, the modeling of the Lagrangian turbulent spectrum will be done in two parts, the integral range along with a portion of the inertial scales will be modeled through RANS while KS will be tasked with modeling the near isotropic part of the spectrum that corresponds to the bulk of the inertial ranges and the dissipative scales information and behavior which is typically absent in RANS modeling.

1.8 Outline of this thesis

The premise for this thesis has been set, the remaining sections will introduce and validate the proposed model. This will be done in several steps, first Chapter 2 will introduce basic concepts of CFD, the openFOAM modeling package that is used for almost all of the calculations within this thesis, along with necessary modification required to the standard Eulerian-Lagrangian solvers included within that distribution. Chapter 3 will introduce the axisymmetric sudden expansion test case and the validation of the Eulerian-Lagrangian solver against experimental measurements. These LES results will serve as a computational benchmark for the presently available RANS dispersion model (*i.e.* the G&I dispersion model) as well as the model proposed in this thesis. It is important to note that the LES results presented are provided to establish a benchmark and to obtain an understanding of the detailed features available in such calculations but are absent in RANS. Due to their increased computational cost it is beyond the scope of this thesis to provide an exhaustive analysis of LES on the chosen test case.

Chapter 4 will describe the combination of KS with the openFOAM package and provide a qualitative representation of the two RANS dispersion models. The proposed model will be validated in Chapter 5 against the currently used dispersion model, the LES results of Chapter 3 and experimental measurements for the sudden expansion test case. Additionally, a few results will be shown in the Appendix of the proposed model implemented within an industrial code and tested on an aviation gas turbine combustor of the type currently in flight. Finally, Chapter 6 will summarize the conclusions of this thesis and recommend future work.

2 CFD Basics and Eulerian-Lagrangian Solver Development

The following chapter will introduce the fundamentals of the Finite Volume Method (FVM) as well as provided an introduction for the options available for turbulence modeling in CFD. It serves as a reminder for terminology introduced at later stages in this thesis and sets the scope for coding modifications that will be described and carried out. This is followed by a section explaining the chosen approach and concludes with a section describing the current capabilities and limitations of the openFOAM software package. Finally, the required modifications to the software program are stated in order to develop the custom Eulerian-Lagrangian solver.

2.1 Computational methods for fluid dynamics

According to Ferziger (1977), the origins of turbulence are instabilities that develop in laminar flows, the precise nature or mechanism in which they arise is still a matter of deliberation after more than a century of extensive research. Luckily, the purpose of this thesis is not to develop an all encompassing theory or explanation of the origins of turbulence rather to develop a phenomenological model for dispersion of passive scalars/particles in high Reynolds number incompressible flows, so we will limit the discussion to those details of turbulence necessary for the subsequent sections of this study. The main characteristics of turbulence according to Durbin & Petterson-Reif (2001) is its ability to stir and mix a fluid and dissipate kinetic energy at rates much greater than possible by molecular diffusion alone and does so over a continuous range of scales.

This last feature, namely, of energy being transferred over successively smaller scales, is called the energy cascade. Small perturbations somewhere in the domain/flow create instabilities in the mean flow leading to turbulent fluctuations which propagate and maintain themselves through further extraction of energy from the mean flow. These processes are the production and transport stages of turbulence. Through shear, the large eddies give rise to successively smaller eddies, as the eddies decrease in size the velocity gradients become larger in turn, increasing the effects of viscosity until eventually the size of the eddies is so small that energy is quickly dissipated through viscosity alone.

The prerequisite of turbulence is shear and under the right conditions inertial forces overcome the effects of viscosity, that is transition to turbulence occurs when the molecular viscosity can no longer dampen the perturbations. It should also be noted here, that although the concept of an eddy as a small round vortex is a useful one for understanding certain concepts of turbulence it is far from the truth. The continuous range of scales and the fact that turbulence is a a three-dimensional feature means that 'eddies' assume many shapes, ranging from connected vortices, known as cat-eyes, to long horseshoes or hairpins and from toroidal rings to spanwise rolls that are constantly evolving in time. We will return to study these features in Chapter 3.

Durbin & Petterson-Reif (2001), while explaining how small scale vorticity is maintained, elucidate the direct relationship of evolving turbulent structures and the work done by Richardson on particle dispersion. They link the growing separation distance of a particle-pair in a turbulent flow to a vortex tube that is stretching[42].

[42] Also supported by Taylor (1935)

2.1.1 Direct Numerical Simulations

Lesieur (2008) conveys one more important characteristic of turbulence; the chaotic nature of the velocity field. That is, a small initial perturbation is amplified as it develops downstream quickly reaching a point a short time later where it is completely uncorrelated to the initial field. The implication is that adopting a deterministic approach to the study and prediction of turbulence is not practical. This is not to say that such an approach is not possible, on the contrary, this is the field of Direct Numerical Simulations (DNS) but even with the presently available computational resources it is still not practical.

DNS attempt to solve the Navier-Stokes equations on a fine enough grid in space and in time in order to resolve the turbulent fluctuations directly. Early pioneers in the field of CFD, Launder & Spalding (1973), recognized the impracticality of trying to discretize temporally and spatially the computational domain to the extent dictated by the smallest energy containing scales. Back then they were limited by the number of computational nodes available. They proposed instead a turbulence model that comprised of a set of differential and algebraic equations that along with some experimental constants and the averaged Navier-Stokes equations would be capable of closely simulating real turbulent flows.

Let us not overlook the contribution of DNS, although they are of little use for real engineering flows where high Reynolds numbers and complex geometries would require nano-second or smaller time steps and micron sized computational cells, when investigating multiphase problems. Today DNS can be of great use in academic flows providing valuable and detailed information on flow quantities than are not realizable through laboratory measurements. Hence, they are invaluable resources when evaluating other CFD methods that rely on models. Ferziger & Peric (1997) provide a list where DNS has been instrumental:

- Understanding the mechanism of turbulence production, energy transfer and dissipation in turbulent flows;
- Simulation of the production of aerodynamic induced noise
- Understanding the effects of compressibility on turbulence
- Understanding the interaction of combustion and turbulence
- Controlling and reducing drag on a solid surface

2.1.2 Large Eddy Simulations

Large Eddy Simulations (LES) came about in an era when it was clear that computational capabilities were increasing at an exponential rate and much faster then previously thought, primarily driven by a desire of the meteorological community to model the global atmosphere. LES attempt to capitalize on the fact that firstly, the large scale motions in a turbulent flow are significantly more energetic than the smaller ones and their size and intensity means that they are responsible for the bulk transportation of the conserved properties and secondly, as noted by Ferziger (1977) the large structures are so different between different flows that it is unlikely that one turbulence model could be universally applicable.

Tennekes & Lumley (1972) make the point that the smaller scales of turbulence are usually independent of any orientation effects resulting from the mean-flow, their averages unchanged after being rotated or reflected, implying that this end of the continuous range of scales is isotropic. Given that the smaller scales/structures share a lot of similarities between different flows, it would seem to make sense to model the part of the flow that appears to be homogeneous and isotropic[43].

What exactly constitutes a small eddy or a large one is open to discussion. Given the existence of a continuous range of scales it is of little importance provided that, the small scales –so determined from the arbitrary cut off scale– behave in the physically sensible manner as determined from the chosen closure model. Any flow variable f may be decomposed into a large and small scale component, $\bar{f}$ & f' respectively:

$$f = \overline{f} + f'$$

The distinction between large and small eddies is achieved through the application of a filter; the filtering function is of the following form:

$$\overline{f(x)} = \int G(x, x')f(x')dx'$$

G(x,x') is called the filter kernel (whether this is Gaussian, box or cut-off filter is of little importance at this stage) associated with a filter width, Δ. Scales larger than the filter width will be resolved while all scales smaller are called sub-grid scales (SGS) and are modeled [44]. The kernel is a function that must satisfy the following condition[45]:

$$\int G(x, x')dx' = 1$$

As the spatial resolution of a LES increases, the size of the small eddies being modeled decreases, in the limit (or at least once the filter width is significantly smaller than the Kolmogorov scale) this implies that an LES eventually reduces/collapses to a DNS. Applying the filtering function to the velocity field yields:

$$\overline{u_i}(x) = \int G(x, x')u_i(x')dx'$$

and similarly the filtered versions of the incompressible Navier-Stokes equations may be obtained:[46]

$$\nabla \cdot \overline{\mathbf{u}} = 0$$

$$\frac{\partial \overline{\mathbf{u}}}{\partial t} + \nabla \cdot (\overline{\mathbf{u}}\overline{\mathbf{u}}) = -\frac{\nabla \overline{p}}{\rho} + \nabla \cdot \nu \left(\nabla \overline{\mathbf{u}} + \nabla \overline{\mathbf{u}}^T\right)$$

This filtered version of the equations bears a striking similarity to the Reynolds-Averaged version

[43] Later sections will show that this is not universally true and an SGS model that accurately reproduces shearing flows is not that good at wall bounded flows as noted by de Villiers (2007)

[44] It is worth pointing out here that the term grid refers to the size of the filter, Δ, and not the computational grid/mesh, although the filter width cannot be smaller than the cell dimensions

[45] It is a localized function; i.e the function is large only when x and x' are not far apart

[46] The last term is $\frac{\partial}{\partial x_j}\left[\nu\left(\frac{\partial \overline{u_i}}{\partial x_j} + \frac{\partial \overline{u_j}}{\partial x_i}\right)\right]$

that will appear in the next section and, just as in that case, the inequality $\overline{\mathbf{u}\mathbf{u}} \neq \overline{\mathbf{u}}\ \overline{\mathbf{u}}$ holds. This is known as one of the Reynolds conditions and the reader is directed to the classical text by Monin & Yaglom (1971) for details that arise when specific periods are chosen for the mean and fluctuating fields[47]. For the present purposes it suffices to note that the difference on either side of the inequality is known as the sub-grid scale stress, $\boldsymbol{\tau}$:

$$\boldsymbol{\tau} = \overline{\mathbf{u}\mathbf{u}} - \overline{\mathbf{u}}\ \overline{\mathbf{u}}$$

The tensor will be shown to be very similar to the Reynolds stress in the following section: however it represents a significantly smaller part of the turbulent energy spectrum implying that the accuracy of the SGS model is less important than in the case of RANS. Applying the filtering decomposition introduced earlier, the Reynolds conditions lead to:

$$\boldsymbol{\tau} = \left(\overline{\overline{\mathbf{u}}\,\overline{\mathbf{u}}} - \overline{\mathbf{u}}\,\overline{\mathbf{u}}\right) + \left(\overline{\overline{\mathbf{u}}\mathbf{u}'} - \overline{\mathbf{u}'}\overline{\mathbf{u}}\right) + \overline{\mathbf{u}'\mathbf{u}'}$$

De Villiers (2007) provides an explanation of the individual terms as follows:

- The first term is known as the *Leonard* term and can be computed from the resolved scales, it represents the interaction of the resolved eddies on the sub-grid scale turbulence.
- The second term, known as the *cross-term* represents the interaction of the resolved and unresolved eddies and the transfer of energy between them. Although this is usually in the direction of decreasing eddy size, it could also flow in the opposite direction.
- The last term, known as the *SGS-Reynolds* stress, represents the effect of small eddies interacting amongst themselves.

There are significant difficulties in trying to model these terms individually. Vreman *et al.* (1994) discuss the peculiarities of the individual terms and the specific kernel functions that must be used to model them without the large errors that usually arise from the correlations used. It is far more typical to try to model the effect of the *SGS* stress as a whole as Pesmatzoglou (2014) notes that the first two terms are considered to be negligible compared to the third one, or at the least may be evaluated from the specific filtering function applied. The *SGS* is labeled a stress because of the way it is treated; physically, it may be thought of as the momentum flux of the larger scales induced by the smaller-unresolved scales (Ferziger & Peric (1997)).

Historically, the first successful SGS model is attributed to Smagorinsky (1963) and is named in his honor. The starting point is the Boussinesq approximation (Boussinesq (1877)) that linearly relates the turbulent stresses to the mean velocity gradients through an eddy viscosity which, for incompressible flows is:

$$\boldsymbol{\tau} = \nu_t \left(\nabla\bar{\mathbf{u}} + \nabla\bar{\mathbf{u}}^T\right) + \frac{1}{3}tr(\boldsymbol{\tau})\mathbf{I} = \nu_t \left(2\bar{\mathbf{S}}\right) + \frac{1}{3}tr(\boldsymbol{\tau})\mathbf{I}$$

or in index notation:

$$\tau_{ij} = \nu_t \left(\frac{\partial \bar{u_i}}{\partial x_j} + \frac{\partial \bar{u_j}}{\partial x_i}\right) + \frac{1}{3}\tau_{kk}\delta_{ij}$$

[47] The additional terms in the momentum equation are spatial derivatives of the turbulent stress tensor

where we have used $tr(\boldsymbol{\tau})$ to denote the trace of the *SGS* stress, that is the contribution from the deviatoric terms/isotropic conditions:

$$\tau_{kk} = 1/2\left(\overline{u_x u_x} + \overline{u_y u_y} + \overline{u_z u_z}\right)$$

$$\bar{\mathbf{S}} = 1/2\left(\nabla\bar{\mathbf{u}} + \nabla\bar{\mathbf{u}}^{\mathbf{T}}\right) = \bar{S}_{ij} = 1/2\left(\frac{\partial\bar{u}_i}{\partial x_j} + \frac{\partial\bar{u}_j}{\partial x_i}\right)$$

is the large-scale or resolved-scale strain rate tensor. By assuming that the resolved and modeled scales are in equilibrium, and that the latter dissipate instantaneously all the energy they receive, a simple algebraic relationship may be derived of the form:

$$\nu_t = (C_{SGS}\Delta)^2\,|\bar{\mathbf{S}}|$$

where $C_{SGS} \sim 0.2$ for isotropic flows, known as the Smagorinsky constant, which is a model parameter and $|\bar{\mathbf{S}}|$ is the modulus of the strain rate tensor,

$$|\bar{\mathbf{S}}| = \sqrt{\bar{S}_{ij}\bar{S}_{ij}}$$

Although successful and widely used, the Smagorinsky model suffers from certain limitations. The constant is found to require adjustment for flows with large shear layers present such as channel flows and stratified geophysical flows. De Villiers (2007) attributes this, based on Prandtl & Wieghardts (1945) findings, to the fact that the deviatoric components of the SGS stress, $tr(\boldsymbol{\tau})$, do not necessarily align with those of the resolved strain rate, $\bar{\mathbf{S}}$, as seen from the small correlation of the two. This does not mean that the model is without its merits, as adjustment of the constant's values will yield reasonable results. However, even for flows where the overall performance of the model is deemed to be satisfactory, it has been found that near the surfaces/walls the Smagorinsky constant requires further adjustment in proportion to the distance from the wall. This led to the adoption of van Driest damping for these regions with the constant varying according to:

$$C_{SGS} = C_{SGS_0}(1 - e^{-n^+/A})^2$$

where C_{SGS_0} is the original constant, $A \sim 25$, $n^+ = {}^{n\,u_\tau}/_{\nu}$ is the normalized distance from the surface and $u_\tau = \sqrt{{}^{\sigma_w}/_{\rho}}$ is the friction velocity based on the shear stress at the wall, σ_w. The breakdown near the wall occurs because the assumption of isotropy no longer holds.

Bardina *et al.* (1983) proposed a way to address the issue of equilibrium/anisotropy of the scales with their *scale similarity model*. They postulate that the eddies that lie on either side/bilateral/ of the cut-off should bear significant similarities. Rather than suddenly applying a cut-off point where isotropy is expected to hold, they apply a second filtering operation resulting in a model that now correlates well with measured SGS Reynolds stresses. The double filtering operation is as follows:

$$\boldsymbol{\tau} = \overline{\mathbf{u}}\,\overline{\mathbf{u}} - \bar{\overline{\mathbf{u}}}\,\bar{\overline{\mathbf{u}}}$$

or

$$\tau_{ij} = \overline{u}_i \, \overline{u}_j - \bar{\overline{u}}_i \, \bar{\overline{u}}_j$$

The implication of the scale similarity model is that it transfers energy from the smaller to the larger scales, which is desirable for boundary flows but results in diminished overall dissipation of energy which is addressed by combining the model with the original Smagorinsky model.

The second filtering operation is common to the dynamic SGS models as well, the first of which was developed by Germano *et al.* (1991). Although called models they are actually procedures which involve filtering the field a second time with a broader filter. Subtraction of the single filtered field from the double filtered one results in an expression for the *Leonard stress* term. Then, in conjunction with two expressions for the effective SGS viscosities of the two fields, the error between the two sides of the subtraction may be minimized and the Smagorinsky constant estimated. Lilly (1992) describes this procedure in detail and later Piomelli (1999) extended it to various mixed models. The dynamic model offers a significant improvement over the early SGS models, with a Smagorinsky constant that changes in space and in time, now capable of dealing with those flows that proved troublesome when solved with the original model. In addition to the increased computational overhead required, there is the troubling fact that the SGS viscosity frequently takes on very negative values, as a result of the wide range of Smagorinsky constants, which may lead to numerical instabilities. Piomelli (1991) explains how this effect might be minimized by appropriate spatial and temporal averaging.

In any case this is far from an exhaustive list of SGS models as this is still a very active field of research and beyond the scope of the present contribution. Rather, hopefully it served as an adequate introduction to the subject and provided the required information for later sections of this thesis.

2.1.3 Reynolds Averaged Navier Stokes

Finally, the last and by far the most common approach to modeling turbulence is to adopt a statistical approach. This method adopts Osborne Reynolds, approach to decomposing the local value of the variable into a mean component and a fluctuating component about that mean. The most common approach is to perform ensemble averaging over a series of identical experiments. Alternatively, in the case of homogeneous turbulence, one can perform spatial averaging for a fixed moment in time. For stationary turbulence one could perform averaging in time for a fixed point in space.

Reynolds averaging for any flow variable, f, is performed by splitting the component into a mean value, $\overline{f}$ and a fluctuating component, f' and is performed as follows[48]:

$$f(\mathbf{x}, t) = \overline{f}(\mathbf{x}, t) + f'(\mathbf{x}, t)$$

$$\overline{f}(\mathbf{x}, t) = \lim_{N \to \infty} \frac{1}{N} \sum_{i=1}^{N} f_i(\mathbf{x}, t)$$

[48] For compressible flows it is typical to perform density-weighted Favre averaging: for more details see Favre (1965)

Applying Reynolds averaging to the Navier-Stokes equations results in what are now known as the Reynolds Averaged Navier Stokes (RANS) equations:

$$\nabla \cdot \overline{\mathbf{u}} = 0$$

$$\frac{\partial \overline{\mathbf{u}}}{\partial t} + \nabla \cdot (\overline{\mathbf{u}}\overline{\mathbf{u}}) = -\frac{\nabla \overline{p}}{\rho} + \nabla \cdot \nu \left(\nabla \overline{\mathbf{u}}\right) - \nabla \cdot \overline{\mathbf{u}'\mathbf{u}'}$$

The last term is known as the Reynolds stress tensor, so named because the turbulent motion may be interpreted as a source that gives rise to stresses in the mean flow. The Reynolds stress tensor is a symmetric tensor, with the diagonal terms resulting from normal stresses which are known quantities. The off-diagonal terms are unknown and hard to estimate resulting in what is known as *the closure problem of turbulence* (i.e. there are more unknowns than there are equations). At this point, several researchers tried to derive equations for the higher order correlations but in turn quickly arrived at a point where models are required to approximate some of those quantities as Ferziger & Peric (1997), Jasak (1996) point out.

A far more common approach it to adopt an *eddy-viscosity model*, similar to the method employed in the previous section on *SGS*. Savill (1987) mentions how most of these rely on the Boussinesq approximation and a relationship for the eddy viscosity:

$$\overline{\mathbf{u}'\mathbf{u}'} = \nu_t \left(\nabla \mathbf{u} + \nabla \mathbf{u}^T\right) + \frac{2}{3} k I$$

where k represents the turbulent kinetic energy:

$$k = \overline{\mathbf{u}' \cdot \mathbf{u}'}/2 = 1/2 \left(\overline{u_x' u_x'} + \overline{u_y' u_y'} + \overline{u_z' u_z'}\right)$$

Zero equation models

In the simplest case Prandtl's mixing length hypothesis is invoked yielding an expression for the eddy viscosity:

$$\nu_t = C_\mu q L$$

where the mixing length, L, may be prescribed for simple flows and $q = \sqrt{2k}$. However, estimating the mixing length is only possible for simple wall bounded flows and it is riddled with errors when applied to separated or complicated 3D flows, resulting in the need for a more universal model[49].

Two equation models

Two equation models came about as a direct result of Kolmogorov's 1941 seminal paper (Kolmogorov (1941)). where focus was shifted to examining velocity differences and a 'multi-step' energy cascade was identified eventually restricting *Taylor's hypothesis* of global homogeneity to the near wall region only and established the concept of local homogeneity and isotropy. Although Kolmogorov's 4/5 law is one of the best-known results in turbulence, Obukhov's si-

[49] Davidson *et al.* (2011) quoting Prandtl (1927b) and Tollmien (1926) point out that Prandtl's original formulation was slightly different defining $\nu_t = qL$ and $q = L\frac{\partial u}{\partial y}$. The model was even shown to predict free shear flows accurately but was later dismissed by the original author.

multaneous work was just as important. Using spectral methods, he derived the 5/3 law for the turbulent energy spectrum [50].

All of the *two-equation models* introduce, as the name implies two more equations that must be solved. There are often small differences in the exact formulations but the fundamental idea is to introduce an equation for the dissipation rate of turbulent kinetic energy, ε, which along with the turbulent kinetic energy allows the effective eddy viscosity to be evaluated from:

$$\nu_t = C_\mu \frac{k^2}{\varepsilon}$$

and

$$\varepsilon = \nu \left\langle \left| \nabla \mathbf{u}' \right|^2 \right\rangle$$

Another very interesting result that arises from the equilibrium of the rate of production and destruction of turbulence relates the length scale, L, to the rate of turbulent energy dissipation and turbulent kinetic energy.

$$\kappa \approx \frac{k^{3/2}}{L}$$

The *two-equation models* solve two additional transport equations –one for k and one for ε– and for further details the reader is directed to one of the original papers in the field by Launder & Spalding (1973) for detailed derivations of the equations and the empirical constants. For the present discussion it is sufficient to know that the $k-\varepsilon$ model although hugely influential and widely used, is not the turbulence panacea, because it lacks the universality desired. A significant amount of work has been done to adjust the model for particular flows and regimes (for examples see Jones & Launder (1972 & 1973), Shih *et al.* (1995)).

To address some of the limitations of the k-ϵ model, namely poor prediction capabilities in boundary layers with adverse pressure gradients. Wilcox (1988) proposed a different two equation model, the $k-\omega$ model. He introduced a relationship for the *specific* rate of dissipation, ω:

$$\omega = \frac{k}{\nu_t}$$

Through the definition used to relate the turbulent viscosity, v_t to the dissipation rate in the $k-\varepsilon$ model, we see that, rather more conveniently, the specific dissipation rate, ω, may be interpreted as the ratio k/ε, the rate of dissipation of turbulence per unit energy. The model's success was superior in predicting the adverse-pressure gradient boundary layers which exhibited good agreement with the experimental measurements. For constant-gradient boundary layers the predictions were similar to the $k-\varepsilon$ model. This improvement is attributed to the ability to specify, perhaps rather arbitrarily, the value of ω on the wall boundaries rather than being limited to von Neuman conditions for ε. The model was limited however by its sensitivity to the boundary conditions specified for the $k-\omega$ at the domain inlet.

The last limitation was addressed by construction of a mixed model by Menter (1993 & 1994), the SST-$k-\omega$ model, which employed the $k-\varepsilon$ model for the bulk of the flow and switched to the $k-\omega$ near the wall boundaries. The modification successfully addressed the $k-\omega$ model

[50] It was later established that Prandtl, independently, derived very similar results in 1945

limitations but still produced excessive levels of turbulence in regions of large normal strain such as stagnation points and large accelerations zones. These are by no means the only closure models available however, they are the ones relevant to present thesis.

Computational Methodology for the Finite Volume Method

The partial differential equations that govern fluid flow through a continuum must be discretized in order to be solvable by a computer. Whether, this is done through the use of the Finite Element Method, Finite Difference Method or as is employed here, the Finite Volume Method (FVM) is usually more a matter of tradition rather than one of absolute scientific need. This stems from a culture where each research group has traditionally been employing a code developed in house. However, with the widespread use of CFD in the past couple of decades and the proliferation of commercial CFD codes, this is now changing.

A particular interesting feature and advantage of the FVM is that the integral formulation ensures that the conservation laws are satisfied exactly. In the following sections a brief overview of the Finite Volume Method will be given along with details on the most commonly used discretization schemes. The momentum and energy conservation equations will be cast in the appropriate framework along with a quick review of the scheme/algorithm to couple the pressure and velocity equations. The approach closely follows that of the standard textbooks on CFD of Ferziger & Peric (1997), Versteeg & Malalasekera (1996) and the papers of Jasak (1996), de Villiers (2004) and Weller *et al.* (1998) who were instrumental in the development of the openFOAM code, used throughout this thesis.

The economic benefits associated with a free code are substantial as the modeler is no longer restricted by a number of licenses but rather by hardware constraints. Perhaps openFOAM's greatest advantage is its open-source nature. For the scientist, the benefit of the open source code is primarily in its transparency and freedom of modification. No longer are solver routines and algorithm obscured by proprietary code, rather one can dive into and freely modify, add solvers, routines and models at will.

2.1.4 Governing Equations

The objective of the following sections is to derive a set of discretized equations that describe the governing equations over a control volume. For an arbitrary scalar $\varphi = f(x, y, z, t)$, flowing through a steady domain (fixed control volume), V, which is part of the real space with bounding surfaces denoted by S one can write the following transport equation:

$$\int_V \frac{\partial \varphi}{\partial t} dV + \int_S \mathbf{u}\varphi \cdot d\mathbf{S} + \int_V C\varphi dV = \int_S \nu \nabla \varphi \cdot d\mathbf{S} + \int_V Q dV$$

or

$$\int_V \frac{\partial \varphi}{\partial t} dV + \int_V \nabla \cdot (\mathbf{u}\varphi) \cdot dV + \int_V C\varphi dV = \int_V \nabla \cdot (\Gamma \nabla \varphi) \cdot dV + \int_V Q dV$$

where $\mathbf{u}$ is the advecting velocity field, C is some reactive constant, Γ is the diffusivity of φ and Q represents some source term within the domain. Here, the first term on the LHS represents the variation of the scalar φ with time, the second term denotes the advective flux through the

domain boundaries and the third the production/destruction due to an internal reaction. On the RHS, the first term represents the flux due to diffusion and the last some source or sink within the domain. Grouping all the surface terms together on one side and the volume terms on the other demonstrates how any imbalance in φ within the domain V is due to the fluxes across its boundary:

$$\int_S (\mathbf{u}\varphi - \nu\nabla\varphi) \cdot d\mathbf{S} = \int_V \left(\frac{\partial \varphi}{\partial t} + C\varphi - Q \right) dV$$

The equation is now in an appropriate form to be discretized into an arbitrary number, n, of smaller domains:

$$\sum_{i=1}^{n} \left[\int_S (\mathbf{u}\varphi - \nu\nabla\varphi) \cdot d\mathbf{S} - \int_V \left(\frac{\partial \varphi}{\partial t} + C\varphi - Q \right) dV \right] = 0$$

Regarding the volume integrals, all this states is that the sum of imbalances of φ within each discrete volume is equal to the total imbalance in the domain. For the boundary integrals, it is interesting to see how the conservative nature of the overall equation is preserved when dealing with the discretized version, as the fluxes through shared internal faces cancel each other out.

2.1.5 Discretization

In general the value of scalar φ is known only at certain locations of the domain and very quickly the need arises to be able to estimate the value of scalar φ at some other location **x,** a known distance $\Delta\mathbf{x}$ away or at a time Δt later on. In the finite volume method the location where this information is usually known is the centroid (φ_P) but we are often interested at the value on the boundary. To obtain a linear variation in space one must take a Taylor series expansion resulting in:

$$\varphi(\mathbf{x}) = \varphi_P + \Delta\mathbf{x} \cdot (\nabla\varphi)_P + \frac{1}{2}(\Delta\mathbf{x})^2 \cdot (\nabla\nabla\varphi)_P + \frac{1}{3!}(\Delta\mathbf{x})^3 \cdot (\nabla\nabla\nabla\varphi)_P + ...$$
$$... + \frac{1}{n!}(\Delta\mathbf{x})^n \cdot (\nabla ... \nabla\varphi)_P$$

And truncating the expression after the second term on the RHS results in an expression accurate to the 2^{nd} order:

$$\varphi(\mathbf{x}) = \varphi_P + \Delta\mathbf{x} \cdot (\nabla\varphi)_P$$

Similarly, for temporal discretization the equation in time becomes:

$$\varphi(t + \Delta t) = \varphi^t + \Delta t \left(\frac{\partial \varphi}{\partial t} \right)^t$$

where the superscripts do not denote an exponent but the value of scalar φ at time t.

Upwind & Central differencing

So far the task has been to approximate each term in the partial differential equation with a

relation that is easier to solve, namely a finite difference approximation [51]:

$$\left(\frac{\partial\varphi}{\partial x}\right)_{x_i} = \lim_{\Delta x\to 0}\frac{\varphi(x_i+\Delta x)-\varphi(x_i)}{\Delta x}$$

Note how this is just the first two terms of the expression derived for the Taylor series expansion with the degrees of freedom reduced to 1. The influence of the definition of a derivative is visible when setting up a finite difference scheme or equation. Any such finite difference requires knowledge of the value at some other location. In CFD the initial values usually lie on the boundaries of the whole domain. A value may be prescribed on the boundary node or the derivative itself may be known, the Dirichlet and von Neumann conditions respectively. The discretized equation should asymptotically approach the partial differential equations as the grid spacing and time step decrease in magnitude.

Very often the grid spacing is not constant and a weighting factor must be introduced for the estimate of φ_i that lies between x_{i+1} and x_{i-1}. The weighting or interpolation factor, is defined as the ratio of the distances : $f = \frac{|\mathbf{x_{i+1}}-\mathbf{x_i}|}{|\mathbf{x_{i-1}}-\mathbf{x_i}|}$ and $\varphi_i = f\varphi_{x+1} + (1-f)\varphi_{x-1}$. Consider, the constantly varying function $\varphi(x)$ at some point i; to solve the finite difference equation one can use information stored at location *i+1, i-1* or both and this is then known as, forward, backward or central differencing respectively.

Which is better suited to a specific application will depend on the behavior of the continuous function. Another approach, is to consider the direction of propagation of information. Whenever there is a significant amount of convection present and the scheme chosen favors the upstream node, *i.e.* an upwind scheme, this improves stability and the boundedness[52]of the solution. However, the truncation errors will often manifest themselves as diffusion and significantly affect the results as outlined in Warming & Beam (1976), which is especially true in the case of LES .

2.1.6 Convective and diffusive operators

Before expressions for the divergence and gradient operators can be derived, some of Gauss's theorems need to be invoked in order to be able to freely switch between volume and area integrals:

$$\int_V (\nabla\cdot\mathbf{B})\,dV = \int_S d\mathbf{S}.\mathbf{B}$$

$$\int_V (\nabla\varphi)\,dV = \int_S d\mathbf{S}\varphi$$

$$\int_V (\nabla B)\,dV = \int_S d\mathbf{S}B$$

[51]Regarding the naming of the neighboring nodes. We have not used the P identifier because the variable must be evaluated independently. Thus the approximation could just as easily be used to calculate a value somewhere on the boundary/face. In general it is quite common to switch between *i, j, k* and E, N, W, S (compass notation).

[52]Here boundedness refers to the solution at a certain a point being bounded by some physical limits. A volume-fraction or concentration must be between 0-100% globally. In a diffusion dominated problem the concentration at some point cannot be greater than at the source. Also, certain properties like turbulent kinetic energy or density must always be positive. Ferziger & Peric (1997) show that only 1st order schemes can guarantee boundedness.

These are Gauss theorems for the gradient and divergence of vectors and scalars respectively. Here d$\mathbf{S}$ represents an infinitesimal surface element associated with a normal unit vector pointing outwards of the control volume. Another equation needed to simplify the integral expressions of the previous section results from the definition of the centroid:

$$V_P \mathbf{x}_P = \int_V \mathbf{x} dV \leftrightarrow \int_V \mathbf{x} dV - \mathbf{x_P} \int_V dV = \int_V (\mathbf{x} - \mathbf{x}_p)\, dV = 0 \leftrightarrow \int_V \Delta \mathbf{x} dV = 0$$

where V_P indicates the volume of the domain surrounding the centroid's location (*i.e.* the volume of the cell). Using this last result along with the truncated expression for the Taylor series results in:

$$\int_{V_P} \varphi(\mathbf{x}) dV \cong \int_{V_P} \varphi_P + \Delta \mathbf{x} \cdot (\nabla \varphi)_P \, dV = \int_{V_P} \varphi_P dV + \int_{V_P} \Delta \mathbf{x} \cdot (\nabla \varphi)_P \, dV$$

But the second integral on the RHS must reduce to zero since P resides at the centroid and $\Delta \mathbf{x} = \mathbf{x} - \mathbf{x_p}$:

$$\int_{V_P} \varphi_P dV + \int_{V_P} (\mathbf{x} - \mathbf{x}_P)\, dV \cdot (\nabla \varphi)_P = \varphi_P \int_{V_P} dV + 0 = \varphi_P V_P$$

A similar expression may be derived for the surface integrals:

$$\int_V (\nabla \varphi)\, dV = \int_S d\mathbf{S} \varphi \int_{S_j} \mathbf{B} \cdot d\mathbf{S} = \mathbf{B_{FC}} \int_{\mathbf{S_j}} d\mathbf{S} + \int_{S_j} \mathbf{\Delta B} d\mathbf{S} \cdot (\nabla \mathbf{B})_{FC} = \mathbf{B_{FC}} \cdot \mathbf{S_{FC}}$$

where $\mathbf{B_{FC}}$ denotes a vector, the subscript FC the value at the face/planar centroid and $\mathbf{S}$ the area vector of the face j. Using these two results one can derive expressions for differential operations. The gradient operator becomes:

$$\int_{V_p} \nabla \varphi dV = \int_S \varphi d\mathbf{S} \leftrightarrow \nabla \varphi = \frac{1}{V_P} \sum_j \varphi_{FC} \mathbf{S_{FC}}$$

And the divergence operator becomes:

$$\int_{V_P} (\nabla \cdot \mathbf{B})\, dV = \int_S d\mathbf{S}.\mathbf{B} \leftrightarrow (\nabla \cdot \mathbf{B})\, V_p = \sum_j \left(\int_{S_j} \mathbf{B_{FC}} \cdot d\mathbf{S_{FC}} \right)$$

$$\leftrightarrow \nabla \cdot \mathbf{B} = \frac{1}{V_P} \sum_j (\mathbf{B_{FC}} \cdot \mathbf{S_{FC}})$$

where we have also invoked the assumption that φ varies linearly across the face and hence the face-centroid value can be used.

Finally, using the above relations (namely the linear variation of φ across a face, the divergence operator and the expression for the surface integral expression) a discretized version of Gauss theorem may be obtained (Jasak 1996): $V_p\, (\nabla \cdot \mathbf{B}) = \sum_f \mathbf{S} \cdot \mathbf{B_{FC}}$ This result may now be used to obtain a discretized version of the convection term:

$$\int_{V_P} \nabla \cdot (\mathbf{u} \varphi)\, dV = \sum_j \mathbf{S_{FC}}\, (\mathbf{u} \varphi)_{\mathbf{FC}} = \sum_j \mathbf{F} \varphi_{\mathbf{FC}}$$

where $F = S_{FC}\mathbf{u}_{FC}$ is the specific flux through the cell face. An important property of the discretized convection equation is that it preserves the boundedness of the initial distribution of φ. A similar procedure is followed to derive an expression for the diffusion term:

$$\int_{V_P} \nabla \cdot (\Gamma \cdot \nabla\varphi)\, dV = \sum_j \mathbf{S_{FC}} \left(\mathbf{\Gamma} \cdot \nabla\varphi\right)_{\mathbf{FC}} = \Gamma \sum_j \mathbf{S_{FC}} \nabla\varphi_{\mathbf{FC}}$$

For the simple case of an orthogonal grid, the face gradient of φ is easily evaluated as $\mathbf{S_{FC}}\nabla\varphi_{FC} = \mathbf{S_{FC}}\frac{\varphi_{i+1}-\varphi_{i-1}}{\mathbf{x_{i+1}}-\mathbf{x_{i-1}}}$ while for non-orthogonal grids the process is slightly more complicated, requiring the face gradient to be decomposed into orthogonal and non-orthogonal components and evaluated independently. The remaining terms in the general transport equation may be treated as source terms which will be first linearized into two components $Q_u \& Q_p$,which may depend on φ, and discretized accordingly:

$$Q(\varphi) = Q_u + Q_p(\varphi) \& \int_{V_P} Q(\varphi) dV = Q_u V_p + Q_p V_p \varphi_p$$

The two relations for the volume and the surface integrals may be used to simplify the final expression of the previous section and from now on the reaction and source terms may be grouped into one variable Q for the sake of simplicity, since their treatment is identical:

$$\sum_{i=1}^{n} \left[\int_S (\mathbf{u}\varphi - \Gamma\nabla\varphi) \cdot d\mathbf{S} - \int_V \left(\frac{\partial\varphi}{\partial t} + C\varphi - Q \right) dV \right] = 0$$

$$\leftrightarrow \sum_{i=1}^{n} \left[\sum_{j=1}^{m} (\mathbf{u}\varphi - \Gamma\nabla\varphi) \cdot \mathbf{S_{FC}} - \left(\frac{\partial\varphi}{\partial t} + C\varphi - Q \right) V_{P_i} \right] = 0$$

where the second summation within the bracket indicates a summation over each face, j, of each control volume i.

2.1.7 Boundary-Conditions Discretization

At the edges of the domain the cell/volume faces will coincide with the boundary of the whole computational domain. The information at these boundaries is a prerequisite for the solution of the algebraic system of equations being assembled. As such it is necessary to make a distinction between physical and numerical boundary conditions. Physical interpretation of the Boundary Conditions(BC) guides the correct formulation of the numerical boundary condition that should be assigned. Numerical boundary conditions are identified as von Neumann or Dirichlet, where a fixed gradient is prescribed or a fixed value respectively.

Numerical/Programming Boundary Conditions

- Dirichlet: The value of φ_b is prescribed along the cell faces (denoted by subscript b) that lie on the boundary of the domain. Although this should be a straightforward implementation it is necessary to consider that following complication. Even on structured and orthogonal grids there is a high probability that the overall domain boundaries are curved hence the need arises to decompose the face area vector $\mathbf{S_{FC}}$ into orthogonal and non orthogonal

components, $\mathbf{S_{FC_O}}$ and $\mathbf{S_{FC_{NO}}}$, respectively. If the value prescribed is constant along the length of a cell face then the orthogonal component will be of equal magnitude to $\mathbf{S_{FC}}$ but no longer acting on the cell face centroid/center. Therefore the need arises to define two more vectors, first $\mathbf{d}$ which connects the cell center to the face center and $\mathbf{d_N}$ which is normal to the face, defined as : $\mathbf{d_N} = \frac{\mathbf{S_{FC}}\,\mathbf{d}\cdot\mathbf{S_{FC}}}{|\mathbf{S_{FC}}|^2}$. For the convection term from the previous section, the boundary face contribution reduces to:

$$\int_{V_P} \nabla\cdot(\mathbf{u}\varphi)\,dV = \sum_j \mathbf{S_{FC}}\,(\mathbf{u}\varphi)_{\mathbf{FC}} = \sum_j \mathbf{F}\varphi_{\mathbf{FC}}$$

$$\Rightarrow (F\varphi_{FC})_{j=b} = F_b\varphi_b$$

where $F_b = S_{FC}\mathbf{u}_{FC}$ denotes the specific flux through the boundary face.

Similarly, for the diffusion term the component of the summation corresponding to the boundary becomes:

$$\int_{V_P} \nabla\cdot(\Gamma\cdot\nabla\varphi)\,dV = \sum_j \mathbf{S_{FC}}\,(\Gamma\cdot\nabla\varphi)_{\mathbf{FC}} = \Gamma\sum_j \mathbf{S_{FC}}\nabla\varphi_{\mathbf{FC}}$$

$$\Rightarrow (S_{FC}\nabla\varphi_{FC})_{j=b} = |\mathbf{S_{FC}}|\,\frac{\varphi_b-\varphi_p}{|\mathbf{d_N}|}$$

[53]

– von Neumann: The value of the normal gradient, g_b, is prescribed to be constant along the cell boundary face:

$$g_b = \frac{\partial\varphi}{\partial n_b} = \mathbf{n_b}\cdot(\nabla\varphi)_b = \frac{\mathbf{S_{FC}}}{|\mathbf{S_{FC}}|}\cdot(\nabla\varphi)_b$$

For convection terms the face value is calculated from the prescribed gradient and the value at the centroid, φ_P:

$$\varphi_b = \varphi_P + \mathbf{d_N}\cdot(\nabla\varphi)_{\mathbf{b}} = \varphi_P + |\mathbf{d_N}|\,g_b$$

$$\Rightarrow (F\varphi_{FC})_{j=b} = F_b\varphi_b = F_b\,(\varphi_P + |\mathbf{d_N}|\,g_b)$$

From the definition of g_b, which is the inner product between the face center area vector and the prescribed gradient, we know that $\mathbf{S_{FC}}\cdot(\nabla\varphi)_b = |\mathbf{S_{FC}}|\,g_b$ and substituting into the discretized version of the diffusion term for the cell boundary face results in:

$$\Rightarrow (S_{FC}\nabla\varphi_{FC})_{j=b} = \Gamma_b\,|\mathbf{S_{FC}}|\,g_b$$

Physical Boundary Conditions

– Inlet boundaries: According to Hirsch (1991) at the inlet to the computational domain usually the values of the velocity fields are fixed and the pressure gradient may be zero or

[53] noting that $\mathbf{d_N} \parallel \mathbf{S_{FC}}$, that is they are parallel to each other

extrapolated from the field. Alternatively, the value of the pressure could be fixed and the velocity gradient be set to zero.

- Outlet boundaries: In the absence of recirculating flows near the exit, the velocity field could be prescribed after scaling from the neighboring cells. However, the presence of even minute inflows from the outlet leads to loss of solution stability and for this reason it is better to set the velocity gradient along the outlet to zero and prescribe a fixed value for the pressure field.

- Wall boundaries: The no-slip condition applies here hence a fixed value is prescribed setting the values of velocity to that of the wall and, since they are typically impermeable the pressure gradients are assigned to be equal to zero as well. In the case of turbulent flows a further complication arises in RANS (and wall modeled LES) as specific boundary conditions need to be prescribed according to the turbulence model being employed

- Symmetry planes: These are often used to reduce the size of the computational domain by taking advantage of known symmetrical patterns in the flow. The normal gradients to the boundary are set to zero while those that are parallel to it obtain the value of the first cells inside the domain after scaling.

- Periodic Boundaries: These are used to model infinitely long domains and are achieved by linking directly the pair of boundaries; when solving the algebraic system of equations the cells/entries of the matrix corresponding to these boundaries are placed adjacent to each other. It can effectively be thought of as a mapping of the values from one boundary to the other creating an infinite domain.

2.1.8 Temporal Discretization

So far the general transport equation has been discretized for the spatial variables but for unsteady flows, or whenever $\frac{\partial \varphi}{\partial t} \neq 0$, the need arises to discretize in time as well. For a single steady (no variation of size in time) continuum volume this becomes:

$$\int_t^{t+\Delta t} \left[\int_S (\mathbf{u}\varphi - \Gamma \nabla \varphi) \cdot d\mathbf{S} - \int_V \left(\frac{\partial \varphi}{\partial t} + Q\varphi - Q \right) dV \right] dt = 0$$

$$\int_t^{t+\Delta t} \left[\sum_{j=1}^{m} (\mathbf{u}\varphi - \Gamma \nabla \varphi) \cdot \mathbf{S_{FC}} - \left(\frac{\partial \varphi}{\partial t} + Q\varphi - Q \right) V_{P_i} \right] dt = 0$$

The process is clearer if the terms in the equation are not factorized and are converted to volume integrals:

$$\int_t^{t+\Delta t} \left[\frac{\partial}{\partial t} \int_V \varphi dV + \int_V \nabla \cdot (\mathbf{u}\varphi) dV - \int_V \nabla \cdot (\Gamma \nabla \varphi)\, dV \right] dt = \int_t^{t+\Delta t} \left[\int_V Q(\varphi) dV \right] dt$$

$$\int_t^{t+\Delta t}\left[\frac{\partial}{\partial t}\int_V \varphi dV + \sum_j F\varphi_j - \sum_j \Gamma \mathbf{S_{FC}}\cdot\nabla\varphi_j\right]dt = \int_t^{t+\Delta t}\left[Q_u V_p + Q_p V_p \varphi_p\right]dt$$

It should be noted here, that there is no requirement for the temporal discretization of the unsteady term to be of the same order as the other terms in the equation. The overall accuracy of the discretization though will depend on the accuracy of each individual term, that is, to achieve second-order accuracy all terms must be discretized to at least second-order. Patankar (1980) mentions that often the temporal variation at the faces may be neglected, leading to a simplified version

$$\frac{\varphi_P^{t+\Delta t} - \varphi_P^t}{\Delta t}V_p + \sum_j F\varphi_j - \sum_j \Gamma \mathbf{S_{FC}}\cdot\nabla\varphi_j = Q_u V_p + Q_p V_p \varphi_p^t$$

The need to evaluate φ & $\nabla\varphi$ after some interval Δt leads to methods very similar to those applied to initial value problems for Ordinary Differential Equations (ODE) and are called two level methods. The manner in which the cell centered and face values may be evaluated yields several different approaches, summarized in the following subsections. These are derived by considering the following ODE and an initial value problem and integrating between times $t \to t + \Delta t$:

$$\frac{d\varphi(t)}{dt} = fn(t, \varphi(t));\ \varphi(t) = \varphi^t$$

$$\int_t^{t+\Delta t}\frac{d\varphi}{dt}dt = \varphi^{t+\Delta t} - \varphi^t = \int_t^{t+\Delta t} fn(t,\varphi(t))dt$$

Explicit or Forward Method

The *explicit method* is obtained when the integral on the RHS is evaluated using the value of the integrand at:

$$\varphi^{t+\Delta t} = \varphi^t + fn(t,\varphi^t)\Delta t$$

Recalling the weighting factor, f, to accommodate asymmetric control volumes and the discretization treatment of the boundary cells from the earlier sections, the face values become:

$$\varphi_j = f\varphi_P^t + (1-f)\varphi_N^t \text{ and } \mathbf{S_{FC}}\cdot(\nabla\varphi)_j = |\mathbf{S_{FC}}|\,\frac{\varphi_N^t - \varphi_P^t}{|\mathbf{d_N}|}$$

[54] resulting in:

$$\varphi_P^{t+\Delta t} = \varphi_P^t + \frac{\Delta t}{V_p}\left[\sum_j F\varphi_j^t - \sum_j \Gamma \mathbf{S_{FC}}\cdot\nabla\varphi_j^t + Q_u V_p + Q_p V_p \varphi_p^t\right]$$

[54] The expressions apply for orthogonal grids, alternatively the non orthogonal contribution has to be included in the latter of the two: $+\mathbf{d_{no}}\cdot(\nabla\varphi)_\mathbf{j}$ where $\mathbf{S_{FC}} = \mathbf{d_O} + \mathbf{d_{NO}}$

The subscript 'N' refers to some neighboring point to the cell center P. The greatest benefit of this first-order method is that the value at the new time can be estimated solely from quantities that are already known (all the terms on the RHS) and hence there is no need for inner time-step iterations. The disadvantage though is that there is a limit to stability as defined by Courant et al. (1967) and the dimensionless quantity named in his honor, the *Courant* number, defined as follows:

$$Co = {}^{U_{mean flow} \cdot \Delta t}/_{\Delta x}$$

must be smaller than unity. In practice the requirement is usually much stricter, requiring the ratio to be in the region of [0.2-0.5] in order to ensure stability.

Implicit or Backward Euler

If, on the other hand, the integrand at point $t + \Delta t$ is used, the *implicit method* is recovered:

$$\varphi^{t+\Delta t} = \varphi^t + fn(t + \Delta t, \varphi^{t+\Delta t})\Delta t$$

In practice this means that the cell values are expressed as functions of the cell centered values at the new time step: $\varphi_j = f\varphi_P^{t+\Delta t} + (1-f)\varphi_N^{t+\Delta t}$ and $\mathbf{S_{FC}} \cdot (\nabla\varphi)_j = |\mathbf{S_{FC}}| \frac{\varphi_N^{t+\Delta t} - \varphi_P^{t+\Delta t}}{|\mathbf{d_N}|}$. As outlined by Hirsch (1991) this approach is not limited by the *Courant* number limitation and is stable and bounded. However, it does require an iterative approach as it results in a coupled system of equations.

A very commonly used scheme, as outlined by Jasak (1996), is the *backward differencing method*, where the face value temporal variations are still neglected but the temporal derivatives are discretized with 2^{nd} order schemes resulting in a scheme that is overall 2^{nd} order accurate. The starting points for such a scheme are Taylor series expansions about $\varphi(t + \Delta t) = \varphi^{t+\Delta t}$ and $\varphi(t - \Delta t) = \varphi^{t-\Delta t}$:

$$\varphi(t) = \varphi^t = \varphi^{t+\Delta t} - \frac{\partial\varphi}{\partial t}\Delta t + \frac{1}{2}\frac{\partial^2\varphi}{\partial t^2}\Delta t^2 + O(\Delta t)^3$$

and

$$\varphi(t - \Delta t) = \varphi^{t-2\Delta t} = \varphi^t - 2\frac{\partial\varphi}{\partial t}\Delta t + 2\frac{\partial^2\varphi}{\partial t^2}\Delta t^2 + O(\Delta t)^3$$

respectively. Combining these, leads to the truncation error dropping out and yields an expression for the discretized version of the temporal derivative:

$$\frac{\partial\varphi}{\partial t} = \frac{{}^3/_2\varphi^t - 2\varphi^{t-\Delta t} + {}^1/_2\varphi^{t-2\Delta t}}{\Delta t}$$

.

$${}^3/_2\varphi^t - 2\varphi^{t-\Delta t} + {}^1/_2\varphi^{t-2\Delta t} = \frac{\Delta t}{V_p}\left[\sum_j F\varphi_j^t - \sum_j \Gamma\mathbf{S_{FC}} \cdot \nabla\varphi_j^t + Q_u V_p + Q_p V_p \varphi_p^t\right]$$

Resulting in a system of algebraic equation that now requires the knowledge of φ at two prior time-steps. The requirement to evaluate φ_P & φ_j at various times necessitates the use of inner-

iterations during each time step, increasing the computational requirements both in terms of memory and solution time. It does result, however, in a scheme that is unconditionally stable but slightly oscillatory in nature often being combined with a first order Euler implicit scheme.

Crank-Nicholson

If one uses a straight line approximation between final and initial points one arrives at a *trapezoidal method*, the most popular one is known as the *Crank-Nicholson scheme*:

$$\varphi^{t+\Delta t} = \varphi^t + \frac{1}{2}\left[fn(t,\varphi^t) + fn(t+\Delta t, \varphi^{t+\Delta t})\right]\Delta t$$

Recalling the *Taylor Series* expansions that result in first order accuracy: [55]

$$\left(\frac{\partial \varphi}{\partial t}\right) = \frac{\varphi_P^t - \varphi_P^{t-1}}{\Delta t}$$

and

$$\int_t^{t+\Delta t} \varphi(t)dt = \frac{\varphi_P^t - \varphi_P^{t-1}}{2}\Delta t$$

Which leads to the fully discretized version of the general transport equation for a single domain:

$$\frac{\varphi_P^t - \varphi_P^{t-1}}{\Delta t}V_p + \frac{1}{2}\left[\sum_j F\varphi_j - \sum_j \Gamma \mathbf{S_{FC}}\cdot\nabla\varphi_j\right]^t - \frac{1}{2}\left[\sum_j F\varphi_j - \sum_j \Gamma \mathbf{S_{FC}}\cdot\nabla\varphi_j\right]^{t-1} =$$

$$= \frac{1}{2}\left[Q_u V_p + Q_p V_p \varphi_p\right]^t - \frac{1}{2}\left[Q_u V_p + Q_p V_p \varphi_p\right]^{t-1}$$

This scheme is second-order accurate and unconditionally stable according to Hirsch (1991) but not necessarily bounded and potentially giving rise to problems especially when used in LES, as mentioned by de Villiers (2007), hence the need for another scheme; namely the backward difference scheme introduced earlier. Ferziger & Peric (1997) note that, although the memory requirements of the Crank-Nicholson scheme are the same as those of the 2^{nd} order backward differencing scheme, its truncation error is four times smaller.

2.1.9 Higher Order Schemes, Errors and Stability of Solution

Higher order schemes may be devised by including more points on either side, introducing weighting factors or fitting higher order polynomials to approximate the derivative (the QUICK scheme fits a parabola to the discretizing points) and many such schemes have been proposed and developed for particular problems.

It should be stressed at this point, as Ferziger & Peric (1997) point out, that the order of the error actually determines the rate at which the error tends to zero as the time step asymptotically reduces to zero and not the size of the error itself. Although, a higher order scheme will produce a smaller absolute error than a lower order one for the same size time-step, very often, methods of similar order will result in absolute errors that differ grossly. Therein lies the problem, as there is no way of knowing beforehand how small the required time-step must be for the desired

[55] where the superscripts refer to the value of φ at the given time step *t-n,..,t-2,t-1,t,t+,t+2,...,t+n*

error. One is required to perform several calculations with progressively smaller timesteps and compare the errors in the end, much like a mesh sensitivity analysis is necessary to estimate the required mesh resolution.

For further details on error estimation the reader is directed to Jasak (1996), where an extensive investigation and comparison of the errors introduced by each method was made. Although there is no deterministic method for relating the size of the error to the size of the time step, there is a way of determining how small the time-step must be in order to ensure stability of the solution. A method is deemed to be stable when it results in a solution that is bounded for a differential equation that itself has a bounded solution. The requirement is as follows:

$$\left| \Delta t \frac{\partial fn(t,\varphi)}{\partial \varphi} \right| < B$$

where B takes the value of 2 for the explicit Euler method and the value of 0 for all others simple methods described here. When the inequality is satisfied the method is deemed to be conditionally stable for the former and unconditionally stable for the latter. Such inequalities serve to indicate the size of the largest time-step for the calculations. However, it is still necessary to evaluate the range of timescales present in the problem in question and the temporal resolution required. In stiff problems, which includes most complex/engineering flows where there is typically a large range of scales, use of the inequality for determination of the time-step might produce a stable solution but one that does not capture the faster changing phenomena. In addition, stability in itself does not necessarily preclude oscillation of the solution.

It should be noted here that using higher order schemes has the tendency of filling a larger part of the A matrix (detailed in the next section) reducing sparsity, because where the coefficient matrix would have been tri-diagonal, for a simple convective 2^{nd} order scheme, it now becomes penta-diagonal for a 3^{rd} order scheme. This becomes especially cumbersome on an unstructured grid where construction of a banded matrix is not possible.

2.1.10 Linear Algebra

The partial differential equation, that is the general transport equation can now be reformulated as a finite difference approximation at each grid point. There is now an algebraic equation (not necessarily a linear equation but one dealing with the non linearity is beyond the scope of this work, suffice to say that there are methods available to treat such cases) for each node/point of the grid/domain of the form:

$$A_p \varphi_p + \sum_{nodes}^{neighbouring} A_k \varphi_k = ABC_p$$

Where the summation is performed over the neighboring nodes (1D: *-i,+i* / E,W, 2D: *-i,+i,-j,+j* / E,W,N,S, 3D: *-i,+i,-j,+j,-k,+k* / E,W,N,S,T,B). Assembling these equations at every grid point and then using matrix notation results in:

$$\mathbf{A} \cdot \overrightarrow{\phi} = \overrightarrow{ABC}$$

Where the vector $\overrightarrow{\phi}$ contains the variable values at all the grid nodes, the vector $\overrightarrow{ABC}$ contains all the known information at those locations and the square matrix A is called the coefficient matrix. Sensible numbering of the grid nodes (at least for a structured grid) will result in banded entries in the square matrix (i.e. diagonal, tri-diagonal, penta-diagonal).

In the case of the general transport equation the matrix is rarely symmetric and various linear equation solvers are employed depending on the specific circumstances. Contingent on the exact nature of the **A** matrix (sparsity, symmetry, polydiagonal-ity, etc), it can be solved through Gaussian elimination, Lower-Upper factorization or a variety of other methods specifically designed for some specific cases of A matrices (Gerritsen (2008)). The most frequently used are Preconditioned (Bi-)Conjugate Gradient, Diagonal Incomplete Cholesky, Geometric Algebraic Multi-Grid, along with various smoothers (Gauss-Seidel, etc.) and pre-conditioners which are used to expedite the solution. Which one will eventually be used depends on the matrix and rarely will the same method be employed to solve the pressure equation and the momentum equations as noted by Iaccarino (2009).

2.1.11 Navier-Stokes and Pressure Equations Discretization

The schemes outlined in the previous sections may now be used to obtain discretized versions of the Navier-Stokes and continuity equations which in tensor notation are:

$$\frac{\partial \mathbf{u}}{\partial t} + \nabla \cdot (\mathbf{uu}) - \nabla \cdot (\nu \nabla \mathbf{u}) = -\frac{\nabla p}{\rho}$$

and

$$\nabla \cdot \mathbf{u} = 0$$

respectively. These are the incompressible versions for low-mach number flows or fluids of constant density.

A difficulty arises as the pressure gradients drive the flow but there is no independent equation for pressure. For compressible flows one may use the continuity equation to determine density in the field, and through the equation of state, calculate the pressure[56]. The way around this is to arrive at an equation that describes the pressure field so that the resulting velocities satisfy the continuity equation. One further complication is introduced by the non-linear term describing convection of momentum, $\nabla \cdot (\mathbf{uu})$. Discretizing this term would result in a quadratic expression requiring non-linear solvers to be implemented in order to manipulate the matrix system. An alternative approach is to linearize the term in the following manner:

$$\int \nabla \cdot (\mathbf{uu}) dV = \sum_j \mathbf{S_{FC}} \cdot \mathbf{u_j} \cdot \mathbf{u_j} = \sum_j F_j \mathbf{u_j}$$

Momentum

The implication of using a linear expression for momentum convection is that an existing velocity field (*i.e.* one computed at a prior time-step) must be used to calculate the flux in the

[56] On the other hand, in compressible flows one must pay attention to the absolute pressure, which is not the case in incompressible flows where we are only interested in pressure differences or the gauge pressure

discretized form, or the coefficient matrices when the equations are cast as a system of linear equations. In this sense the flux used to calculate the term is lagging the current velocity field [57].

$$\sum \mathbf{S_{FC}} \cdot \mathbf{u_j} \cdot \mathbf{u_j} = \sum_j F_j \mathbf{u_j} \approx \sum \left(\mathbf{S_{FC}} \cdot \mathbf{u}\right)_j^{t-\Delta t} \cdot \mathbf{u_j} = \sum_j F_j^{t-\Delta t} \mathbf{u_j} = A_p \mathbf{u_p} + \sum_k A_k \mathbf{u_k}$$

For steady flows the linearization of the momentum convection term with the lagging velocity field is insignificant. For unsteady or transient flows it will be necessary to introduce inner iterations. Although this will increase computational cost, provided the time step is small, the temporal behavior will be well resolved and the initial premise of lagging the non-linear term well founded.

Pressure

The treatment for the pressure term outlined here follows closely the method of Rhie & Chow (1982) where the pressure term remains undiscretized. A semi-discrete equation of the following form is used for the momentum:

$$A_P \mathbf{u}_P = \mathbf{H} - \nabla p$$

The coefficient matrix, A_p, contains the contributions of the coefficient matrix from the momentum convection term as well as the contributions from the temporal scheme, denoted by subscripts u and t respectively.[58]

$$A_P = A_{uP} + A_{tP}$$

On the other hand the vector $\mathbf{H}$ includes the contribution of all neighboring matrix coefficients multiplied by their respective velocities as well as a contribution from the non-linear sources (including the transient terms) apart from the pressure gradient contribution. It may be thought of as the sum of advective and viscous terms:

$$\mathbf{H} = \sum_k \left(A_u \mathbf{u}\right)_k + A_{ut}$$

An expression for $\mathbf{u}_p$ may be obtained by dividing the initial expression of this subsection by A_p, as well as one for the face value through interpolation, respectively:

$$\mathbf{u}_P = \frac{\mathbf{H}}{A_P} - \frac{\nabla p}{A_P} \tag{1}$$

$$\mathbf{u}_j = \left(\frac{\mathbf{H}}{A_P}\right)_j - \left(\frac{\nabla p}{A_P}\right)_j$$

[57] Where k indicates summation over the neighboring cell centroids

[58] Two things should be noted here. First, that in the case of turbulent flows there will be one more contribution from the effects of turbulent diffusion and second, that both sides of the equation have been divided by the cell volume to permit face interpolations.

Recalling the continuity equation which may be discretized in the following form:

$$\nabla \cdot \mathbf{u} = \sum_j \mathbf{S_{FC}}_j \cdot \mathbf{u_j} = 0$$

Equation 1 may now be substituted into the latter resulting in :

$$\nabla \cdot \left(\frac{\nabla p}{A_P}\right) = \nabla \cdot \left(\frac{\mathbf{H}}{A_P}\right) = \sum_j \left(\mathbf{S_{FC}} \frac{\mathbf{H}}{A_P}\right)_j$$

This result may be used to obtain the final form of the discretized Navier-Stokes equations:

$$A_P \mathbf{u}_P = \mathbf{H} - \sum_j (\mathbf{S_{FC}} p)_j$$

$$\sum_j \left[\mathbf{S_{FC}} \cdot \left(\frac{1}{A_P} \nabla p\right)\right]_j = \sum_j \left[\mathbf{S_{FC}} \cdot \left(\frac{\mathbf{H}}{A_P}\right)\right] \tag{2}$$

A discretized version of the face flux will also be useful for certain steps of the pressure-velocity coupling described in the subsequent section:

$$F = (\mathbf{S_{FC}} \mathbf{u})_j = \mathbf{S_{FC}} \cdot \left[\left(\frac{\mathbf{H}}{A_P}\right) - \left(\frac{1}{A_P} \nabla p\right)\right]_j$$

2.1.12 Coupling of Pressure and Momentum

The Navier-Stokes equations have now been reduced to a system of linear equations. There are two options available at this point; the first is to try to solve the pressure and momentum equations simultaneously over the whole domain while the other calls for a sequential approach with special consideration required when coupling the pressure-velocity system. The approaches that fall in the first category are only practical for very small systems as their computational overheads are very high. Sequential methods are the industry norm today and most will resemble to some extent the simple method outlined by Ferziger & Peric (1997) and presented below:

- Start solving the velocity field (at time t) based on an some initial value for the pressure, this is assumed to be divergence free (if not this can be corrected)
- Compute $\mathbf{H}$ and its divergence
- Solve the Poisson equation for pressure at time t
- Compute the velocity field (this should now be divergence free) at the new time step $t+dt$
- Repeat procedure

In the following sections the two methods most commonly used in industry and throughout this thesis will be described. The first is the SIMPLE algorithm and the second is the PISO algorithm:

The SIMPLE algorithm

The SIMPLE algorithm was proposed by Caretto *et al.* (1972) and is suitable for steady-state flows. As the time steps are typically large the effects of non-linearity become significant. On the other hand because of the steady nature of the flow subsequent solutions of pressure-velocity couplings vary little.

- The first step is to approximate the velocity field from the momentum equations with the pressure gradient calculated either from a prior iteration or if this is the first time step from a guess (p^{guess} or p^{old}). (The velocity is typically under-relaxed $rf_U \sim 0.8$). This step is known as the momentum predictor step.

- The pressure field (p^p) can now be computed using the pressure equation. This is known as the pressure solution.

- The fluxes are computed with the updated pressure (p^p). Two options are then available; first to calculate the pressure once more before starting again or to simply under-relax the pressure as follows: $p^{new} = p^{guess} + rf_p(p^p - p^{guess})$. This is possible due to the steady state nature of the problem and the importance of the non-linear terms. As mentioned already, it is sufficient to calculate the updated coefficients **H** from the new convective fluxes for use in the first step of the next iteration. This last step is known as the velocity correction.

The PISO algorithm

Issa (1986) developed the PISO algorithm for transient flows. The algorithm is very similar to SIMPLE with differences found in the third step.

- Momentum predictor step

- Pressure solution step

- Convective fluxes are computed from the updated pressure field and eq.2 (similarly to SIMPLE) and then the velocity field is corrected explicitly with eq.1. This is known as the explicit velocity correction step. The explicit nature of the correction means that only the first term (the contribution of pressure gradient term) on the RHS of eq.1 is considered and as such it is necessary to account for the contribution of transported influences from neighboring cells (the $\mathbf{H}/A_p$ term). This is done by recalculating the coefficients of **H,** obtaining a new pressure field, and explicitly correcting the velocity field as many times as needed until the predetermined tolerance is met.[59]

Addition of Turbulence modeling equations

Regardless of the turbulence modeling approach chosen, the modifications required to the solution algorithms of the previous section are similar. The momentum and pressure equations are solved using the value of turbulent/eddy viscosity of the previous time-step or the initial guess. Subsequently an updated evaluation of the discretized closure equations is performed and

[59] A combination of these two algorithms, PIMPLE, may also be constructed and the reader is directed to Ferziger & Peric (2007) for further details.

an improved estimate of the eddy viscosity may be obtained. This is then followed by a more accurate (technically this is a more precise estimate but not in the sense of increased numerical precision) solution of the momentum and pressure equations before the whole process is repeated for the next time step.

2.2 Development of the Eulerian-Lagrangian solver

From the beginning of this thesis, the adoption of an Euler-Euler approach for the study of multiphase phenomena was ruled out due to the immense computational requirements described. The Euler-Lagrangian approach is warranted from a desire to develop a method to address some of the current limitations of Lagrangian dispersion models, namely limited particle entrance into the recirculation zones, as well as limited physical representation of the actual turbulence driving the dispersion, thus hindering the observation of more complicated phenomena such as particle preferential concentration. The carrier gas phase would be treated in an Eulerian framework and a Lagrangian approach would be adopted to track the particle evolution. The choice is further merited from the need to develop a tool for industrial purposes, that is one that can be used with the presently available computational hardware rather than what is thought will be widely available in the coming years.

2.2.1 Necessary modifications to openFOAM solvers

The openFOAM distributions (versions 1.6-2.2) lack a coupled incompressible Eulerian-Lagrangian solver so the first step of the process was to develop one. For incompressible flows, the only existing Eulerian-Lagrangian solver ("icoUncoupledKinematicParcelFoam") is capable of evolving only Lagrangian particles through a steady Eulerian field accounting for their drag and as such the two phases are uncoupled. This means that there can be no interaction imposed on the Eulerian field from the presence of the Lagrangian particles.

Another limitation of the existing solver was that it is only a steady-state solver for the Eulerian phase. As such this solver was unsuitable for the task at hand, where the mass loading on the carrier phase from the Lagrangian particles would be significant. However, there exists a two-way coupled compressible Eulerian-Solver ("rhoPimpleCoupledKinematicFoam") within the distributions, used primarily for automotive engine modeling. This was used as a template for the simpler incompressible solver, simpler because, unlike the compressible case, this solver can handle only non-reactive flows.

OpenFOAM is written in the C++ programming language and modification and creation of new solvers is a straightforward process, taking advantage of the object-oriented structure of the underlying code. Different classes can be combined to create a solver suitable to specific needs. For the present application the modifications required the substitution of the incompressible transient solver for the Eulerian phase (*i.e.* "pimpleFoam" in place of "rhoPimpleFoam"), removal of the Poisson equation for calculation of the density across the field since this is an incompressible solver\ [60]and linking to the corresponding libraries for incompressible turbulence

[60]These are standard FVM solvers and as the names imply, capable of using either the SIMPLE or PISO algorithms for solution with arbitrary selection of the number of inner, outer corrector steps and non-orthogonal correctors.

modeling. Regarding the discrete phase, several of the sub-models pertaining to reactive flows (such as reactions, break-up & evaporation) were removed maintaining only those Lagrangian classes relevant to the injection and dispersion of particles. Figure 1 depicts a flowchart of the solver. It should be noted that these modifications were performed in order to have as simple and transparent solver as possible. Once the proposed model is tested and validated the object-oriented structure of openFOAM allows easy integration with any of the Euler-Lagrangian, solvers available within the distribution or those that may be developed in the future based on similar approaches.

2.3 Summary

The approach to the solver development proved to be well founded, since a similar procedure was adopted by fellow openFOAM users and the developed codes were extensively discussed on the openFOAM online forum[61] and were evaluated in a simple lid driven cavity test case. The developed solver was fully capable of using a wide range of Lagrangian sub-models present within openFOAM such as collision, injection and dispersion models amongst others. It is this flexibility and adaptability available within openFOAM that was the main reason for its selection and use as a base to develop the phenomenological dispersion model described in later sections.

[61] www.cfd-online.com, openFOAM forum

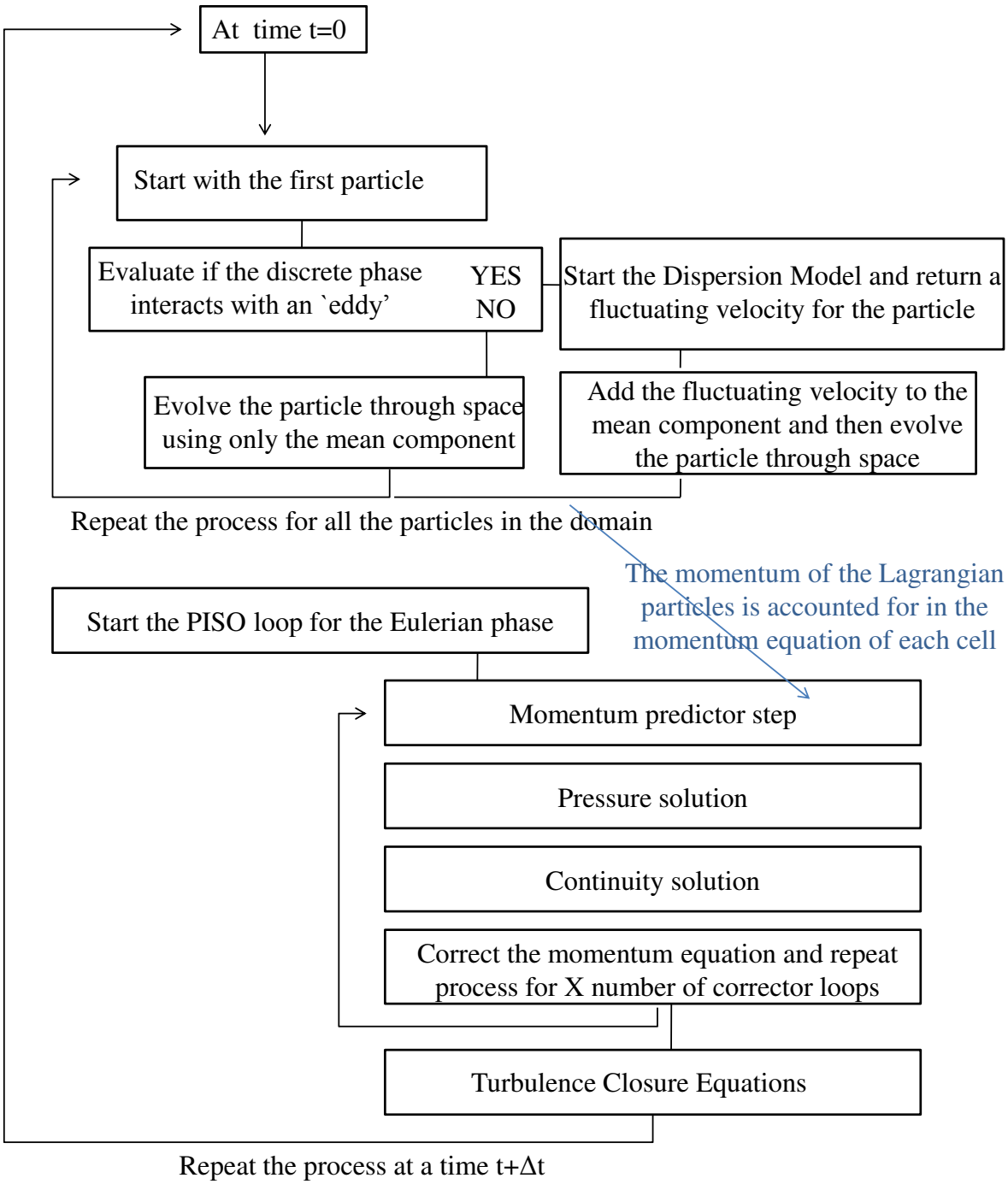

Figure 1: Flow chart for the developed two-way coupled Eulerian-Lagrangian solver within openFOAM. For details regarding the implementation of the KS dispersion model see Chapter 4

3 Large Eddy Simulations of an Axisymmetric Sudden Expansion

The purpose of the work described in this chapter is twofold; first to establish the groundwork on which the phenomenological model will be developed and secondly to create a detailed LES data set for comparison with the experimental observations and the proposed model that will be presented in the following chapter. The former entails the development of a suitable computational solver for an Eulerian-Lagrangian framework within the openFOAM package while the latter necessitates the selection of a suitable test case along with a review of the validity of the selected methods before the generation of the data set. However, the usefulness of the LES data set is not limited to establishing a benchmark for the RANS simulations since it also serves an additional role, as it may be used to investigate certain characteristics of the Eulerian phase that promote preferential concentration in the Lagrangian phase.

An important note to make is that the objective from this chapter of the thesis is not a computer program or the actual code *per se* since the development of the solver is a relatively straightforward process within the openFOAM environment, rather it is the LES data set that is of primary interest here. The work performed in this chapter forms the foundation for the subsequently presented phenomenological RANS model and hence details regarding the phenomenological code, will be given in the corresponding section. Here the discussion will be limited to the work that lead up to the initial formulation of the phenomenological code while describing along the way the LES model was developed and how it is used to evaluate the performance of the phenomenological model. Subsequently, the chosen test case will be introduced and the reasoning behind its selection will be provided.

The first section of this chapter will provide details of the test case setup along with a sensitivity analysis for the required mesh resolution. This will be followed by a comparison between the computational and experimental results for the validation of the Eulerian phase. The final section of this chapter will validate the predictions of the Lagrangian phase from the developed solver. At this point it is necessary to remind the reader that the development of a detailed LES dataset is itself no small endeavor. Due to their increased computational cost; obtaining accurate statistics requires significant computational resources, which is precisely the reason why uRANS models are still relevant for industrial purposes. Here, the LES results are used to provide context and establish a base for comparison with the uRANS results of the next chapters. It is understood that the simulation time calculated is not adequate to provide statistically converged results at the far end of the experimental domain as will be seen in subsequent sections. However the main purpose of these simulations is to provide insight regarding the detailed structural information available in an LES calculation that is absent in a uRANS one.

3.1 The sudden expansion test case

The groundwork has now been set and the developed solver may be evaluated within the LES context. The particular test case selected is an axisymmetric sudden expansion particle laden flow. This flow is particularly suited to this work for several reasons; Firstly, the presently used

dispersion models were developed and tuned on very similar geometries (Gosman & Ioannides (1981), Shue *et al.* (1983), Burry & Bergeles (1993).

Secondly, there is an inherent similarity between the axisymmetric sudden expansion, with its corresponding three-dimensional recirculation zone, and the recirculation zones formed downstream of actual aviation air-blast atomizers. As the academic configuration bears some similarity to the intended application –a section of an annular or can-annular combustor– with the omission of the inner recirculation zone created by the swirler within the injector, they exhibit similar traits, such as the high Re of the order of tens of thousands over a backwards facing step. More precisely, a backward facing step creates external recirculation zones between the jet exit and the cylinder walls. Furthermore, it is on such a geometry and within these recirculation zones that the current dispersion models predict limited particle entry, contrary to experimental observations.

Finally, Hardalupas *et al.* (1992) in their laboratory experiments investigated the dispersion of different sizes of particles through an axisymmetric sudden expansion for a range of air flow rates and for several different mass loadings for each particle size class. This particular set of experimental data is interesting, because the measurements report both gas flow and particle velocities for two different particle sizes with nominal diameters of 40 and 80 micrometers and a range of gas velocities with high Reynolds number of the order of 10^4. At the same time there is a breadth of knowledge developed regarding computational flows over backward facing steps, from which the modeling process will benefit.

3.2 Experimental Details - Operating Conditions

The computational domain for the particle laden axisymmetric sudden expansion test case was modeled on the experimental setup of Hardalupas *et al.* (1992). The computational setup follows that of the experiment closely, in term of overall dimensions, orientation and procedures. The domain models the whole geometry, avoiding common practices of introducing planes of symmetry in the azimuthal direction or using periodic boundary conditions, as such practices tend to subdue some of the non-symmetric flow structures observed in three dimensional flows. Deviating from these common practices results in an increase in computational costs for the calculation but it ensures that no computational artifacts are introduced from the periodic boundary conditions. In addition, compared to modeling only a section, modeling the whole domain permits improved statistics to be obtained for those quantities that may be averaged in the circumferential direction. This procedure will be explained in a subsequent section.

The computational domain, like the experimental one, constituted of the inlet tube diameter, d, of $15mm$ and $500mm$ length exiting into the expansion chamber, another concentric tube of $75mm$ diameter, D, and a length of $600mm$, resulting in a expansion ratio, $D/d = 5$. Figure 2 provides a schematic of the experimental setup with the direction of the flow being from the bottom right hand corner towards the top left hand corner. Furthermore, the orientation of the setup was such that the principal direction of the flow was aligned with the direction in which gravity acted.

In the experiment of Hardalupas *et al.* (1992), the gas flow was seeded with kaolin for the Laser Doppler Velocimetry (LDV) measurements of the carrier phase velocity. The discrete

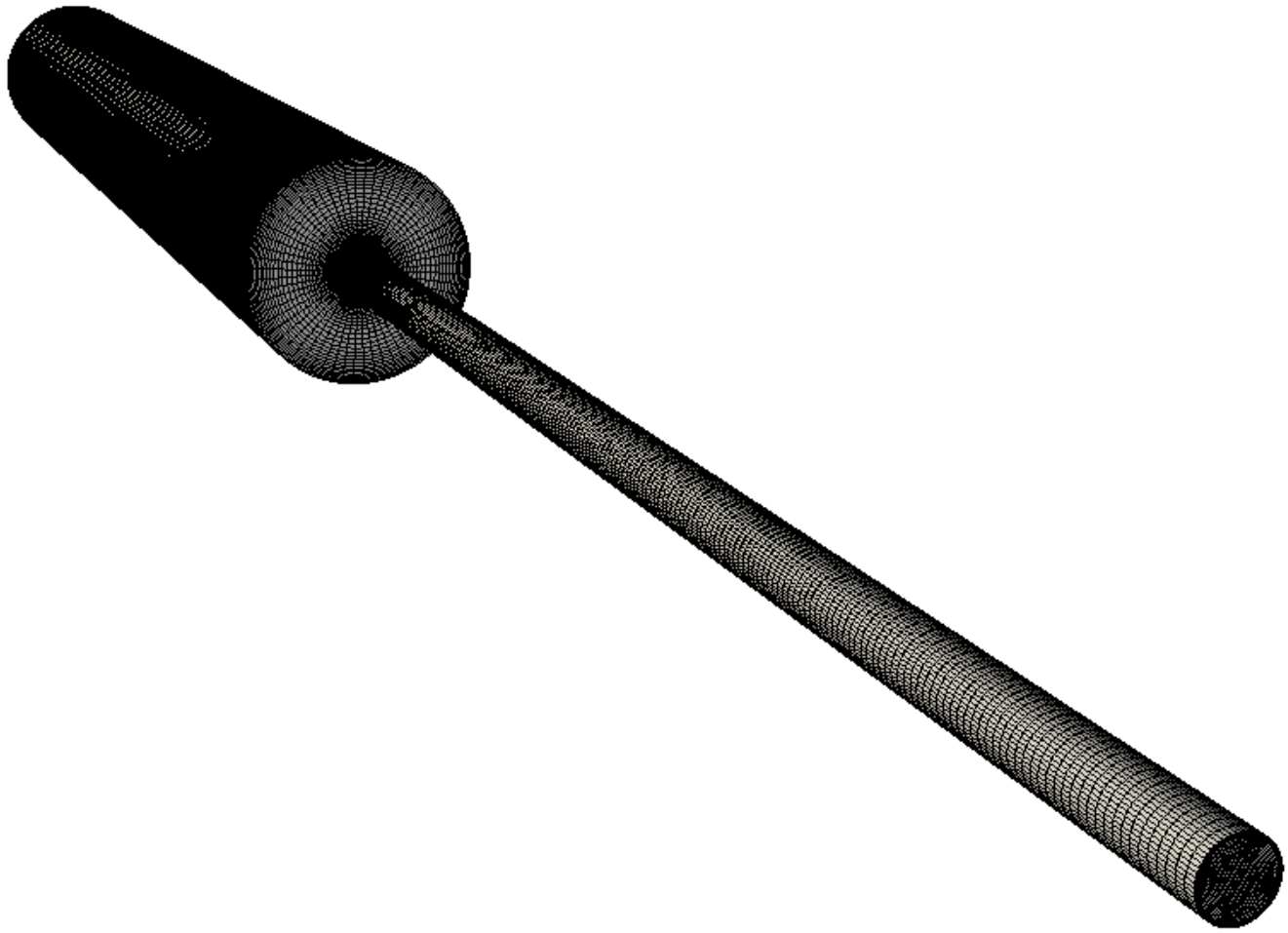

Figure 2: Perspective view of the D/d=5 sudden expansion computational domain. Viewed from the inlet tube at the bottom right of the figure to the expansion tube at the upper right corner. Characteristic dimensions for the inlet and expansion tubes are $15mm$ & $75mm$ diameters and $500mm$ and $600mm$ length respectively.

Table 1: Operating conditions and characteristic dimensions for the sudden expansion test case of Hardalupas *et al.* (1992)

Sudden Expansion Operating Conditions & Characteristic Dimensions				
Expansion Ratio	3.33		5	
Particle Nominal Size Class	$40\,\mu m$	$80\,\mu m$	$40\,\mu m$	$80\,\mu m$
Diameters				
Inlet Tube, d		$15\ mm$		
Expansion Tube, D	$50\ mm$		$75\ mm$	
Step Height, h	$17.5\ mm$		$30\ mm$	
Lengths				
Inlet Tube, l_i		$500\ mm$		
Expansion Tube, l_o		$600\ mm$		
Bulk Velocity at the				
Inlet Tube Exit, U_i	$13.2\,ms^{-1}$	$14.2\,ms^{-1}$	$14.2\,ms^{-1}$	
Expansion Tube Exit, U_o	$1.19\,ms^{-1}$	$1.27\,ms^{-1}$	$0.57\,ms^{-1}$	
Re based on				
d	13000	14000	14000	
D	3900	4200	2800	
h	15200	16400	28000	

phase were glass beads, particles of nominal $40\,\mu m$ and $80\,\mu m$ size classes, with corresponding uniform distribution between $37-44\,\mu m$ and $60-95\,\mu m$ respectively, these were introduced into the inlet tube by a screw feeder several diameters upstream of the step. In the computational domain, there is no need for kaolin seeding particles to obtain Eulerian phase predictions and the Lagrangian particles are at introduced at a similar distance upstream of the step. In an axisymmetric sudden expansion the step height is defined as the difference between the inlet and expansion tube radii. The relevant characteristic dimensions are summarized in Table **1** above. It should be mentioned that some additional tests, both experimental and computational, were performed with an expansion tube of $50mm$ diameter and a corresponding expansion ratio of $D/d = 3.33$. Throughout this thesis where measurements are given they refer to the $D/d = 5$ case, unless it is explicitly stated that they are for the $D/d = 3.33$ geometry. The former mainly serve to further prove the validity of the methods. The calculations performed on the $D/d = 3.33$ geometry are of reduced interest, as the discrepancies between experimental observations and RANS computations are reduced. This is especially true where particle entrance within the recirculation is concerned. The reader is referred to the publication describing the experiments for further details regarding the original setup.

3.3 Large Eddy Simulations - Eulerian Phase

To initialize the flow field for the LES, a steady state RANS calculation was performed using the standard $k-\varepsilon$ closure model for the carrier phase. The three-dimensional domain consisted initially of 1.1 million hexa-hedral cells with Cauchy boundary conditions prescribed at the inlet and exit. Specifically, Dirichlet conditions were prescribed for the velocity and the pressure, respectively, at the inlet and the outlet, and conversely Neumann conditions for the same quan-

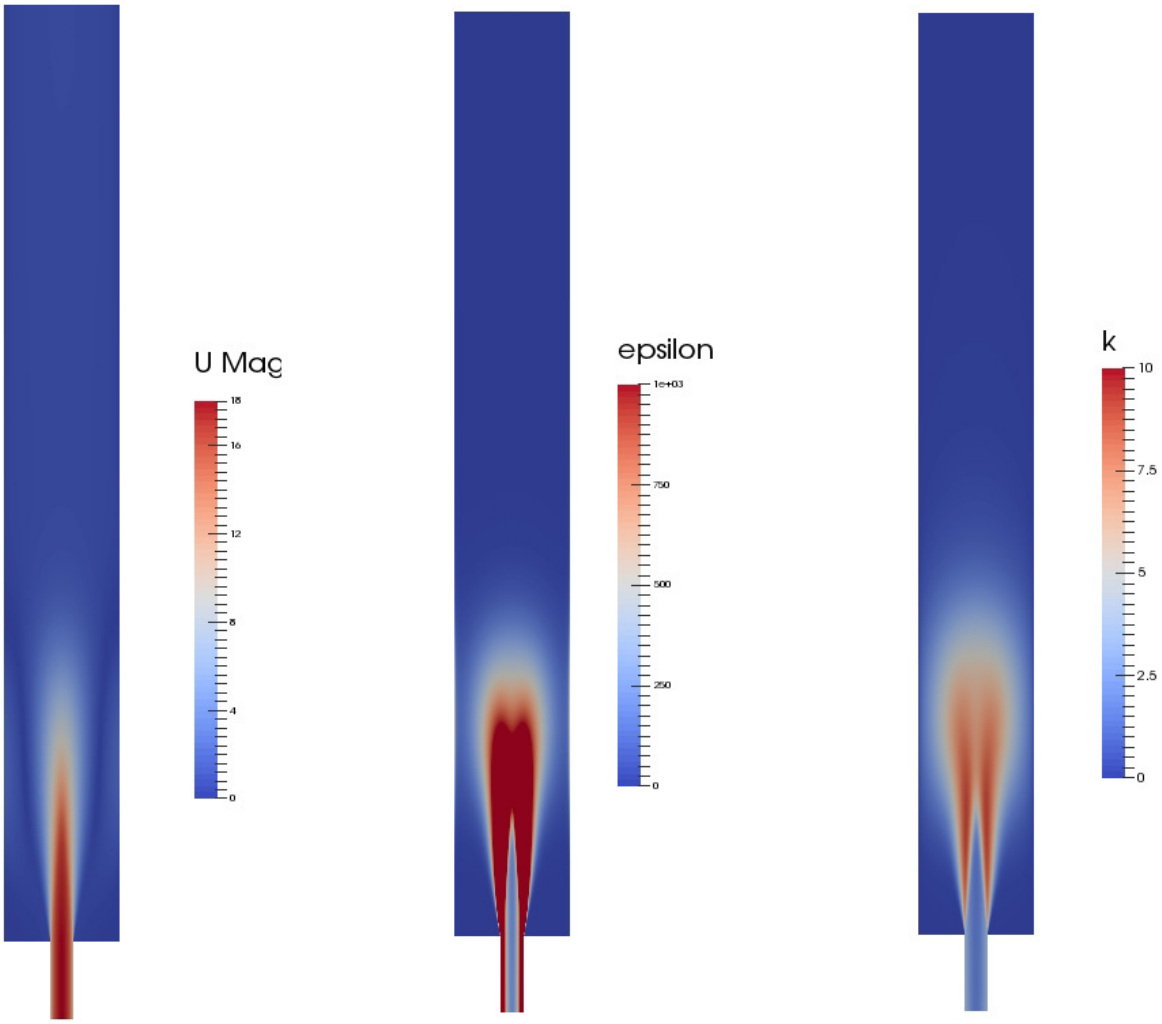

Figure 3: Slices through the RANS simulation used to initialize the LES calculation. Visible at the bottom is the $15mm$ inlet tube and the whole domain of the expansion tube of $75mm$ diameter and $600mm$ length. Flow is from the bottom of the page to the top. Depicted from left to right; velocity magnitudes colored for a range [0, $18m/s$]; dissipation rate of specific turbulent kinetic energy colored between [0, $1000m^2/s^3$] and specific turbulent kinetic energy colored between [0, $10m^2/s^2$]

tities at the outlet and the inlet respectively. All the remaining boundaries were treated as walls, with the no-slip condition imposed along with the appropriate assignment of wall models. Figure 3 depicts a slice through the RANS computational domain showing from left to right the magnitude of the velocity field, the dissipation rate of specific turbulent kinetic energy the specific turbulent kinetic energy. The latter two are of particular interest for particle dispersion in the RANS framework since a function of the two will determine the size of the 'under-resolved' eddy while the magnitude of the prescribed fluctuating componentent will be dictated in part by the value of the specific turbulent kinetic energy.

These results were subsequently used to initialize the LES calculations and to perform an analysis on the required mesh resolutions. Regarding the timestep, it was set to $10\mu s$, sufficiently small to ensure the Courant number, Co, did not exceed 0.2 anywhere within the domain while

iteration control was imposed through sufficiently small initial and final residual targets rather than limitation on the maximum number of iterations.

3.3.1 Discretization & SGS

Higher order schemes were progressively employed to minimize the effects of numerical diffusion before finally selecting the Crank-Nicholson scheme for time discretization, a 3^{rd} order Total Variation Diminishing scheme for the spatial discretization of velocity and 2^{nd}order schemes for all other variables. This proved to be a step in the right direction. However, after comparison with experimental results, it was clear that this was not the sole cause of the poor prediction of the location of the recirculation zone. Continuing, the SGS models for the closure equations were investigated next. Both standard and dynamic versions of the Smagorinsky and the one-equation model were tested. These tests showed little difference between them as far as the prediction of the location of the recirculation zone is concerned. The standard one-equation model was chosen over the Smagorinsky model for the sub-grid scale as it has been shown to give the better results for channel flows over backwards facing steps and weirs (Monterfano (2011)). For the solution of the algebraic set of equations, a preconditioned conjugate gradient solver was employed for pressure and a bi-conjugate version for all other variables. Finally, the PIMPLE algorithm (a merged version of the PISO and SIMPLE algorithms) was employed for the coupling of the pressure and momentum equations although, due to the small timesteps, this was effectively operating in PISO mode alone.

It should be noted here, that even after successive refinements of the computational domain increased the cell count by several factors the misrepresentation of the recirculations zone position persisted, indicating that it was not a discretization problem alone. Rather, the prescribed boundary conditions appeared to be at fault. Evidenced from the shape of the velocity profile across near the exit of the inlet pipe which was closer to a parabolic shape rather than the characteristic $1/7$ power law.

3.3.2 Boundary Conditions

An investigation was carried out to determine a suitable turbulent boundary condition for the velocity at the inlet, as either the inlet pipe was not sufficiently long to allow the flow to transition into the turbulent regime or there was some form of internal damping caused by the numerical schemes. It should be noted that turbulent inlet boundary conditions for LES are themselves an active field of research and their development no trivial issue. The need for an improved inlet BC was apparent from qualitative inspections that showed the location of the recirculation region was being miscalculated. Rather than being predicted to lie close to the expansion step it lay farther downstream. Several approaches were employed, ranging from the included openFOAM turbulent inlet boundary condition to custom developed ones available on the online repository based on spectral methods (see Davidson (2007) & Piscaglia (2011)). Incremental improvements in the prediction of the recirculation zone location with the use of these improved BCs indicated this might be the source of the error.

The decision was made to try to physically perturb or 'trip' the flow within the inlet tube, in order to allow the flow to transition from the laminar to the turbulent regime. This was

done by separating the upstream tube from the remaining computation domain, introducing a zero-thickness step[62] and modifying inlet and outlet conditions to periodic in order to simulate an infinitely long pipe. After approximately fifteen flow-through times had been modeled, the step was removed and the flow field was allowed to cycle through several more times whilst maintaining the periodic conditions at its ends. Through qualitative observations and inspection of the mean velocity profile across the pipe it was determined that the flow field was sufficiently turbulent and was not dissipating over several flow through times. The whole solution of the inlet pipe flow field was the mapped back onto the initial domain and the turbulent conditions preserved by introducing a periodic BC between a station 2/3 down the length of the pipe and the inlet of the computational domain.

Figure 4 shows a slice through the upstream tube with the step visible at the first spanwise section visible in the foreground. The mapped turbulent conditions were maintained within the inlet tube of the sudden expansion domain by introducing periodic planes within it, similarly to the approach of Tabor *et al.* (2004). Effectively, an infinitely long turbulent pipe was being modeled, eventually resulting in the proper inlet conditions and Figure 5 depicts the whole domain with the improved prediction of the recirculation zone, now predicted just downstream of the step, rather than half-way down the expansion tube.

3.3.3 Measurement Locations And Normalizing Quantities

Before continuing the discussion concerning the investigation into the required mesh resolution, we should first introduce the normalizing quantities that will be used in the following sections. All spatial dimensions are normalized by the respective expansion tube diameter (D). For the D/d=5 case this results in an expansion tube length of z/D=8, an inlet tube length of z/D=6.67 and for the D/d=3.33 these quantities are 12 and 10 respectively. Velocities were normalized by the outlet tube mean values, U_o, summarized in Table 1 except for the near wall analysis where the friction velocity has been used for normalizing the mean axial velocity.

The spanwise measurements were performed at three different axial locations downstream of the step z/D = 0.08, 2.67 & 5.33 where the radial variation of the quantities of interest will be probed. The variation in the axial (*i.e.* streamwise) direction was investigated by probing the flow along the centreline and at the wall, at y/D = 0 & 0.5 respectively. These measurement stations correspond to the locations where the experimental measurements were performed. It is worth noting that the measurements at the wall are not exactly on the wall since, the no-slip condition limit the usefulness of any velocity measurement there. Rather, the measurement are performed slightly offset of the wall as detailed in a later section. The origin of the coordinate system lay on the centreline at the plane of the step, with the x,y-components of the Cartesian system lying on a plane whose normal is parallel to the z-component aligned with the streamwise direction. Visible in Figure 6 is a section of the computational domain along with the aforementioned measurement locations.

[62]The height of the step was approximately a quarter of the inlet tube diameter, d, and the zero thickness dimension was in the direction of the flow. The rational behind choosing the unphysical thickness of the step was to permit easier mapping of the flow domain back onto the original inlet pipe.

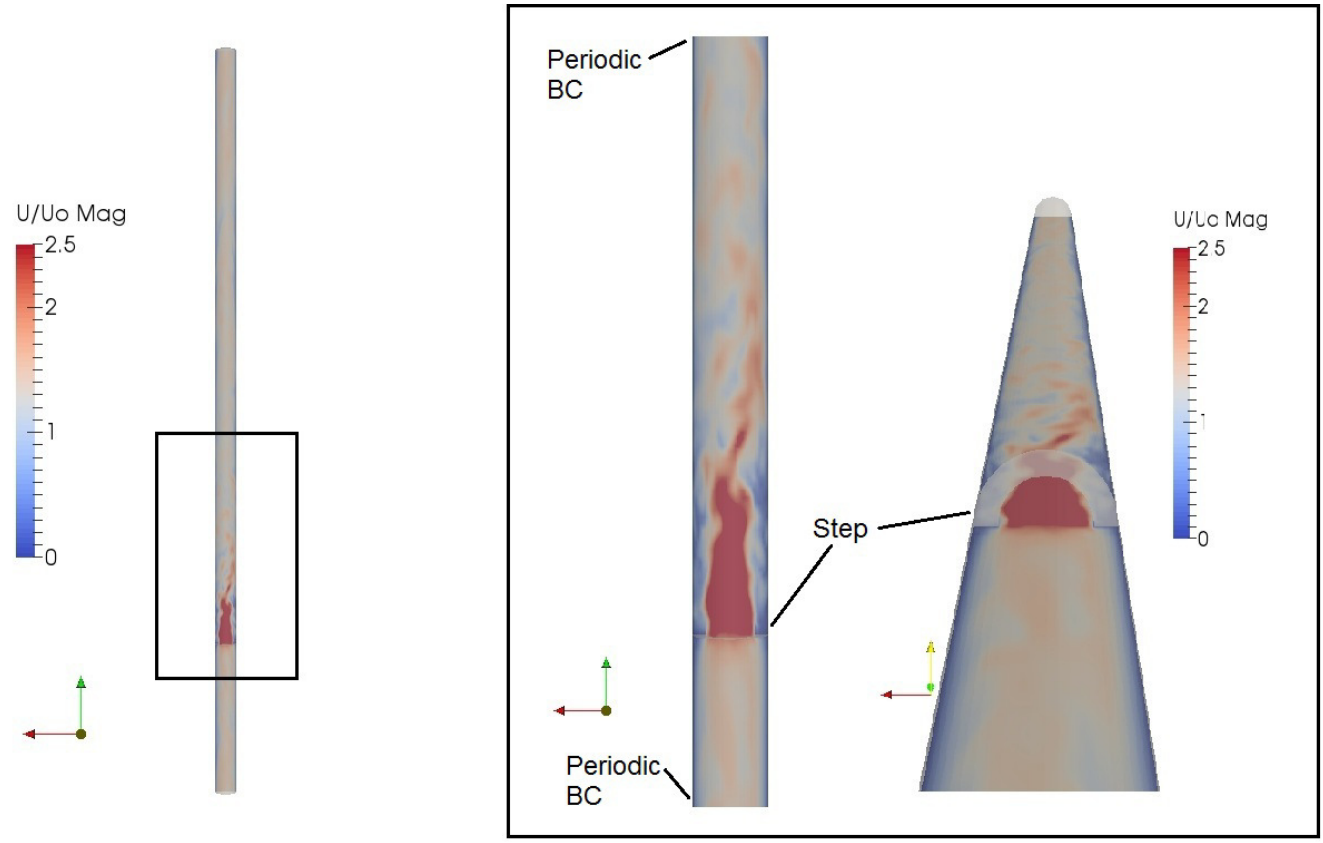

Figure 4: Spanwise and streamwise sections through the inlet tube with the step in place. Detail on the right hand side shows the zero thickness step of $3mm$ introduced into the inlet pipe to trip the flow. Coloring is by normalized velocity magnitude (U/U_o)and range of scale is [0, 2.5].Characteristic dimensions for the inlet tube diameter and length are $15mm$ and $500mm$ respectively. Flow direction is from the bottom of the page to the top.

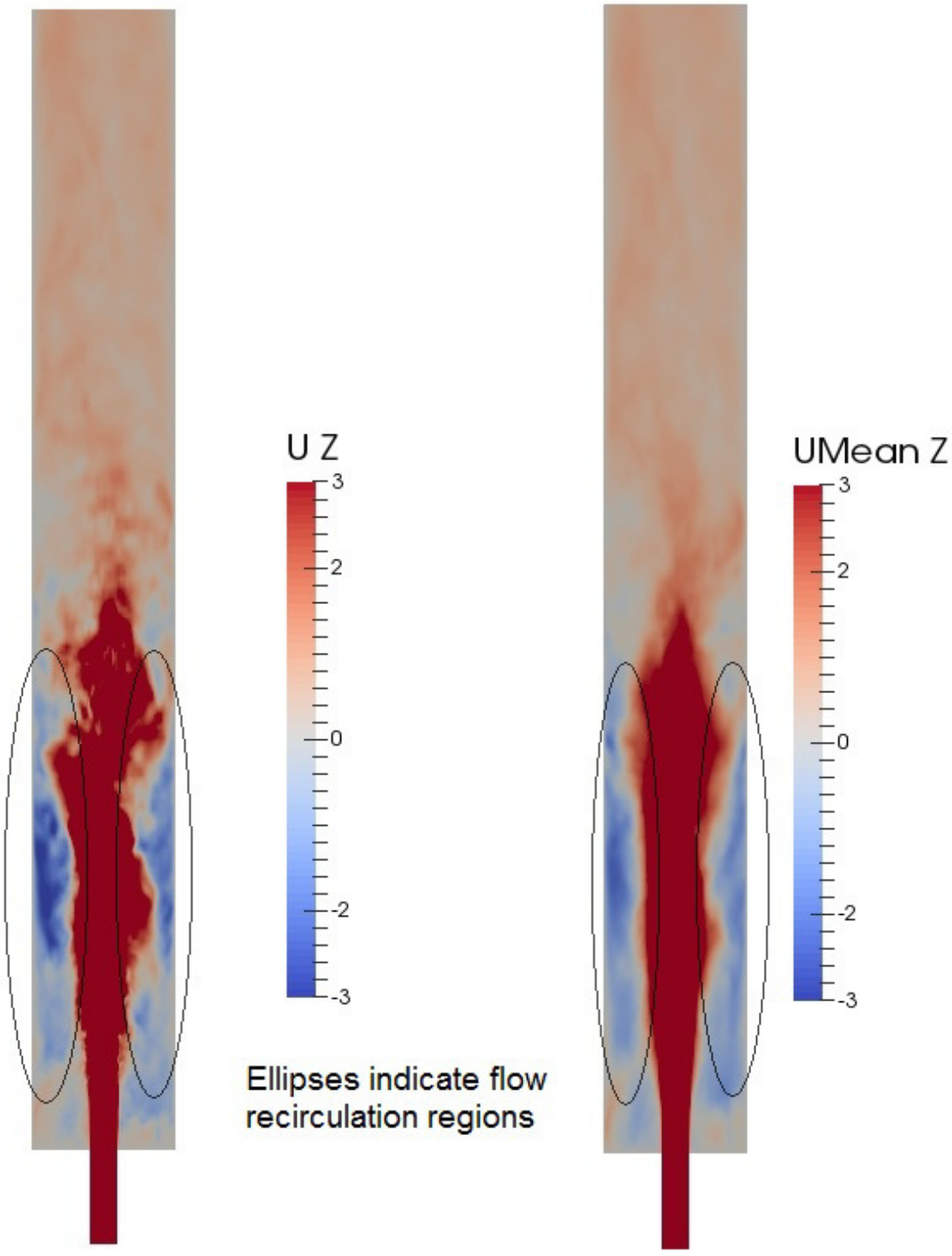

Figure 5: Section through LES domain showing an improved prediction of the position of the recirculation zone. Colored by the axial velocity component with a range [-3, 3m/s]. Flow direction is from the bottom of the page to the top. Blue colors indicate flow reversal.

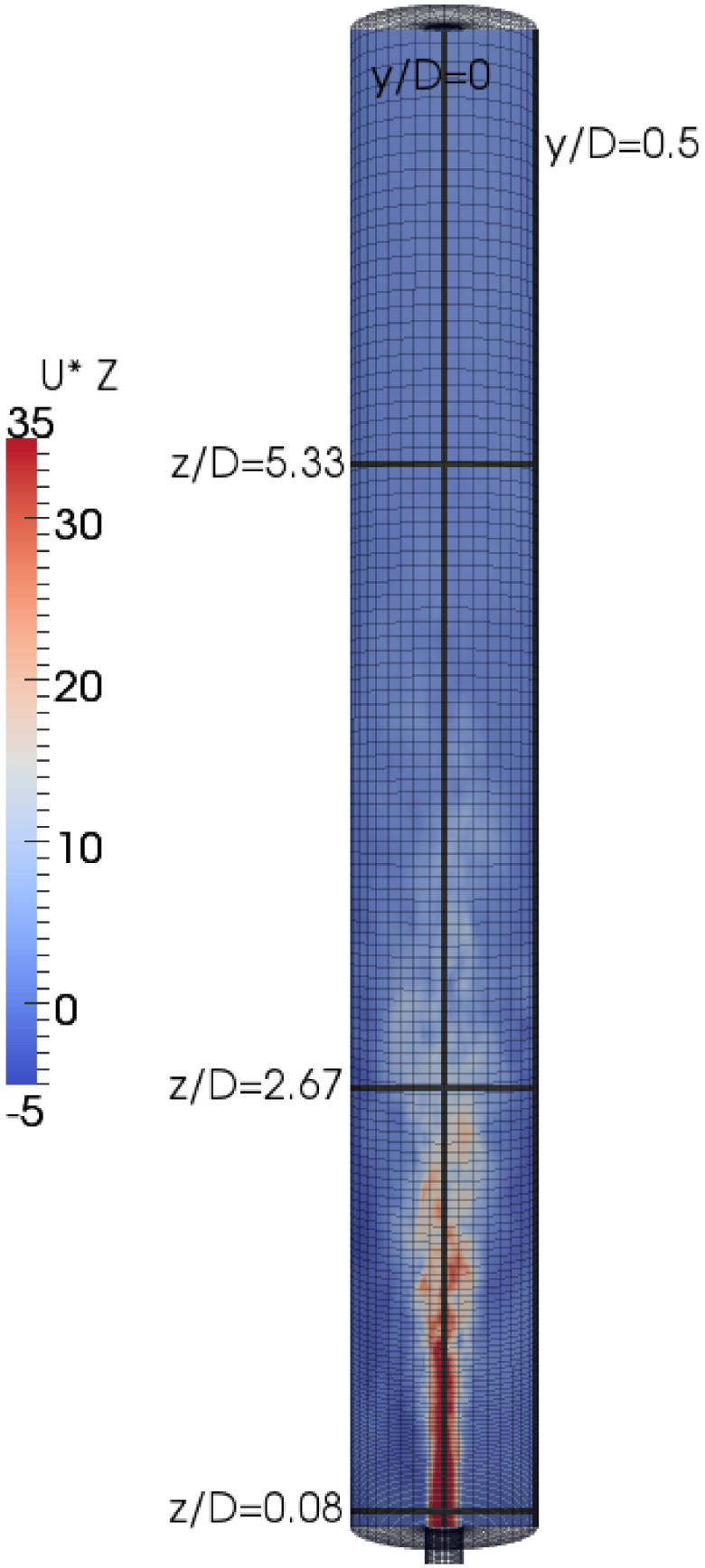

Figure 6: Computational mesh of the expansion tube with the measurement locations indicated by the black lines. Also shown is a slice depicting the normalized axial velocity colored by the normalized axial velocity ($^{U_z}/_{U_o}$) with a range [-5, 35]. Expansion tube dimensions are $75mm$ and $600mm$ for the diameter and length respectively. Flow direction is from the bottom of the page to the top.

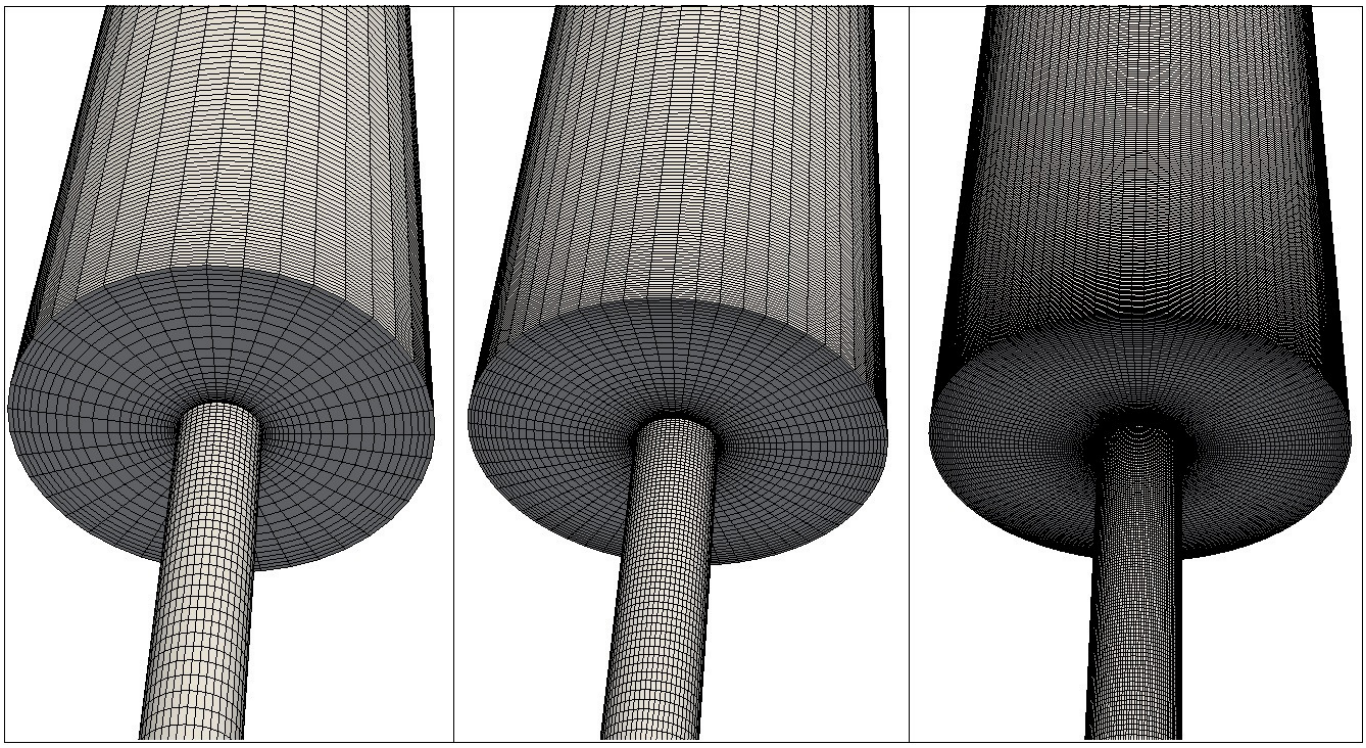

Figure 7: Representation of the 3 meshes depicting the mesh at the step from a perspective view, from left to right; the coarse (800k cells), the standard (1,300k cells) and the fine grid (8,800k cells). Inlet and expansion tube diameters are $15mm$ and $75mm$ respectively.

3.3.4 Mesh Sensitivity Analysis

The tools were now in place to perform an investigation on whether the mesh resolution was satisfactory for the remaining LES calculations. In addition to the initial mesh, which by now had been refined locally in the near wall region and whose cell count had increased to 1.3 million hexa-hedrals, two further meshes were constructed. One was coarser with approximately eight hundred thousand cells and the other was finer through equal refinement in all directions, resulting in cell dimensions half of the original ones and eight times the original cell count. The relevant information is tabulated below in Table 2 and the Figures 7- 11 show portions of the three computational domains depicting the differences in the generated meshes.

The remainder of this section is devoted to the comparison of the results between the three meshes and the differences in predicted quantities. Figures 8 and 10 show details of the meshes at the step and at the inlet to the computational domain, clearly discernible is mesh grading to ensure that the cells by the walls are sufficiently small to adequately resolve the boundary layer and to ensure that turbulent conditions are achieved. Also visible, in Figure 9, are the details of the mesh right at the step location, and the fact that the mesh grading that was introduced by the walls of the inlet tube is extended throughout the rest of the domain, visible also at the outlet location in Figure 11, in an effort to avoid unnecessary discretization errors that might arise by using a non-structured grid. This grid also aids in resolving the shear stresses properly between the fast moving jet upon its entrance into the near quiescent conditions of the expansion tube, in turn ensuring that the interfacial instabilities between the two streams of different velocity are properly predicted.

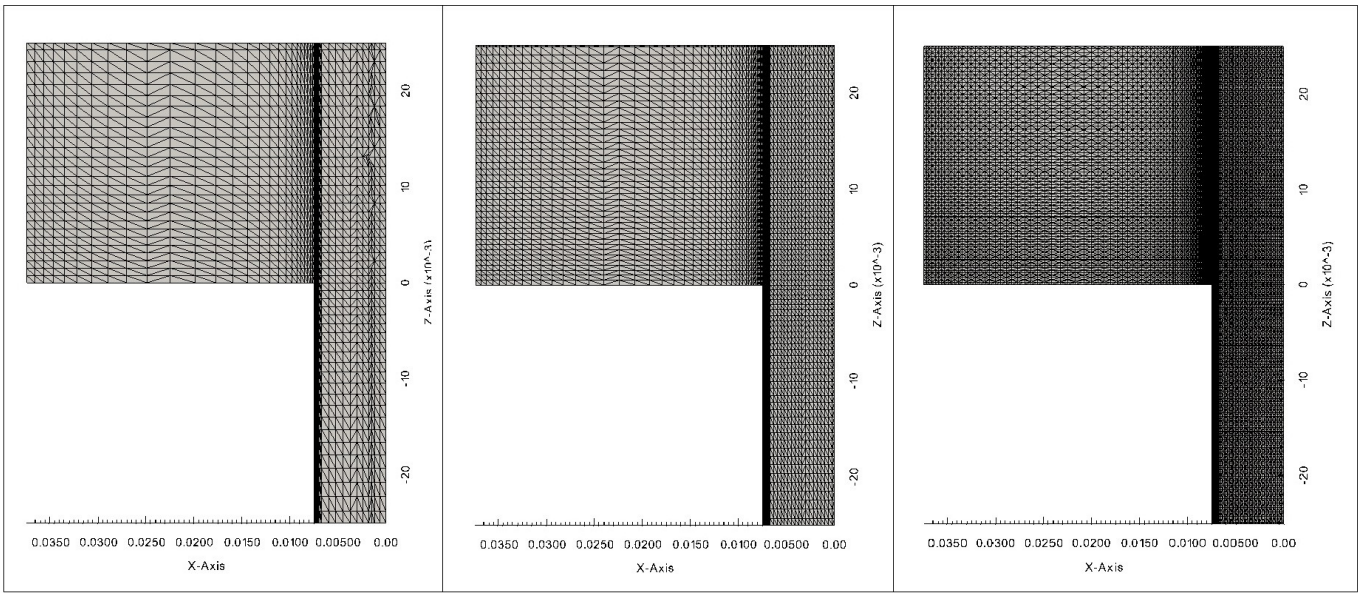

Figure 8: Representation of an axisymmetric portion of the 3 meshes depicting the mesh at the step. Shown from left to right; the coarse, the standard and the fine grid. The cells are all hexa-hedral despite appearing to be prisms due to an issue with the rendering process of the post-processing software.

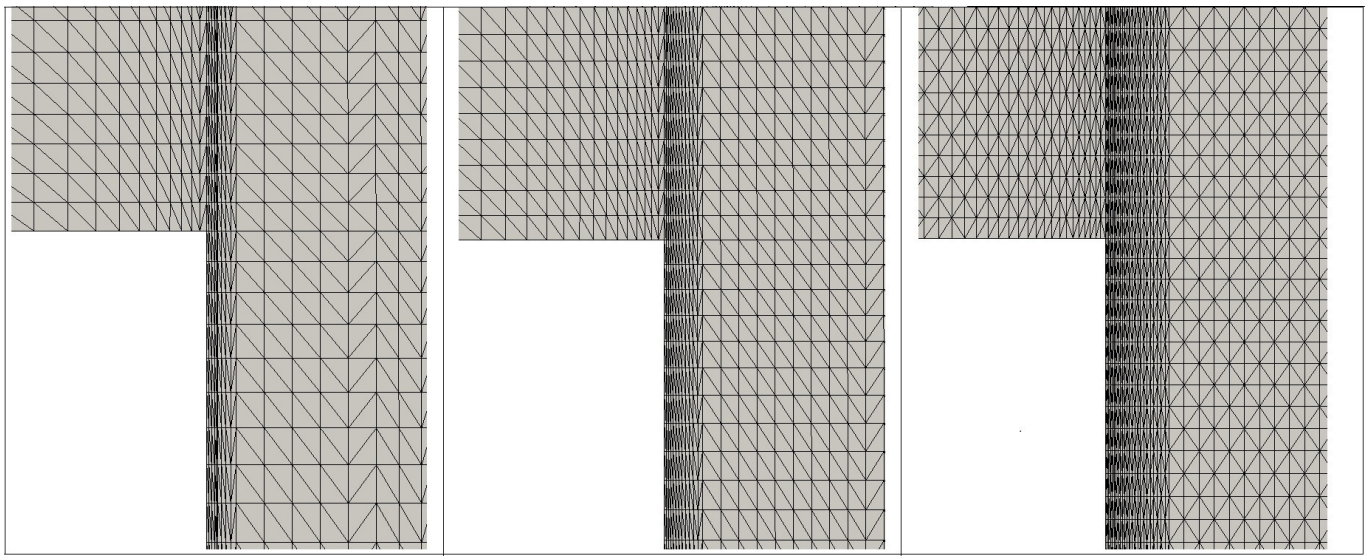

Figure 9: Representation of the 3 meshes depicting details of the mesh at the step location Shown from left to right; the coarse, the standard and the fine grid.

Table 2: Mesh details for the three grids tested....

Computational Mesh Details			
Mesh Name	Coarse	Standard	Fine
Number of Hexa-Hedral Cells	$8.8\,\mathrm{x}\,10^5$	$1.33\,\mathrm{x}\,10^6$	$8.8\,\mathrm{x}\,10^6$
Average Cell Size	$0.42mm$	$0.31mm$	$0.23mm$
Average Cell Size by Wall	$0.075mm$	$0.05mm$	$0.025mm$
y^+ value at the Inlet Tube Wall	1*	1.2	1
*Employing wall modeling			

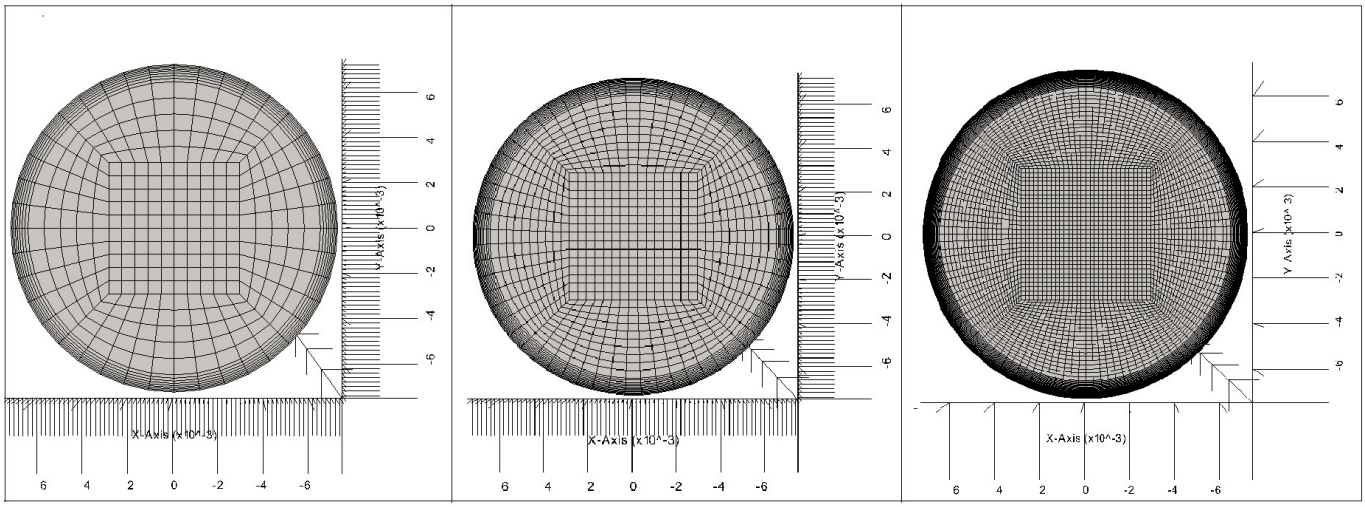

Figure 10: Representation of the 3 meshes depicting details of the mesh at the inlet, diameter is $15mm$, from left to right; the coarse, the standard and the fine grid.

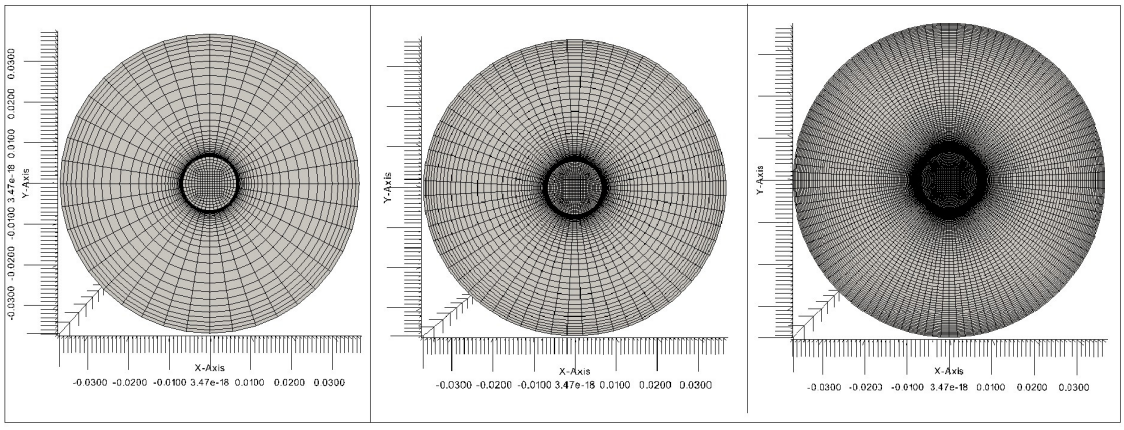

Figure 11: Representation of the 3 meshes depicting details of the mesh at the outlet, diameter is $75mm$, from left to right; the coarse, the standard and the fine grid.

3.3.5 y^+ Analysis

Figure 12 shows a qualitative representation of the y^+ values in the expansion tube downstream of the step. This should be considered a qualitative representation only as the calculation of the wall friction velocity inevitable involves some uncertainty whenever there exists flow reversal and the calculation is not a DNS. This arises from the way the wall shear stress, σ_w, is calculated from the gradient of the axial velocity in the normal direction to the wall and in an LES calculation there inevitably exists some interpolation due to the finite size of the cell next to the wall:

$$\sigma_w = \mu \left(\frac{\partial U_z}{\partial y} \right)_{y=0}$$

Perhaps a more accurate analysis of the near wall region requires one to limit the analysis to the upstream tube where the pressure drop is constant and a value for the wall shear stress, σ_w, may be obtained through evaluation of the forces acting on the tube walls. From analysis of the pressure drop, Δp, along the inlet tube the wall friction velocity, U_τ, may be estimated according to:

$$U_\tau = \sqrt{\frac{\sigma_w}{\rho}}$$

In turn the estimation of the wall shear stress is straightforward for a fully developed flow[63] and may be calculated by balancing the forces on the inlet tube:

$$\sum F = 0 \leftrightarrow \Delta p \left(\frac{\pi d^2}{4} \right) - \sigma_w \pi d \cdot l_i = 0 \leftrightarrow \sigma_w = \frac{\Delta p \cdot d}{4 l_i}$$

Figure 13 shows the normalized velocity profiles in the near wall region along with the theoretical predictions (teal and purple colors) at location $z/D = -0.33$, a short distance upstream of the step. The aforementioned mesh resolutions result in y^+ values of approximately 1*, 1.2 & 1 for the coarse, standard and fine meshes respectively. From inspection of the y^+ variation with u^+ it might appear that all three meshes are predicting acceptable values for an LES, however one should bear in mind that the coarse meshes employ LES wall functions to achieve just that, whereas the standard and fine meshes avoid the use of wall modeling altogether. The wall modeling produces satisfactory results within the wall shear dominated region of the inlet tube but the mesh density is inadequate to capture accurately the physics of the recirculation zone. Figure 13 suggests that all three meshes struggle to capture the logarithmic region accurately and the benefits of the fine grid are small especially given the small improvement observed in the log-law region (y^+ [30-1000]). Despite the fact that all three meshes are resolving to similar levels the flow within the inlet pipe the large variation observed in Figure 12 seems to suggest that further analysis is required before a satisfactory mesh resolution is selected.

3.3.6 Instantaneous Values

The following section will describe the evaluation of the calculated quantities from the three meshes amongst themselves in an effort to make a decision regarding the required mesh resolution and in order to validate the methodology. Evaluations will be made for instantaneous and time

[63] The introduction of cyclic BC in in the inlet pipe ensures that an infinetely long pipe is being modeled.

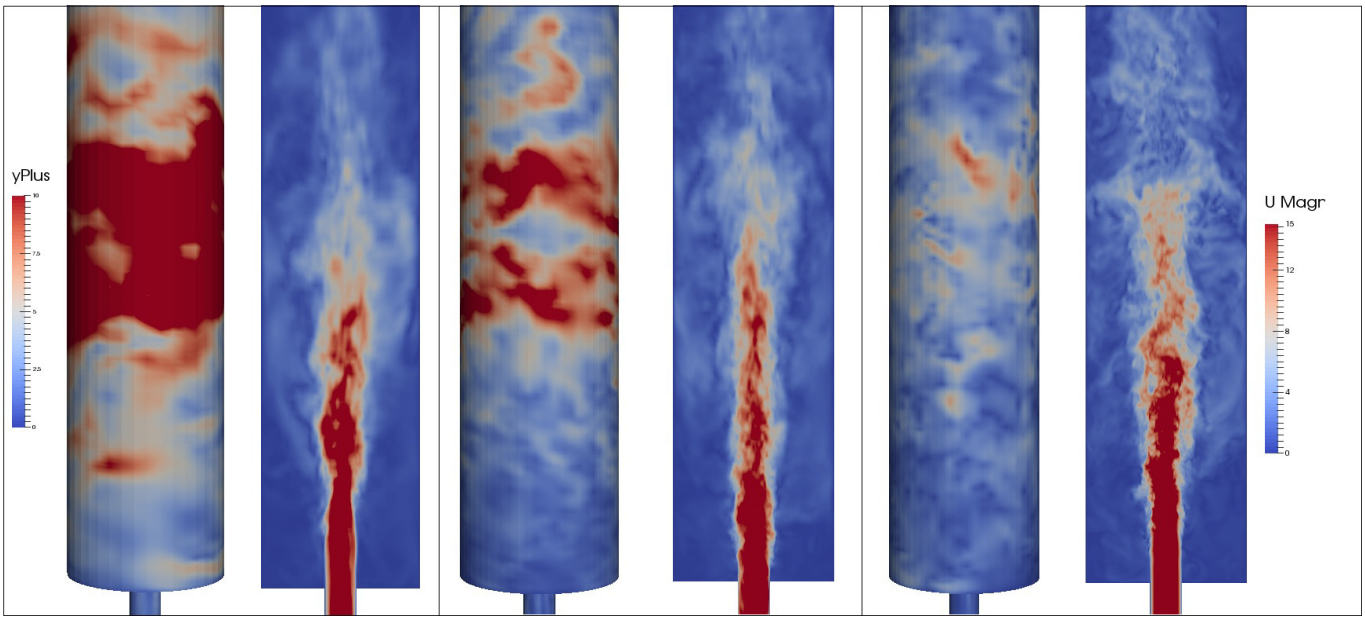

Figure 12: From left to right details of; the coarse, the standard and the fine meshes, respectively, depicting on the left the y^+ values plotted on the surface of the domain as calculated within openFOAM, with a range [0,10] and the magnitude of velocity on the right of each pane, with a range [0, $15m/s$]. Flow direction is from the bottom of the page to the top.

averaged quantities along the three spanwise and two streamwise locations identified in Section 3.3.3 while the comparison with the experimentally measured quantities will be presented in the following section here the experimental data is included in the figures to provide a baseline for the trends we expect to observe.

Although not constructive in making a definitive choice, the instantaneous data is interesting in itself; First, it reveals to the reader the large fluctuations typically observed in highly turbulent LES flows and secondly when the information for the three mesh resolutions is compared amongst themselves one can observe from the smaller period of the sinusoidal patterns the effect of the finer grid on the size of the calculated eddies. All results presented below are after a sufficient number of flow-through times (between 20-30) have been calculated. Here a flow through time is defined as the time required for the bulk inlet velocity to traverse the whole domain. Figures 14 to 18 show the axial velocity at the probing locations for two distinct instances in time.

It would appear that there is a discrepancy when it comes to predicting the near wall velocity with all three meshes. However, it seems that this is a result of the limitation of how near to the wall the experimental probe volume could actually measure when compared to how close to the wall the calculation can be probed. The experimental measurements were limited to measuring at a distance of a $\sim 1mm$ from the wall due to the experimental arrangement. The size of the measuring probe in a LDV setup is determined from the diameter of the laser beams and the angle formed at their intersection. The size of the probe may be roughly determined as follows based on documentation by a commercial manufacturer of such systems (DANTEC 2006):

$$d_x = \frac{d_f}{cos\,(\theta/2)},\; d_y = d_f \;\&\; d_z = \frac{d_f}{sin\,(\theta/2)}$$

where d_f and θ are the beam diameter and the angle of intersection respectively ($1.25mm$ &

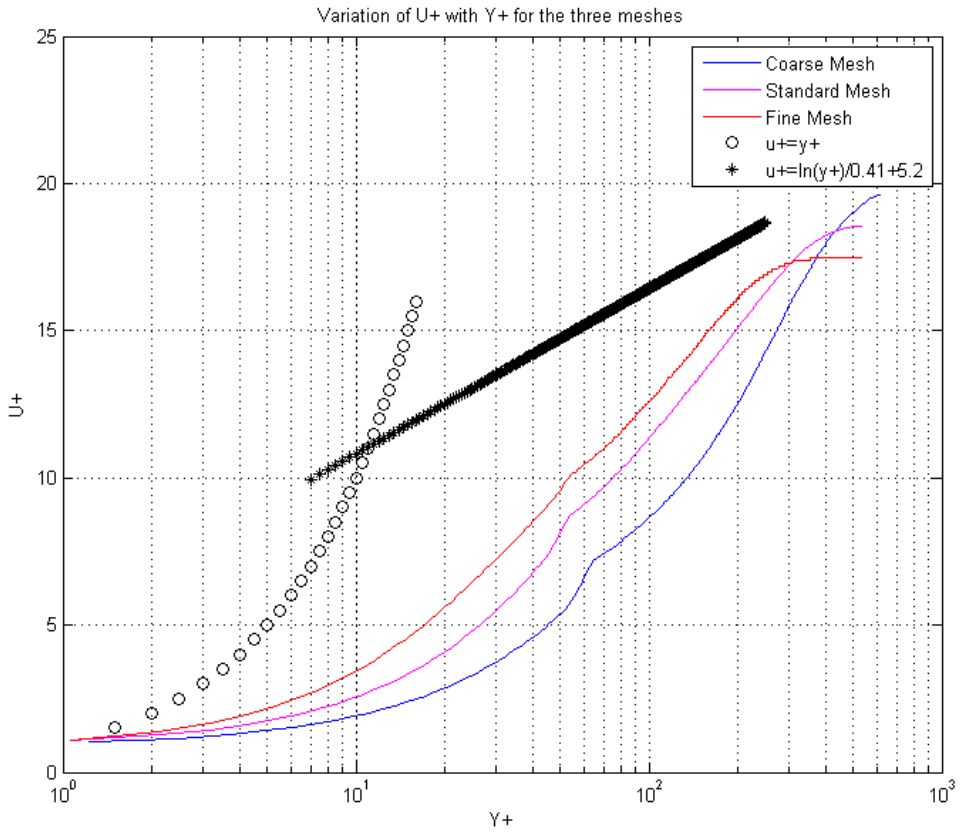

Figure 13: Variation of y^+ with u^+ in the inlet pipe at at location $z/D = -0.33$ upstream of the step for the three mesh densities along with the theoretical predictions. Note that the coarse gird makes use of wall functions.

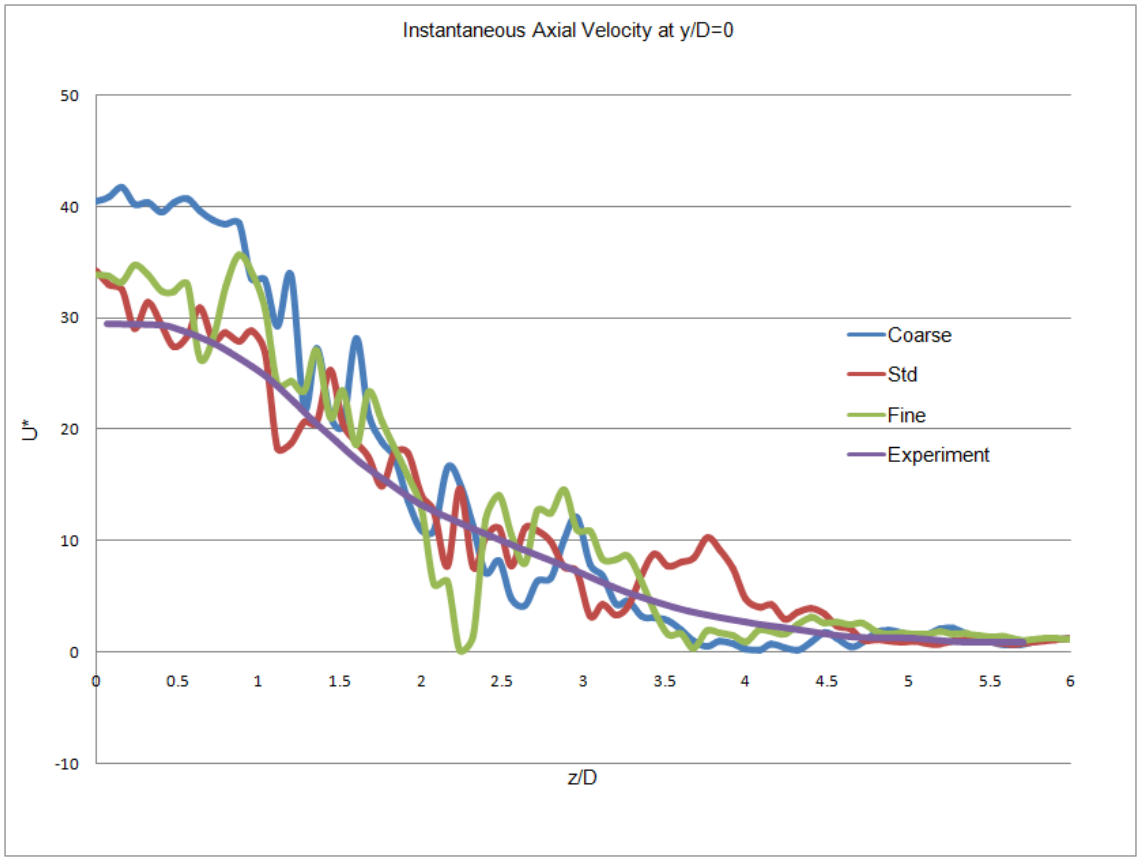

Figure 14: Streamwise variation of the instantaneous axial velocity along the centreline ($y/D = 0$)

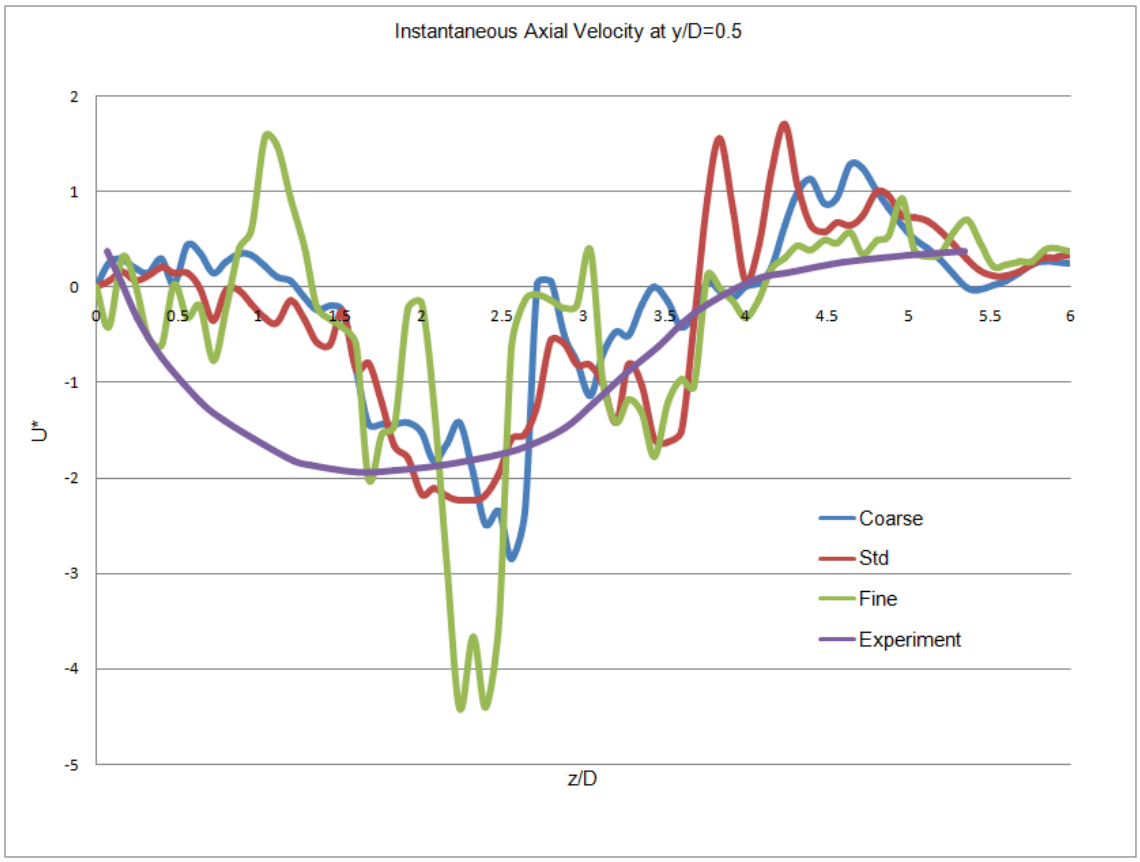

Figure 15: Streamwise variation of the instantaneous axial velocity along the wall ($y/D = 0.5$)

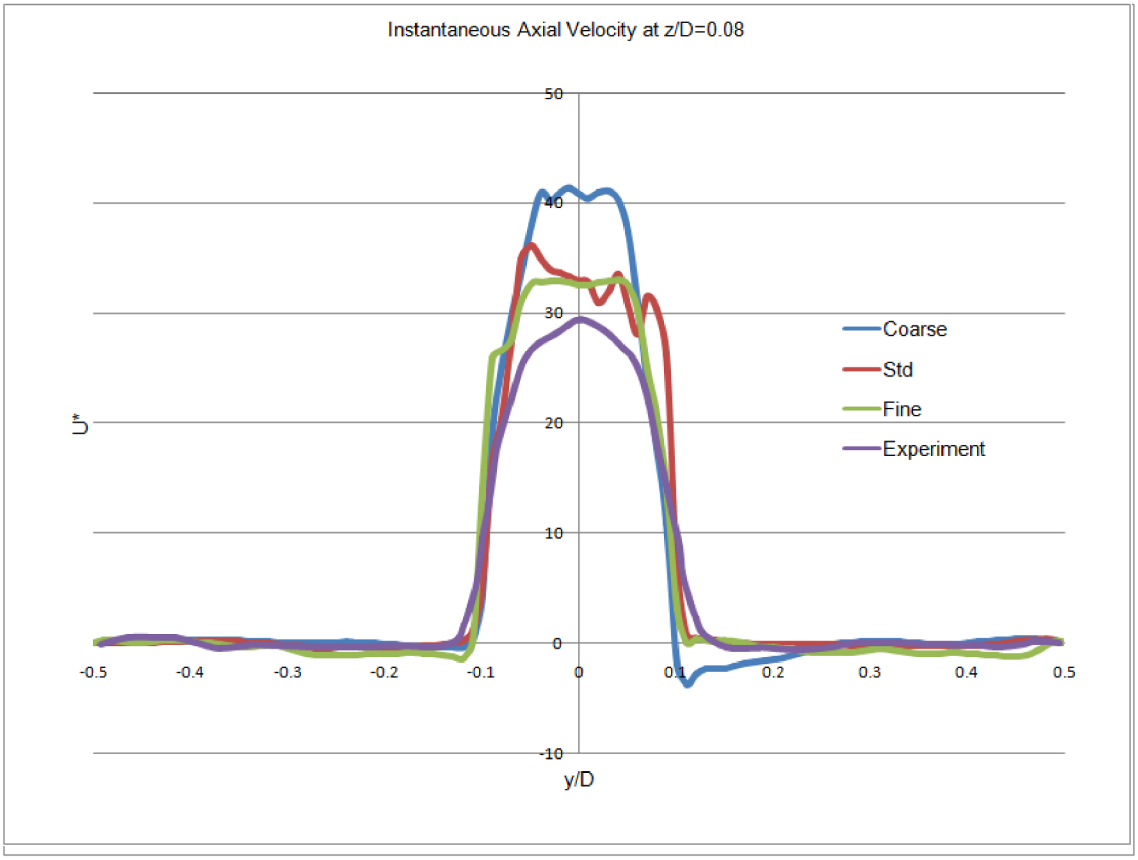

Figure 16: Spanwise variation of the instantaneous axial velocity at $z/D = 0.08$

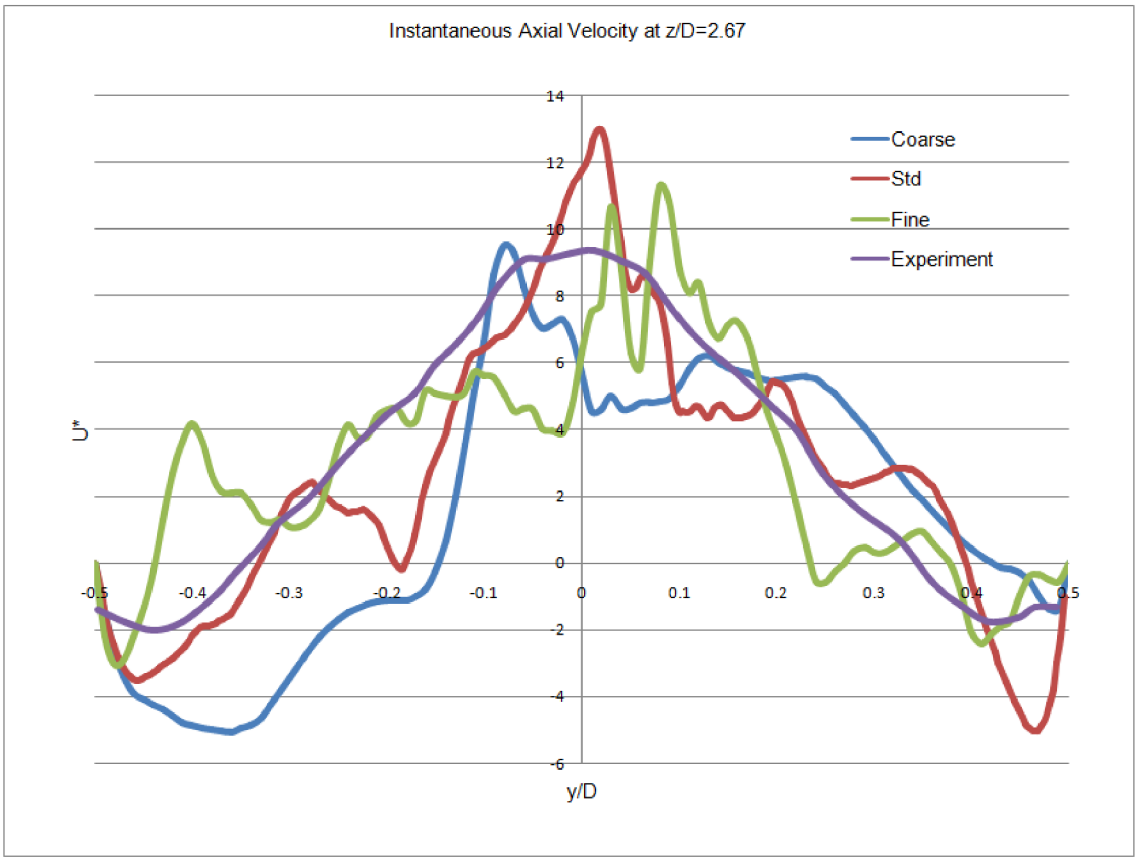

Figure 17: Spanwise variation of the instantaneous axial velocity at $z/D = 2.67$

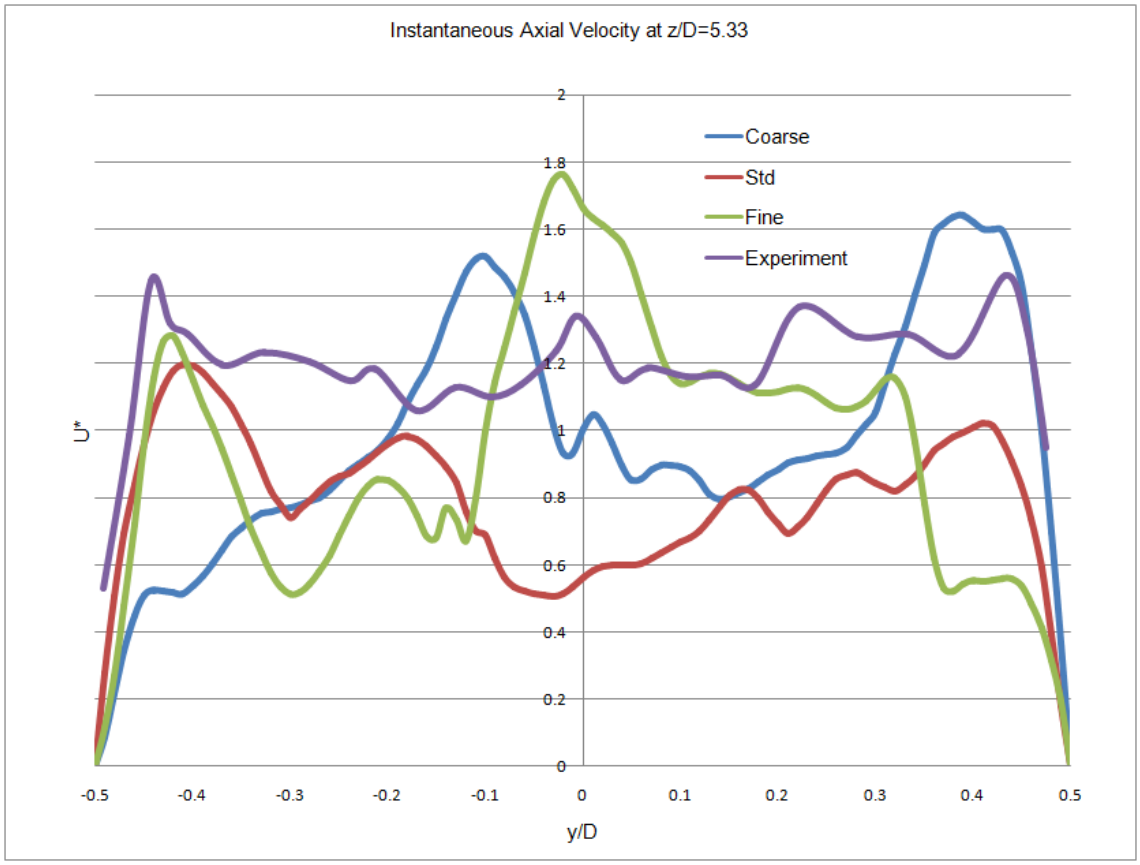

Figure 18: Spanwise variation of the instantaneous axial velocity at $z/D = 5.33$

2x2.64deg). These values result in an ellipsoidal probe volume with overall dimension of 1.252mm x 1.25mm x 27.2mm. However, this does not necessarily mean that $^{1.252mm}/_{2}$ is the distance from the wall where the experimental measurement were performed as that would inevitably result in a significant amount of laser light reflecting off the glass tube walls. Nonetheless, the information from the calculations presented here was made at a distance of 0.5mm from the expansion tube walls which, in normalized terms corresponds to $y/D = 0.493$. However, for the remainder of this thesis this location will be referred to as $y/D = 0.5$. It is important to note that this distance from the wall corresponds to a point outside of the first cell from the wall boundary for but the coarsest of the three meshes used.[64]

Figure 19 shows the instantaneous axial velocity variation at three locations 1, 1.5 & 2mm from the wall as taken from the calculation with the standard mesh. The trends in streamwise variation are predicted correctly but the magnitude is dependent on the distance to the wall, as would be expected. However, what is of primary importance is predicting the length of the recirculation zone, indicated by the inflection in the sign of the normalized velocity, which is captured precisely at the same location in all three calculations.

[64]Unlike the experiment, within the calculations there is no limitation as to how close to the wall one can probe the flow. Hoever, one must bear in mind that, for meshes employing wall modeling measurements within the first cell from the wall, the velocity profile is governed by the prescribed wall model.

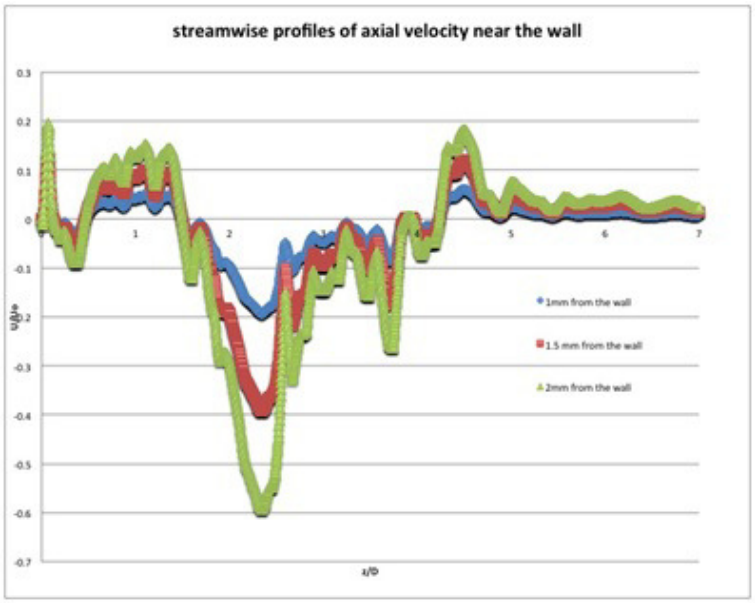

Figure 19: Streamwise (y/D) variation of the instantaneous axial velocity at 1, 1.5 & 2mm from the wall

3.3.7 Comparisons With Experiments-Time Averaged Results

The level of agreement between the calculations and the experimental measurements needs the information from the simulations to be averaged over time. Details of the approach adopted to perform time averaging and estimate the error bars are included in Appendix B. Once again let us reiterate that all the information used in generating the following figures was extracted after 20-30 flow through times had been calculated. This ensured that all the information was extracted only after the flow had reached fully developed and statistically steady-state conditions so that any transient phenomena are due to the unsteadiness inherent to the flow itself, rather than due to a developing simulated flow.

The largest discrepancy between calculations and the measurements exists at the spanwise measurement station at z/D=0.08, shown in Figure 22 especially along the centreline and also seen in Figure 20 between z/D [0-1]. At a distance of $0.05D$ either side of the centreline the numerical predictions are in agreement with the experimental measurements. Examination of the streamwise comparison at y/D=0 indicates that the discrepancy along the centreline continues for approximately one D downstream of the step for the standard and the fine grids, thereafter the agreement is satisfactory when the uncertainties are taken into account, whereas the discrepancy is still significant for the coarse grid for more than $2D$ downstream of the step. These discrepancies seem to be a result of the under-resolution of the level of turbulence within the inlet tube despite the efforts employed to address the issue. This is further supported by the shape of the velocity profiles at the first spanwise station. For all practical purposes this location is close enough to the step that it may safely be assumed that the profiles will not look substantially different just a little bit upstream, within the inlet tube. And therein lies the problem as there is a clear indication that the finer the mesh used, the closer the calculated velocity profiles attains the characteristic '1/7 power-law' like profile of fully developed turbulent pipe flow. At the same time the two sides of the base of the parabolas provide a further clue

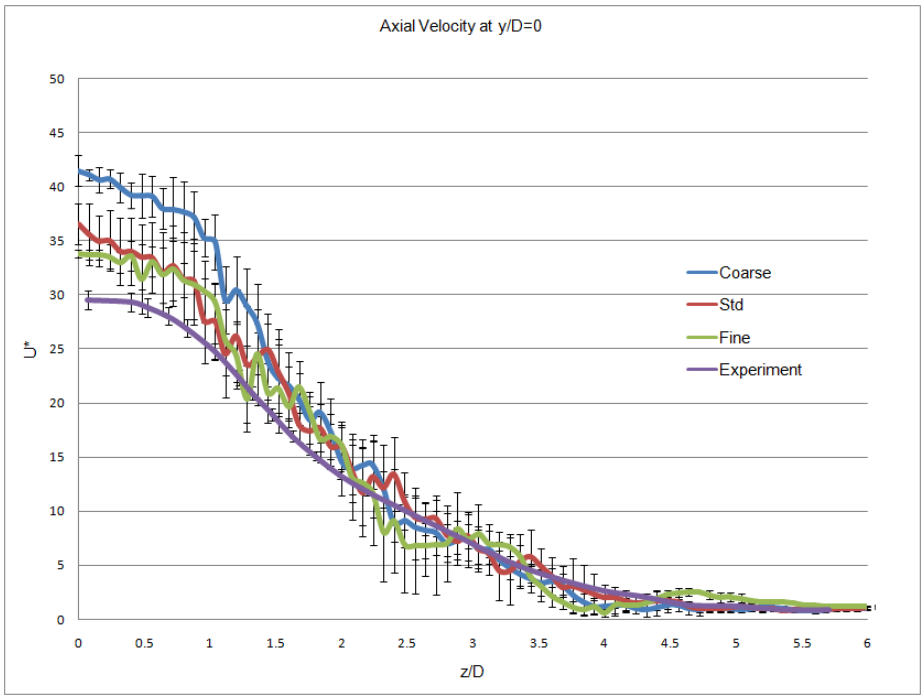

Figure 20: Streamwise variation of the time-averaged axial velocity along the centreline (y/D=0)

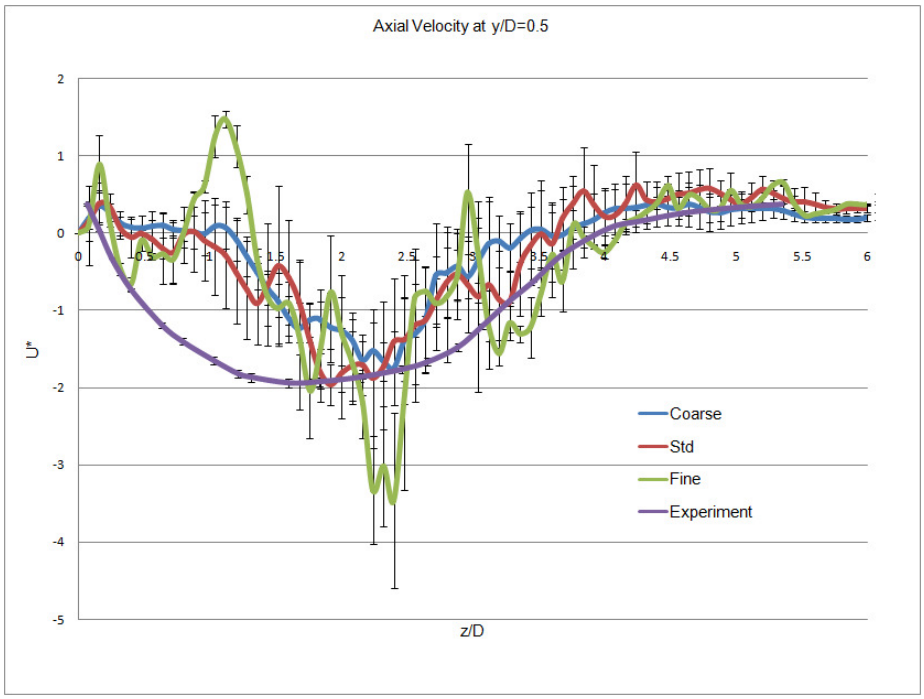

Figure 21: Streamwise variation of the time-averaged axial velocity at the wall (y/D=0.5)

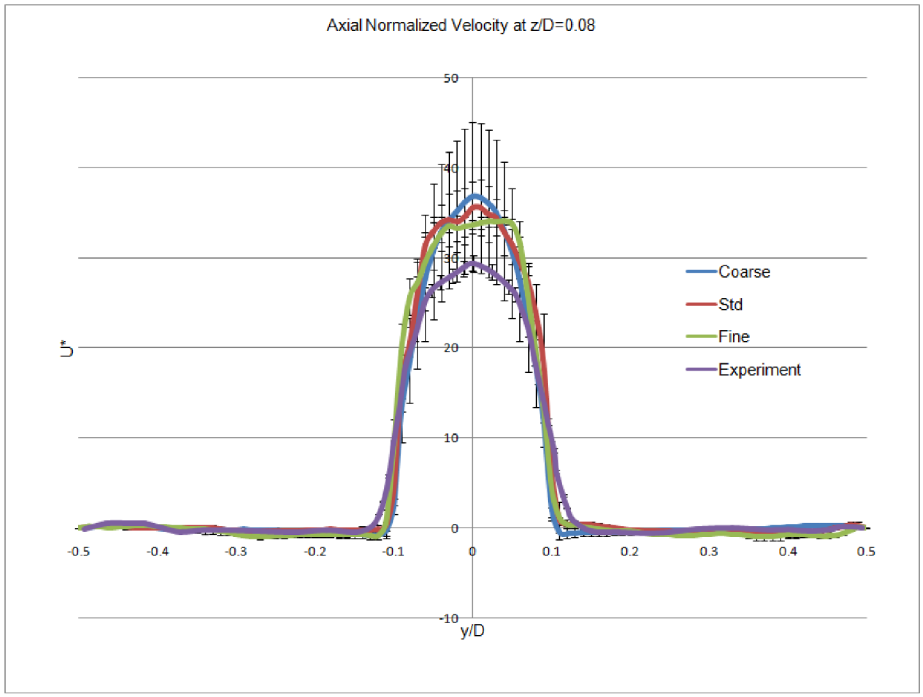

Figure 22: Spanwise variation of the time-averaged axial velocity at z/D=0.08

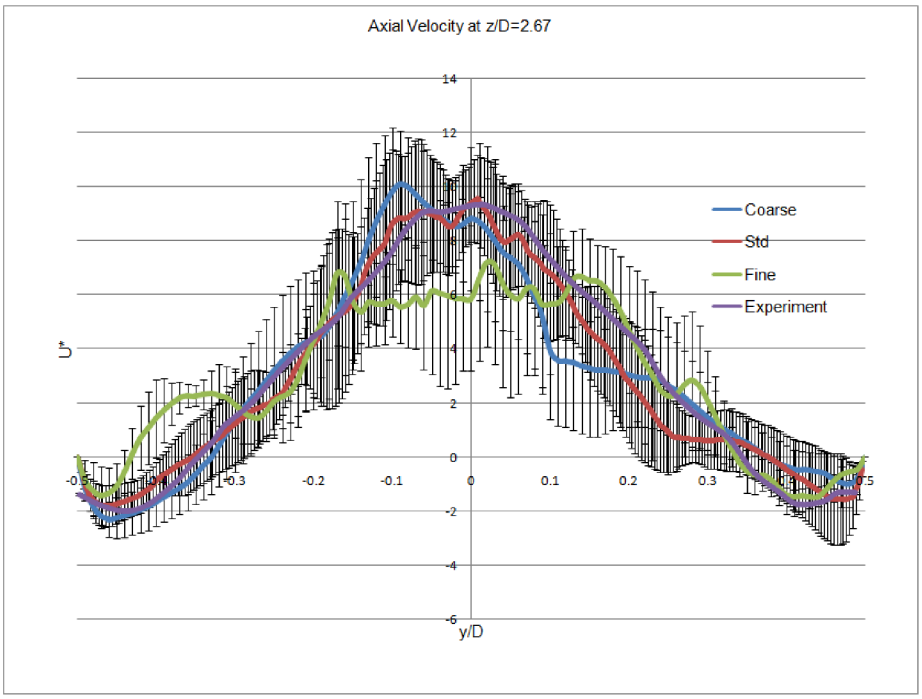

Figure 23: Spanwise variation of the time-averaged axial velocity at z/D=2.67

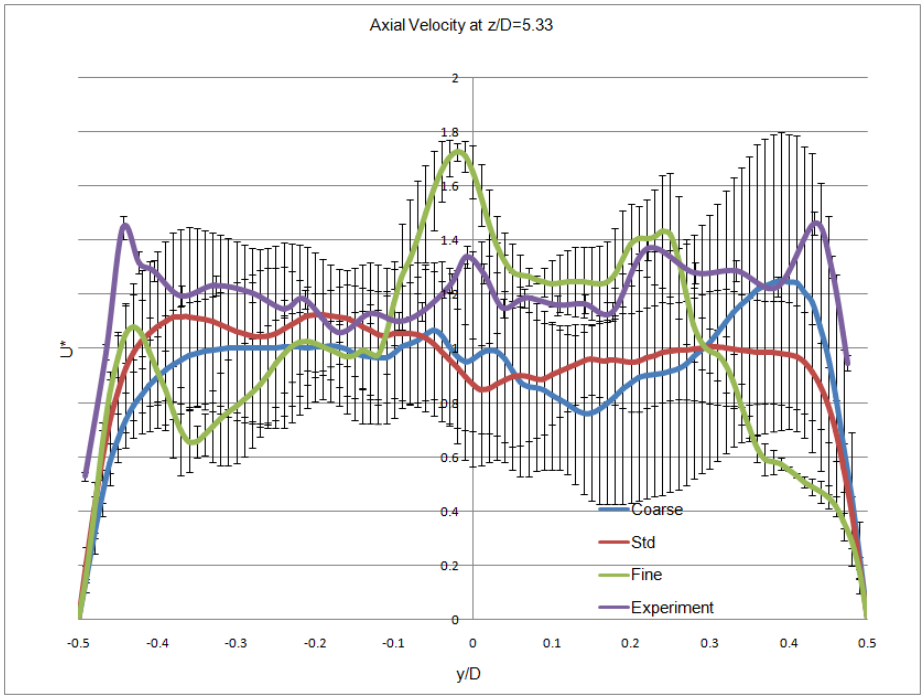

Figure 24: Spanwise variation of the time-averaged axial velocity at z/D=5.33

as it appears the difference between the calculations and the experimental measurements bear a remarkable resemblance to turbulent pipe flow in rough and smooth walled pipes, respectively.

At the next measurement station, at z/D=2.67, shown in Figure 23, the agreement is overall good, bar the coarse mesh right at the centreline at y/D=*0* and an unaccepted asymmetry observed in the fine mesh prediction at y/D=-0.5. This might be a result of the averaging method and the random selection of timesteps, indicating a false bias towards one side of the flow or it might be an indication that the finer mesh, with its more detailed structure is more susceptible to individual realizations than was thought and an increased number of samples would resolve the issue. Meanwhile, at station z/D=5.33, shown in Figure 24, the standard and coarse meshes seem to be capturing the overall trend observed in the experiments more accurately, although all three calculations agree with the measured lines within error. Finally, regarding the streamwise comparison near the wall, shown in Figure 21, the discussion made earlier still holds true and the important aspect of accurate inflection point prediction, indicating the extents of the rcirculation zone, is achieved by all three meshes.

It is possible to apply *Reynolds Averaging* to the instantaneous velocity and then make comparisons between the meshes and the experimental measurements. Temporal averaging over successive iterations of the instantaneous velocities was performed, resulting in the value *UMean*. Results are shown in Figures 27 to 31. The qualitative representation is given in Figure 25 where the effect of the different size scales is evident between the three meshes. For the coarse grid the result is near identical to that predicted by the $k-Epsilon$ calculation, the standard grid exhibits some smaller fluctuations while for the fine grid the flapping motion of the jet is still clearly discernible behavior. The effect of *Reynolds Averaging* on the different mesh densities on a LES flow is similar to the application of a filtering kernel and is more discernible for the spanwise velocity components shown in Figure 26. Although the 'smoothed' lines make the comparison of

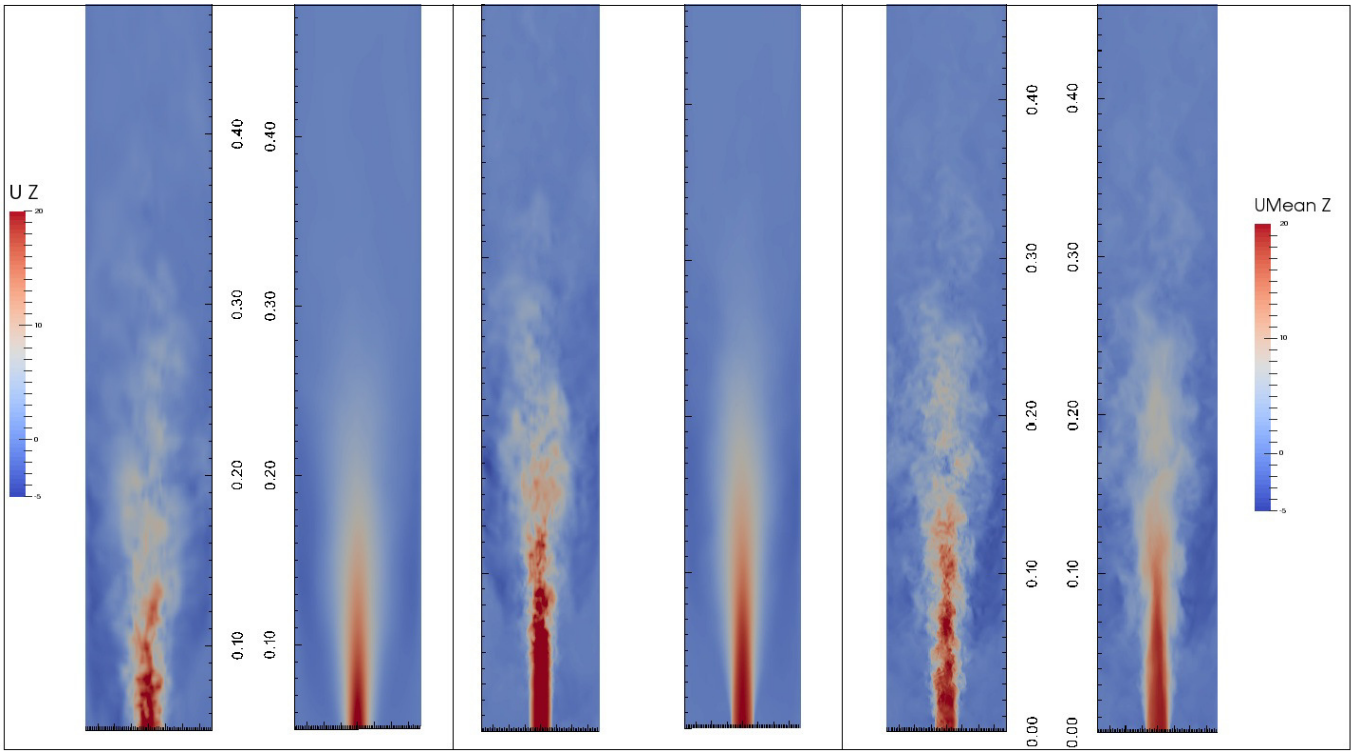

Figure 25: Comparison between the instantaneous and *Reynolds averaged* axial velocities, colored between [0, $20m/s$] on the left and right respectively for the coarse, standard and fine meshes; from left to right. Flow direction is from the bottom of the page to the top.

the measurements at the streamwise and spanwise locations more discernible limited additional conclusions may be drawn.

Overall the *Reynolds averaged* velocities exhibit very similar behavior, albeit it with some of the fluctuations smoothed-out, to the instataneous data as expected and as they should. Finally, from the comparison performed to this point it would seem that the coarse mesh is not suitable due to the significant discrepancies along the centreline extending for several D downstream of the step. The following sections will attempt to shed some light into the benefits of the finer grid over the standard one. Also of note is the apparent asymmetry between the left and right hand sides, observable for the fine mesh in Figures 3031. This would seem to indicate that there are an insufficient number of flow-through times calculated for the fine mesh and that statistics have yet to converge. For the present analysis this is of minor importance since the main objective of the thesis is not to produce the most detailed LES data available for this test case rather, to investigate what features of the Eulerian and Lagrangian phase are lost when a uRANS approach is adopted.

3.3.8 Sub-Grid-Scale Viscosity Comparison

Another measure of grid resolution is the ratio of turbulent viscosity to the physical one. The finer the resolution the smaller the ratio. While the difference between the coarse and the two finer ones is large, the difference between the standard mesh and the fine mesh is very small as is evident in Figure 32. In general, ratios close to unity are acceptable, as the greater the ratio the larger the effects of the SGS model on the flow. Instantaneous and time averaged

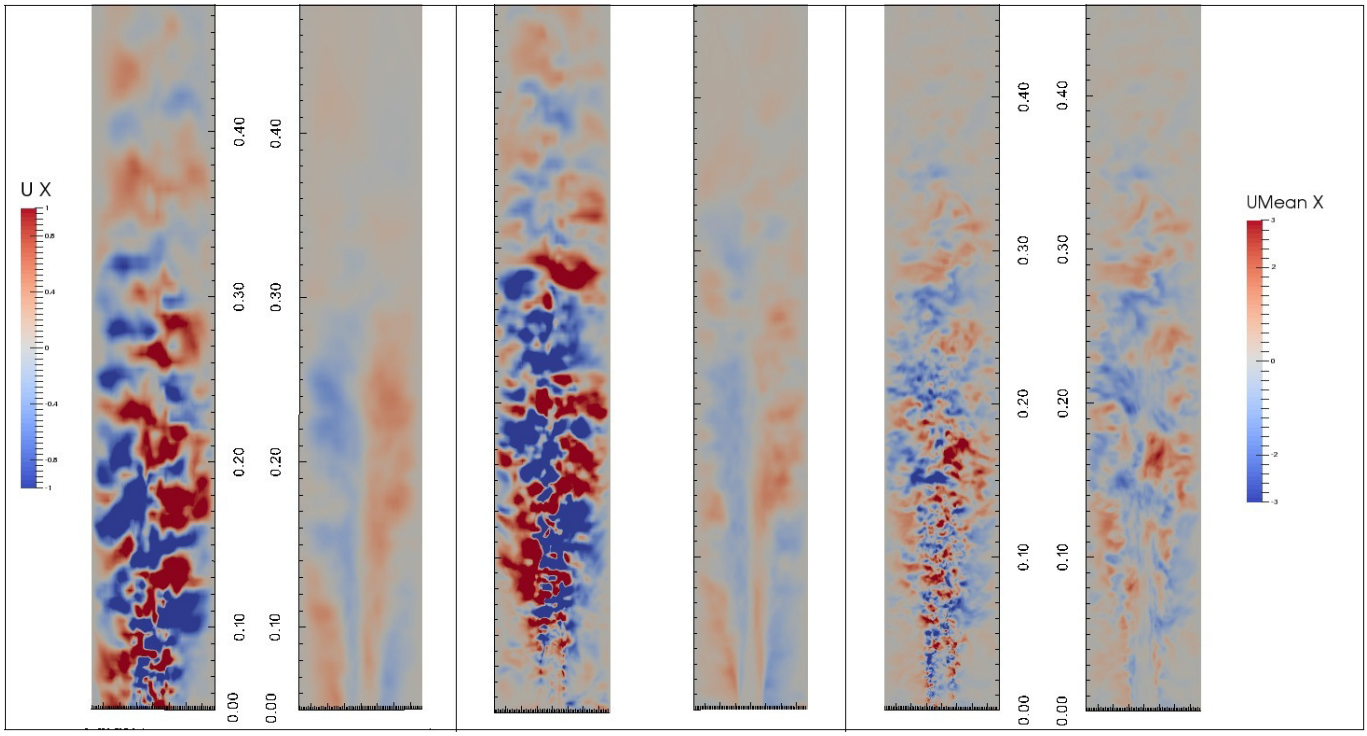

Figure 26: Comparison between the 'instantaneous' and *Reynolds-Averaged* radial velocities, colored betwen [-1, $+1m$], on the left and right respectively for the coarse, standard and fine meshes; from left to right. The orientation of the schematics is such that the x- component is normal to the page. Flow direction is from the bottom of the page to the top.

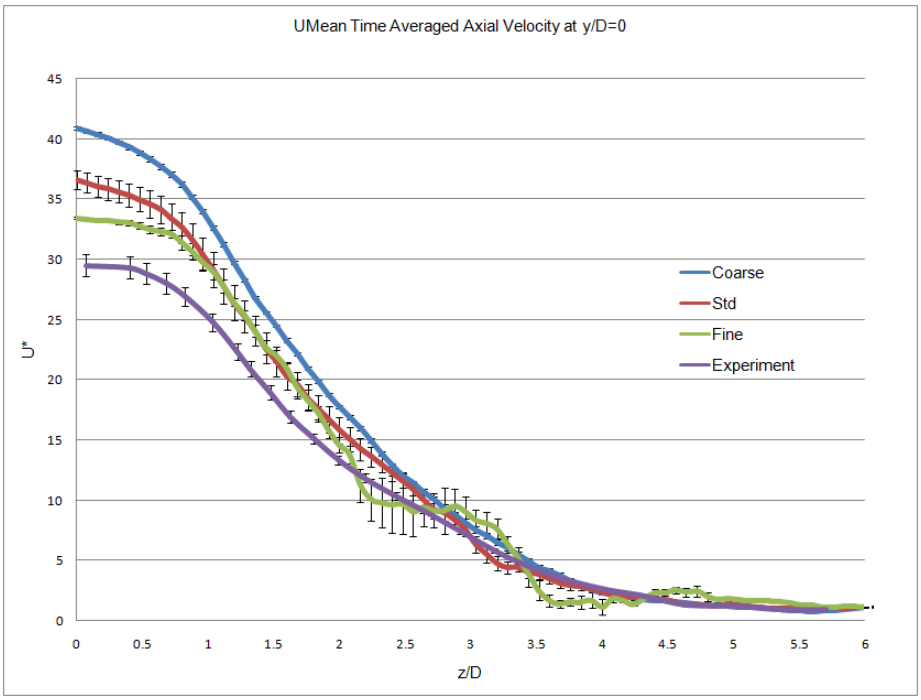

(a) Streamwise variation of the **time averaged** *Reynolds Averaged* Axial Velocity

Figure 27: Streamwise variation of the *Reynolds Averaged* Axial Velocity along the centreline ($y/D = 0$)

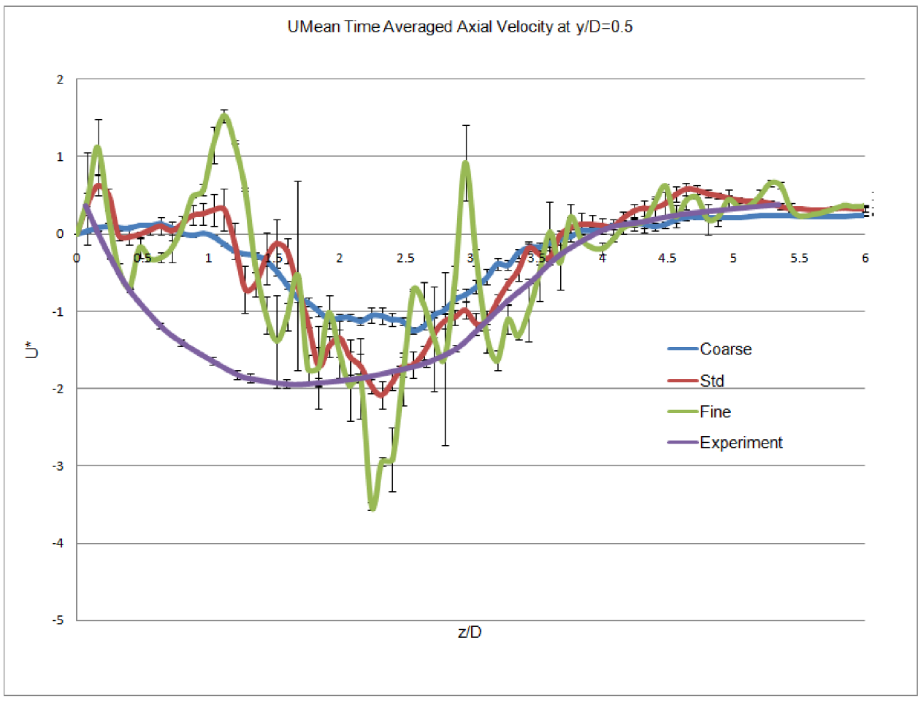

(a) Streamwise variation of the **time averaged** *Reynolds Averaged* Axial Velocity

Figure 28: Streamwise variation of the *Reynolds Averaged* Axial Velocity along the wall ($y/D = 0.5$)

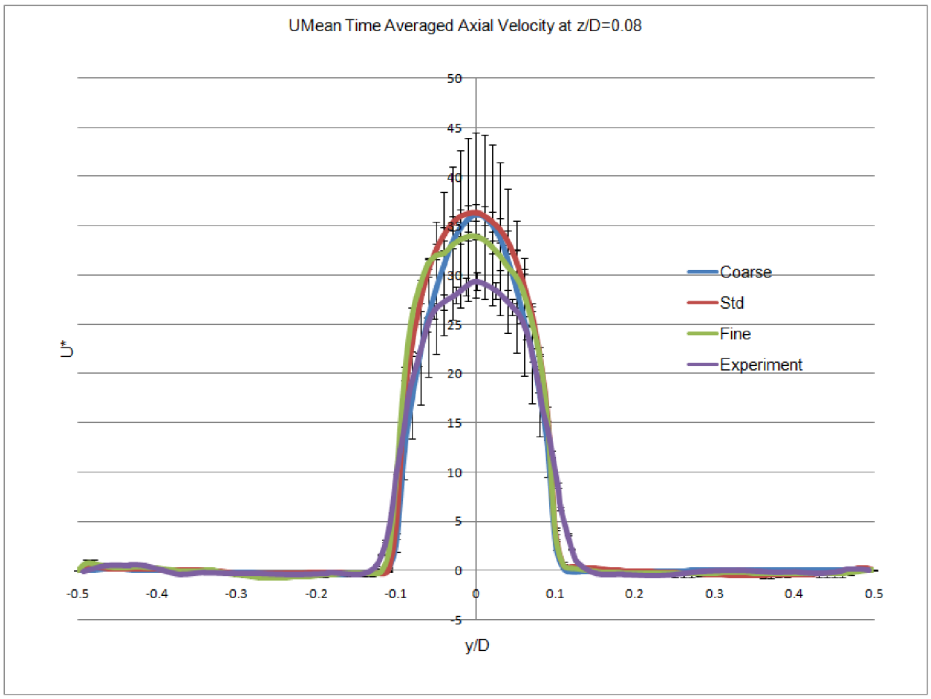

(a) Spanwise variation of the **time averaged** *Reynolds Averaged* Axial Velocity

Figure 29: Spanwise variation of the *Reynolds Averaged* Axial Velocity at z/D=0.08

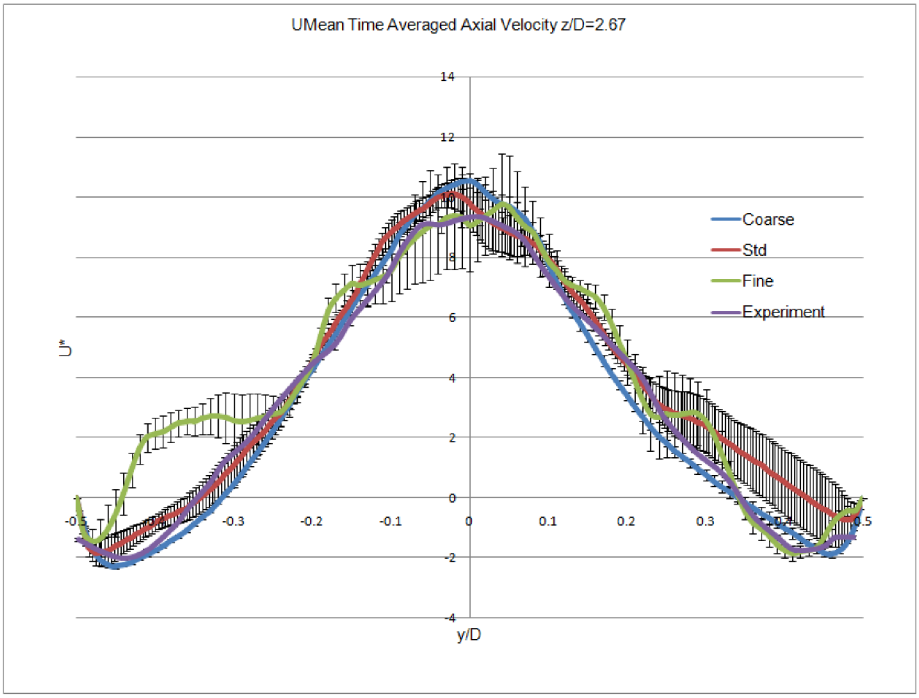

(a) Spanwise variation of the **time averaged** *Reynolds Averaged* Axial Velocity

Figure 30: Spanwise variation of the *Reynolds Averaged* Axial Velocity at z/D=2.67

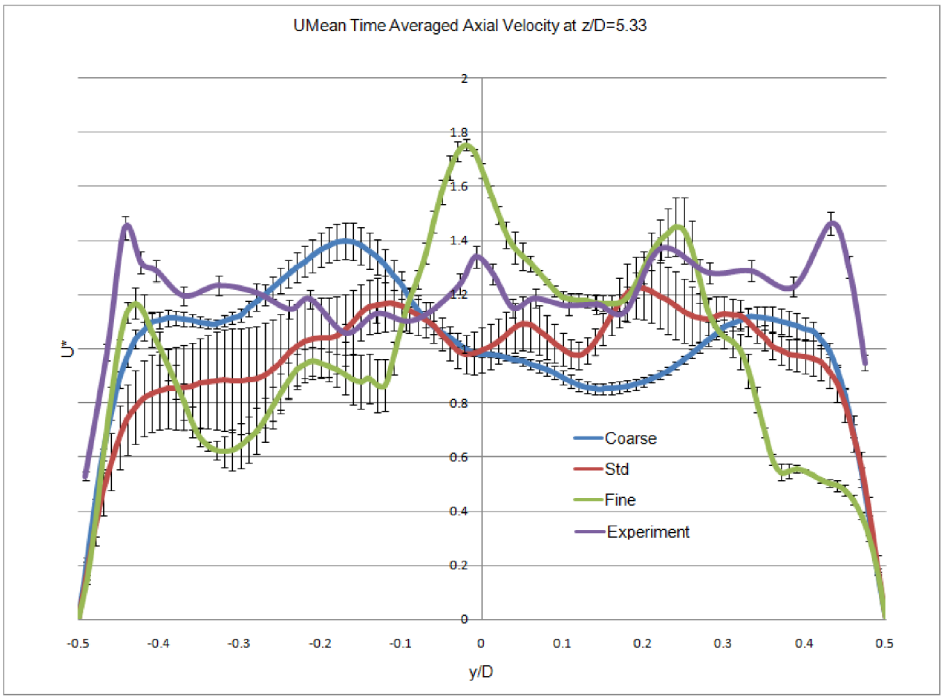

(a) Spanwise variation of the **time averaged** *Reynolds Averaged* Axial Velocity

Figure 31: Spanwise variation of the *Reynolds Averaged* Axial Velocity at z/D=5.33.

results are given in Figures 32 and 33 for the streamwise variation along the centreline and one spanwise location at z/D=2.67 with both locations exhibiting similar behavior. In the spanwise direction, at $0.1D$ on either side of the centreline the sharp drop in the ratio for all three mesh densities is the result of extending the much finer mesh of the inlet tube into the expansion chamber that was discussed earlier. Dombard & Iaccarino (2012) note that SGS-viscosity to physical viscosity ratios less than 0.8 may be considered to be coarse-grained DNS calculations, as such the fine grid would seem to be excessive for the present purpose. Figures 32 and 33 suggest that the standard grid with 1.3 million cells is sufficient to reproduce the experimental data and that there is little to gain by switching to the finer grid especially when the increased computational cost and the remaining discrepancies between measurements and calculations are taken into consideration.

3.3.9 Velocity fluctuations

Suprisingly, and disappointingly, little insight is provided from the comparison, between the three grid resolutions, of the velocity fluctuations that are shown in Figures 34 & 35 as there is no clear trend between the three grid resolutions: note that Figure 34 provides the comparison at two instants in time, separated by $0.1s$. The only comment that may be made is that they are of the correct order of magnitude and the overall trend of greater velocity fluctuations near the centreline is observed in the calculations as well in the experiments.

3.3.10 Recirculation Zone *Loci*

Finally, Figure 36 depicts the loci of the recirculation zone near the step, defined here as the location along an axial/streamwise direction where the axial velocity changes signs from positive to negative. In order to determine the extent of the recirculation zone, an approach similar to that in the experimental measurements was used. Starting from a line parallel to the centreline and close to the axis of symmetry, the calculation was probed for the location where the axial velocity changes sign. The process was then repeated for a new line parallel to the centreline, at a greater radial position, until the wall was reached. Due to the time consuming nature of this process the results were not averaged in time in this instance: rather the same process was repeated for each quadrant of the expansion tube and averaged spatially. Acceptable agreement is observed between calculated and measured locations.

3.3.11 Eulerian Phase Summary

From the last several sections, and bearing in mind the increased computational cost of the finer grids, it was deemed that the resolution provided by the "standard mesh" was adequate and that the increased detail provided by the fine mesh was not significant and did not warrant its use. The improvement in predicted axial velocity is small while at the same time the velocity fluctuations from the fine grid are not resolved to a greater accuracy. Finally, the improvement in the ratio of SGS viscosity to actual viscosity was deemed insignificant to warrant its use. Overall, in terms of agreement with the experimental measurements the Eulerian phase predictions are far from perfect with the inlet boundary condition being the most likely culprit. However, the

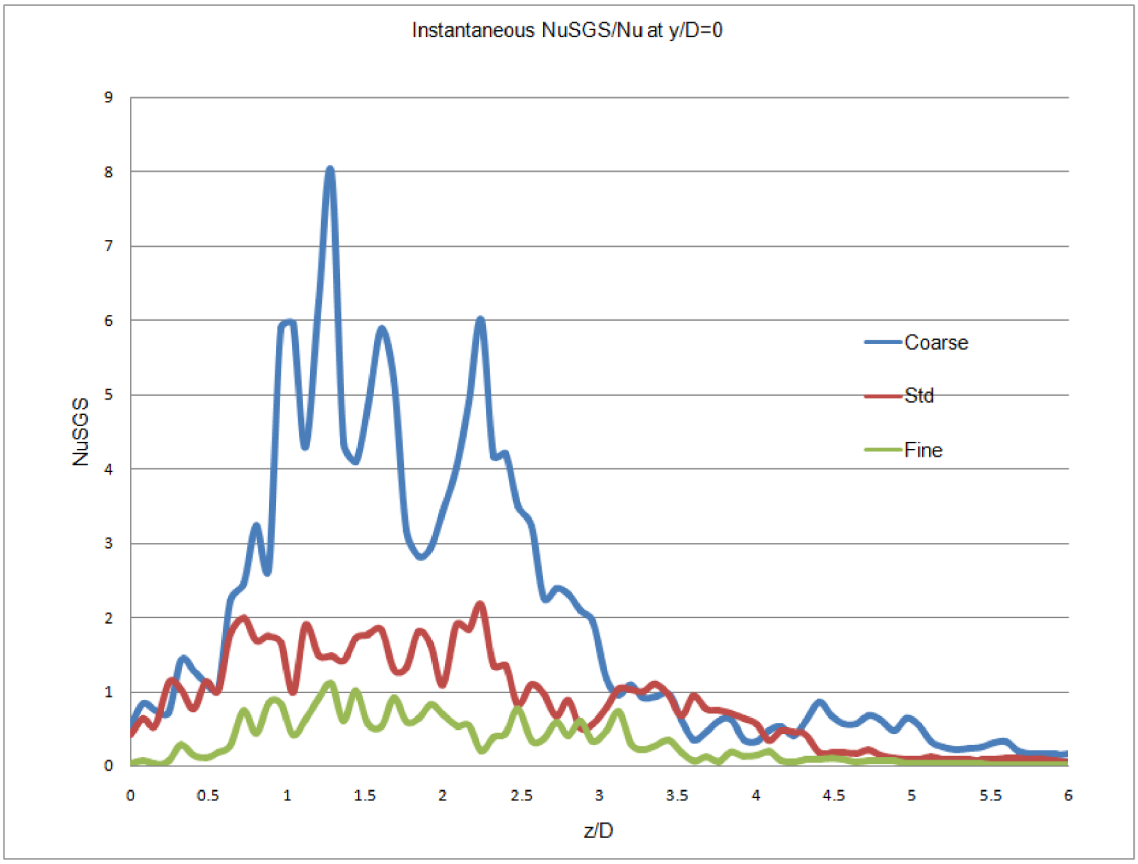

(a) Streamwise variation of the ratio of viscosity to physical at y/D=0

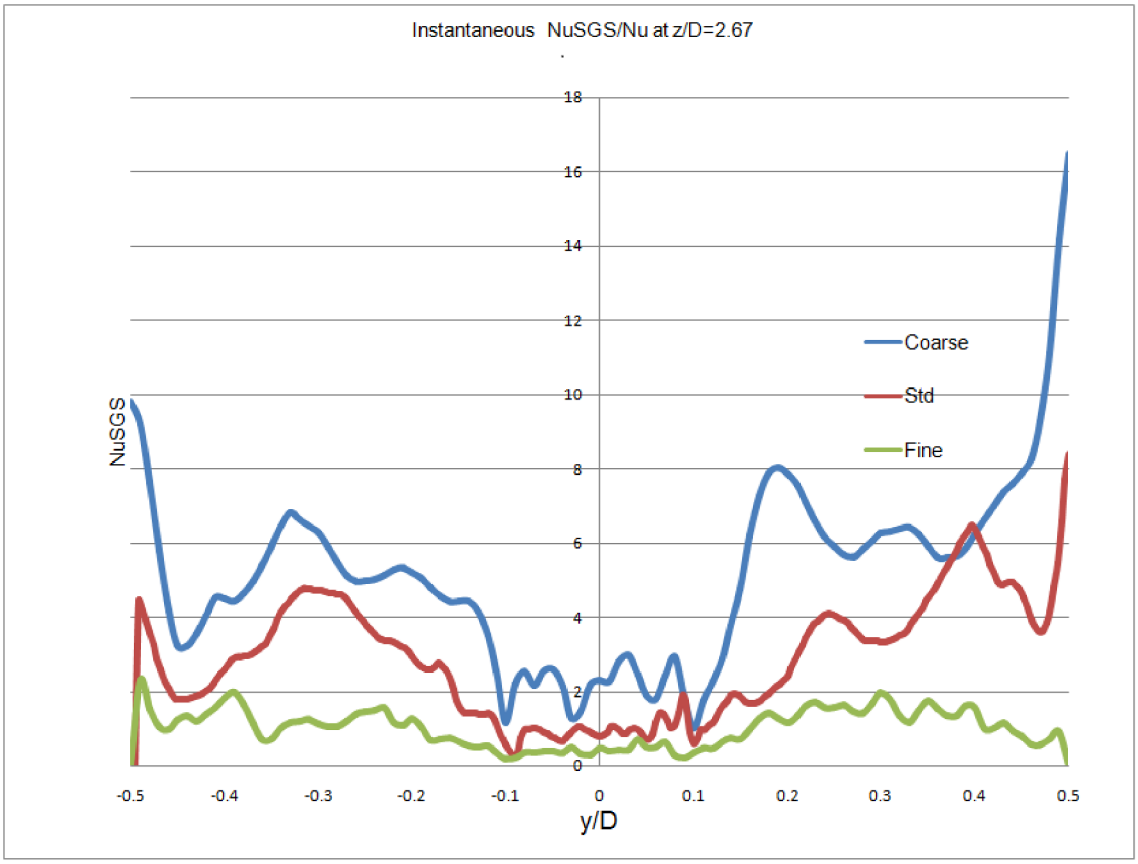

(b) Spanwise variation of the ratio of turbulent to physical viscosity at z/D=2.67

Figure 32: Variation of the ratio of **instantaneous** turbulent to physical viscosity

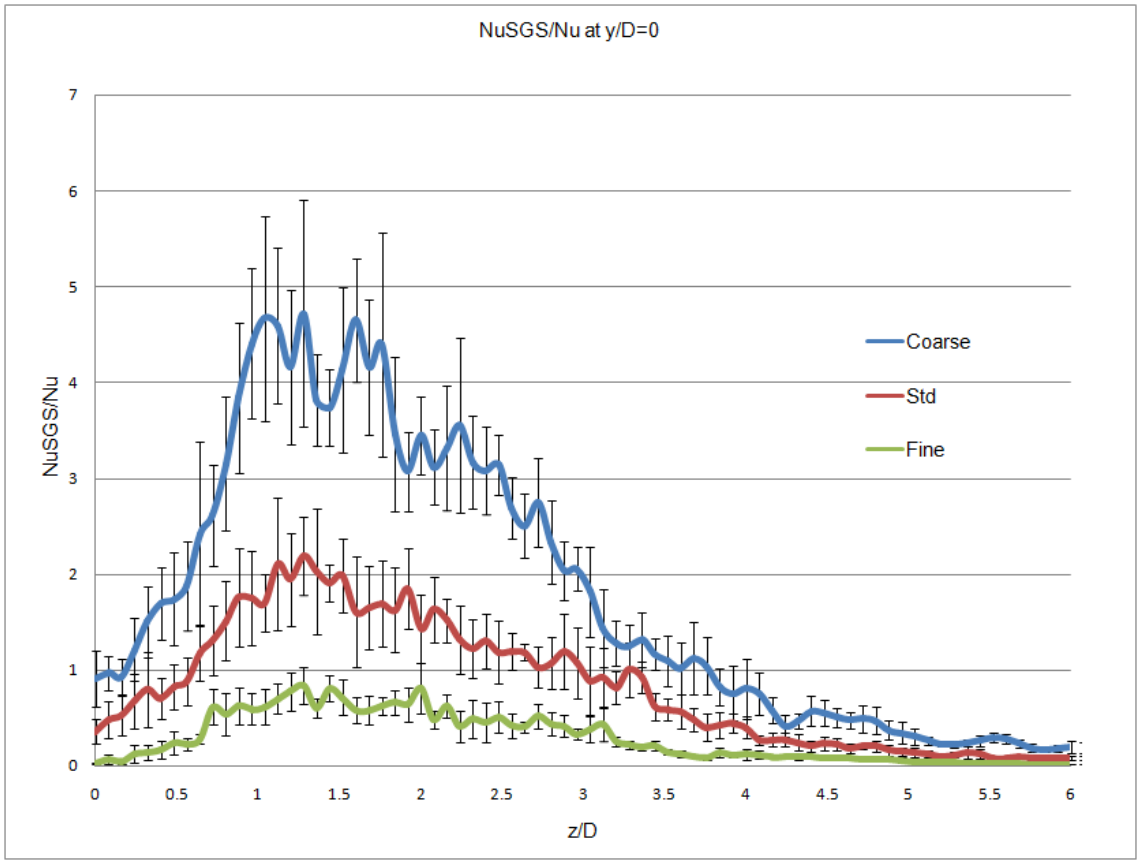

(a) Streamwise variation of the ratio of turbulent to physical viscosity at y/D=0

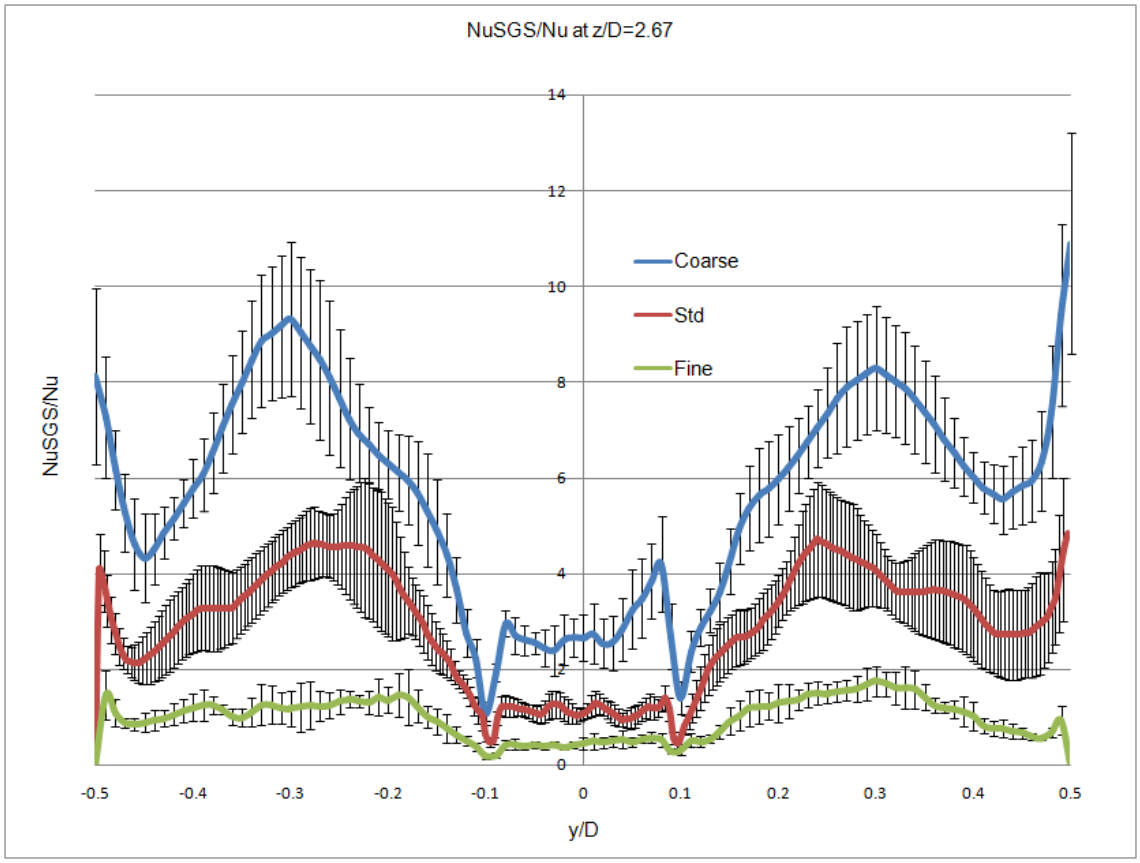

(b) Spanwise variation of the ratio of turbulent viscosity to physical viscosity at z/D=2.67

Figure 33: Variation of the ratio of **time averaged** turbulent to physical viscosity

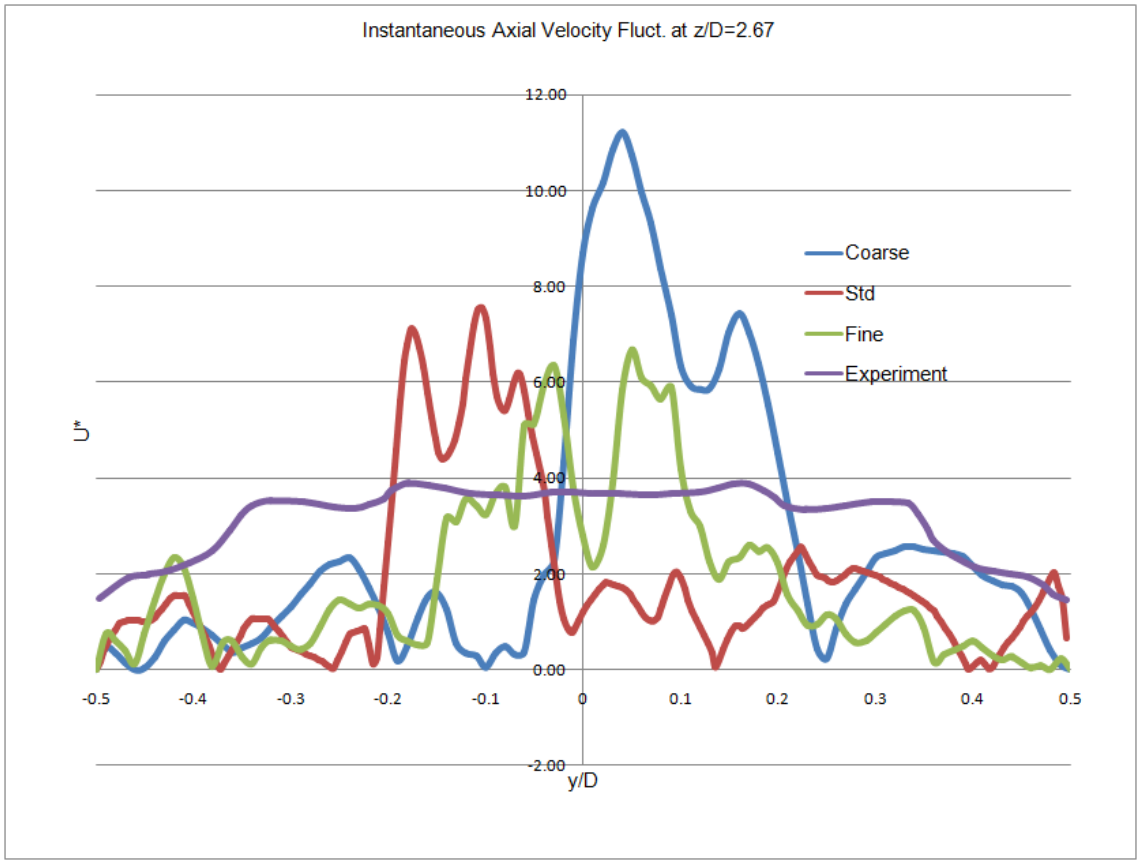

(a) Time instant A

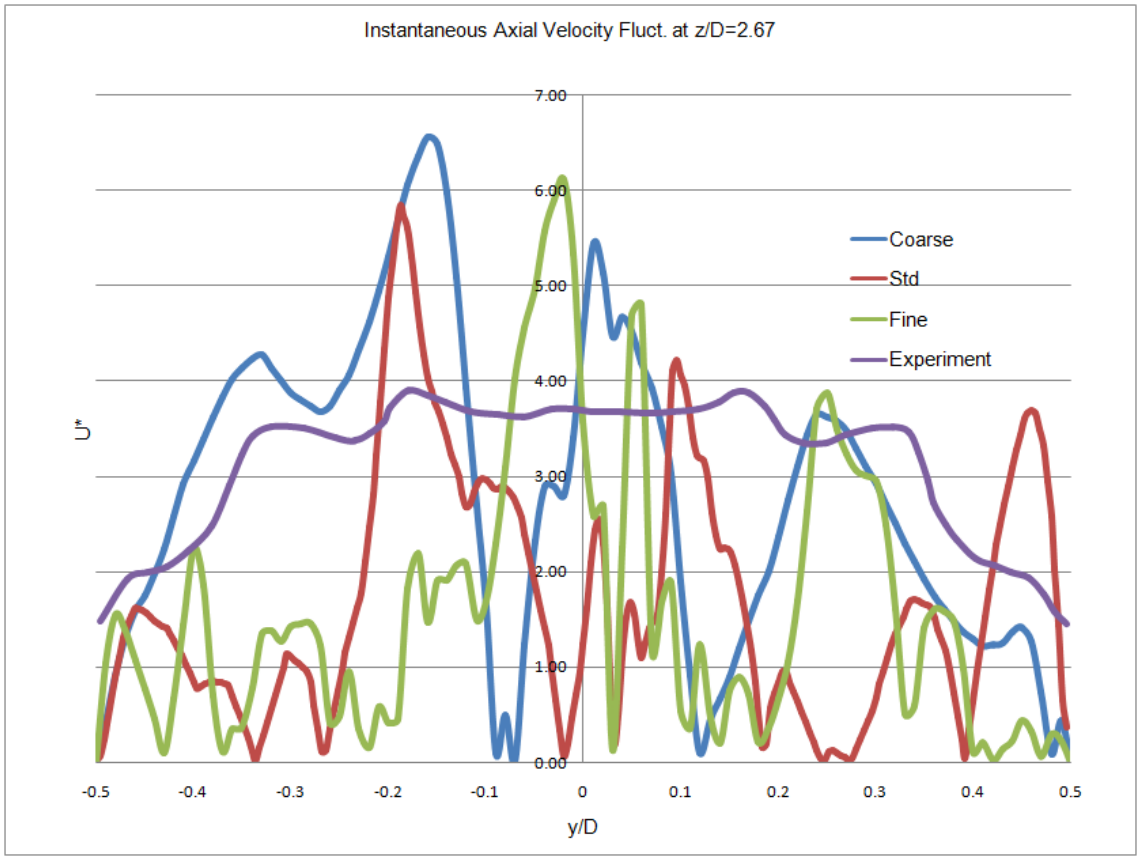

(b) Time instant B

Figure 34: Spanwise profile of the instantaneous axial velocity fluctuations at time instants A & B separated by $0.1s$

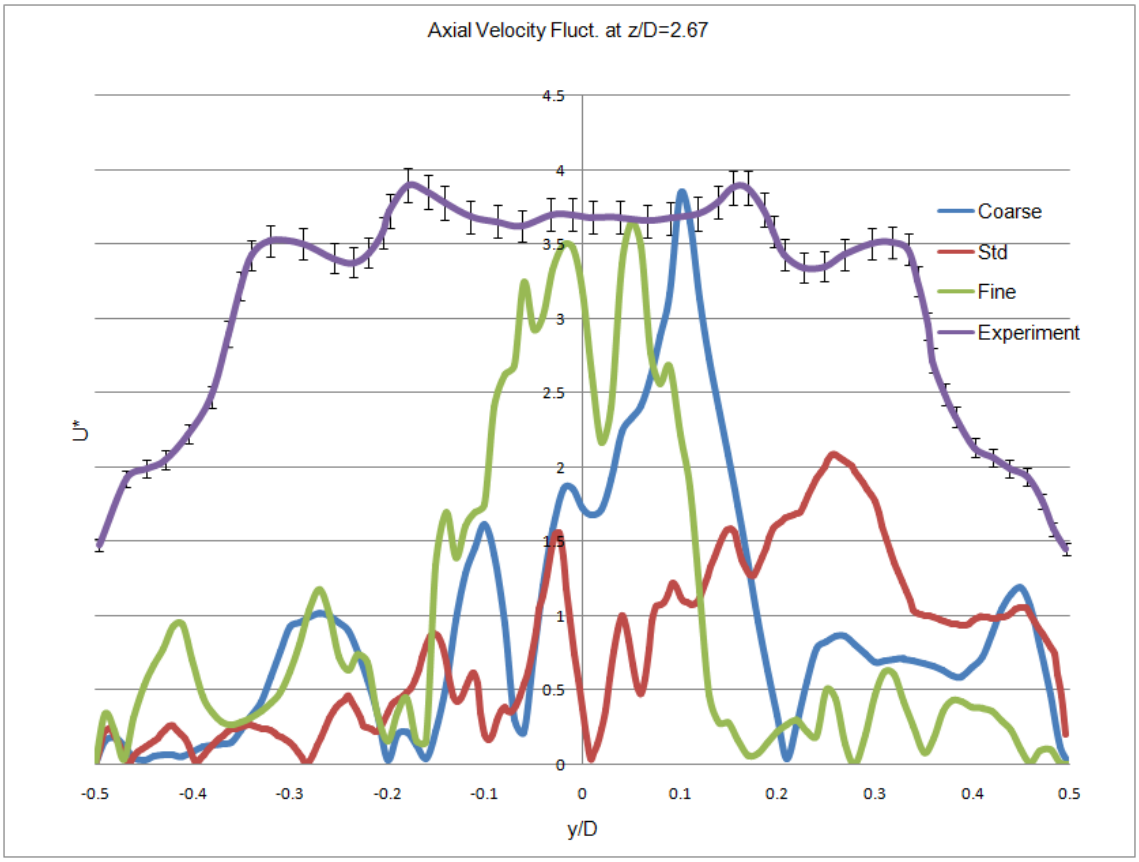

Figure 35: Spanwise profile of the time averaged axial velocity fluctuations.

acceptable recirculation zone predictions and the unsteady velocity field are still usefull for the Lagrangian investigations, presented in the following section.

3.4 Large Eddy Simulations - Lagrangian Phase

With the Eulerian phase validated against the experimental results, the groundwork was in place to evaluate the performance of the Lagrangian solver in an LES environment on the standard mesh. Two distinct particle size classes, with two mass loadings for each size class, were introduced into the simulation several diameters upstream of the step similarly to the experimental arrangement. The information pertaining to the Lagrangian particles is summarized in Table 3 below. At this point it is worth mentioning that the Lagrangian solver takes into account only the effects of drag and gravity (acting in the downstream direction) on the particles as the rest of the forces mentioned are one order of magnitude smaller and their effect should be minimal as mentioned in the previous chapter. All intra-particle and particle wall collisions are treated elastically and there are no coalescence models in place.

In this section only comparisons between calculated and measured particle velocities will be made and the evaluations of concentrations are left to the following chapter. The particles introduced within the calculations match the dimensions and densities of the glass-beads (of two distinct size-classes) used in the experiments. The particles were introduced halfway down the length of the inlet tube with an initial velocity equal to the bulk flow-rate of the carrier phase in the inlet tube,U_i, and with a uniform spatial distribution. Figure 37 depicts the spatial

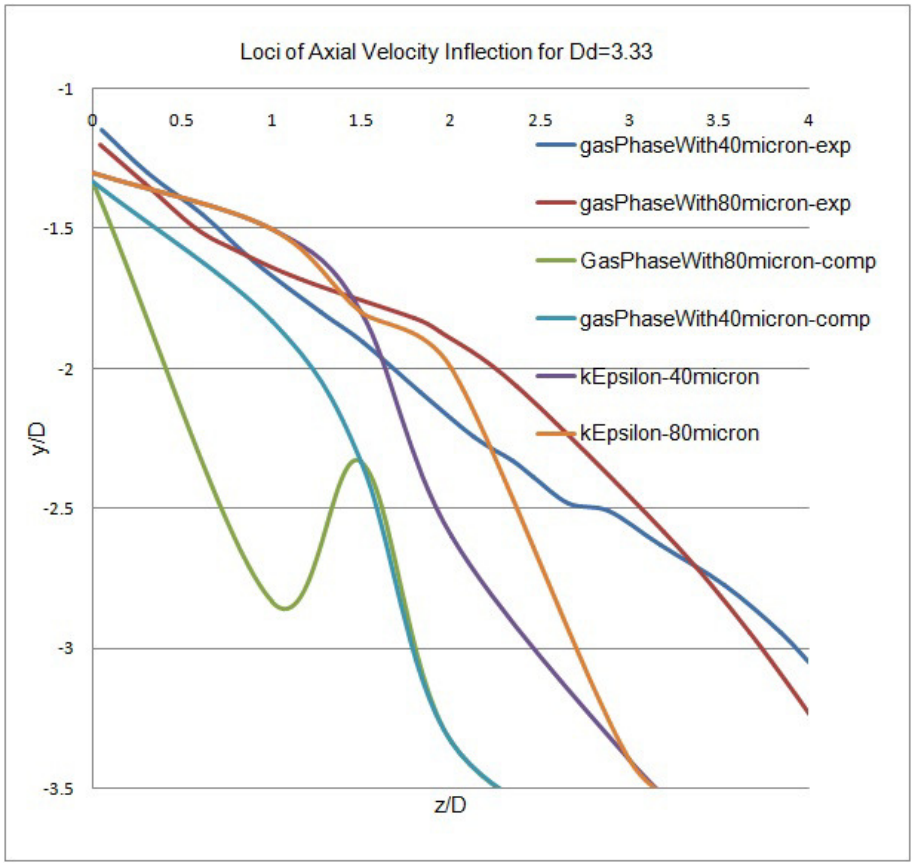

(a) Recirculation zone for expansion D/d=3.33

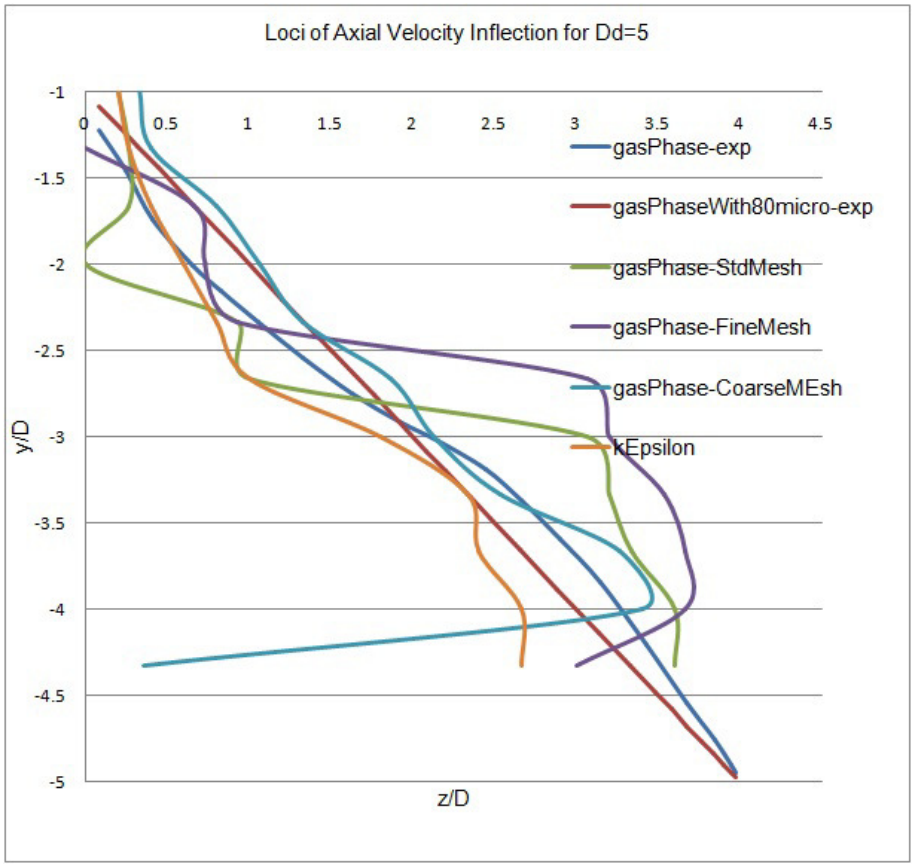

(b) Recirculation zone for expansion D/d=5

Figure 36: Spanwise instantaneous variation of the axial velocity fluctuations.

Table 3: Lagrangian Phase Characteristic Dimensions and Properties

Particle Size Class	$40\,\mu m$	$80\,\mu m$
Uniform Distribution Range	$37-44\,\mu m$	$60-95\,\mu m$
density, ρ_p	$2420\,kgm^{-3}$	$2950\,kgm^{-3}$
Stokesian time constant, τ_p	$11.9\,ms$	$58.0\,ms$
terminal velocity, U_p^T	$11.1\,cms^{-1}$	$44.8\,cms^{-1}$
Large Eddy *Stokes* no., St_e	0.23	1.12
Centrifuge *Stokes* no.,St_c	0.10	0.49
Transit *Stokes* no., St_{tr}	0.30	1.48
SGS *Stokes* no., St_{SGS}	21	106
Flapping Jet Stokes no., St_{fl}^1	0.48	2.32
Flapping Jet Stokes no., St_{fl}^2	0.24	1.16
Mass Loading Condition 1, ML1	13%	23%
Mass Loading Condition 2, ML2	40%	40%

distribution of the Lagrangian particles within the expansion tube for three distinct instances in time. The purpose of the figure is to show the sheer number of particles in the expansion tube domain at any instant in time and the need to limit the comparisons not only to certain locations but also to a small number of stored timesteps as the post-processing quickly gets out of hand. Figure 38 shows the Lagrangian particles along the two streamwise locations and at three spanwise measurements planes for the smallest mass loading[65] case, ML1. These are the locations where experimental measurements exist and validation with the calculations is limited to these positions. What is also clear in this image is the large difference in the absolute number of particles between the $40\,\mu m$ and $80\,\mu m$ cases. Although, the difference between mass loadings of 13% and 23%, corresponding to ML1 conditions for the $40\,\mu m$ and $80\,\mu m$ respectively, is small, the larger diameter results in a reduction of the number of particles by a factor of 2^3 which is further reduced by a factor of 4/5 due to the greater density of the larger particles (see Table 3). Also evident in these two figures is the reduction in number of particles entering the recirculation zone and traveling upstream (in the schematic towards the bottom of the page) for the $80\,\mu m$ particle case, the implication being that there is a smaller number of samples and the accuracy is somewhat reduced.

Figure 39 serves to show what the instantaneous Lagrangian information extracted from the calculations looks like in a qualitative sense. Here the particle locations are shown across the three spanwise locations z/D=0.08, 2.67 & 5.33 for a representative instant in time and are colored by their normalized axial velocity. The discussion relating to the spatial non-uniformity observed especially for the $40\,\mu m$ is left for the following section. The dimensions of the sampling locations were limited to the size/thickness of the experimental sampling probe with the following difference; for the streamwise sampling locations, the z-component of the computational probe was extended to the whole length of the expansion tube rather than only sampling at several axial points. Similarly, for the spanwise locations, the particles were extracted for all the radial and circumferential locations corresponding to each of the three axial positions. The statistics may be improved further by averaging in time and, as before, the results shown below were obtained from 10 instances in time, randomly selected from the total number of stored

[65]Mass loading here is defined as the ratio of mass flow-rate of the particles to the mass flow-rate of the fluid.

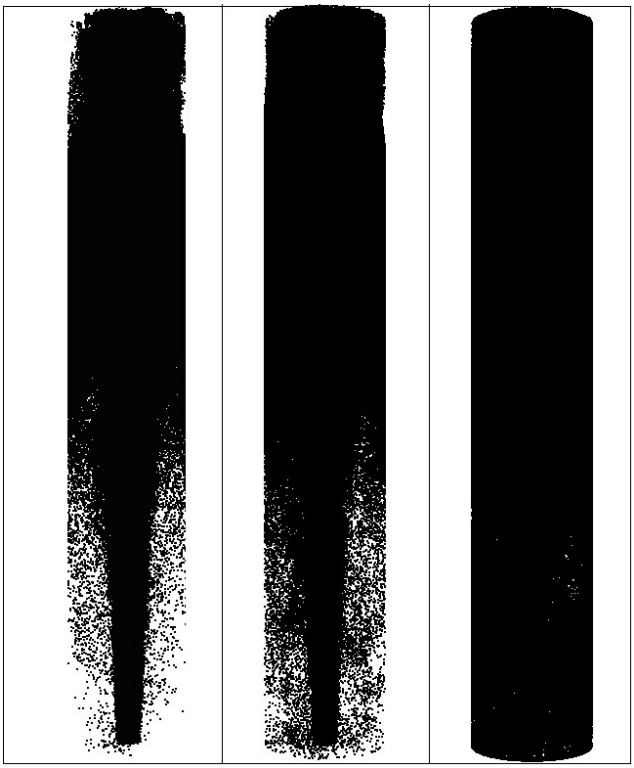

(a) $40\,\mu m$ Particle positions for the ML1 case

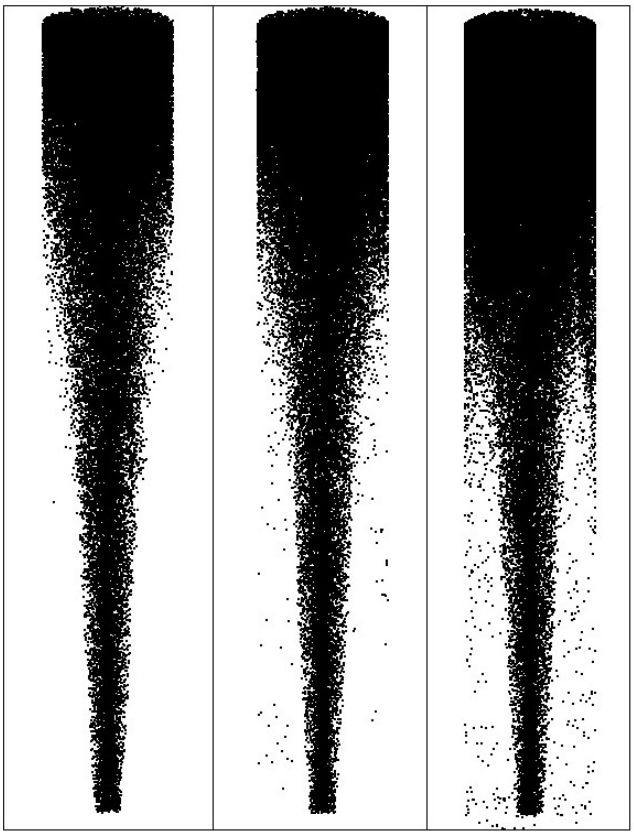

(b) $80\,\mu m$ Particle positions for the ML1 case

Figure 37: Representation of Lagrangian particles within the expansion tube for the ML1 case from left to right at an early, intermediate and fully developed time instant. Flow direction is from the bottom to the top of the page similarly for the direction of gravity. Sub-Figure (a) shows the $40\,\mu m$ and Sub-Figure (b) the $80\,\mu m$ particles.

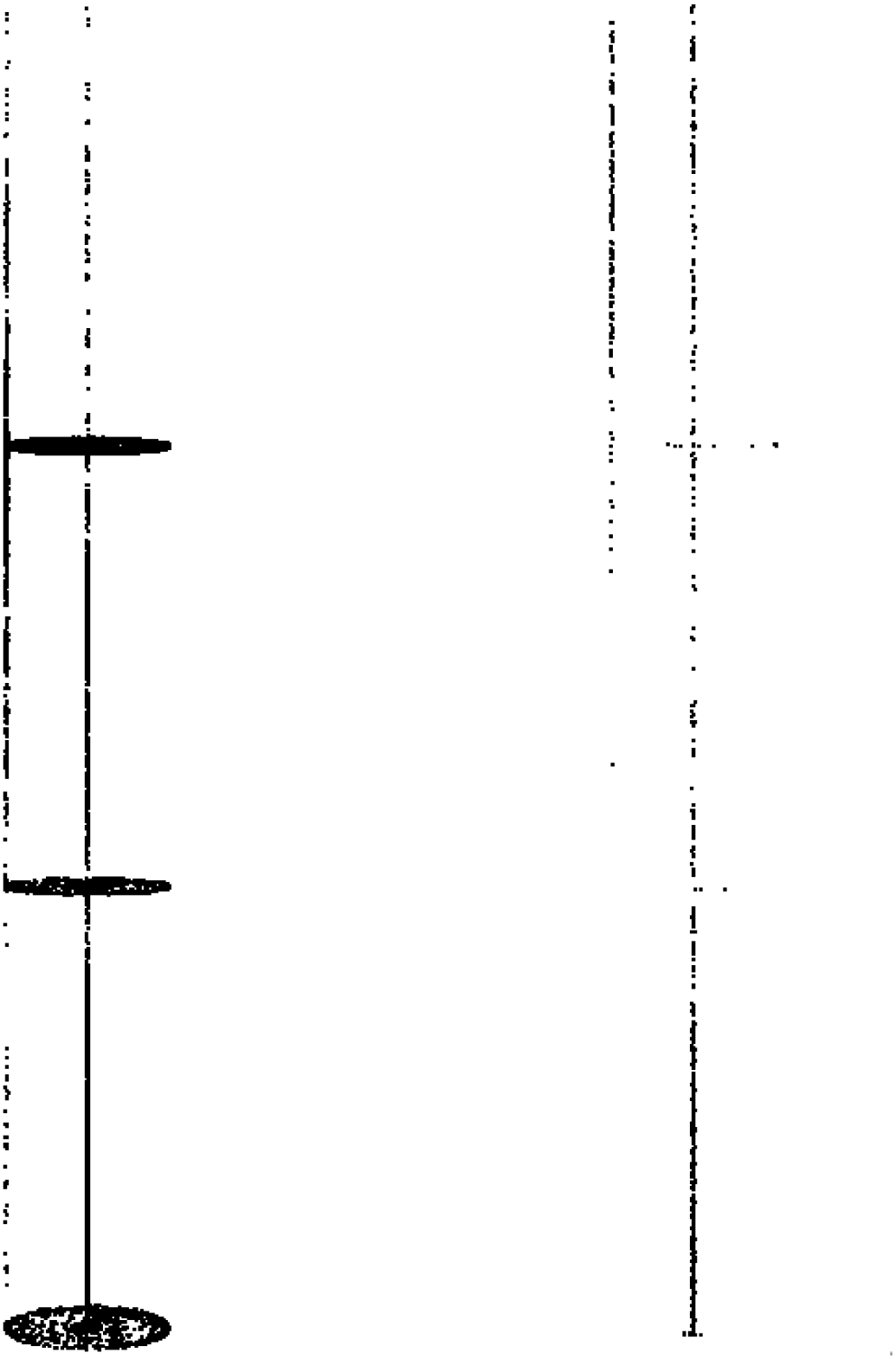

(a) $40\mu m$ (b) $40\mu m$

Figure 38: Extracted instantaneous data at measurement locations for Lagrangian phases at ML1 conditions; spanwise at z/D=0.08, 2.67 & 5.33 from the bottom of the image to the top, and for the streamwise direction at y/D=0 & 0.5, from the centreline and the wall, respectively. Flow direction is from the bottom to the top of the page. Of note is the limited number of particles away from the centreline for the larger particle size class. Sub-Figure (a) shows the $40\,\mu m$ and Sub-Figure (b) the $80\,\mu m$ particles.

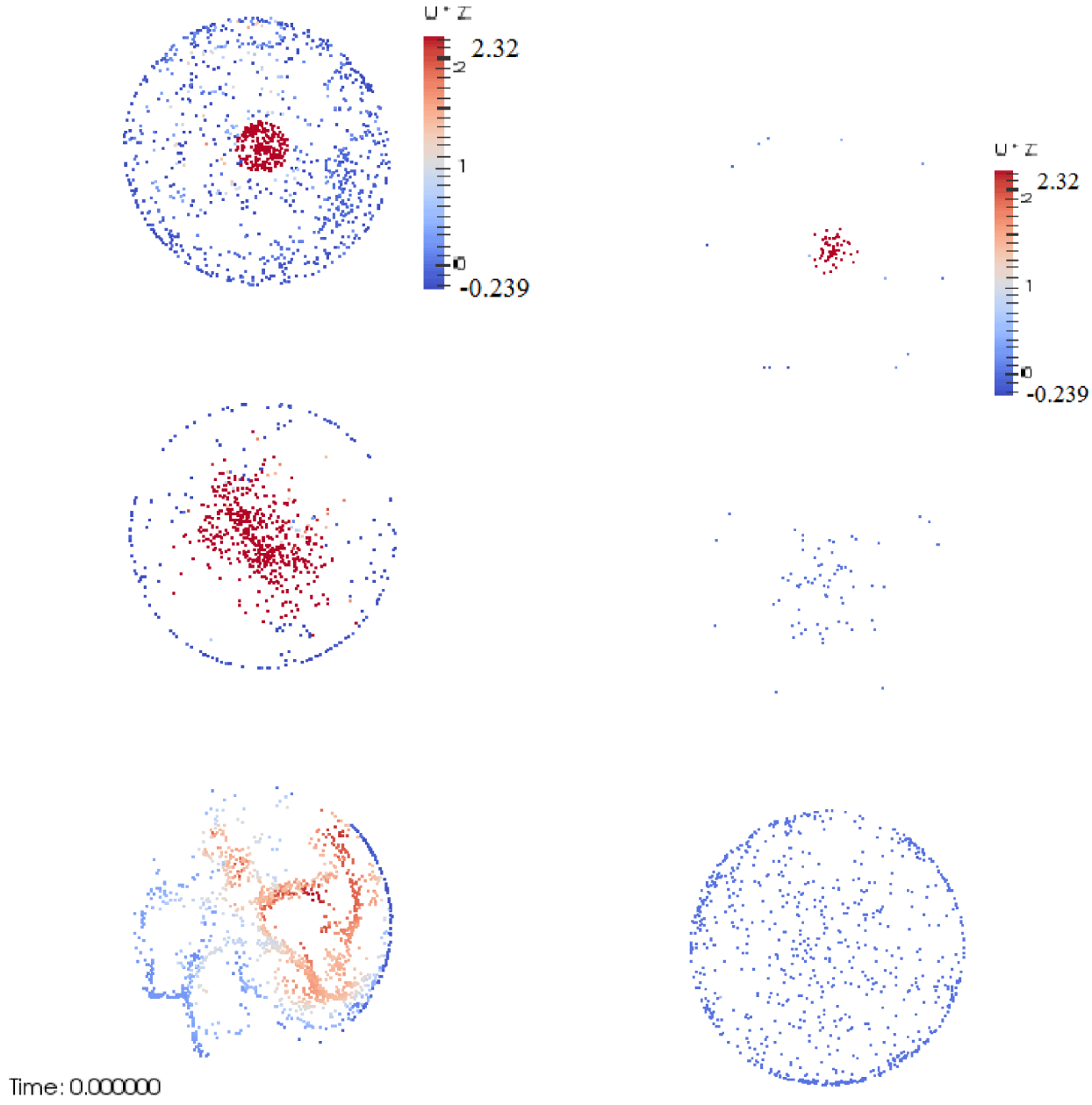

(a) 40μm

(b) 80μm

Figure 39: Qualitative representation of the instantaneous Lagrangian axial velocity at the three spanwise measurement locations at ML1 conditions, from top to bottom, z/D=0.08,2.67 & 5.33, for the two particle size classes. Particles are colored by their normalized axial velocity, (U_z/Uo) for a range between [-0.239, +2.32]. Sub-Figure (a) shows the 40 μm and Sub-Figure (b) the 80 μm particles.

timesteps.

Before proceeding to the comparisons for the discrete phase it should be noted that just as was noticed in the experiments, the introduction of the particle several diameters upstream of the step and not at the entrance of the inlet tube results in the Lagrangian velocities 'lagging' behind the Eulerian ones. Figure 40 depicts sample histograms of the axial velocities recorded for the Eulerian and Lagrangian phases at the inlet tube exit just by the step location at $z/D = -0.05$. For the computations, for both the $40\,\mu m$ and $80\,\mu m$ sized particles the normalized axial velocities range between [20, 30] whereas the Eulerian phases show maxima in the region of 40 for the normalized axial velocity.[66]The figure depicts sample histograms of the axial velocities recorded for the Eulerian and Lagrangian phases at the inlet tube exit just by the step location.

Figures 41 & 42 show the agreement between the calculations and the experiments for particles lying on the centreline and near the wall, respectively, but now two curves are fitted, a Gaussian and a Smoothing spline. Along the centreline, Figure 41, the agreement is good especially when the fact that the velocity in the Eulerian phase was being over predicted is taken into account. The calculations capture the measured effect of the Lagrangian velocity reaching a maximum slightly downstream of the step as well as the kink in the curve around z/D=3. Similarly for the measurement along the wall, the calculations correctly capture the larger extremities in both maximum and minimum velocity.

Similarly, scatter plots 43 to 48 show the position of the particles from 10 stored timesteps along with their normalized axial velocity plotted on the vertical axis at three distinct axial stations, namely at z/D=0.08, 2.67 & 5.33. Also shown, along with the scatter plots are linearly interpolated surfaces depicting the variation in Lagrangian velocity with radial location. For comparison with the experimental data, that was measured solely across a diameter, it is necessary to collapse the particles' two dimensional positions onto a line, in effect performing spatial averaging in addition to the implied temporal one, due to the superposition of the results from 10 timesteps. These are shown alongside the previous scatter plots and show the comparison against experimental data along with the 95% confidence intervals for the data from the simulations, calculated by fitting a Gaussian curve to the scatter plots. The Gaussian fit might not be optimal but is a good guide and the spread of the data is consistent with the measured values and overall the agreement is good for the Lagrangian phases.

For the spanwise measurement the calculations correctly capture the slower response of the large particles with the peak values at station z/D=0.08 being smaller than that of the $40\,\mu m$ particles, comparing Figures 43 and 46 respectively. As the time constant is larger for the $80\,\mu m$ particles, they have not had time to decelerate upon entrance into the expansion and this is also observed at the next station, z/D=2.67 where the $40\,\mu m$ particles are now traveling at a slower speed than the $80\,\mu m$ having reacted faster to the Eulerian conditions and having shed more of their velocity visible, in Figures 44 and 47, respectively. For the final measurement station at z/D=5.33, shown in Figures 45 & 46 for the $40\,\mu m$ & $80\,\mu m$ particles respectively, trends are predicted correctly overall with the exception of the particles lying close to the wall, where the computations are over predicting the axial velocity. This may be attributed to the fact the

[66]The Eulerian histograms extend to zero velocities as a result of the no-slip condition imposed at the walls, whereas the particles reflect elastically the walls and do not experience zero velocities in this section of the domain.

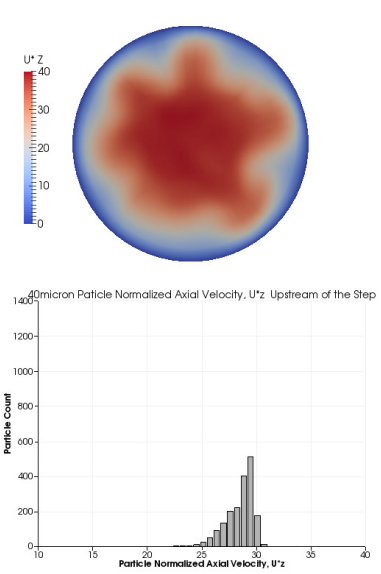

(a) Top: Section through the Eulerian domain depicting axial velocity. Bottom: Histogram of Lagrangian Axial Velocities at the same location

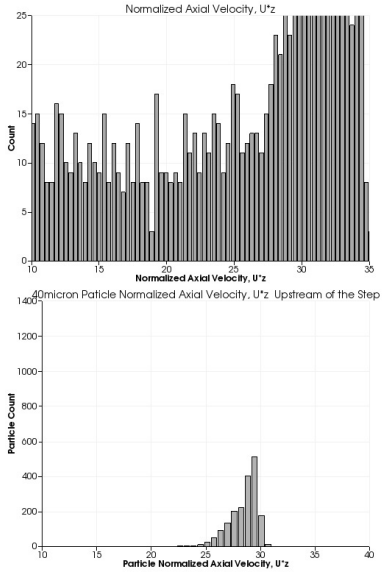

(b) Histograms for the axial velocity for the Eulerian and 40 μm Lagrangian phases, top and bottom, respectively.

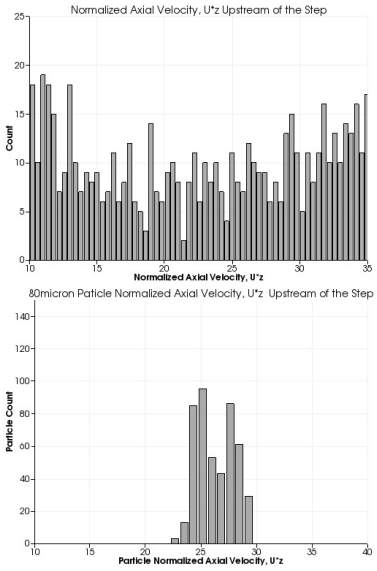

(c) Histograms for the axial velocity for the Eulerian and 80 μm Lagrangian phases, top and bottom, respectively

Figure 40: Discrepancy between Eulerian and the Lagrangian velocities at the step. Histograms for the Lagrangian data generated from all particles within that domain section for a given instant in time. Similarly, the Eulerian data extracted from the cells lying within that same section of the domain with zeros values corresponding to cells by the walls and the no slip condition imposed. At $z/D = -0.05$ upstream of the step.

simulations are modeling intra-particle and particle-wall collisions in a completely elastic manner whereas the experimental observations noted a significant quantity of particle attachment to the expansion chamber walls.

There remains, for both particle size classes, the issue of the slight discrepancy for the z/D =5.33 station where the calculations in fact lie between measured mean velocities of the continuous and discontinuous phases. This may be due to some uncertainty in the estimation of the drag coefficient over the sphere which is still an issue especially at the relatively low Re number range. A fact that should be further amplified when surface roughness uncertainty is taken into account. In the absence of experimentally measured drag coefficients for these particular particles to use as an input into the Lagrangian solver, the agreement is deemed more than satisfactory. Alternatively, it could be that the particles are reflecting off the wall with low velocities and are then convected by some slow sweeping structure back towards the centreline.

3.5 Turbulent structures

Figures 49 & 50 show, slices through the sudden expansion test case for several distinct time instances, corresponding to the three spanwise stations downstream of the step. The qualitative inspection is limited to those particles lying close to either side of the cross-sectional plane corresponding to the spanwise locations which are the only ones shown. What is evident from a simple qualitative inspection is that the spatial distributions are far from uniform especially for

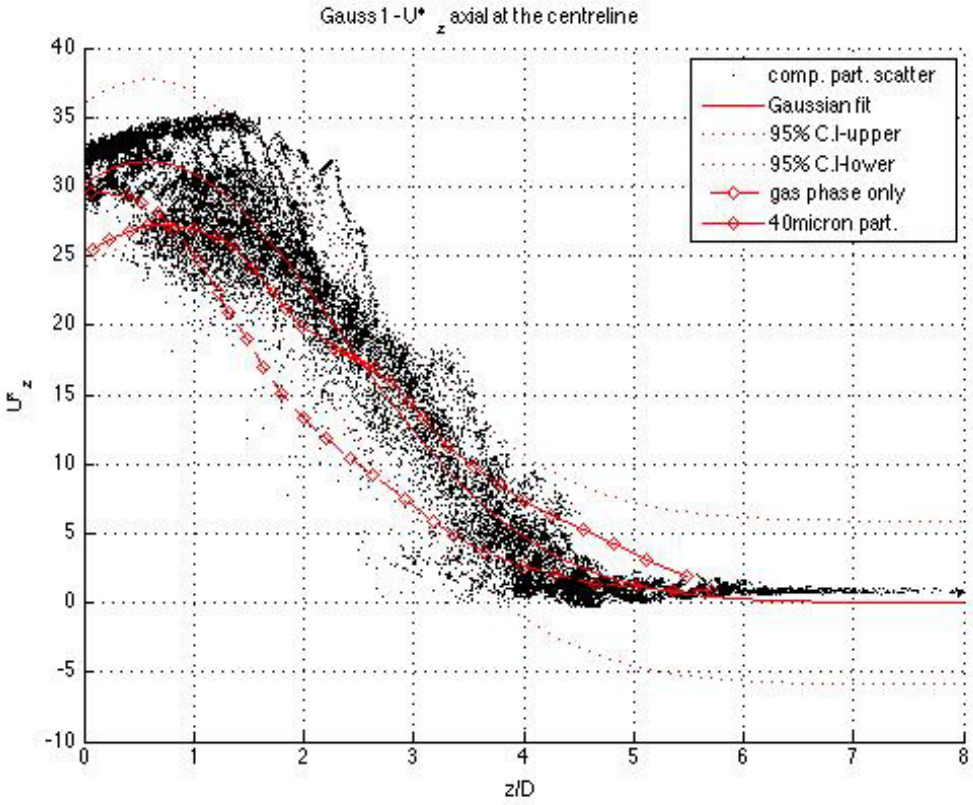

(a) Gaussian fit through the Lagrangian data with 95% confidence bands

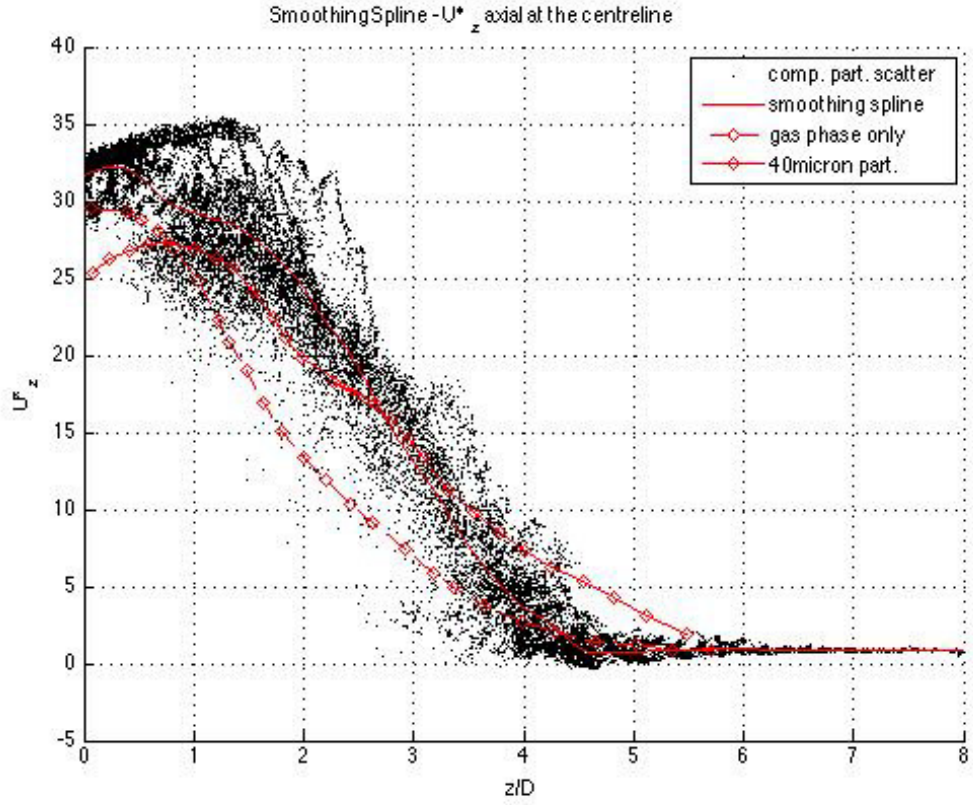

(b) Smoothing spline through the Lagrangian data

Figure 41: Lagrangian instantaneous axial velocity for the $40\,\mu m$ particles along the centreline ($y/D = 0$)

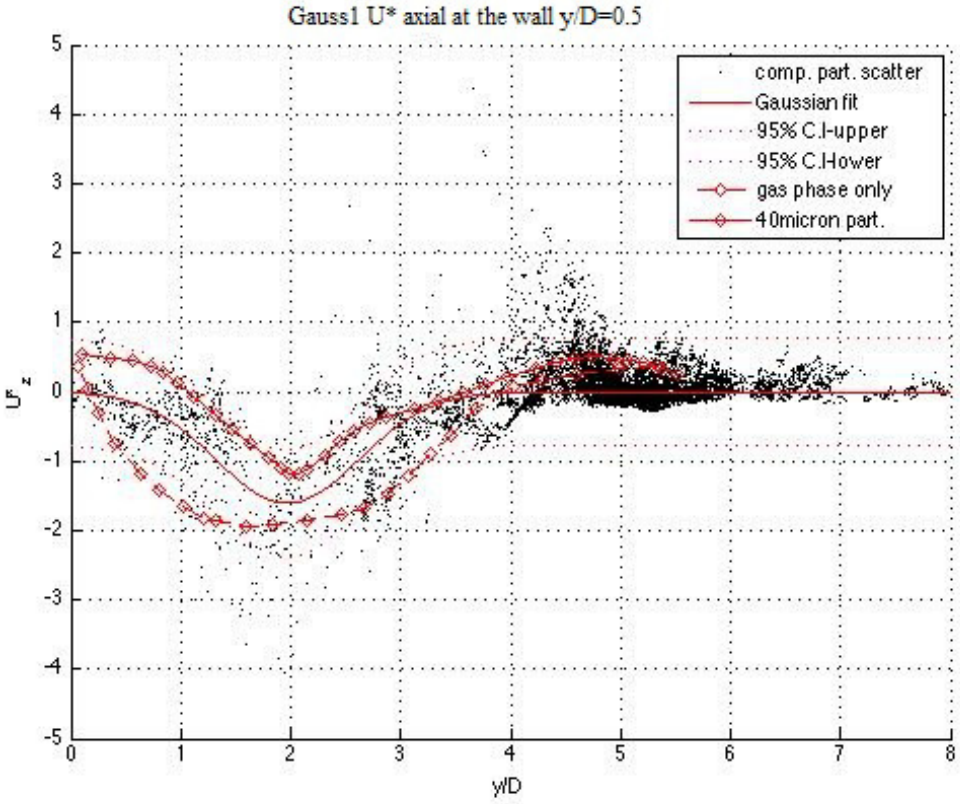

(a) Gaussian fit through the Lagrangian data with 95% confidence bands

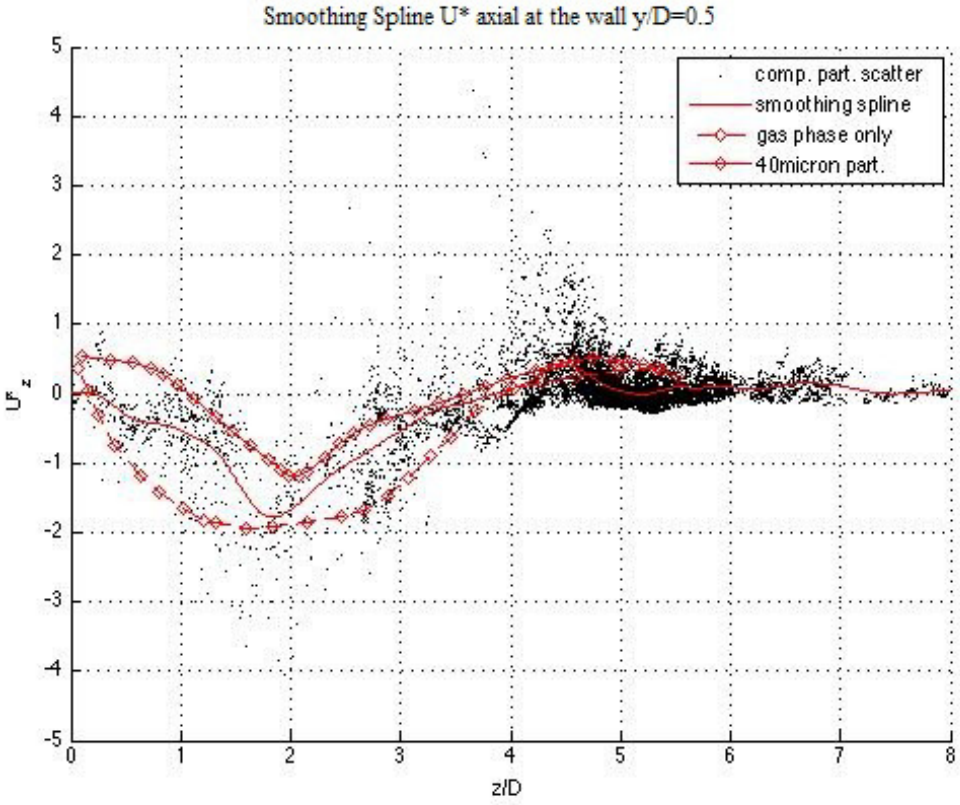

(b) Smoothing spline through the Lagrangian data

Figure 42: Lagrangian instantaneous axial velocity for the $40\,\mu m$ particles along the wall ($y/D = 0.5$)

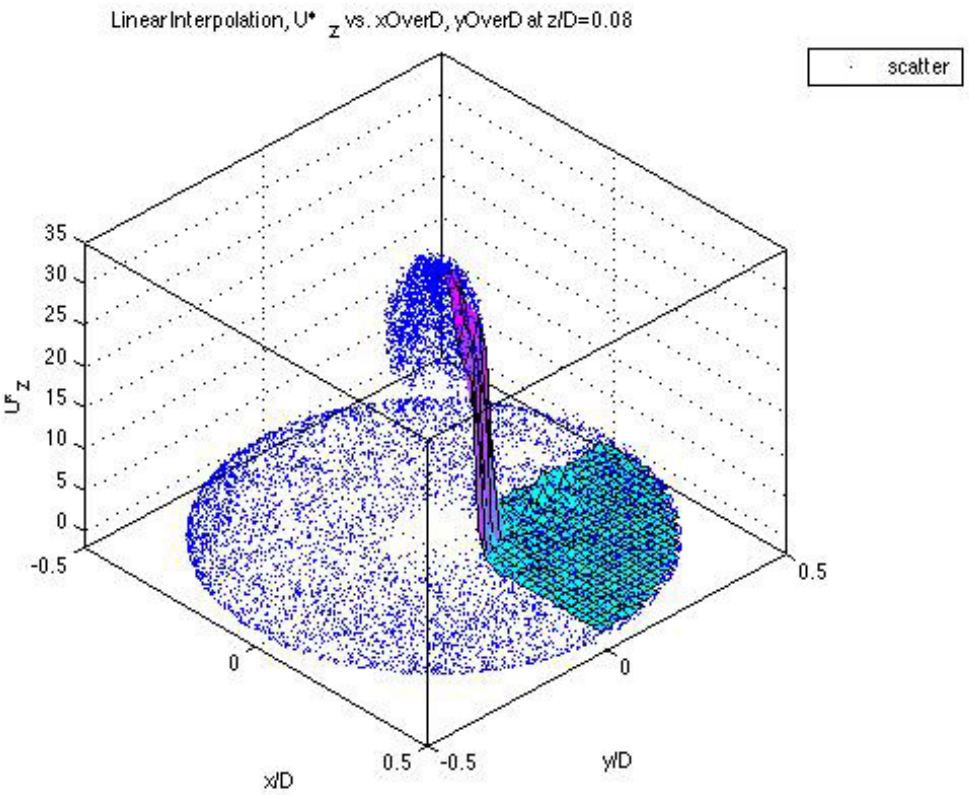

(a) Lagrangian data across the station with Linear fit

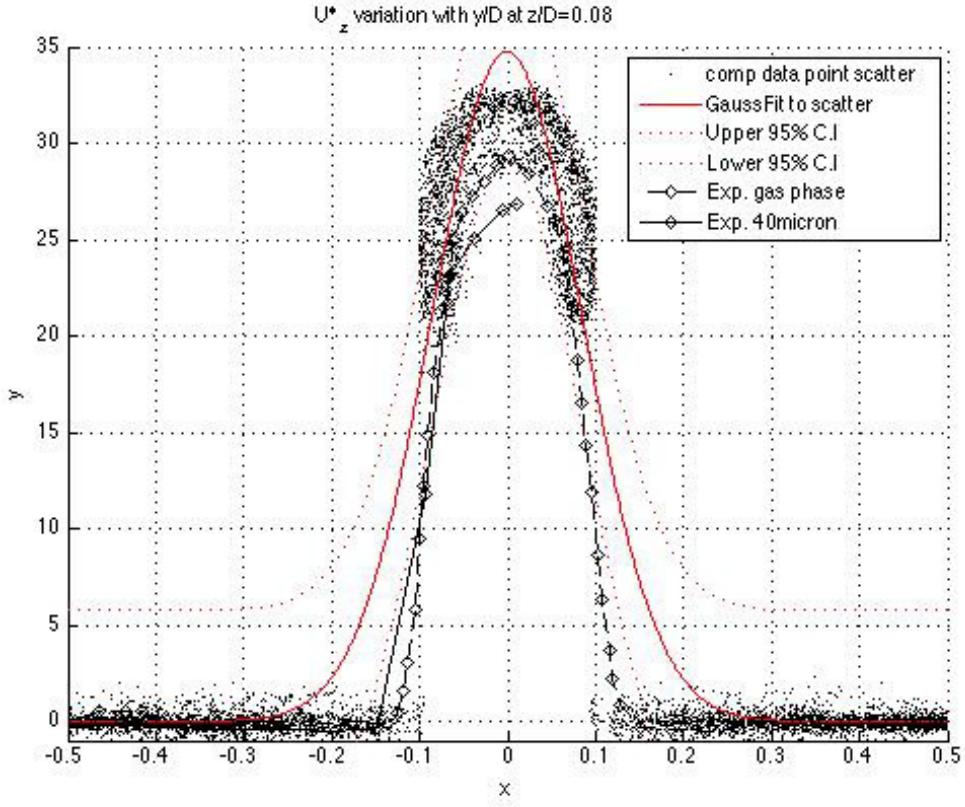

(b) Lagrangian data across the station collapsed to a line

Figure 43: Lagrangian instantaneous axial velocity for the 40 μm particles at z/D=0.08

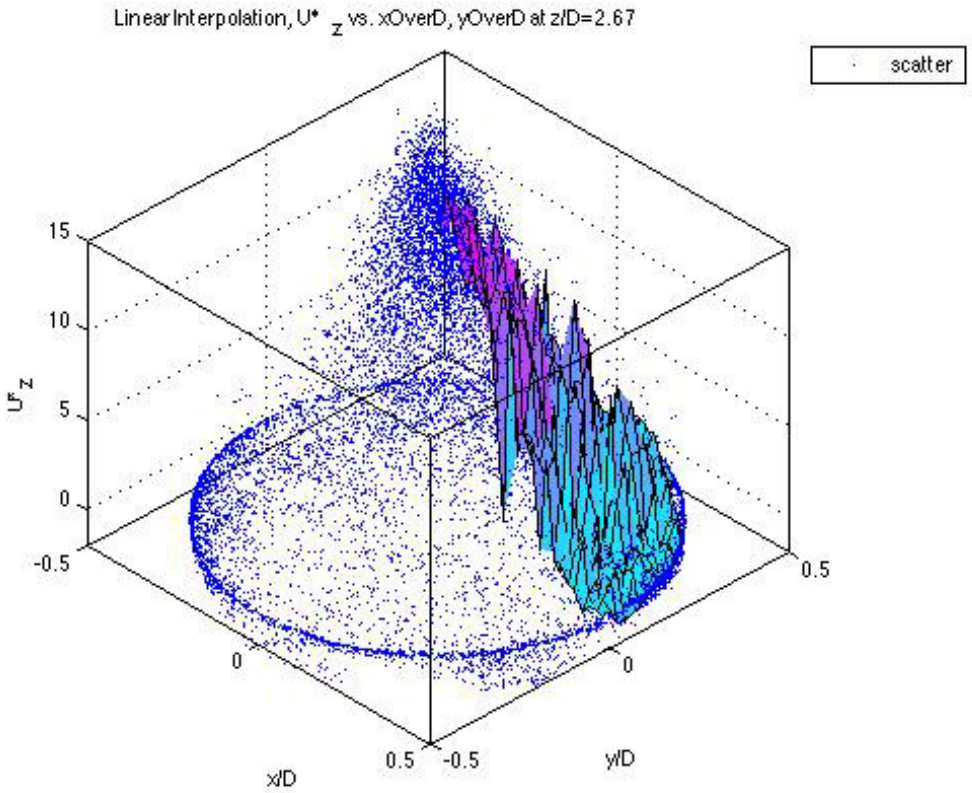

(a) Lagrangian data across the station with Linear fit

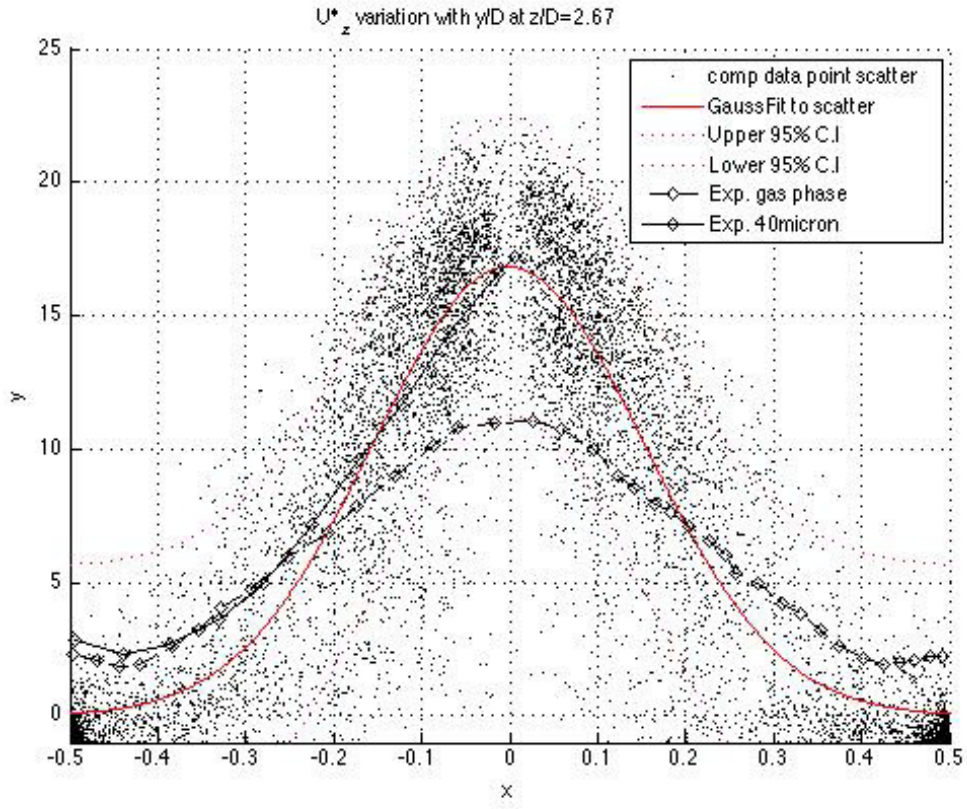

(b) Lagrangian data across the station collapsed to a line

Figure 44: Lagrangian instantaneous axial velocity for the 40 μm particles at z/D=2.67

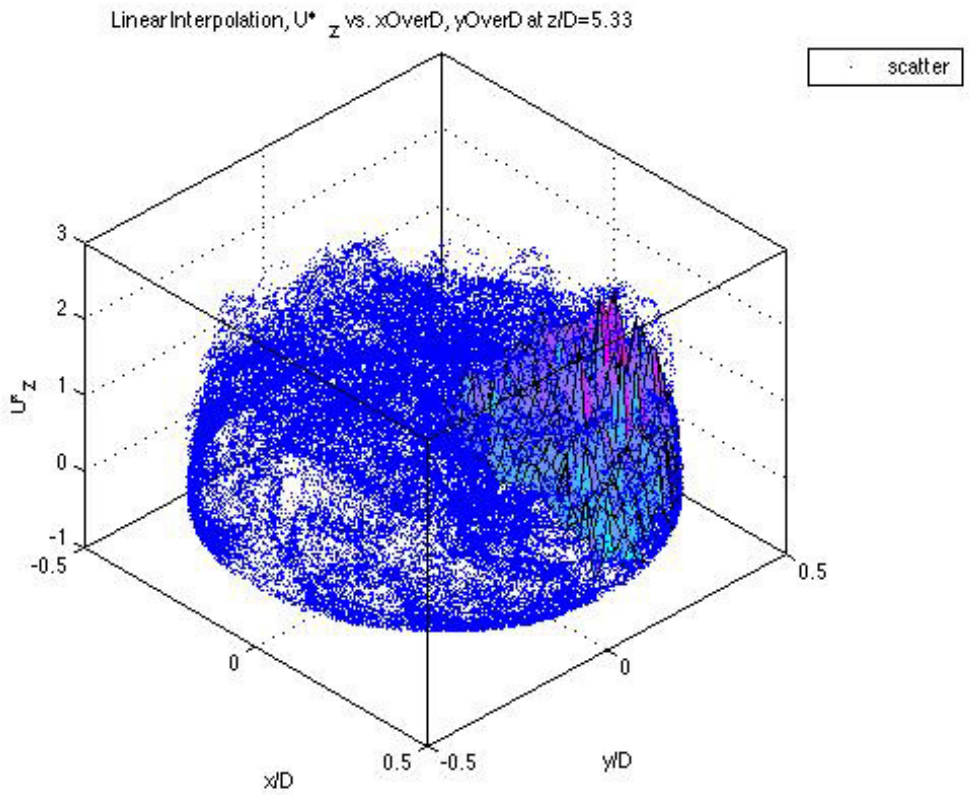

(a) Lagrangian data across the station with Linear fit

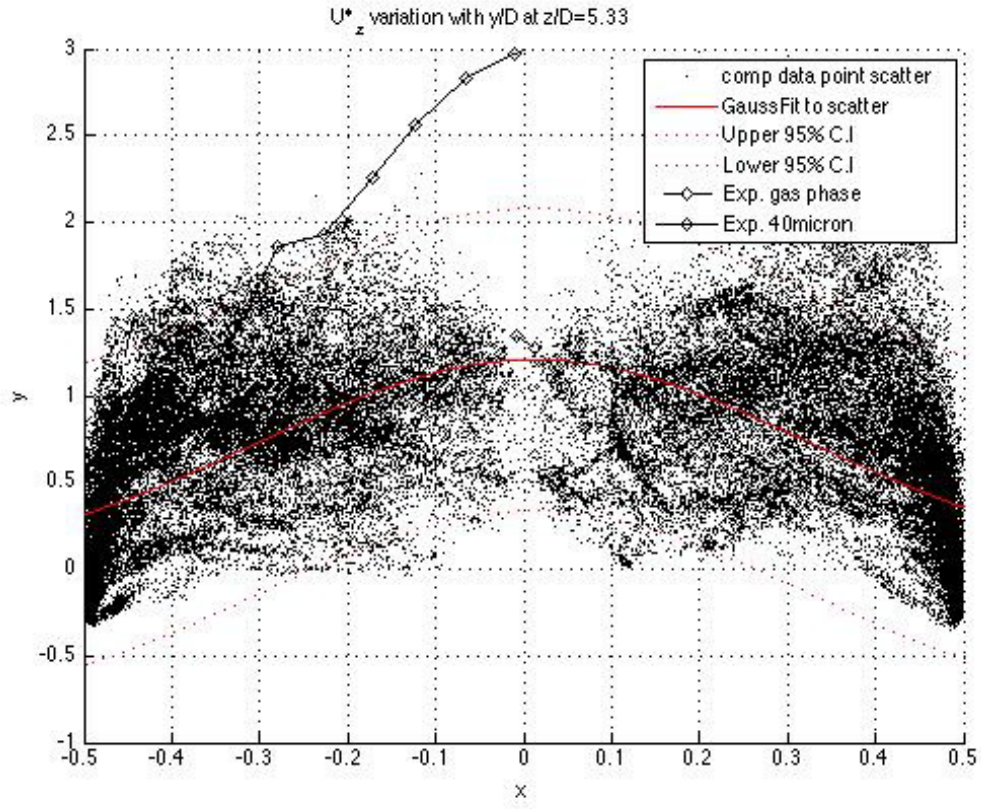

(b) Lagrangian data across the station collapsed to a line

Figure 45: Lagrangian instantaneous axial velocity for the 40 μm particles at z/D=5.33

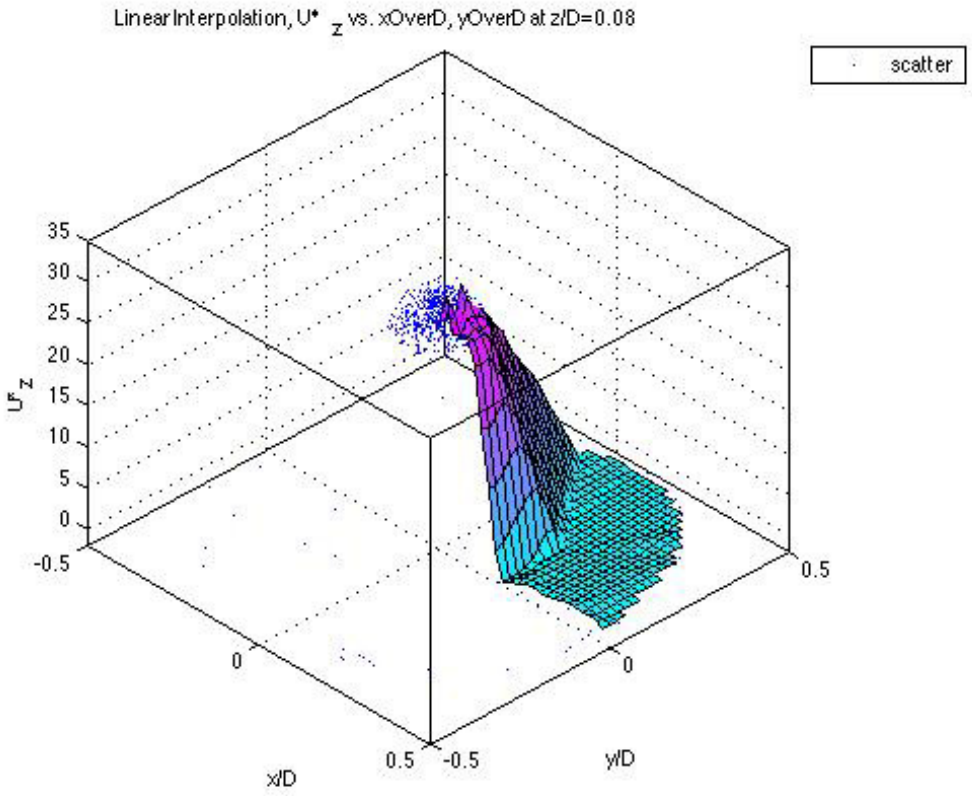

(a) Lagrangian data across the station with Linear fit

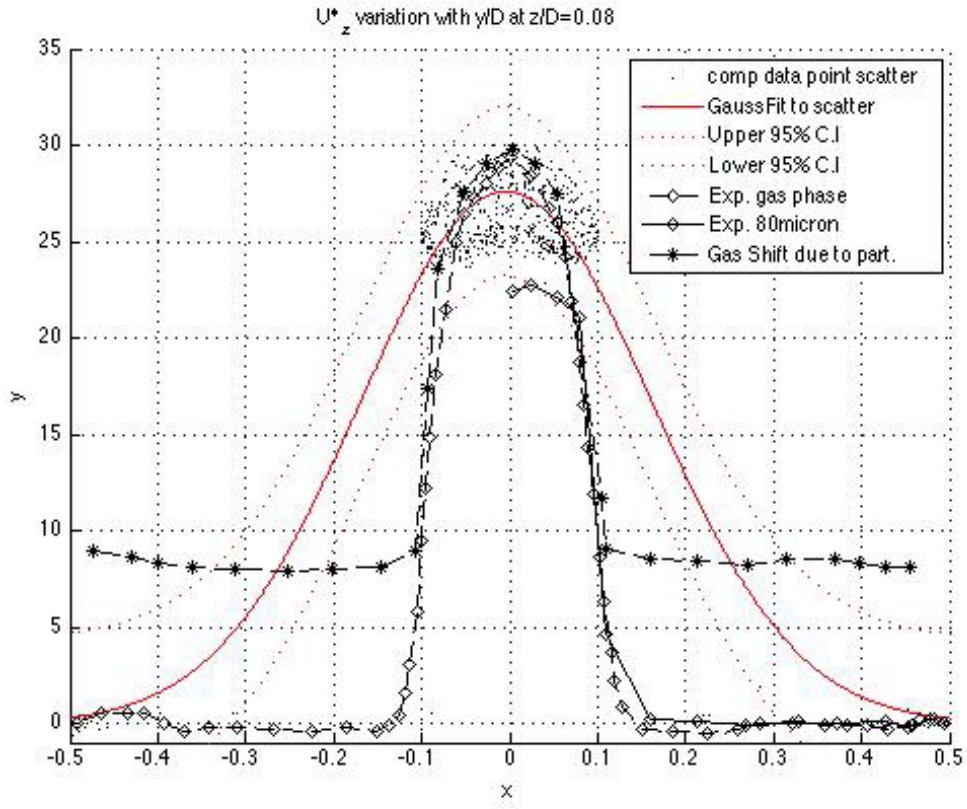

(b) Lagrangian data across the station collapsed to a line

Figure 46: Lagrangian instantaneous axial velocity for the 80 μm particles at z/D=0.08

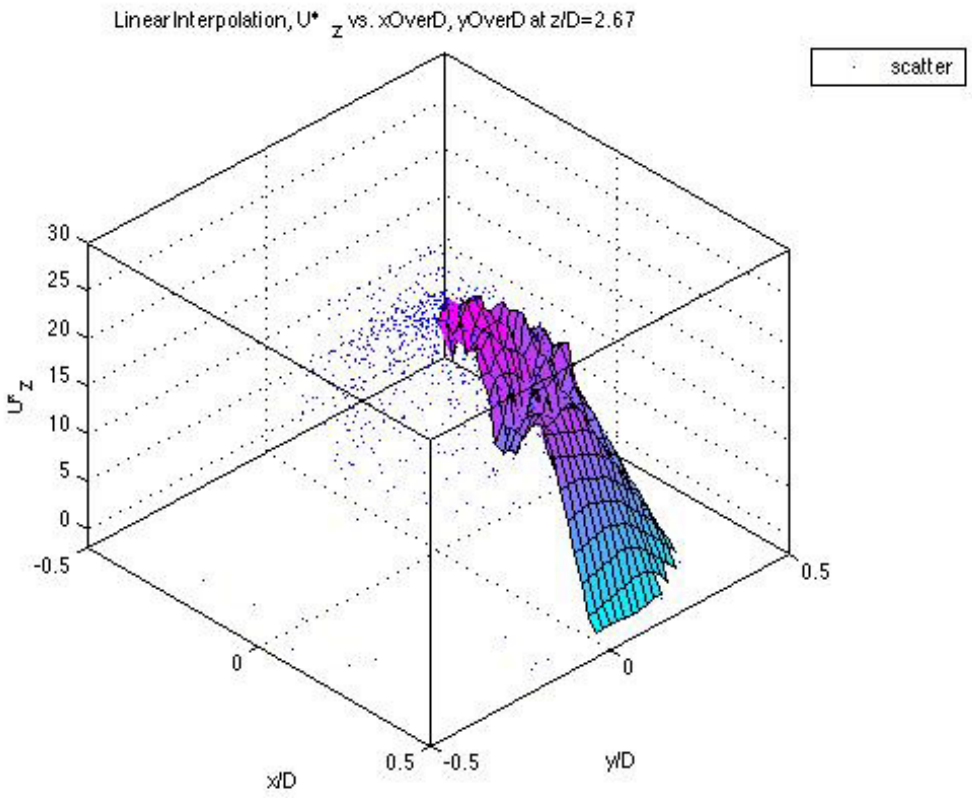

(a) Lagrangian data across the station with Linear fit

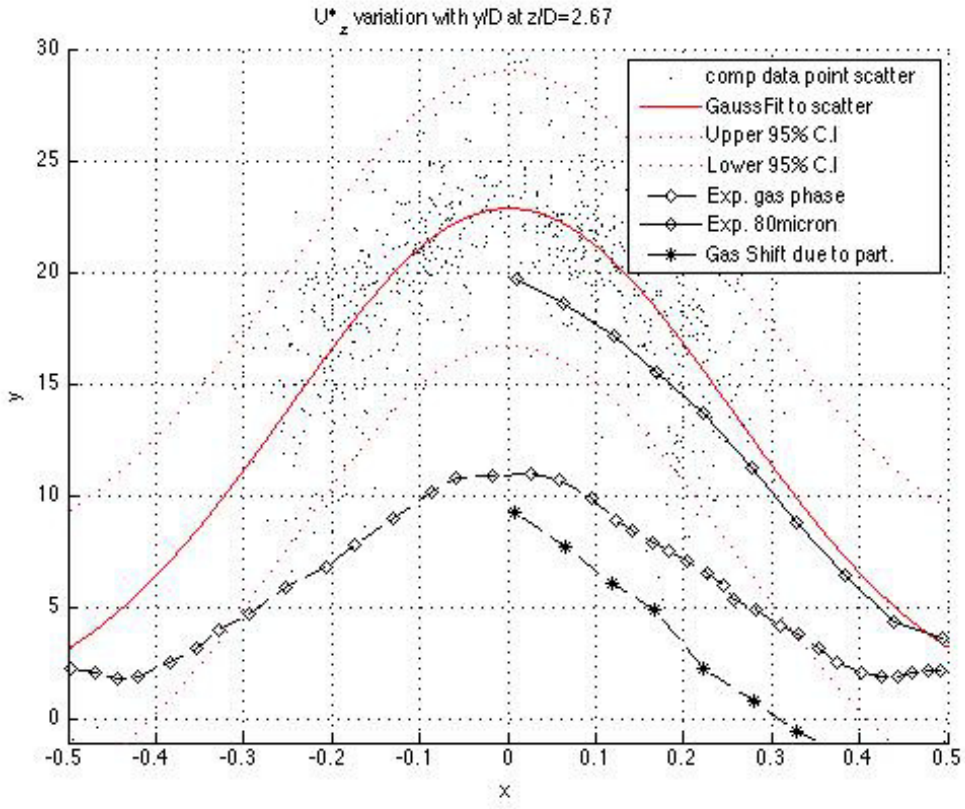

(b) Lagrangian data across the station collapsed to a line

Figure 47: Lagrangian instantaneous axial velocity for the 80 μm particles at z/D=2.67

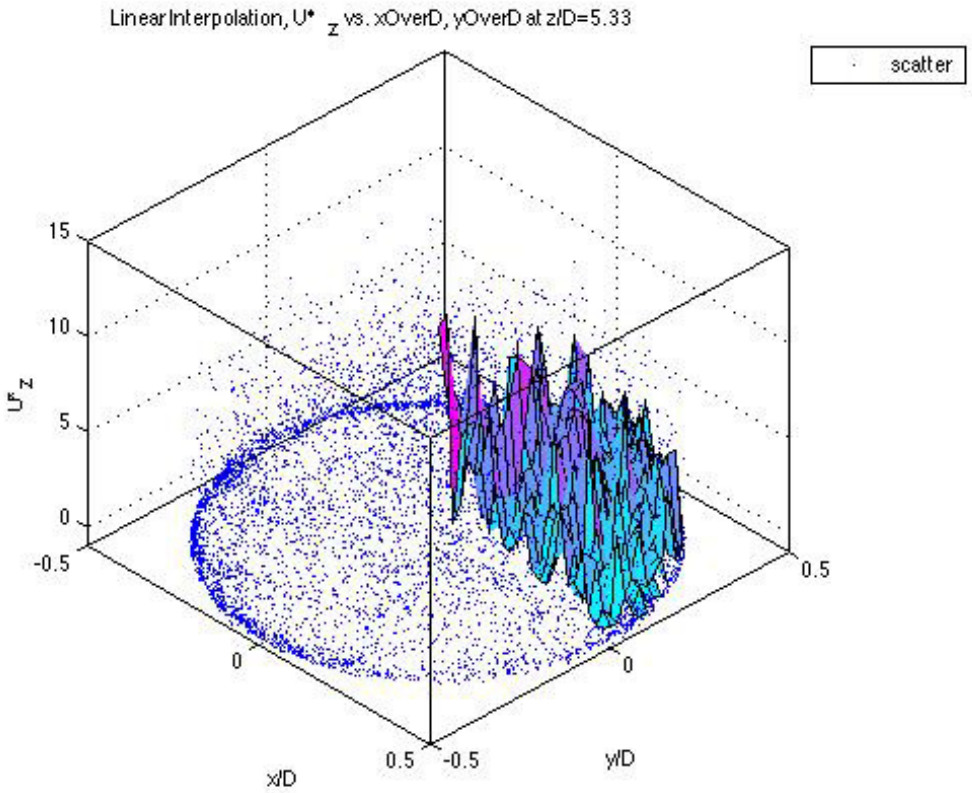

(a) Lagrangian data across the station with Linear fit

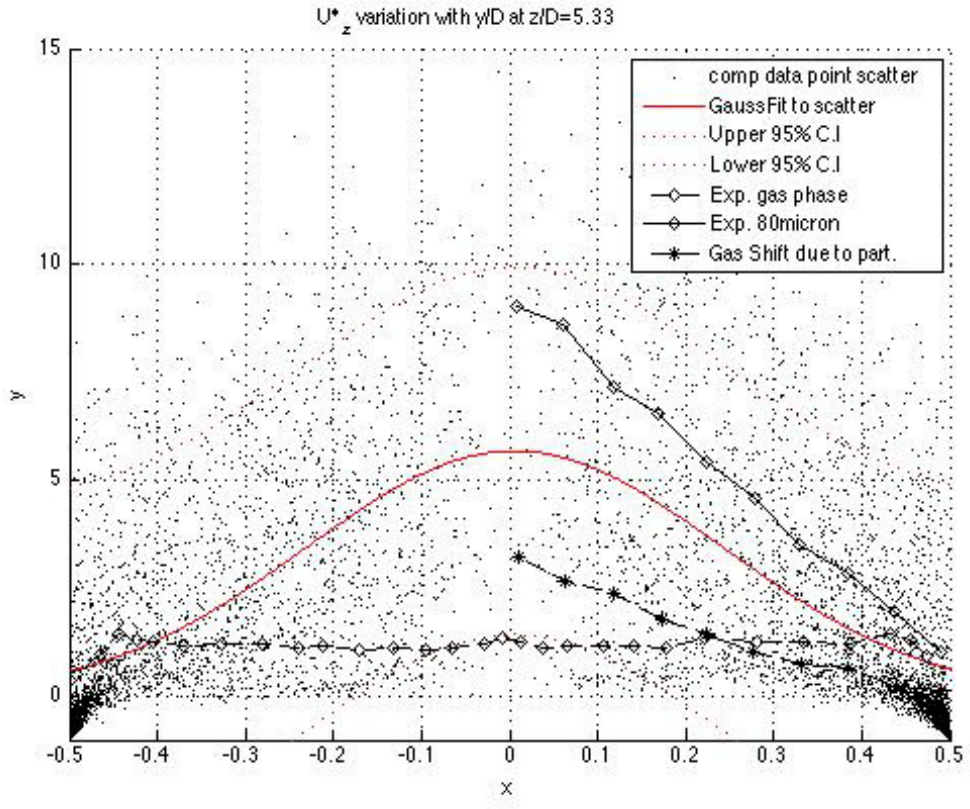

(b) Lagrangian data across the station collapsed to a line

Figure 48: Lagrangian instantaneous axial velocity for the 80 μm particles at z/D=5.33

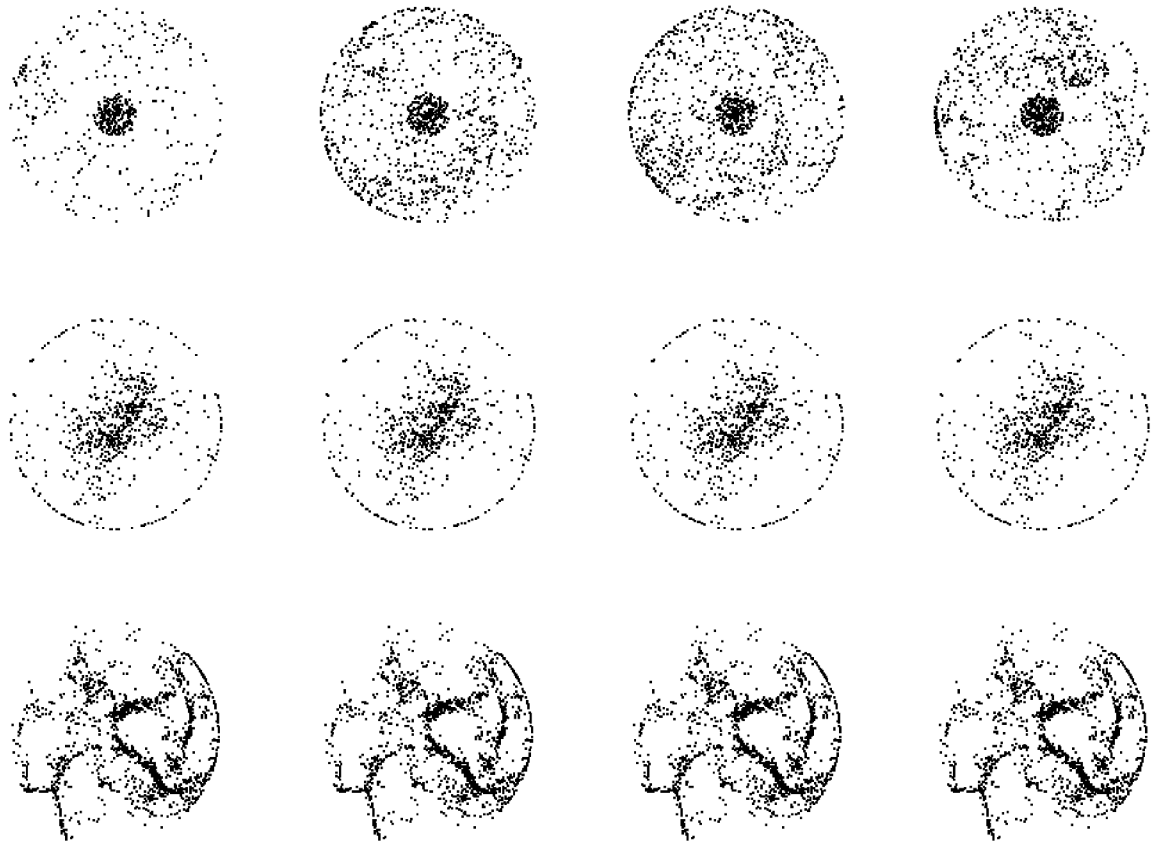

(a) Time instant A (b) Time instant B (c) Time instant C (d) Time instant D

Figure 49: Spatial non-uniformity of $40\,\mu m$ particles at ML1 conditions at four distinct time instances for the three spanwise measurement stations at z/D=0.08, 2.67 & 5.33, from top to bottom respectively

the $40\,\mu m$ particles.

The correlation with the surrounding flow structures with sudden changes in the curvature of the particle trajectories may provide insight into which structures are responsible for sudden and large changes in particle trajectory directions and eventually clustering. For example, the separation distance between two particles lying on a vortex tube their separation distance increases when the vortex tube increases as explained by Durbin & Petterson-Reif (2001). Vorticity however is not a convenient method for vortex identification as it is hard to distinguish between regions of strain and regions of vorticity.

Adrian *et al.* (2000) and Adrian & Liu (2002) note that a key requirement for the identification of vortices is that they be viewed in the same frame of reference as the vortex core. However, the whole process presents a particular difficulty as it would require an iterative approach to the post-processing process: first a cluster would have to be identified, subsequently the Eulerian fields have to be probed in the region surrounding the cluster at the same and prior instances in time, before finally repeating the process at a later instant in time to observe whether the cluster has persisted in space or had been dispersed. Meanwhile the implication is that, contrary to the

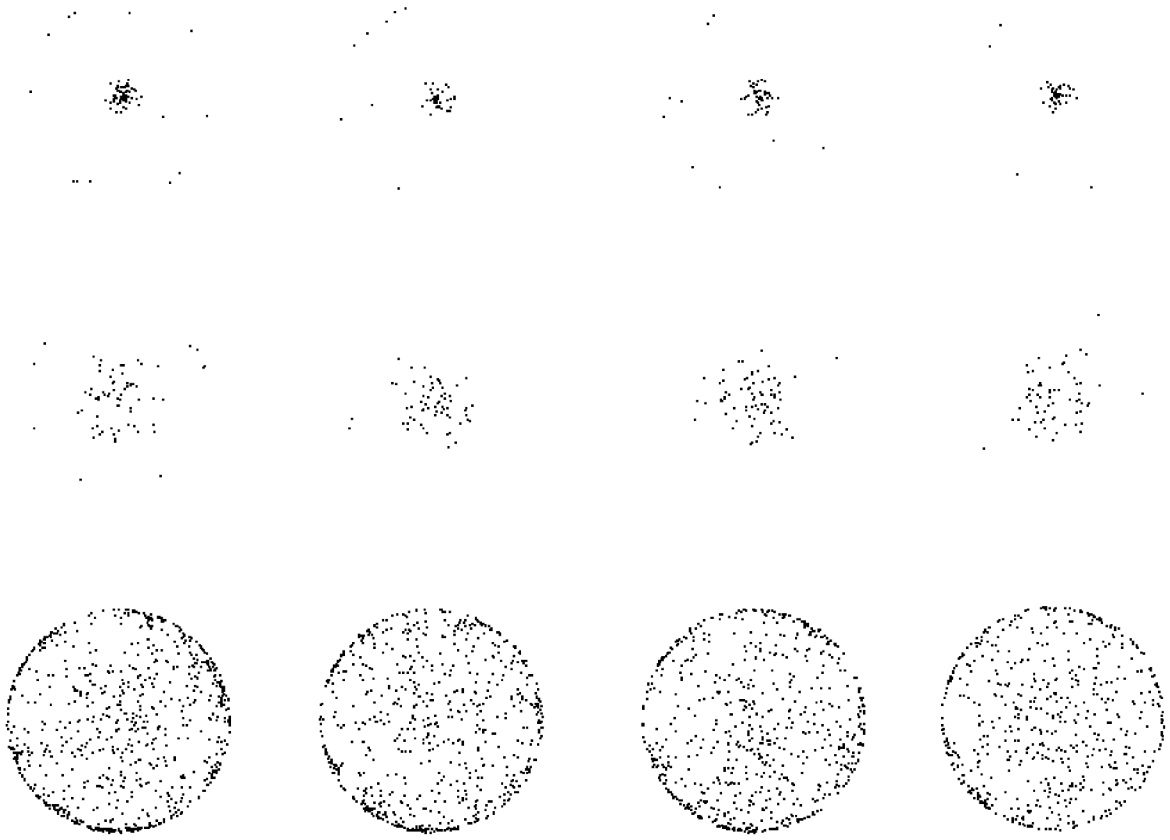

(a) Time instant A (b) Time instant B (c) Time instant C (d) Time instant D

Figure 50: Spatial non-uniformity of $80\,\mu m$ particles at ML1 conditions at four distinct time instances for the three spanwise measurement stations at z/D=0.08, 2.67 & 5.33, from top to bottom respectively

approach adopted up until this point, the investigation cannot be limited to a few measurement stations. Rather it should be done for the whole domain as the structure and cluster are being advected downstream.

On the right hand side of Figure 51 clusters of particles are shown within a downstream portion of the sudden expansion along with contours of enstrophy[67] in an effort to identify structures (similar to the approach followed by Rogers & Moser (1991)). Holmes *et al.* (1996) state that -provided the conditions that give rise to turbulence vary slowly- it is sufficient to solely study the Reynolds stress (R_{ij}) to investigate the coherent structures as these will scale the same way as the mean momentum flux due to turbulent fluctuations. Such an approach did not prove to be suitable for the present test case, perhaps because the aforementioned provision is not met.

In the middle pane of Figure 51, contours of the second invariant of the velocity gradient tensor, Q, are shown in the sudden expansion flow along with those clusters of particles that lie close to the plane. The need for velocity gradient invariants arises from the desire to identify vortex cores unambiguously given the aforementioned limitations of vorticity. For a 3D flow field with a velocity field given by $u_i = A_{ij}x_j$, Chong *et al.* (1990) define the first invariant of the the velocity gradient tensor A_{ij} as its trace:

$$P = A_{ii}$$

the second invariant, Q as:

$$Q = \frac{1}{2}[P^2 - S_{ij}S_{ji} - W_{ij}W_{ji}]$$

the third invariant R as:

$$R = \frac{1}{2}\left[-P^3 + 3PQ - S_{ij}S_{jk}S_{ki} - 3W_{ij}W_{jk}S_{ki}\right]$$

where

$$S_{ij} = {}^{(A_{ij}+A_{ji})}/_{2} \;\&\; W_{ij} = {}^{(A_{ij}-A_{ji})}/_{2}$$

Positive values of Q indicate points within a vortex and zero and negatives values indicate regions of shear. The authors recommend investigating complex flow field structures by inspecting surfaces of the invariants and their combinations. Such information was thought to be useful to further improve the cluster simulating abilities of the phenomenological model of the subsequent chapters. However, after careful investigation in 2D and 3D frameworks, shown in Figures 51 & 52 no conclusive insight was gained. This might be a limitation of the test method because they are more suitable to flow fields with strong symmetry planes or stationary turbulence: even small deviations from these conditions complicate the post processing procedure significantly. In any case these approaches seemed to be further complicated by the fact that the selection of the appropriate contour level is an arbitrary process. More, importantly, though is the fact that the particles have finite relaxation times. They do not respond immediately to changes in the flow-field conditions so that an inspection of the instantaneous flow-field may not be ideal. Rather, it may be necessary to store all the timesteps to permit post-processing. Such an approach may

[67] Equal to half the square of the vorticity, as defined by Frisch (1995)

permit the correlation of the clustering of the Lagrangian phase observed at a time t to some Eulerian structure that is responsible for the formation of the cluster at a time $t - \Delta t$.

The large advecting velocity and periodicity observed here may require a different approach, such as an investigation of the finite time Lyapunov exponents. Some recent work (Shadden *et al.* (2009) & Garcia-Olivares *et al.* (2007)) suggests that this is a more suitable criterion for evaluating the particle-gas interaction when the velocities are significant.

3.5.1 *Stokes* Numbers

Although the identification of turbulent structures responsible for the preferential concentration of the particles proved to be troublesome, there are still some qualitative comparisons that may be made in terms of the *Stokes* number. Several different St may be defined based on various characteristic flow scales. For the particles entering the expansion tube, one relevant parameter is the large eddy *Stokes* number, St_e, based on the step height, h:

$$St_e = \frac{\tau_p}{(h/U_0)}$$

resulting in values of 0.23 & 1.11 for the $40\,\mu m$ and $80\,\mu m$ particles respectively. The calculations are consistent with the implied characterization by values of this number and even the large particles, with a value close to unity, disperse across the diameter of the domain. For the smaller particle class the value of the St_e, is significantly smaller than unity, and a much larger number of particles enter the recirculation zone. A more relevant parameter in this case is the centrifuge *Stokes* number, St_c, defined as:

$$St_c = \frac{\rho_p d_p^2 \omega}{36 \mu_f}$$

where ω is a representative value for the mean vorticity in the expansion tube. The significance of the parameter, as Hardalupas *et al.* (1992) note, is that it relates the centripetal force 'felt' by the particle to the viscous drag acting on its surface. The greater the angular velocity of the eddy the more likely it is to centrifuge the particles as the St_c will be correspondingly smaller. Using a representative value for the vorticity in the region of the recirculation zone yields St_c of 0.10 & 0.49 for the $40\,\mu m$ and $80\,\mu m$ respectively. The much smaller St_c of the smaller particles is a further justification of the existence of a greater number of particles in the recirculation zone but also of the preferential concentration observed downstream visible in Figure 60. However, the St_c of the larger particles is also smaller than unity and as such one would perhaps expect more particles in the recirculation zone than those observed. Evaluating a transit *Stokes* number, St_{tr}, provides for an explanation for the smaller, than expected, number of $80\,\mu m$ particles within the recirculations zone. A characteristic timescale, T_{tr}, for the recirculation zone may be obtained through consideration of the re-attachment length, Z_r, and the velocity at that point, U_{Zr}.

$$T_{tr} = \frac{Z_r}{1/2(U_{centreline} + U_{Zr})} \;\&\; St_{tr} = \frac{\tau_p}{T_{tr}}$$

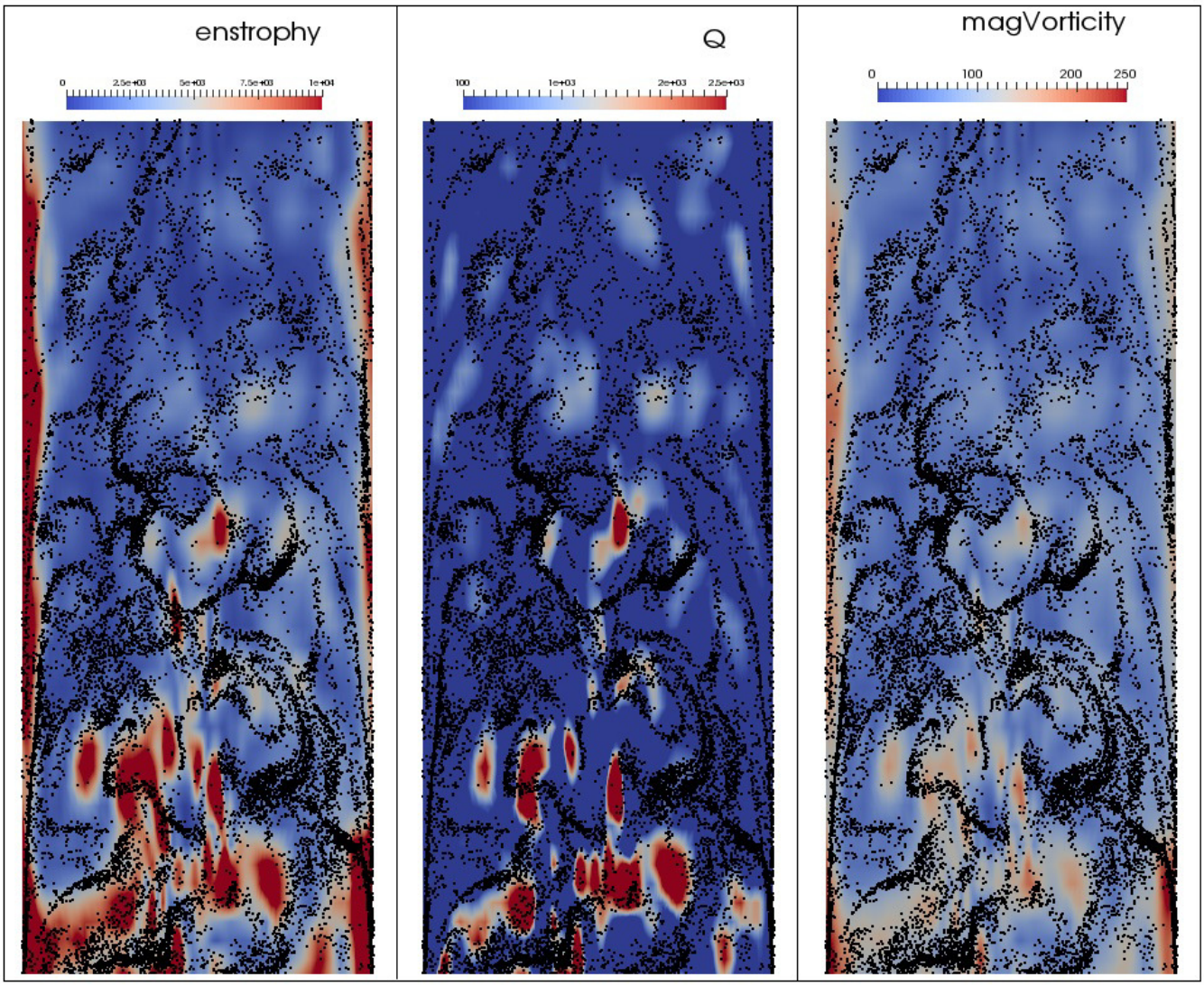

Figure 51: Sample sections though the LES domain for $40\,\mu m$ ML1 case, near the expansion tube outlet, showing only the clusters of particles that lie close to the slices through the domain depicting from left to right; enstrophy colored by a range [0, $10^4 s^{-2}$]; Q, the second invariant of the velocity gradient tensor colored by a range [100, $2\text{x}10^3 s^{-2}$] and the magnitude of vorticity colored by a range [0, $250 s^{-1}$]

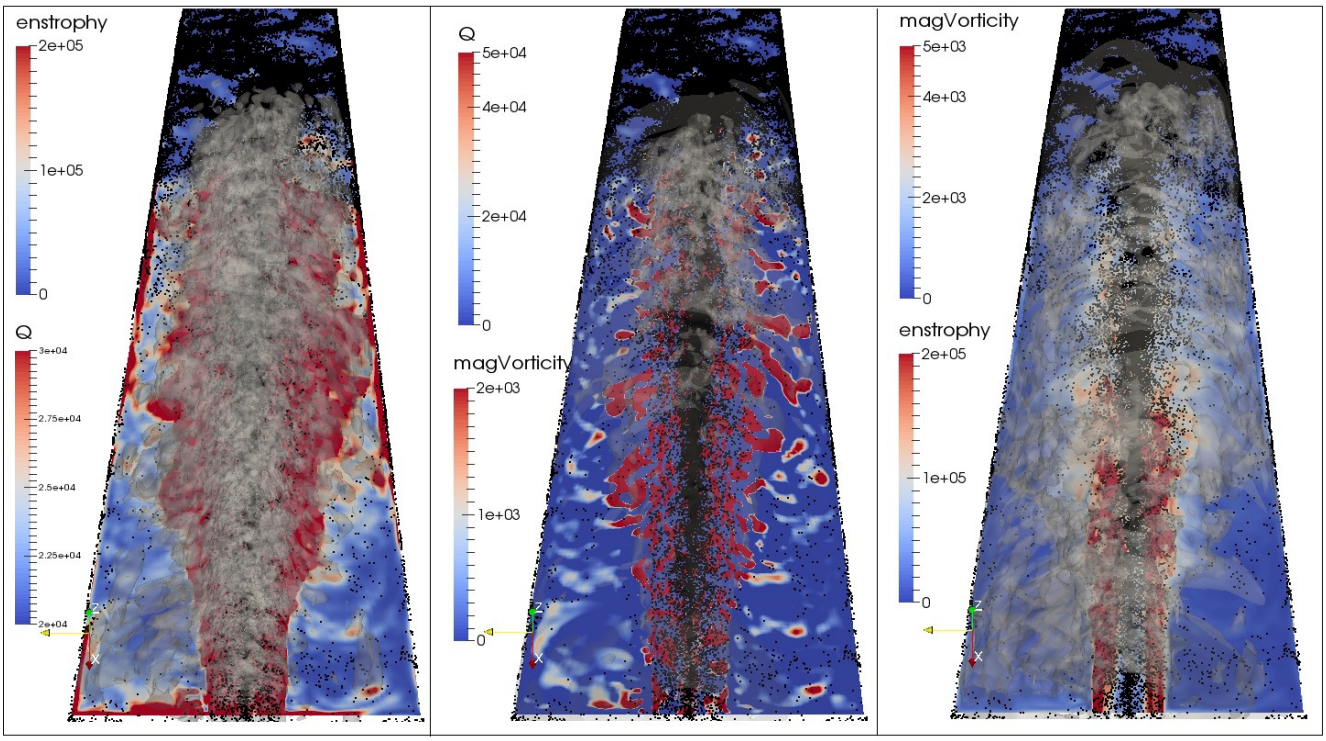

Figure 52: Sample sections though the LES domain of the expansion tube outlet for the $40\,\mu m$ ML1 case , viewed from the step towards the expansion tube outlet. the view shows, in black, only the particles that lie close to slices through the domain. The left panel shows enstrophy colored by a range [0, $2\text{x}10^5 s^{-2}$] and a contour of Q at $2.5\text{x}10^4 s^{-2}$. The middle pane shows a plane colored by the magnitude of Q for a range [0, $5\text{x}10^4 s^{-2}$] along with contours of the magnitude of vorticity at $10^3 s^{-1}$. The right hand pane shows a plane colored by the magnitude of vorticity for a range [0, $5\text{x}10^3 s^{-1}$] along with contours of enstrophy at $10^5 s^{-2}$.

For the $40\,\mu m$ and $80\,\mu m$, the St_{tr} is found to be 0.30 & 1.48 respectively, explaining the smaller number of $80\,\mu m$ particles within the recirculation zone when compared to the $40\,\mu m$ particles.

A *Stokes* number may also be used to evaluate whether a SGS dispersion model is required within the calculation. A characteristic SGS timescale, T_{SGS}, may be obtained by evaluating the ratio of the average cell size to the bulk velocity, U_0.

$$St_{SGS} = \frac{\tau_p}{T_{SGS}}$$

resulting in St_{SGS} of 21 & 106 for the $40\,\mu m$ and $80\,\mu m$ particles respectively indicating both particles sizes respond too slowly to any changes of the flow-field on the SGS level and the use of a dispersion model is not warranted. If on the other hand these where nano-sized particles there might be a need for a SGS dispersion model.

3.5.2 Large scale oscillations of the jet

A further complication arises when trying to identify turbulent features of the flow responsible for particle clustering on the chosen data set and this is perhaps evident in Figure 60 where it appears that there is some periodicity to the spatial distribution of the particles at a few diameters, *D,* downstream of the step. This may be attributed to the large scale oscillations of the jet exiting the inlet tube. Just as the flow past a cylinder[68] will shed downstream vortices originating in an alternating fashion on either side of the obstacle, so too will a jet flap from side to side as explained by Schlichting (1968) and Birkhoff & Zarantonello (1957). More precisely, the oscillations occur at various alternating points around the jets azimuthal direction similarly to the situation with a sphere. This oscillating jet results in a significant number of particles being shed in alternating directions creating substantial voids in the spatial distribution. The process is very similar to the break-up of a liquid sheet by a stream of high momentum gas, (Fuster *et al.* (2013)) where the wave formed along the interface eventually gives rise to a sufficiently energetic vortex that will break the liquid sheet sending droplets in an completely unexpected but periodic and reproducible angle, every other wave.

Figures 53-55 serve to show the large scale oscillations of the jet under consideration at several distinct time steps. Visible in the detailed snapshots of the same images of Figures 56-58 is the increase in resolution of structures associated with increasing mesh density. This last observation may provide a qualitative explanation to the significant differences observed in the large scale oscillation structures. The purpose of including the less detailed depictions of Figures 53-55 is to show that the large scale oscillating motion persists farther downstream in the expansion tube when finer grids are used. This lrge scale oscillations of the jet results in particles being shed in clusters along with the vortices (or perhaps lagging them) in alternating directions before being advected downstream. The pattern persists and is clearly visible in Figure 60 for the smaller diameter particles whereas for the $80\,\mu m$ particles with the larger *Stokes number* the effects are limited to a slight oscillation of the particles lying along the centreline. The large number of particles present required rendering of the Lagrangian phase

[68] At least for cases of engineering interest; that is, not for those particular circumstances achievable solely under laboratory conditions.

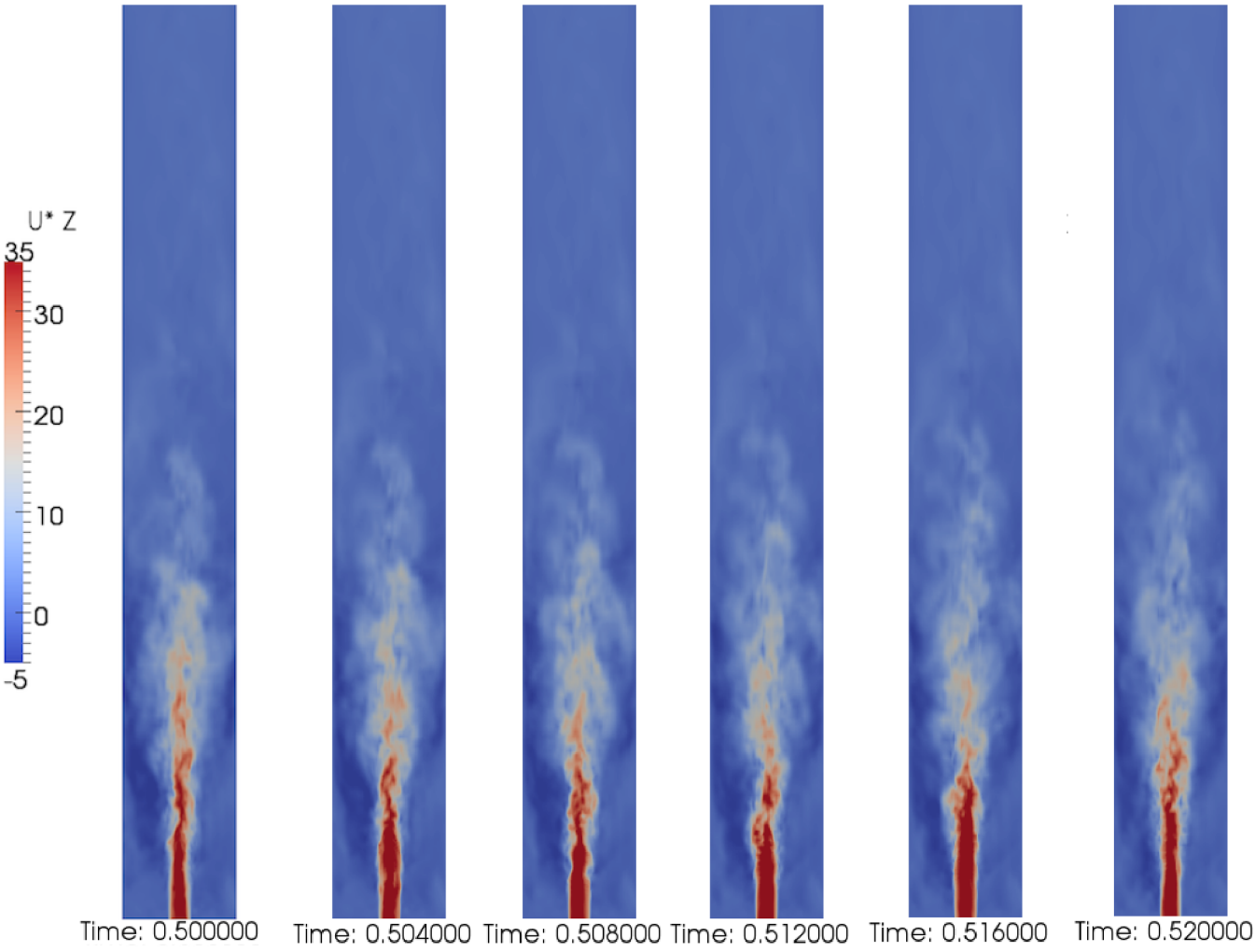

Figure 53: Large scale oscillations of coarse mesh jet, showing the normalized axial velocity (U_z/U_o) colored for a range [-5,35]. Flow direction is from the bottom of the page to the top.

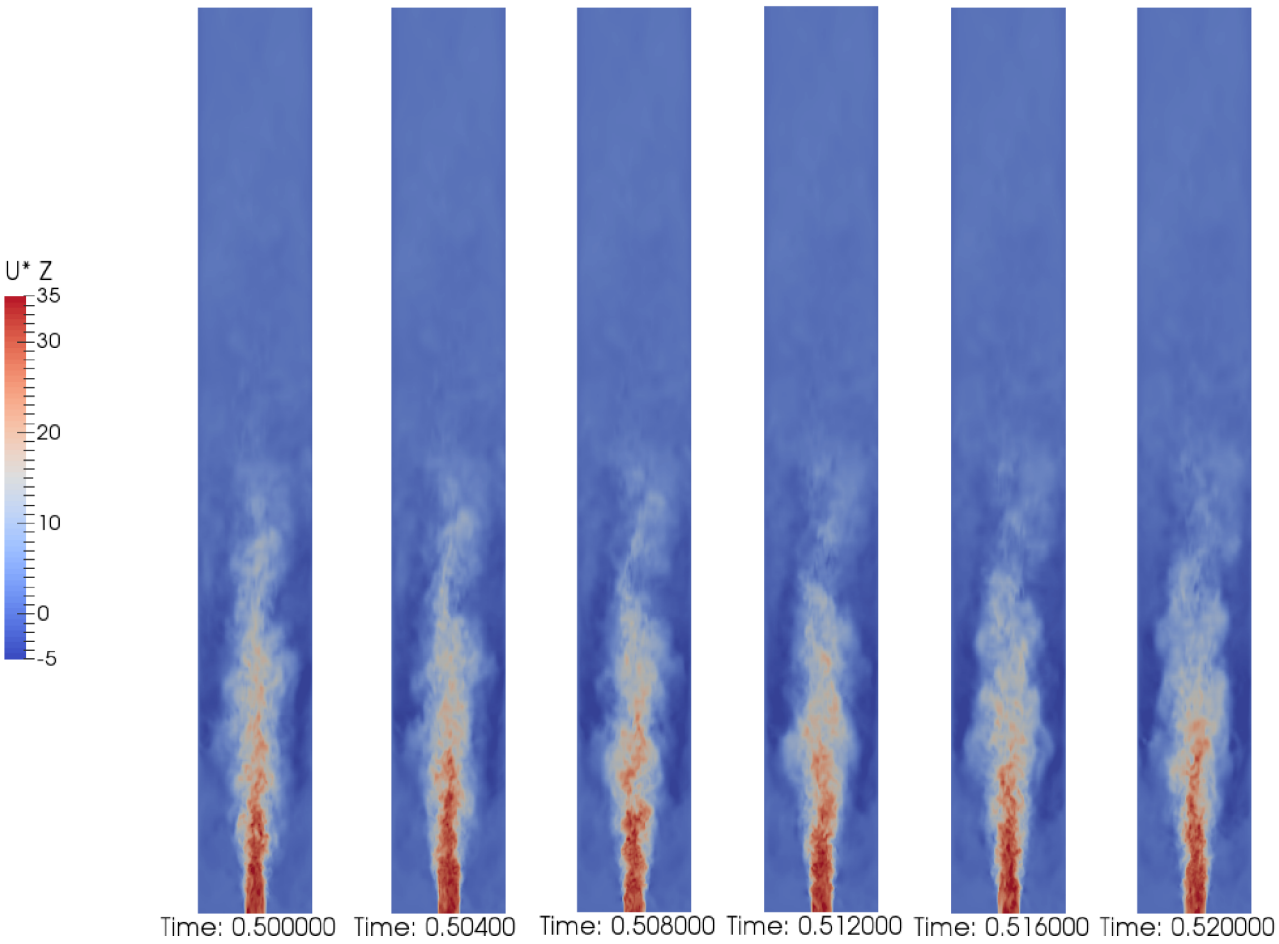

Figure 54: Large scale oscillations of the standard mesh jet , showing the normalized axial velocity (U_z/U_o) colored for a range [-5,35]. Flow direction is from the bottom of the page to the top.

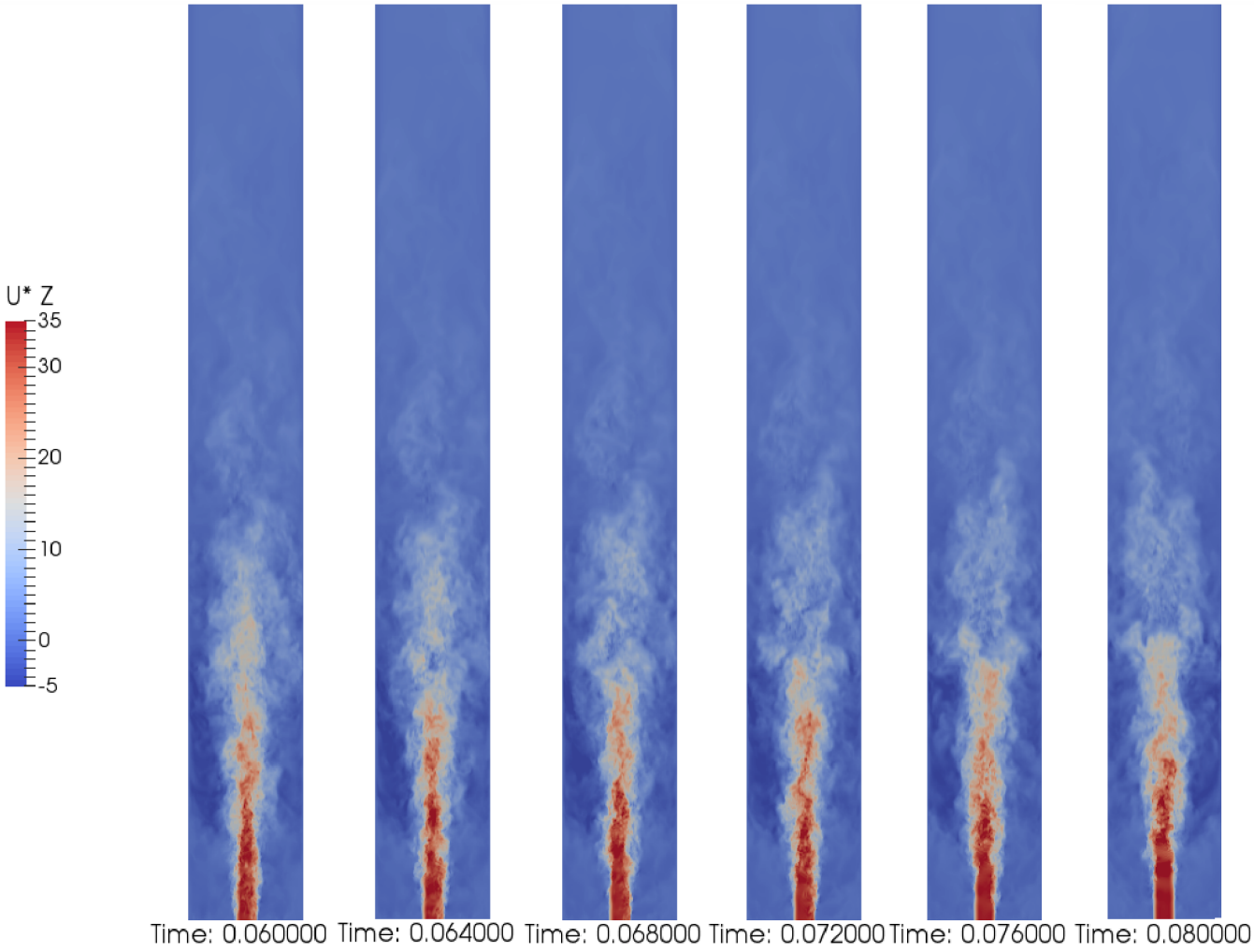

Figure 55: Large scale oscillations of the fine mesh jet, showing the normalized axial velocity (U_z/U_o) colored for a range [-5,35]. Flow direction is from the bottom of the page to the top.

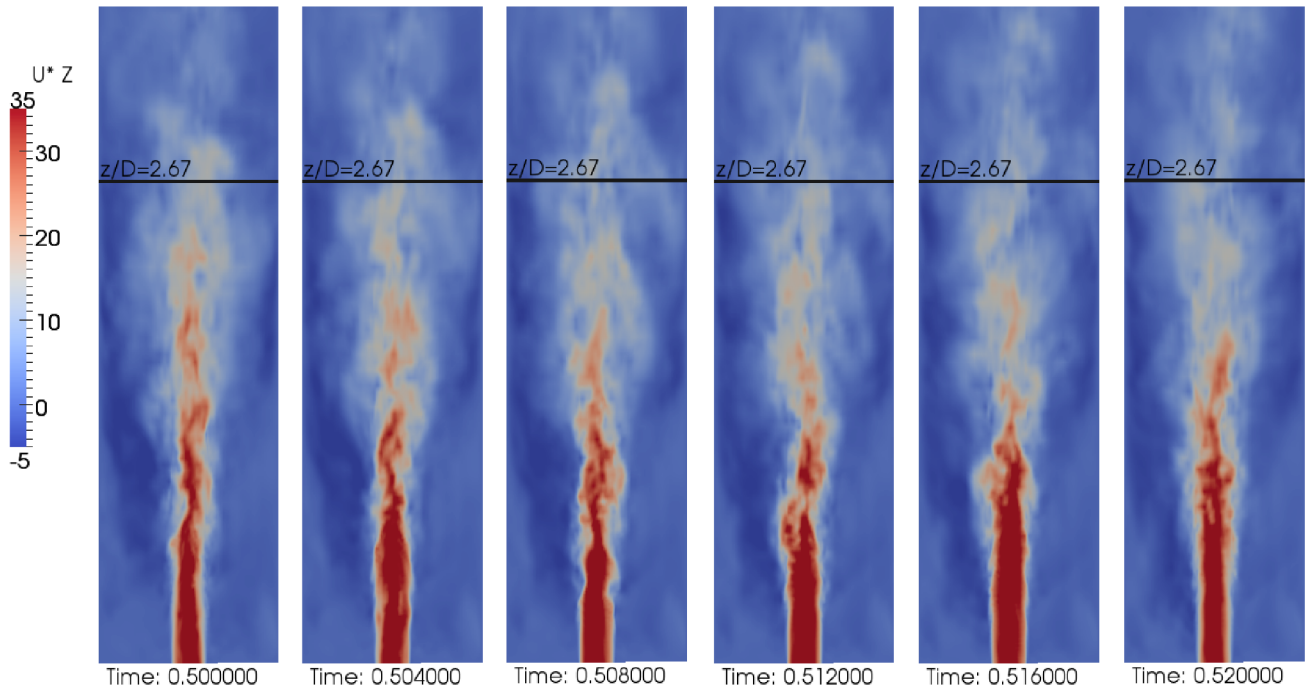

Figure 56: Detailed view of the large scale oscillations of the coarse mesh jet, showing the normalized axial velocity (U_z/U_o) colored for a range [-5, 35]. Flow direction is from the bottom of the page to the top.

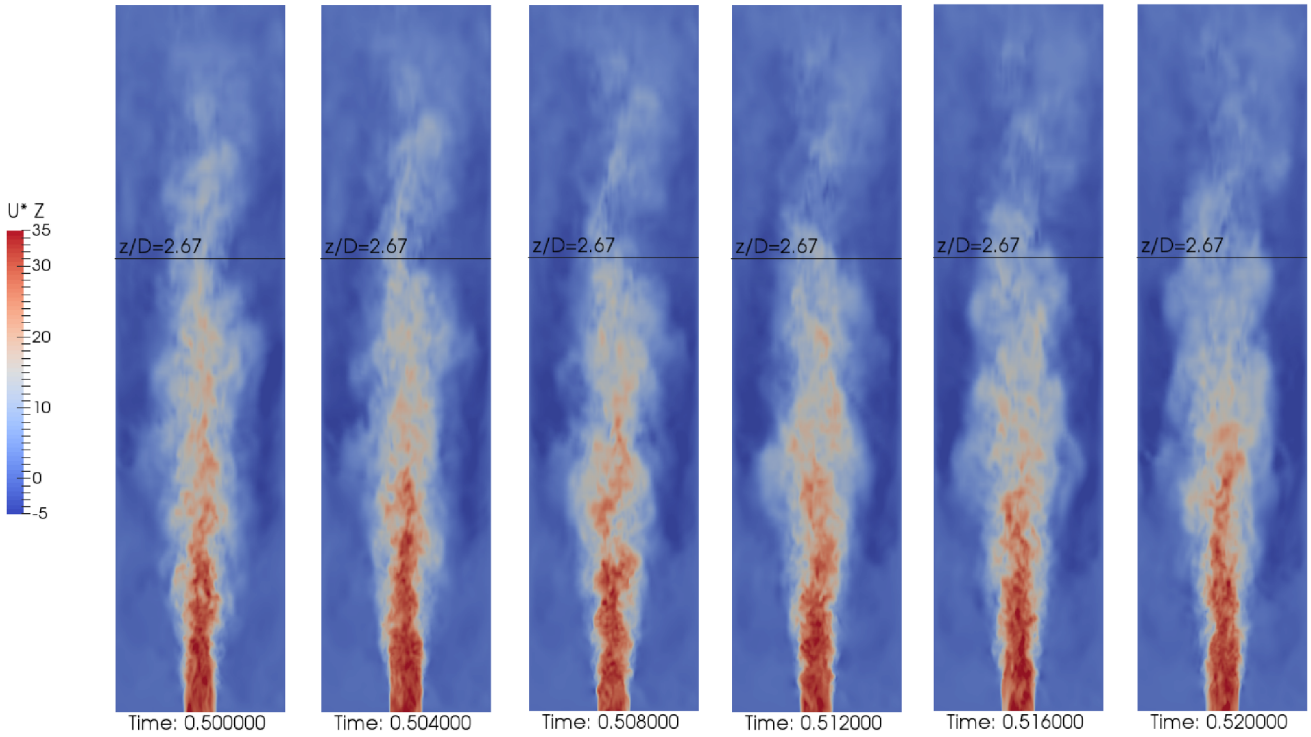

Figure 57: Detailed view of the large scale oscillations of the standard mesh jet, showing the normalized axial velocity (U_z/U_o) colored for a range [-5, 35]. Flow direction is from the bottom of the page to the top.

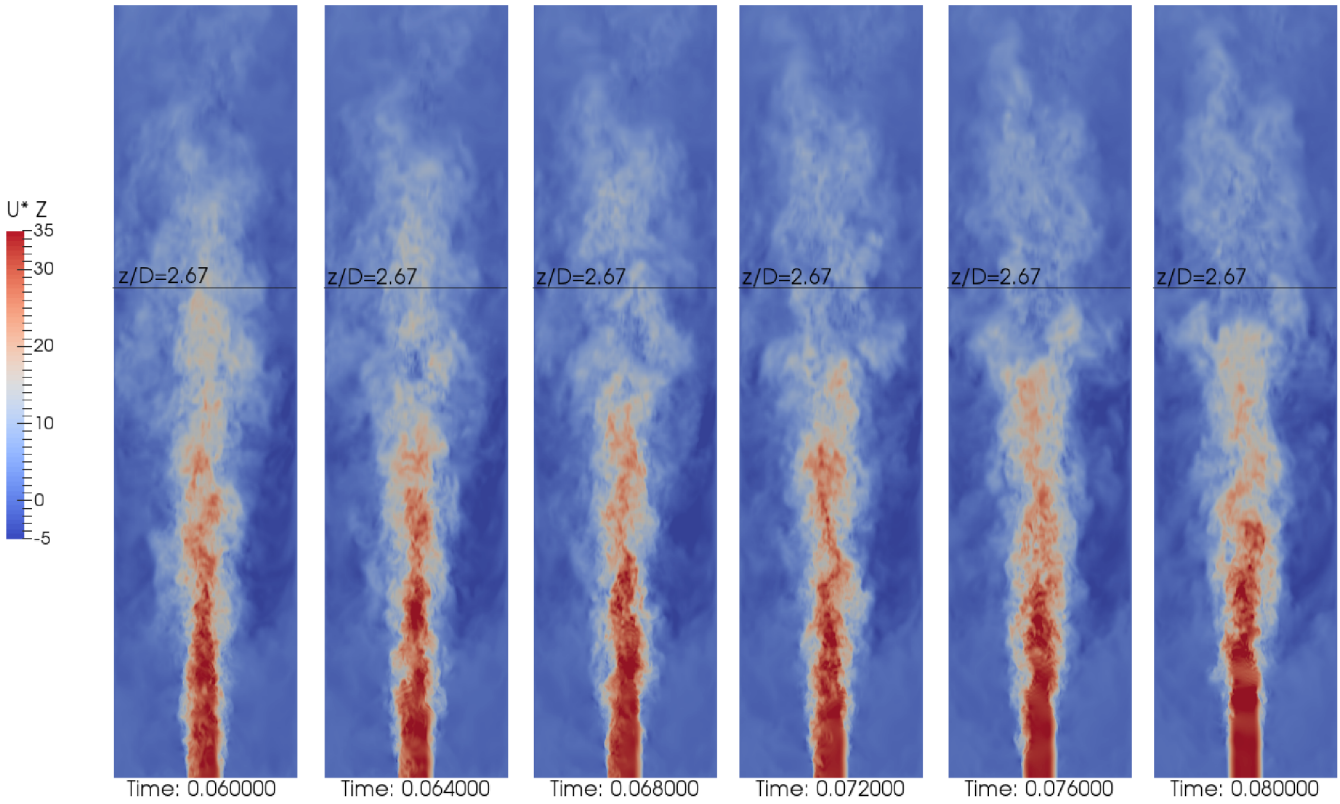

Figure 58: Detailed view of the large scale oscillations of the fine mesh jet, showing the normalized axial velocity (U_z/U_o) colored for a range [-5, 35]. Flow direction is from the bottom of the page to the top.

to be restricted to a parallelepiped of small thickness in the normal direction of the page. An additional *Stokes* number may be defined at this point to compare the period of the large scale oscillations of the jet, ΔT_{fl} to the particle characteristic timescales:

$$St_{fl} = \frac{\tau_p}{\Delta T_{fl}}$$

Unlike the case for a planar jet, when probing the axisymmetric sudden expansion to determine the oscillating period, the result was a broad spectrum FFT with no single peak clearly visible, this again is probably a result of the limited number of flow through times performed. The broad spectrum is consistent with the experimental observations and , in an alternative approach for the determination of the oscillating period, the probe's time signal was investigated. The probe location was positioned approximately at z/D=1.75 and half an inlet diameter off the centreline. The field was probed for the axial velocity through that point, resulting in a recorded signal with a clear sinusoidal pattern although it was also evident that there was more than one frequency present. Two periods may be identified at $0.05s$ and at $0.025s$, ΔT^1_{fl} & ΔT^2_{fl} respectively. Figure 59 depicts a recorded sample trace at one of the probe locations tested. The corresponding St^1_{fl} for the $40\,\mu m$ and $80\,\mu m$ particles are 0.48 and 2.32 respectively or, for St^2_{fl} the values are 0.24 and 1.16. In both cases the values indicate that the jet flapping should have a substantial effect on the spatial distribution of the smaller particles, which is consistent with the qualitative observations of Figure 60. A probable explanation for the presence of multiple frequencies is the

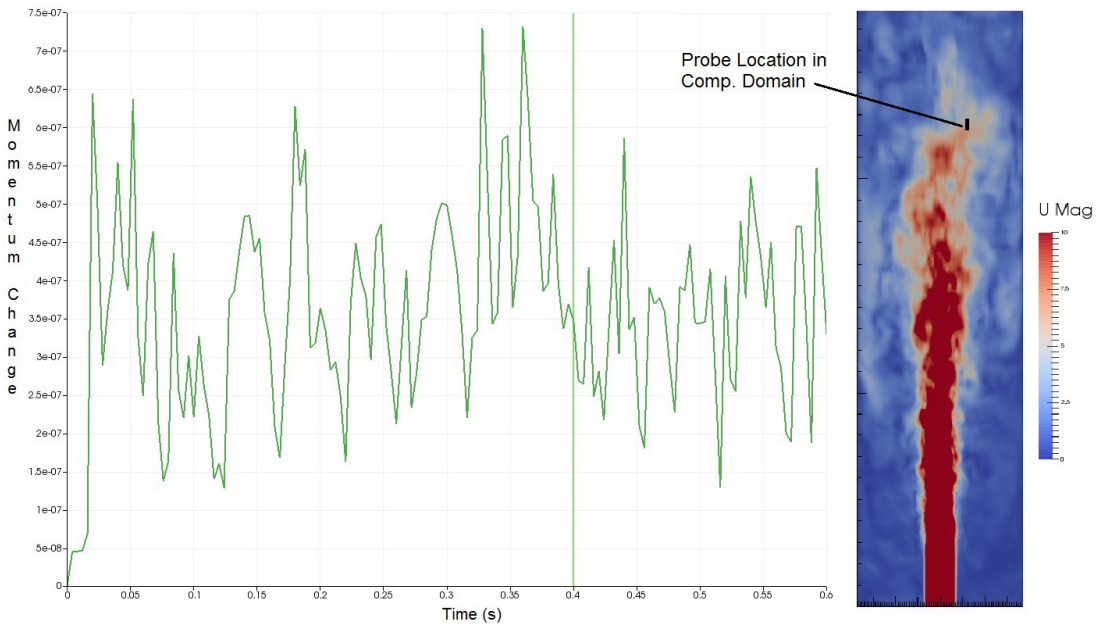

Figure 59: Probe Location and sample time trace

fact that, unlike a planar jet that will oscillate solely in the one, unique cross-stream direction, to the mean flow, an axisymmetric one is free to oscillate in the radial direction but is also free to oscillate in the circumferential one. Figure 61 shows slices through the computational domain at different circumferential angles with the clustered particles persisting in all directions.

3.5.3 *Voronoi* Analysis

A different approach for cluster identification is the use *Voronoi* plots, as they provide a quantitative measure for cluster identification. Sack & Urrutia (1999) define two dimensional *Voronoi* diagrams as a representation where every cell may contain only one site, in this case a particle. The boundaries of each cell are drawn in such a manner that the Euclidean distance from any point within the cell to the site/particle is smaller than the distance to any other neighboring site/particle. The implication is that a cell boundary delineates the equidistant points between two sites/particles while a *Voronoi* vertex marks the equidistant point between three sites/particles. Shading/coloring of the triangles and quadrilaterals by the size of their area would yield a convenient measure of clustering. Figures 62 to 67 show *Voronoi* plots for the two particle sizes at the spanwise measurements locations.

Applying such an approach may allow particle preferential concentrations to be evaluated in a qualitative manner through evaluation of the *Voronoi* cell areas. A perfectly uniform spatial distribution of particles should result in all *Voronoi* cell areas to be nearly identical if edge effects are disregarded. Meanwhile, a random spatial distribution of particles should result in a near *Gaussian* distribution of *Voronoi* cell areas with a specific standard deviation. In turn, a flow with significant amount of clustering should start exhibiting an almost bi-modal pattern and an increased standard deviation when its distribution of *Voronoi* cell areas is evaluated. Since the voids should result in an increase of larger *Voronoi* cell areas creating a peak near the tail end of the *Gaussian* distribution and the clusters should result in an increase of the smaller areas near

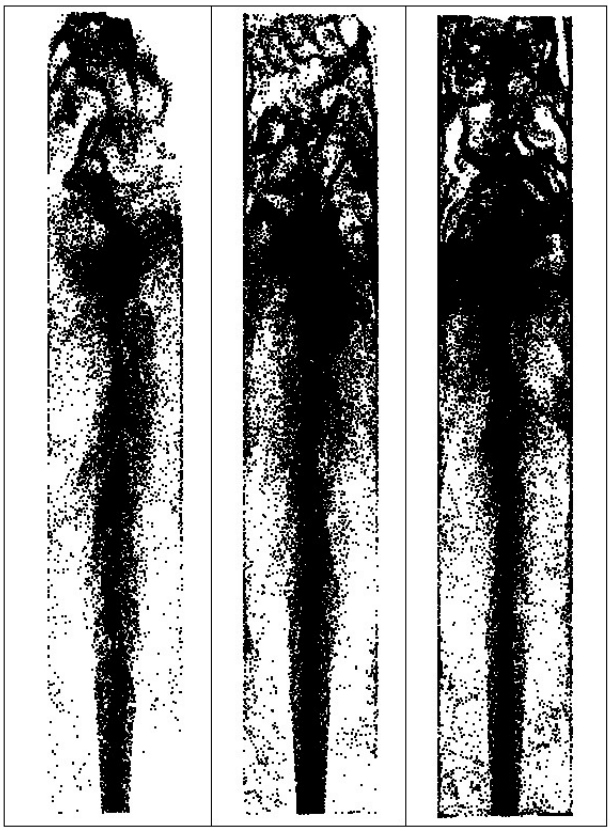

(a) $40\,\mu m$

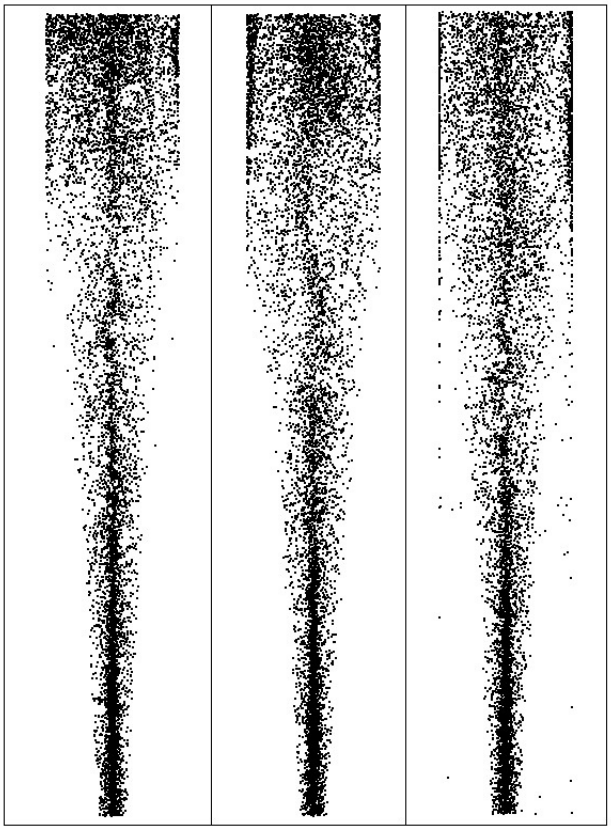

(b) $80\,\mu m$

Figure 60: Effect of jet flapping on particle spatial distribution at an early, intermediate and fully developed time instance , from left to right. Flow direction is from the bottom to the top of the page.

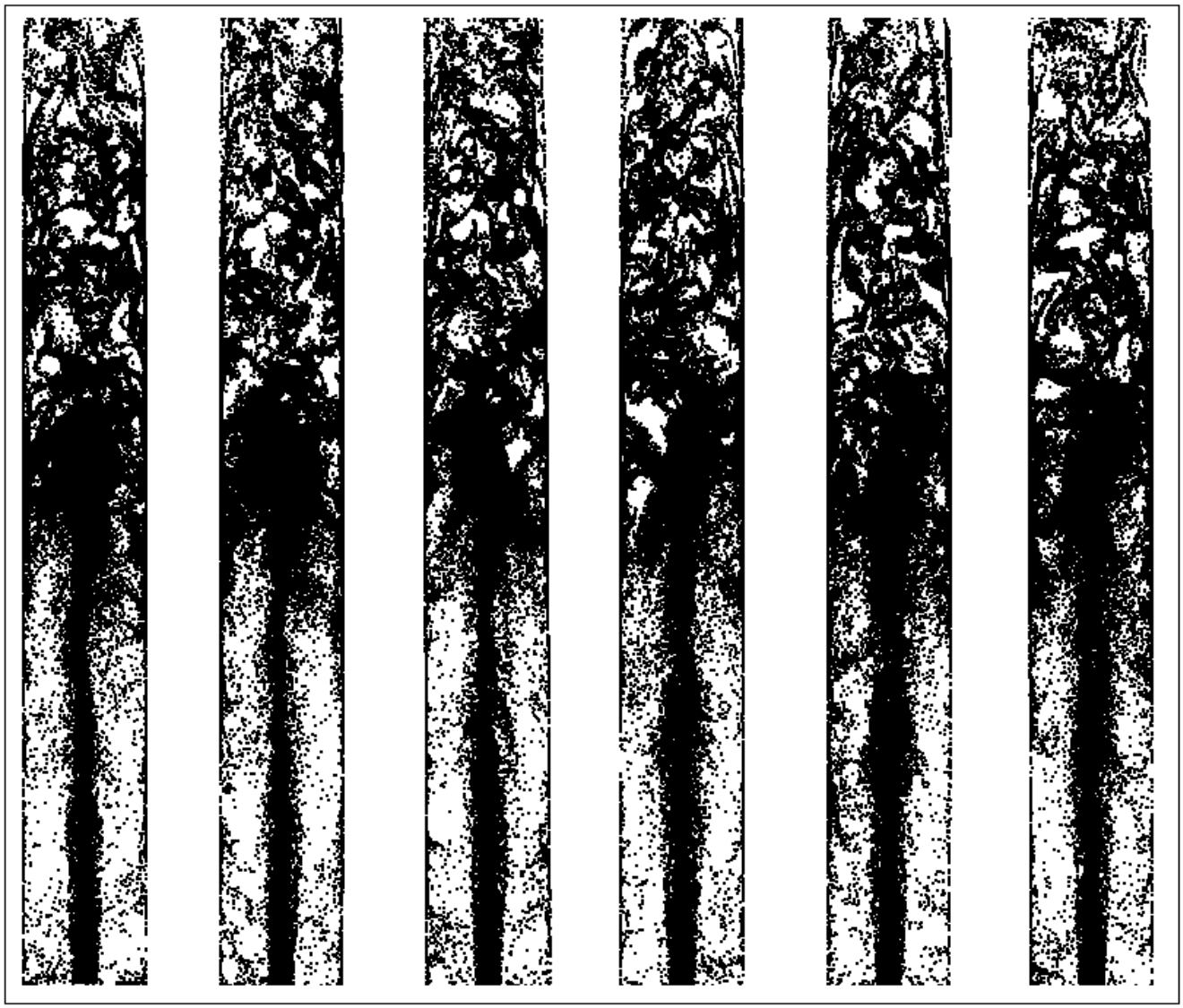

Figure 61: Details of the instantaneous $40\,\mu m$ particle spatial distribution viewed as a slice of the Lagrangian domain at 0, 30, 60 90, 120 & 150 degrees from the normal of the xy-plane. Flow direction is from the bottom of the page to the top.

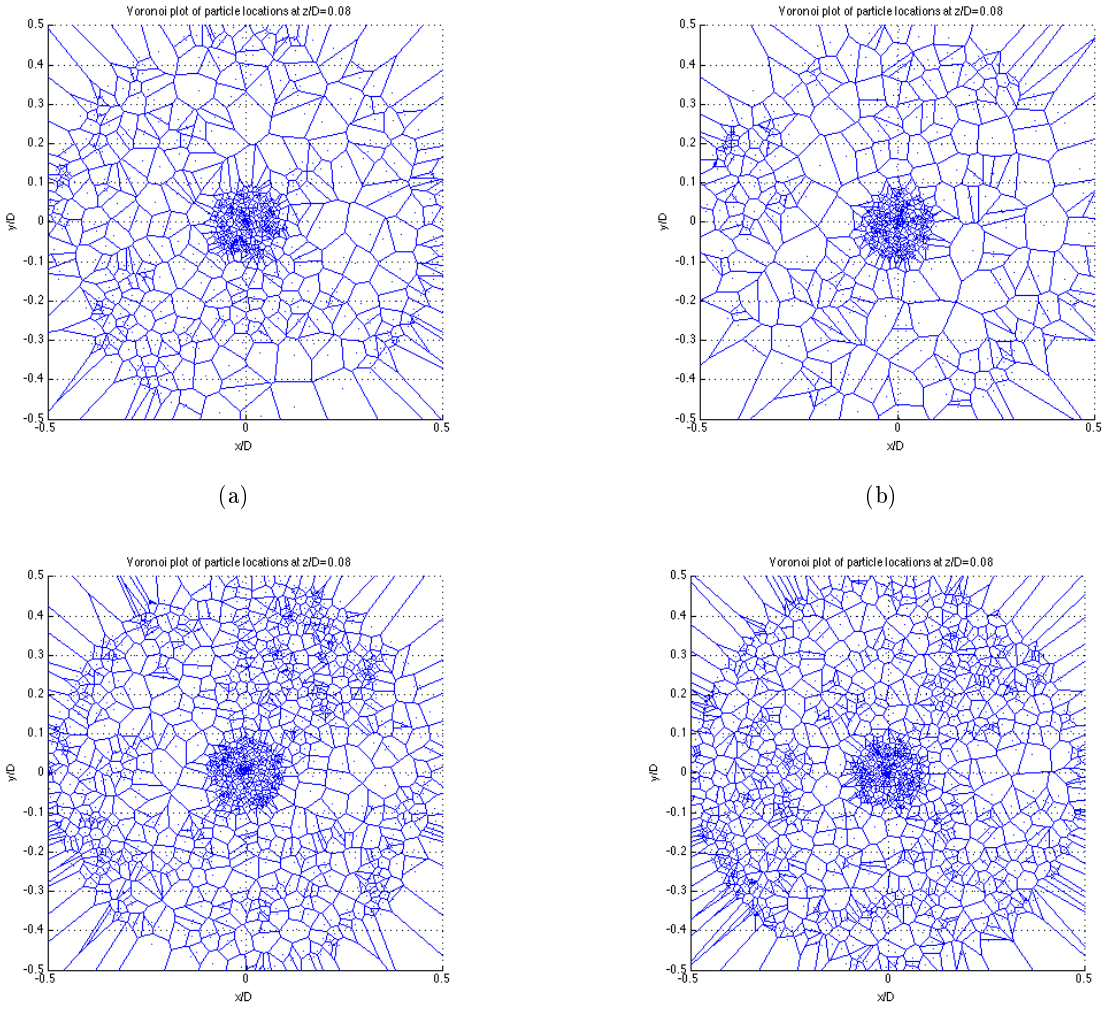

Figure 62: Voronoi plots for the $40\,\mu m$ particles at z/D=0.08 for 6 instances in time

the centreline of the distribution. In a similar manner, the *Voronoi* analysis could be extended to three dimensional space and the location of clusters be identified through the evaluation of the *Voronoi* cell volumes.

What is evident in Figures 62 to 67 is the increased level of clustering observed for the particles $40\,\mu m$ compared to the $80\,\mu m$. At the z/D=2.67 but especially at z/D=5.33 the preferential concentration of particles is clearly discernible. Of particular interest is the size of the clusters,whose largest scale appear to be of the order of the expansion tube diameter dimensions but also of note is the fact that these features/clusters persist a significant distance downstream of the step where the characteristic dimension of the dominant eddies should have attenuated significantly in size. The size of these clusters is substantially larger than those observed in DNS calculations where they are typically observed to be of the order of the *Kolmogorov* scales.

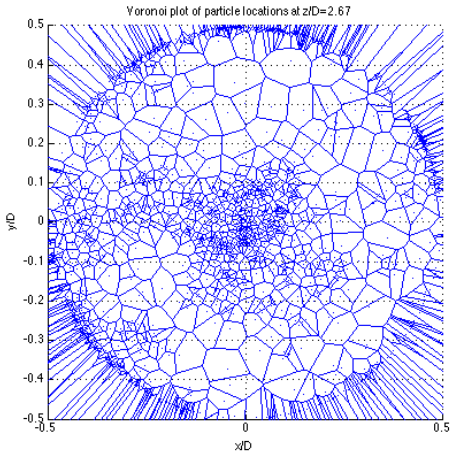

(a)

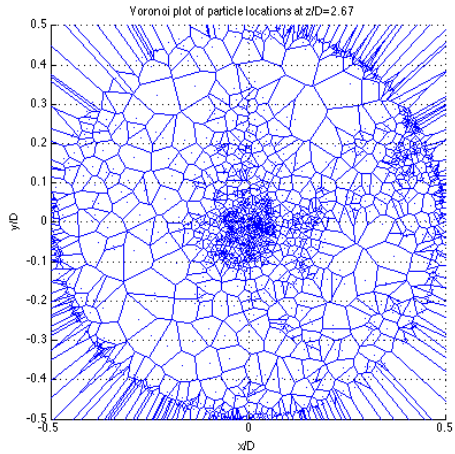

(b)

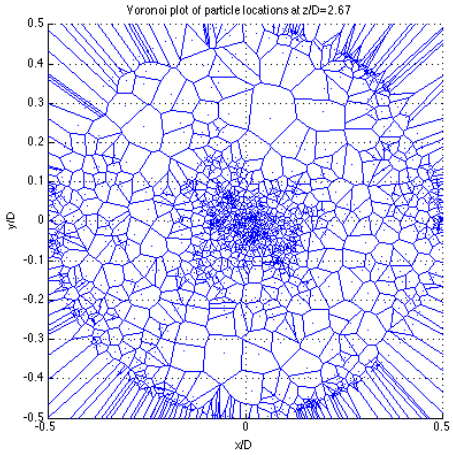

(c)

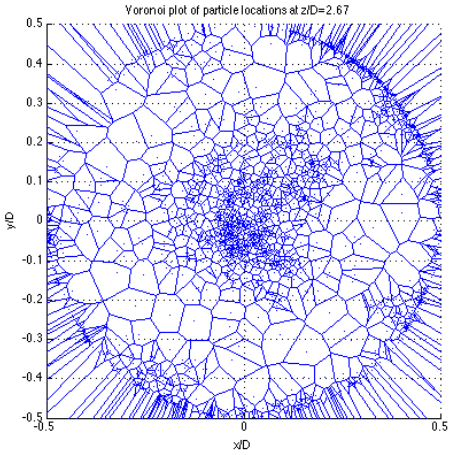

(d)

Figure 63: Voronoi plots for the 40 μm particles at z/D=2.67 for 6 instances in time

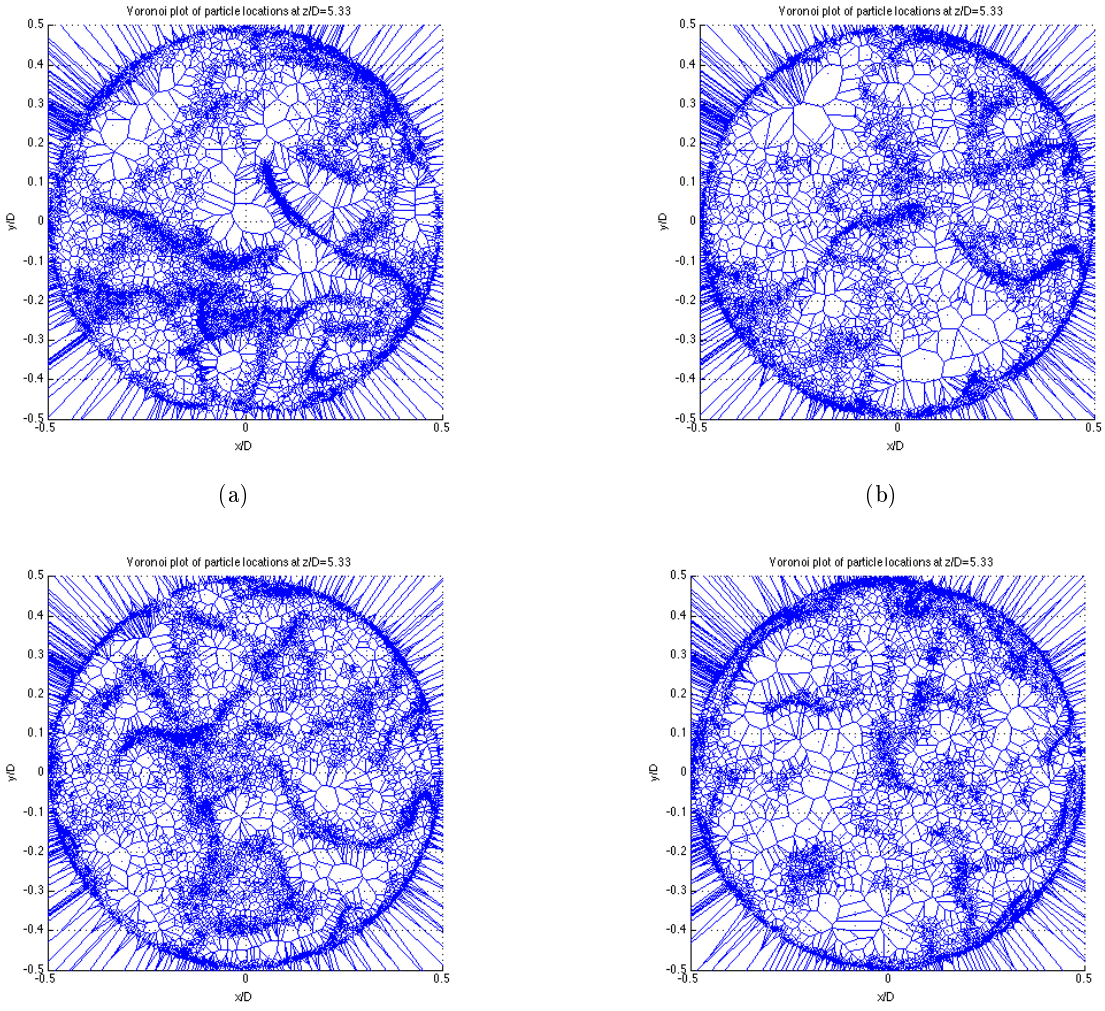

(a) (b)

(c) (d)

Figure 64: Voronoi plots for the $40\,\mu m$ particles at z/D=5.33 for 6 instances in time

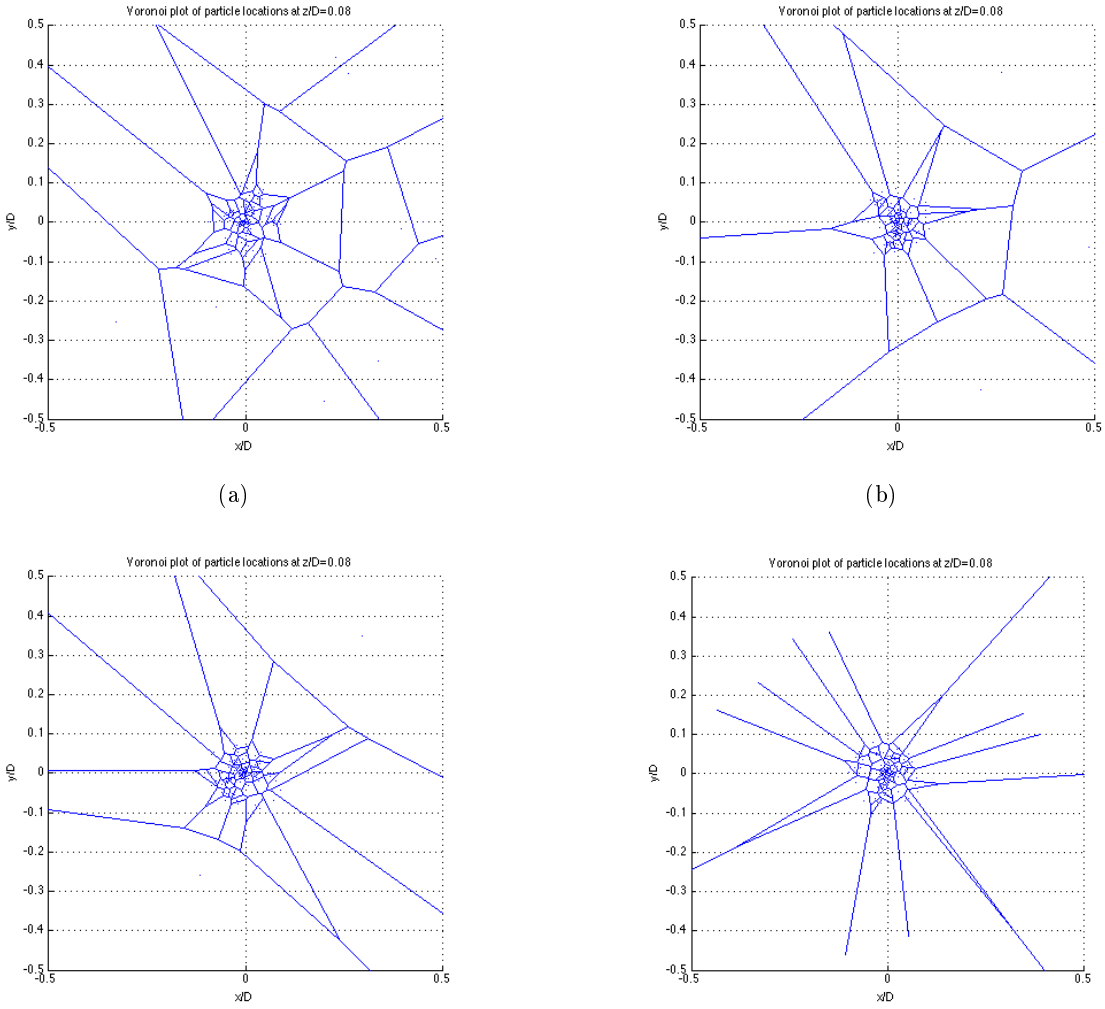

(a) (b)

(c) (d)

Figure 65: Voronoi plots for the 80 μm particles at z/D=0.08 for 6 instances in time

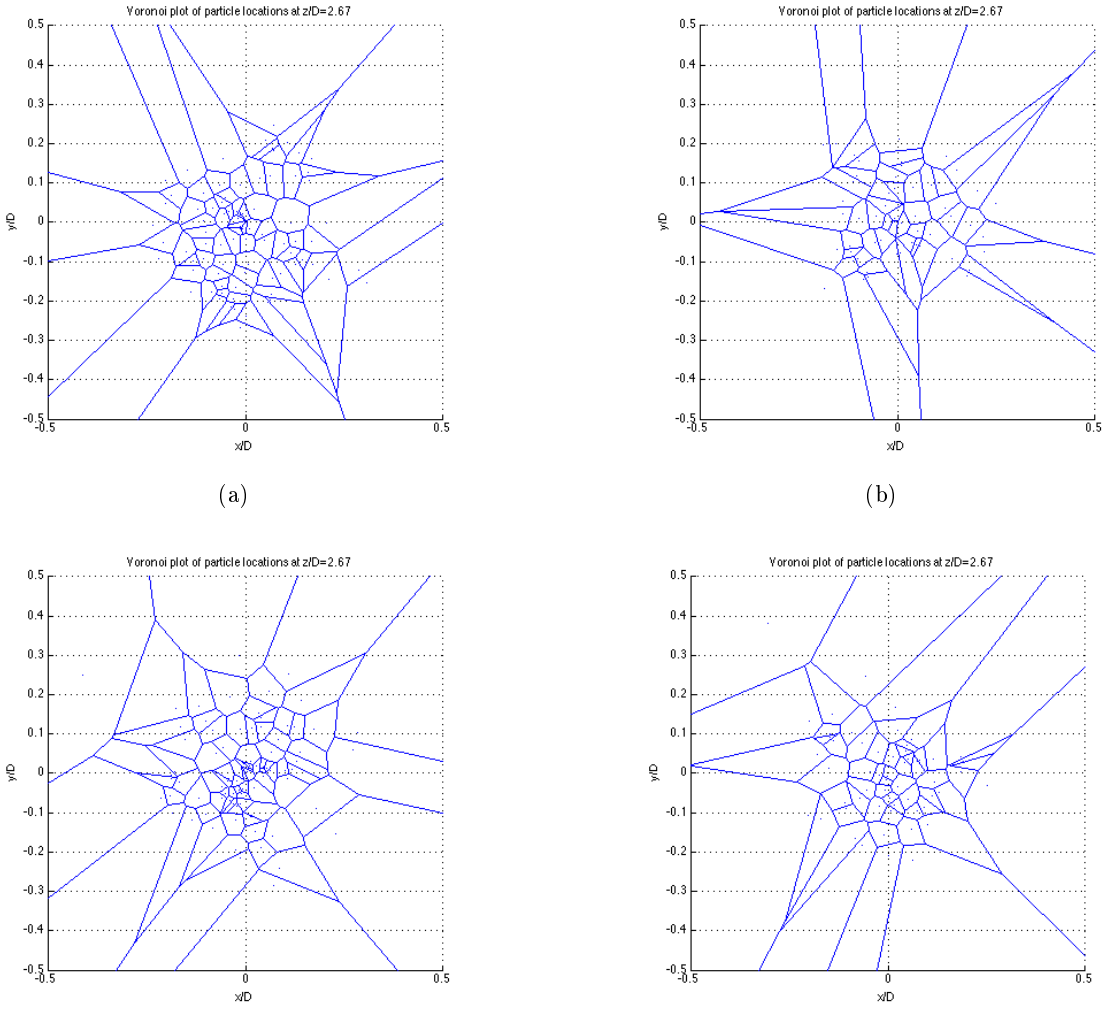

(a) (b)

(c) (d)

Figure 66: Voronoi plots for the 80 μm particles at z/D=2.67 for 6 instances in time

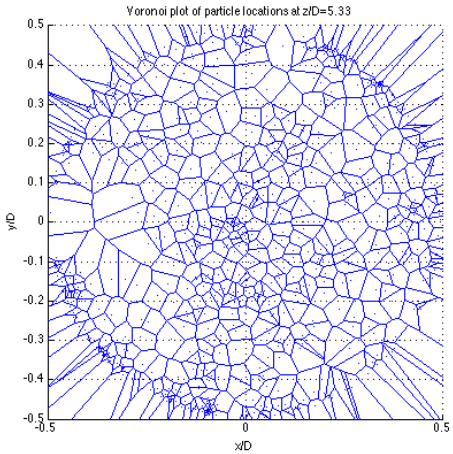

(a)

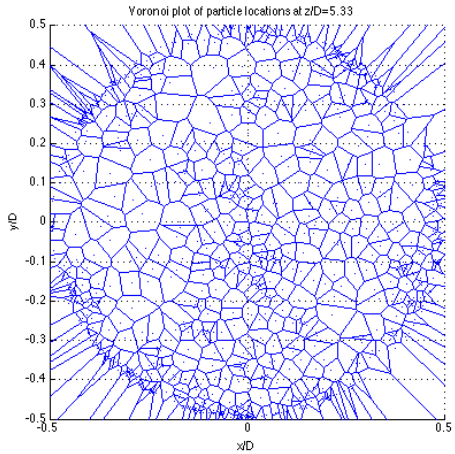

(b)

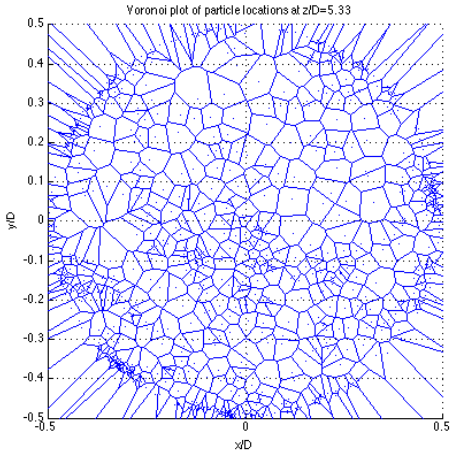

(c)

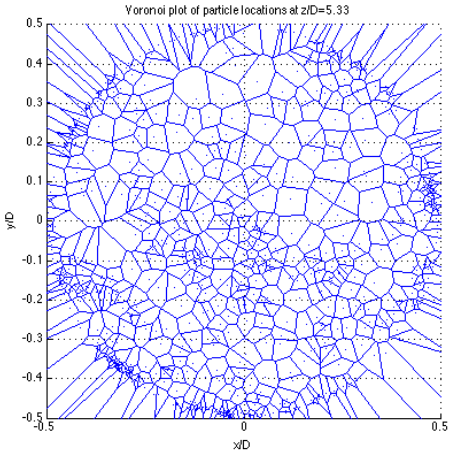

(d)

Figure 67: Voronoi plots for the 80 μm particles at z/D=5.33 for 6 instances in time

3.6 Summary

Chapter 3 presented a summary of the work performed regarding the LES calculations. This included the development and validation of the required Eulerian-Lagrangian solvers for the RANS and LES calculations within the openFOAM environment. Then the sudden expansion test case was introduced along with an investigation to determine the required mesh resolution. This was followed by a validation of the solver's capabilities; first in terms of the Eulerian phase through the comparison of the calculations and the experimental data showing acceptable agreement, for th epresent purposes, between the measured quantities and predicted recirculation zones. Subsequently, the Lagrangian calculations where found to agree satisfactorily with the experimental measurements. The results demonstrate the formation of instantaneous particle clusters in the flow, observed for the $40\mu m$ particles but not for the $80\mu m$ particles. An effort was made to identify dominant vortical structures throughout the LES calculation, using enstrophy, vorticity and the 2^{nd} invariant of the velocity gradient tensor, but this posed several difficulties primarily due to the complexity of the flow. No clear correlation was identified between the location of particle clusters and these characteristics features of the gas phase. Finally, *Voronoi* analysis was used to quantify the scale of the particle clusters and indicate that their dimensions, in the cross-stream direction, could be of the order of the expansion tube radius. This is much larger than the cluster dimensions reported in the literature from DNS calculations, which tend to link the size of the clusters to the *Kolmogorov* scale.

4 Implementation of Kinematic Simulations within openFOAM

The objective of this chapter is to introduce a novel method for modeling flows at engineering and atmospheric Reynolds numbers in a coupled Eulerian-Lagrangian framework. The stimulus for this work is the inability of the currently available modeling tools to predict certain phenomena in the behavior of the dispersed phase that have been observed experimentally. Namely, particle preferential concentration and particle trajectories in recirculation zones and regions of flow separation. The consequences of these limitations are that the non-uniformity/in-homogeneity of particle distributions observed experimentally at high Reynolds number flows are not observed in the corresponding modeling efforts. Regions of high strain and/or high vorticity result in regions where particle voids and clusters are formed. The implication is that although the statistical approach adopted by most of the presently available tools may result in acceptable predictions of mean quantities, when non-linear mechanisms such as combustion are being modeled there can be significant discrepancies. This is especially true when pollutant formation and prediction is concerned. Many of these discrepancies may be attributed to the use of mean quantities in place of the actual range of values. It may be argued that the source of the discrepancy is the accuracy of combustion models, but without accurate initial conditions for the fuel-air stoichiometry, even the most precise of combustion models would still result in significant errors. A second area where currently available models fall short is in the prediction of droplet or particle transport within shear layers and in recirculation zones. This is of primary significance when investigating the effects of particle erosion, but also, as before, when investigating the spatial distribution of particle concentrations in flows.

Direct numerical Simulation (DNS), whilst capable of predicting the aforementioned limitations, is still years away from being applicable to flows of engineering and environmental interest due to its prohibitive computational cost even at relatively low Reynolds numbers. Meanwhile, Large Eddy Simulations (LES) have only recently being adopted by industry for their modeling needs and are still considered too expensive both in terms of time and computational requirements for everyday simulations.

What we propose here is a novel dispersion model for implementation within an (unsteady) Reynolds Averaged Navier-Stokes ((u)RANS) computation. The limitation of current RANS dispersions models, for example using the two equation k-epsilon model of turbulence, may be traced back to the fact that the velocity and lengthscale of the 'computed' eddies are prescribed only from the local values of the turbulent kinetic energy and the local dissipation rate of the flow field, from which a stochastic fluctuating component of velocity interacts with the particle. There is no further flow within these computationally 'constructed' eddies. What we propose is the use of the standard (u)RANS technique for modeling the bulk of the flow field but then employing Kinematic Simulation (KS) within each such eddy in order to introduce a more realistic flow structure (an example of such a flow field with the dispersion of fluid elements is shown in the figures of the following section) for the smaller scales of the flow, which are not computed in a typical (u)RANS calculation.

In the following sections of this chapter the differences betweenthe proposed model and the industry standard will be investigated through simulated trajectories of particle pairs. First, a comparison will be made to show how the stochastic models differ on conceptual levels by

evolving a pair of fluid elements through isotropic turbulent fields. The motion of the particles is governed solely by the underlying dispersion mechanism and not by the mean flow. This will be followed by a section detailing the implementation of KS within the CFD modeling package along with details of the algorithm structure. Subsequently, particle pairs will be tracked through isotropic turbulent fields but now the models will be used as they where orignially intended –as dispersion models– prescribing fluctuating velocity components of the continuous phase to the Lagrangian phase to complement the lack of information that exists in the contiuous (Eulerian) phase from the filtering or averaging operations introduced in the modeling process.

4.1 Particle Pair Evolution In Isotropic Turbulent Fields by Stochastic Motion

In this section attention is focused on how the underlying dispersion mechanism governs particle pair separation. The task at hand requires evolving a pair of particles, in this case fluid elements, through an isotropic turbulent field and comparing the different trajectories as predicted by the G&I *'Brownian-like'* motion and KS motion. The purpose is to elucidate what would happen to the discrete phase inside an under-resolved 'eddy' if the Lagrangian solvers actually attempted to track a particle trajectory within that 'eddy' –albeit an isotropic one.

For this comparison, the implementation of the KS model was based on the version of Mallik & Vassilicos (1999) outlined in earlier sections. As the present investigation calls for the investigation of trajectories through an isotropic field, KS may be used as they were originally preented requiring minimal modifications. The minimum and maximum wavenumbers were adjusted to the characteristic and *Kolmogorov* length scales, respectively, of the aforementioned domain ($k_{min} = 2\pi/L$ & $k_{max} = 2\pi/\eta$). The particles were modeled as fluid elements and were released within a separation shorter than the *Kolmogorov* length scale, rather than being released within a time interval shorter than the *Kolmogorov time scale* as was the case for the G&I-like motion, as the two approaches are interchangeable.

For the G&I-like motion, at every instant in time the particle velocity is prescribed through random sampling of a *Gaussian* curve whose standard deviation and amplitude are determined by the local field values of the turbulent kinetic energy and the dissipation rate of turbulent kinetic energy. The DNS solver included within openFOAM was chosen to perform this simulation. However, several modifications were required. Unlike many other DNS codes, the one included within OpenFOAM is not a spectral one, rather it explicitly solves the Navier-Stokes equations, relying on a spectral method to ensure that the turbulence is not attenuated with the passage of time. The forcing is achieved through the inclusion of a force term in the momentum equations and the calculation of the required force at each cell in order to ensure that the overall/mean energy content complies with the prescribed value[69]. As such it provides a convenient basis for investigating the problem at hand, as the Lagrangian particle classes may be included with the required modifications to the code structure being relatively straightforward.

[69]This is adequate for the qualitative purpose of this section: however it would not necessarily be correct for the generation of turbulence statistics as Mashayek & Pandya (2003) mention that forcing of the large scales alone does not result in accurate replication of spatial and temporal turbulence correlations. Rather the recommendation quoted therein, following Eswaran & Pope (1988), is to apply a more flexible form of stochastic forcing based on an Uhlenbeck-Ornstein process at the lower end of the wavespace.

Similar to the procedure described earlier for the development of the fully coupled Eulerian-Lagrangian solver, the momentum equations are modified to included the source term contribution of the discrete phase. On the other hand the Lagrangian C++ classes[70], and specifically those pertaining to the G&I model, were modified to return a particle velocity rather than returning only a fluctuating component. The latter would typically be added to the particle's mean velocity commonly calculated from the cell's Eulerian quantities once drag and other forces have been accounted for. Effectively, the domain is used to generate the time varying field of turbulent kinetic energy, k, values required by the G&I model, to sample the *Gaussian* and to prescribe a velocity vector. Where this velocity vector, is calculated and prescribed at every timestep, and not only when the TCT criterion is met (for the definition see Chapter 1, Section 1.3 near the end). The velocity vector for the discrete phase is calculated by randomly sampling a Gaussian distribution whose standard deviation is determine by the local flow conditions, $\sigma = \sqrt{2k/3}$. As there is no turbulence closure model employed in this DNS-like solver –that would typically be responsible for the solution of the additional set of equations and the calculation of these fields– a final pair of modifications are required to the solver structure. These are the explicit calculation of the turbulent kinetic energy fields, k, and dissipation rate fields, ε, at every cell from the velocity field.

The computational domain used to perform the following simulations is a cube with sides of $3\,m$, an extended geometry similar to that typically used to simulate box of turbulence experiments for the investigation of isotropic turbulence flow. There are no walls in this computational domain, rather periodic boundaries. The extension of the geometry is not dictated by physical requirements but rather one necessitated by the need to qualitatively present the particle trajectories and evaluate the distance between the pair. When using a smaller computational domain the particles often reached the locations of these periodic boundaries, consequently appearing at the opposite boundary, causing the trajectories to appear discontinuous. The computational domain comprised 32^3 cells and thus the smallest scales of the flow, for the most energetic of the three cases, are not adequately resolved as the grid mesh size, l, is only half the *Kolmogorov* length scale, η. Typically a fully resolved DNS would be performed on such a domain, however the present extended geometry would require a significant increase in computational resources to adequately resolve all scales and such an investigation is beyond the scope of this thesis and, for the present section, the focus is limited to qualitative evaluations.

Sample trajectories were calculated for three different specific energy contents, $Ea = 10,\ 20,\ 30\,m^2/s^2$, and relevant information is summarized in Table 4. The timesteps were set to be a tenth of a millisecond with 5 seconds of simulation time calculated. The former ensured that the maximum *Courant* number for the FVM domain remained below a value of 0.1 . The two Lagrangian particles in this case are of identical density to the carrier fluid and of negligible diameter, effectively fluid elements, responding to changes of the surrounding carrier phase immediately. The two particles are released within a time interval much shorter than the *Kolmogorov* time scale, τ, ensuring that the surrounding flow conditions experienced are very similar and that the two trajectories remain close initially.

[70] For the remainder of this chapter the word class is a reference to the C++ terminology and not a particle size class.

Figure 68 shows a schematic of the computational domain viewed from perspective and plan views while Figures 69 to 72 depict individual realizations of the particle pair trajectories through the isotropic turbulent field. The plan views have been included to show the complexity of the trajectories through three dimensional space in a more suitable manner for the present medium. It should be noted here that the present trajectories although representative are unique. There is no reason that these should be reproducible due to the nature of the KS spectral method and the random sampling of the 'G&I-like' vector velocities however, successive simulations yield qualitatively very similar trajectories they should never yield identical ones. At this point it is important to clarify that although the comparison of this section is made for isotropic turbulent fields with the same specific energy the actual flow fields are different. The KS trajectories are computed from a purely spectral method while the 'G&I-like' trajectories are modeled in a domain that uses the FVM and spectral forcing is only employed to ensure that the turbulence does not 'die-out'. Thus although the fields are statistically similar for the KS and the 'G&I-like' calculations they are by no means identical. Perhaps the most important result that may be drawn from this qualitative comparison is not how the individual trajectories evolve through space but rather how the pair evolves.

Figure 73 shows graphs of the evolution of the magnitude of particle pair separation vector with trajectory length for the three different energy contents. Of particular interest should not be the final value of the separation vector nor necessarily the inflection points as these again would change if the simulations were repeated or if the particles were released at different parts of the domain. Rather, the interesting conclusion is that while the 'G&I-like' mechanism results in a steadily increasing separation, the KS separation is almost steady until it abruptly increases. In the first case the distance between the two particles grows at a steady rate due to the random sampling process until the two particles drift into regions where the Eulerian conditions are significantly different to cause a notable change in the extents of the Gaussian and the ensuing stochastically sampled velocity. Meanwhile the KS trajectories remain very close to each other until Fourier components of the spectral method align in such a manner to create a highly-straining region, effectively an eddy, causing the two trajectories to separate suddenly. The particle pair separations shown are not the mean square separation distance $\left(\left\langle \Delta^2 \right\rangle\right)$ but the outcome of individual realizations. For reasons outlined in Footnote 69 the spectral forcing employed for the FVM domain does not lend itself to reproducing higher-order statistics.

It should be noted that although the KS trajectories appear to be shorter in length both the spectral method and the FVM DNS were calculated for the same number of timesteps and differences in length are attributed to the fact that the more convoluted KS trajectories result in the particles staying closer to the centre of the isotropic field where velocities are smaller. The importance of modeling realistically the evolution of the particle pair separation is that it is a prerequisite for the accurate prediction of clustering.

Initially the more convoluted KS trajectories were believed to be a result of miscalculating the largest wavenumber however this proved to not be the case; as halving the maximum wavenumber still resulted in a significantly more convoluted trajectory than that predicted by the FVM DNS. It was found that the trajectory complexity was sensitive to the number of modes that the wavespace was being decomposed into. This is reasonable as the number of modes (or Fourier

Table 4: Information on the Isotropic Turbulence Domain

Isotropic Turbulent Field, $Ea = 20\,m^2/s^2$	
representative velocity for larger scales, U	$1\,m/s$
characteristic length, L	$3\,m$
kinematic viscosity, ν	$0.0025\,m^2/s$
Reynolds number, $Re \sim UL/\nu$	120
integral length scale, $l \sim L\,Re^{-1/2}$	$0.27\,m$
cell size, Δx	$0.094\,m$
mean dissipation rate,[71] $\langle\bar{\varepsilon}\rangle$	$0.0105\,m^2/s^3$
Kolmogorov length scale, $\eta \equiv (\nu^3/\varepsilon)^{1/4}$	$0.035\,m$
Kolmogorov time scale, $\tau \equiv (\nu/\varepsilon)^{1/2}$	$0.5\,s$

components) are to a spectral approach (and hence gridless method) what mesh density is to the FVM.

An additional validation of the implementation of the KS method within this work is provided in Figure 74. The figure shows that by repeating the particle particle pair evolution experiments in the spectral space allows the t^3 law –discussed in the literature review– to emerge. Multiple realizations of the KS trajectories were performed and the particle pair separations were then averaged after 2, 5,10 & 50 realizations. Figure 75 shows what these averaged trajectories look like in space (although for this schematic it was necessary to impart an initial velocity to the particles to avoid the trajectories appearing like a bowl of spaghetti). Effectively, the particle pairs are evolved through turbulent isotropic fields that are statistically identical but might be very different in detail as in each realization of the spectral space the Fourier components and the orthogonal wavemode vectors are different. Here the t^3 dependence is observed for all three levels of isotropic field energy content tested, although an estimation of the *Richardson* constant would require significantly greater number of realizations to be performed and is beyond the scope of this work.

At this point it might be necessary to re-iterate that this comparison was not intended to be a DNS study and should not be confused with one because the range of scales are inadequately resolved. Rather, some approaches from DNS were borrowed and modified in order to generate an isotropic turbulent field where the turbulent kinetic energy and dissipation rate were known and thus allowed sample trajectories for 'G&I-like' motion to be constructed. At the same time the lack of small scale resolution is not expected to significantly change the shape of the 'G&I like' trajectories since the smaller scales would contribute to smaller fluctuations and not result in significant changes of the main features of the trajectories. Finally, the repetition of the DNS-like calculations for the investigation of the particle pair separation statistics is too costly to be performed within this thesis.

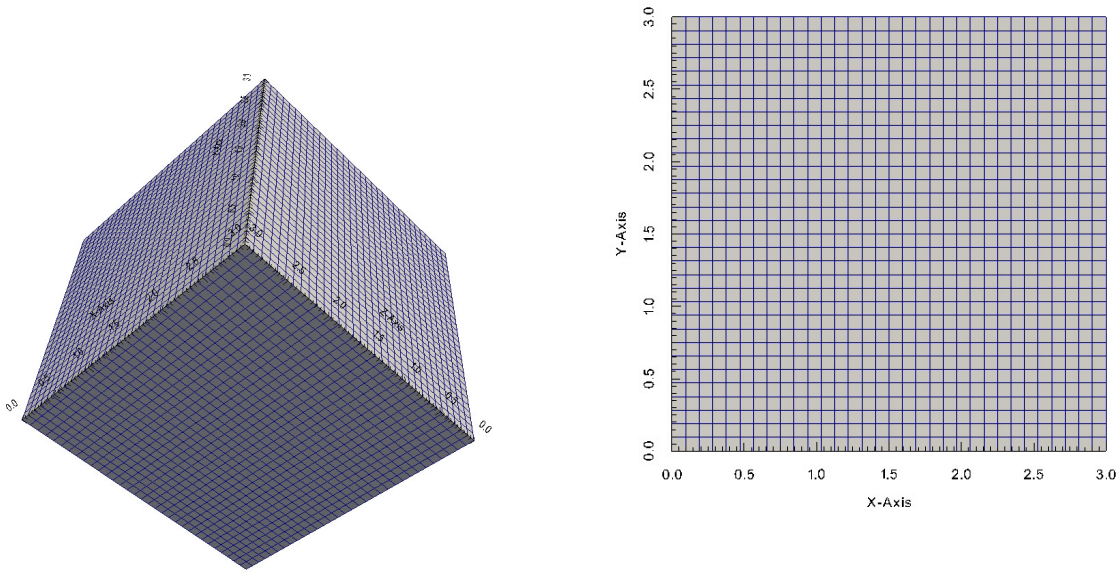

(a) Perspective view

(b) Plan view

Figure 68: Domain details

4.2 Kinematic Simulations implementation within openFOAM

The premise for the proposed model is to allow the standard (u)RANS implementation of the modeling package to treat the bulk flow and to introduce KS for modeling the effect of the fluctuating components of the Eulerian phase –absent in the Reynolds Averaged approach– on the Lagrangian phase. This is typically treated with some version of the Gosman & Ioannides (1981) dispersion model (GI). The implication is that we are using the (u)RANS approach to model the mean and larger scales of the flow (of the order of the integral scales) and only for the Lagrangian phase, will we introduce KS to provide what we hope will be an improved interpretation of the turbulence at the inertial and dissipative ranges of the energy spectrum.

We chose to implement the proposed model within the openFOAM framework due to the relative transparency of the code structure and its open source nature. The coupled unsteady Lagrangian-Eulerian solver for incompressible flows developed within the openFOAM package, and used here, was presented and evaluated in the Chapter 3. Once again the object oriented structure of openFOAM aided in the development and implementation of the proposed model, as it was implemented as a dispersion model using the same class structure that was used for the GI model in the compressible versions of Eulerian-Lagrangian solver.

The version of KS implemented follows closely that of Mallik & Vassilicos (1999) and Maihy & Nicolleu (2005) and the algorithm specifics will be presented subsequently. However, some differences exist between the original KS and the implementation here, namely that for every fluid element evolved through the spectral field only one realization is performed and that the range of the wave-space modeled needs to be extended over several decades of the wavespace to reflect the turbulent conditions of the selected geometry/model. The latter of the two is a

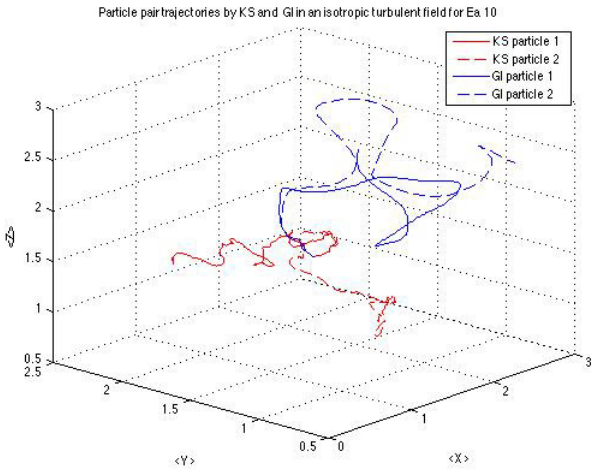

(a) Perspective view

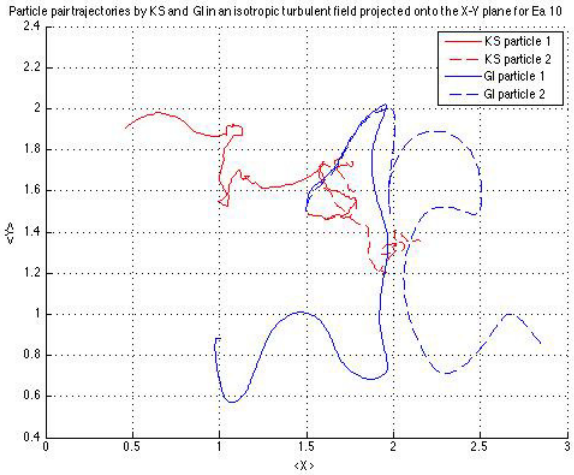

(b) XY-plane

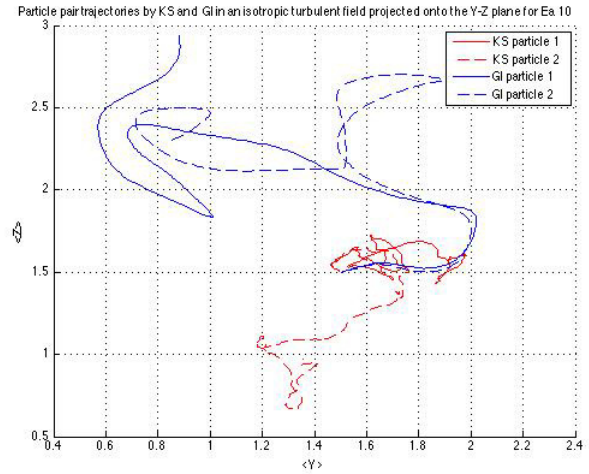

(c) YZ-plane

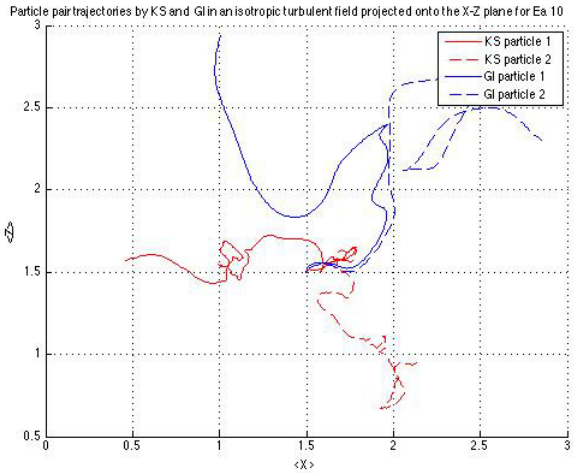

(d) XZ-plane

Figure 69: Particle pair trajectories by 'G&I-like' motion and KS in blue and red respectively, for $Ea = 10\,m^2/s^2$

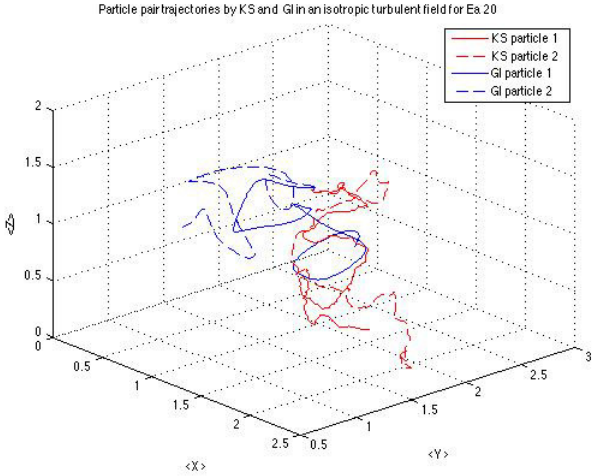

(a) Perspective view

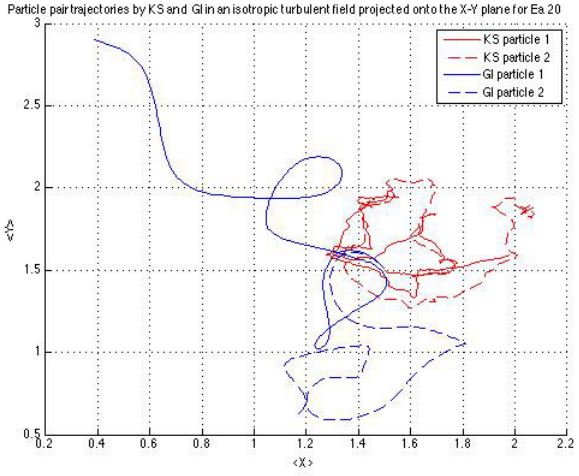

(b) XY-plane

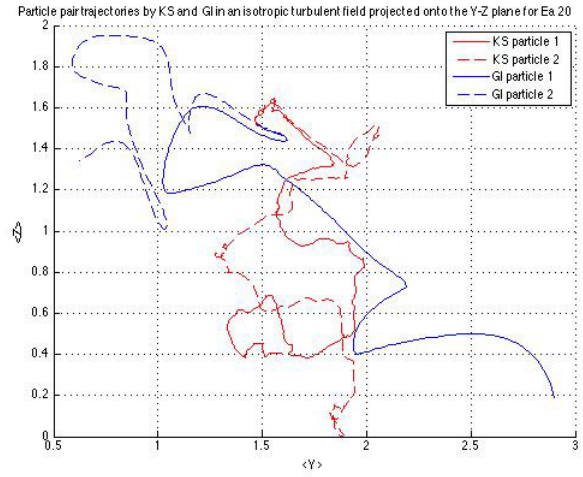

(c) YZ-plane

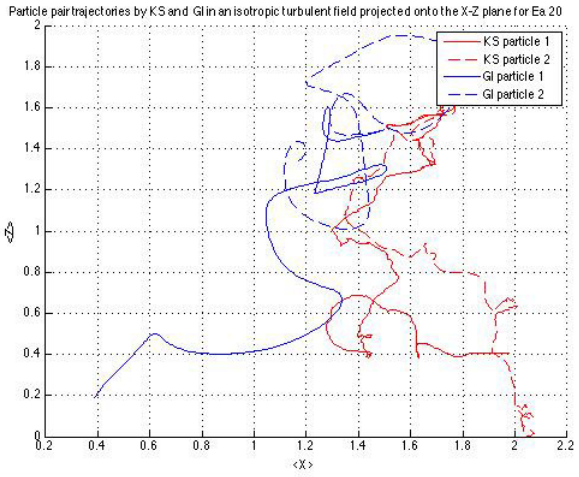

(d) XZ-plane

Figure 70: Particle pair trajectories by 'G&I-like' motion and KS in blue and red respectively, for $Ea = 20\,m^2/s^2$

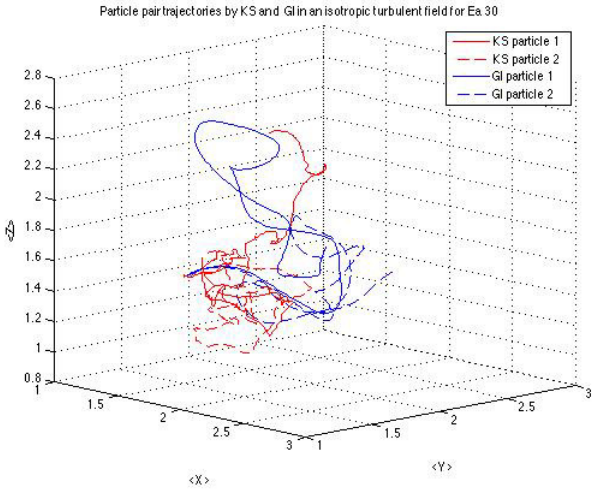

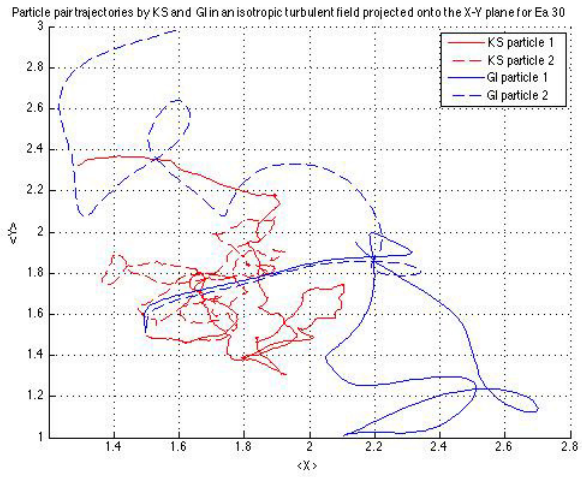

(a) Perspective view

Figure 71: XY-plane

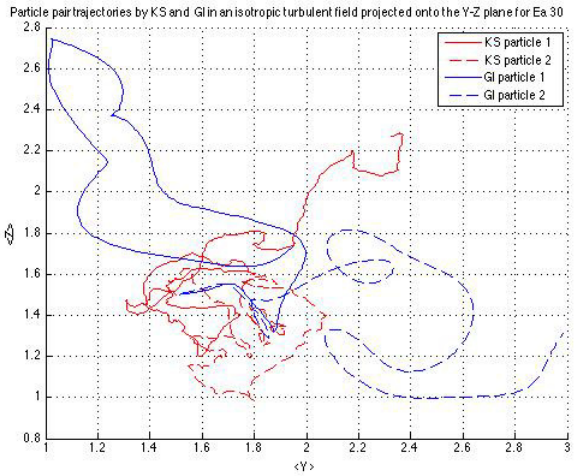

(a) YZ-plane

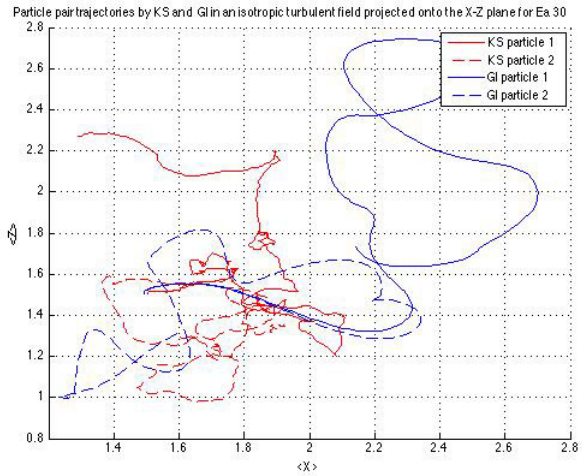

(b) XZ-plane

Figure 72: Particle pair trajectories by 'G&I-like' motion and KS in blue and red respectively, for $Ea = 30\,m^2/s^2$

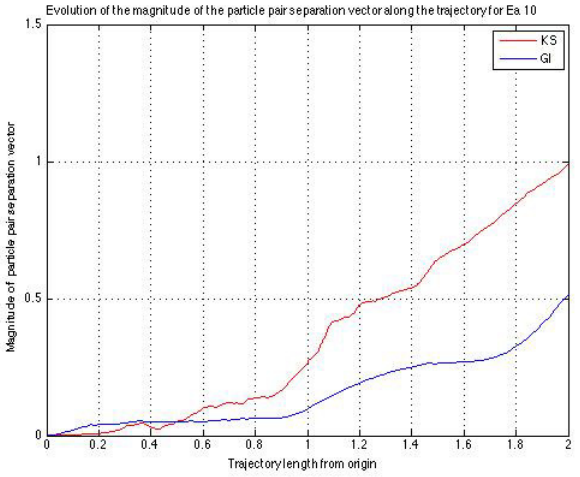

(a) for $Ea = 10\,{}^{m^2}/_{s^2}$

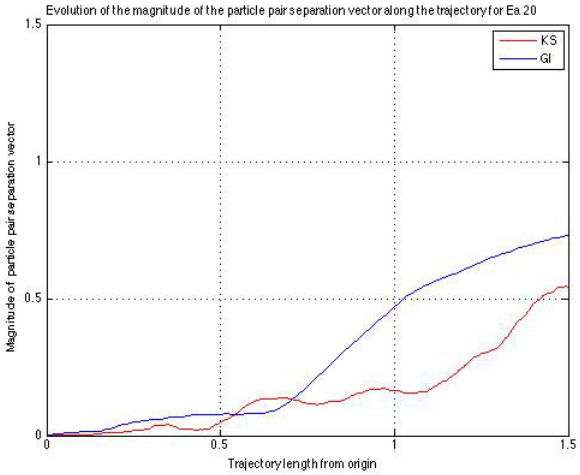

(b) for $Ea = 20\,{}^{m^2}/_{s^2}$

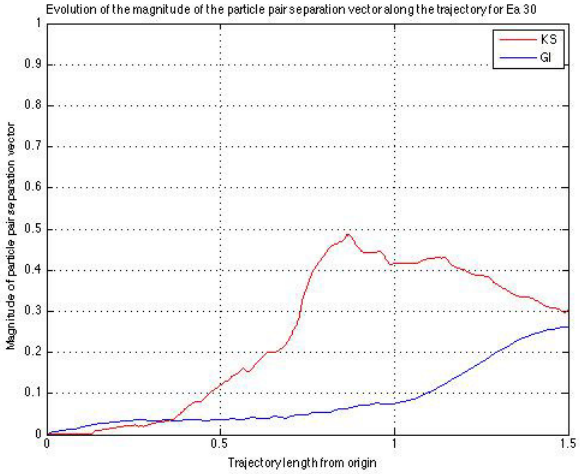

(c) for $Ea = 30\,{}^{m^2}/_{s^2}$

Figure 73: Evolution of the magnitude of the particle pair separation vector by 'G&I-like' and KS models

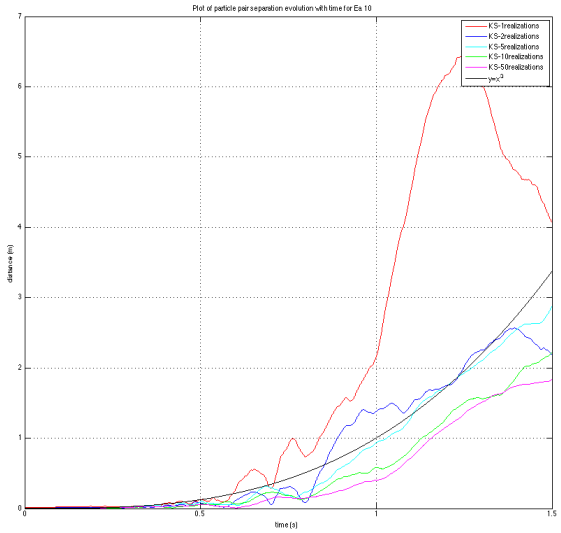

(a) for $Ea = 10\,{}^{m^2}/_{s^2}$

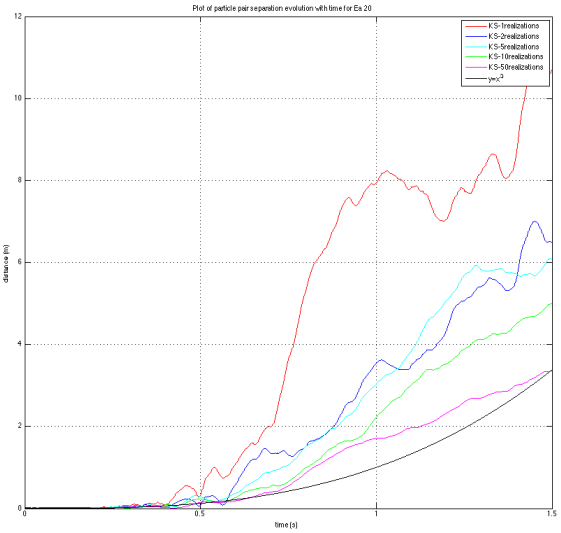

(b) for $Ea = 20\,{}^{m^2}/_{s^2}$

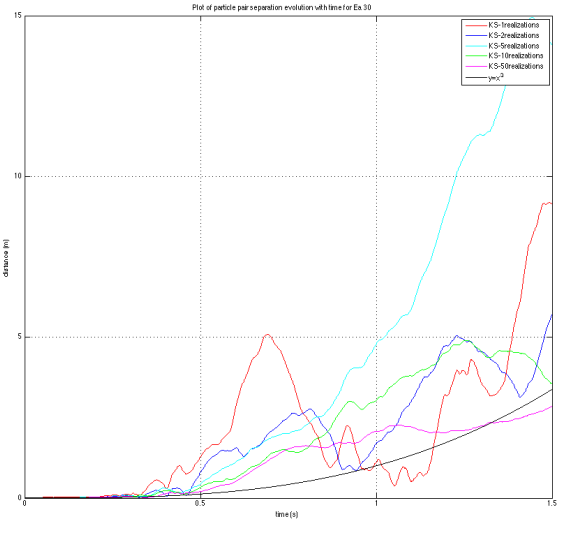

(c) for $Ea = 30\,{}^{m^2}/_{s^2}$

Figure 74: Evolution of the magnitude of the particle pair separation vector with an increasing

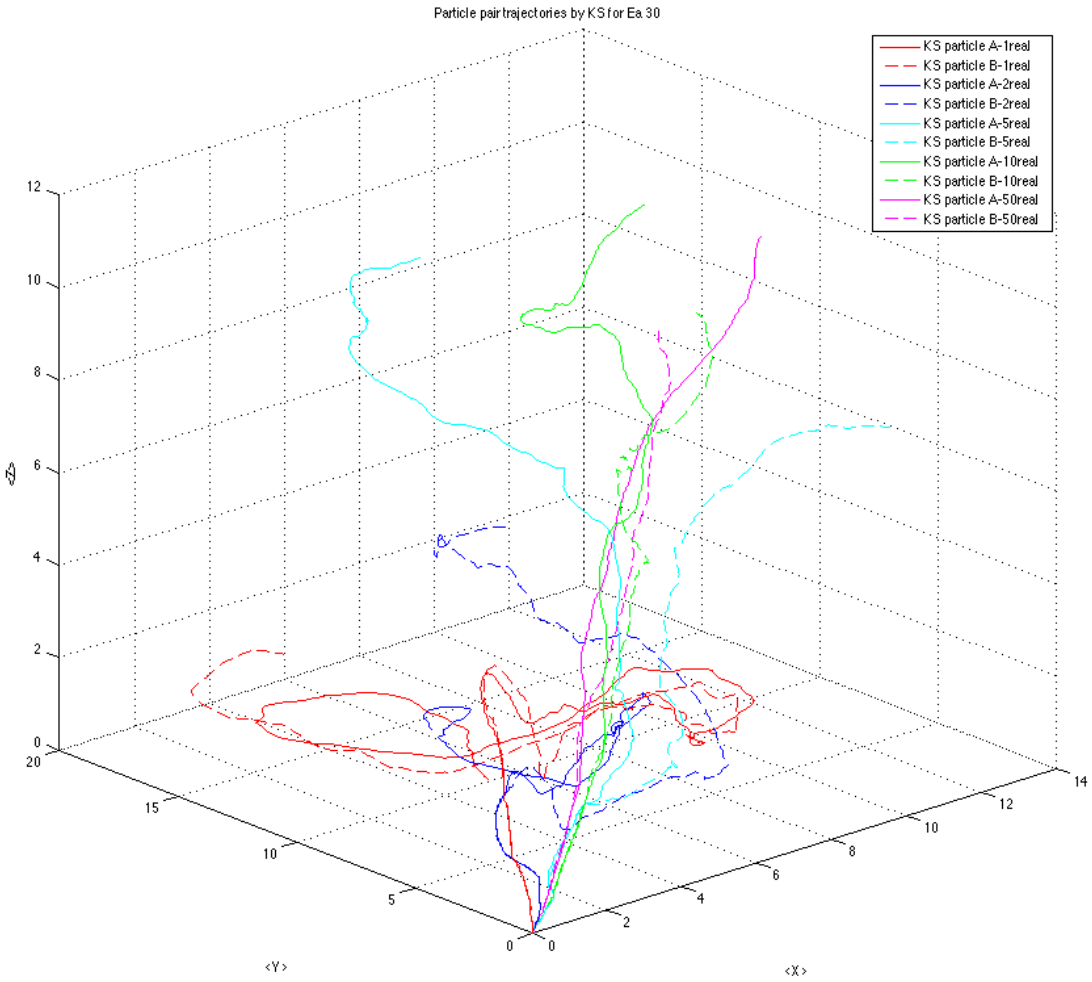

Figure 75: Averaged particle pair trajectories from KS for $Ea = 30\,m^2/s^2$ after 1,2,5,10 & 50 realizations

logical extension of KS, when used in such a hybrid form. In order to generate appropriate fluctuating velocity components for the averaged or unresolved scales, these should be generated from turbulent like fields that are representative of the actual turbulent flow conditions (namely the intensity and extent of length scales) present in the domain in question. The former of the two is justified, since the purpose of the KS implementation is not necessarily to generate accurate turbulent statistics but rather, a more realistically generated instantaneous particle velocity. While the sheer number of particles introduced into the model, thanks to the large mass loadings of the dispersed phase, results in a sufficient number of independent samples for generating accurate statistics for comparison with the experimental results.

The conditions for selecting whether a particle is prescribed a fluctuating component were detailed earlier in the section on dispersion models and are identical to the implementation of the Gosman & Ioannides (1981) model included in the openFOAM distribution, which uses the updated constants of Shuen *et al.* (1983). The length of time a particle evolves through the KS field is also determined at this stage by comparing the particle relaxation time with the eddy turnover time (or more precisely the TCT) and then allowing it to move through the KS field for an integer number of time steps. Due to the relatively small time steps required for the uRANS implementation, this means that the vast majority of particles progress for only a single or a few time-steps[72] and only the particles that are determined to be trapped within an eddy will undergo tens of KS operations.

At this point it is necessary to clarify that although the initial intention was to alter the particle position in addition to the particle velocity, as predicted by KS, for each individual particle this posed some complications. A problem arises, as moving the particle from one cell into another farther downstream constitutes a violation of the conservation equations unless the movements are accounted for through inclusion of source terms in the momentum equations of the Eulerian phase. It might appear that the solution is trivial and simply requires the introduction of additional corrector steps in the solution algorithm, ensuring that particle presence has been accounted for through inclusion of source terms in the Navier-Stokes. However, this would still result in a falsely coupled Eulerian-Lagrangian solver, since the cells in between the original and final particle position would not have been altered accordingly. By this we mean that the Eulerian field would be coupled to the Lagrangian in the originating and terminating cells, but not the intermediate cells that lie along the particle trajectory. An alternative solution would be to reduce the Lagrangian time step to such a size that one could ensure that the vast majority of particles would raverse only from one cell to the neighboring in the allocated time. This, in turn, would ensure that the conservation equations are not violated anywhere. At the same time, however, this would increase the computational requirements significantly and the net effect would be of prescribing solely a particle velocity rather than significantly changing the particle position, since it would move only to an adjacent cell. Provided the number of particles were small, the code had enough numerical damping to account for this violation of conservation laws. However, there was no guarantee that the same would be true when the mass loadings were increased to the desired levels.

[72]Note that we are now discussing about KS time steps and these usually are smaller than the uRANS by at least an order of magnitude.

It was decided to adopt the robust approach of prescribing solely a fluctuating velocity generated by a KS field for the following reasons. By comparing the particle trajectory generated by the KS with the size of the originating cell, it was seen that for most particles the computed trajectories were of the same order as the grid dimensions, if not smaller. Only for a very small number of particles did the computed KS trajectory result in a final particle position several cells away.The small length of the computed trajectories is not a limitation of the KS method but rather a result of the small time step imposed by the requirement for uRANS framework. Given a larger time-step, typical of uncoupled RANS simulations, the computed KS trajectories would be significantly longer and in an uncoupled framework the presence of source terms in the Eulerian phase is not an issue and with very minor modifications the developed model may be adapted to such use.

An additional benefit of prescribing solely a fluctuating velocity is that the model may be implemented with little modification into existing software packages, provided that they already include some version of the commonly employed dispersion models. For the reasons mentioned above, it was determined to adopt the more physically sound approach of prescribing only a velocity fluctuation, at least for the present fully-coupled version of the model, and not to include a 'forced' particle location, avoiding altogether any issue of violating any conservation principles.

4.2.1 Version A

The first implementation calls for selecting the extent of the wavespace modeled from either turbulence scaling arguments or, ideally, from an energy spectrum measured experimentally or generated from an LES computation. From this spectrum one can then determine the extent of the inertial range and input to the KS model, in a sense it is a 'hardcoded' version. However, because we have adopted a field average range for the scales being modeled through KS, scaling is required to bring these generated velocities to the appropriate magnitude for every location of the Eulerian flow field. The scaling of the fluctuating component generated is achieved through calculating the value of the Turbulence Intensity (TI) for the cell in which the particle lies. This approach generates suitable results and has the desired qualitative effects as will be presented in the following sections. An additional benefit of this approach is that, with a few modifications to the code, the wavemodes need only be generated once at the beginning of the computation and then the orthogonal vector components would be chosen at random for each step. Figures 76 & 77 depicts flowcharts for the version of the KS implementation.

4.2.2 Version B

Additional modifications were implemented in order to remove the requirement for user input at the case-setup stage. First, the scaling by the local value of Turbulence Intensity is removed. Although a physically sound scaling argument, it is not the sole scaling parameter that can be formulated. By removing this step the robustness and universality of the proposed method is improved as the performance of the model is no longer subject to the selection of the particular scaling argument over an alternative. The scaling is replaced by sampling the local value of the turbulent kinetic energy, modifying the energy content of each generated KS, adjusting the peak

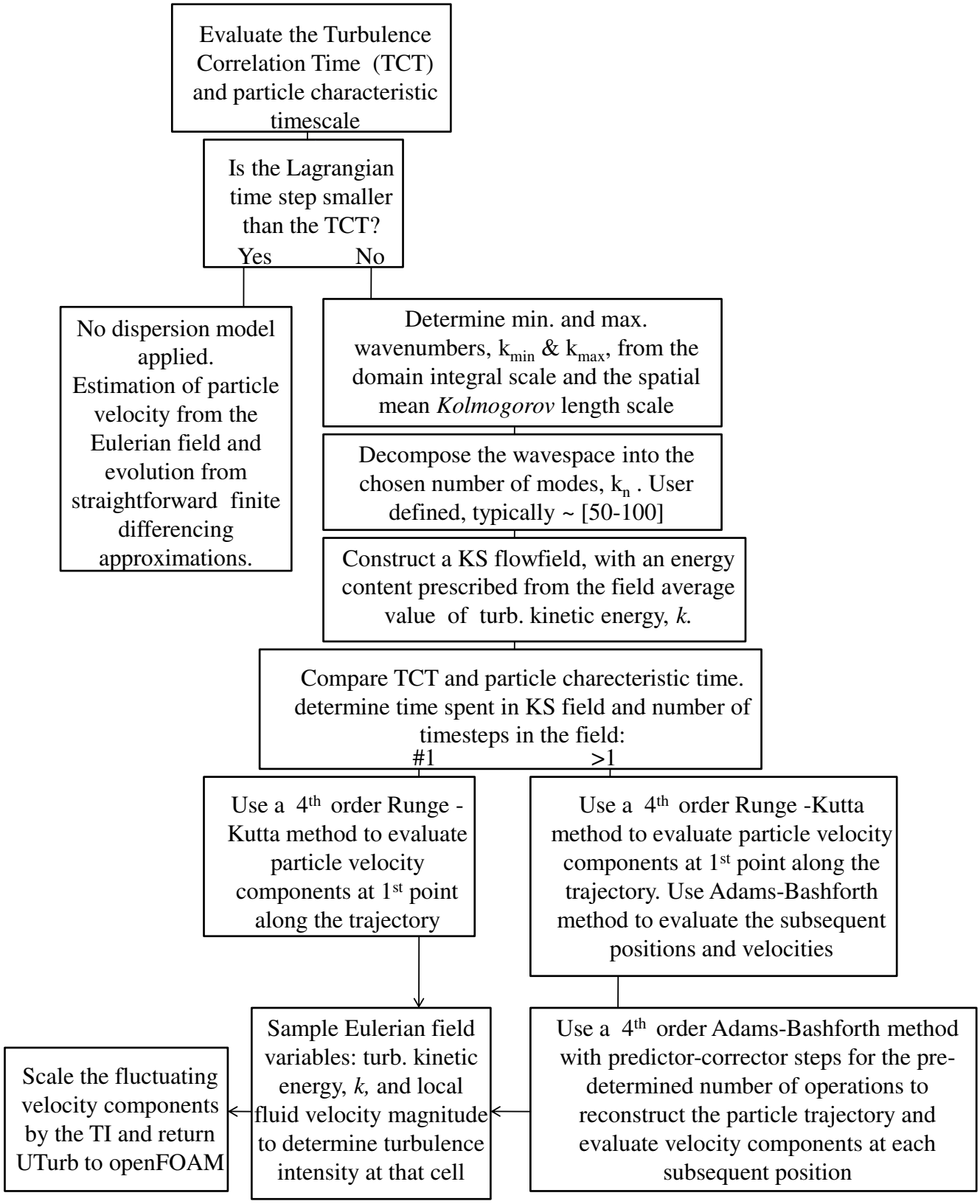

Figure 76: Flowchart for KS version A (descriptive)

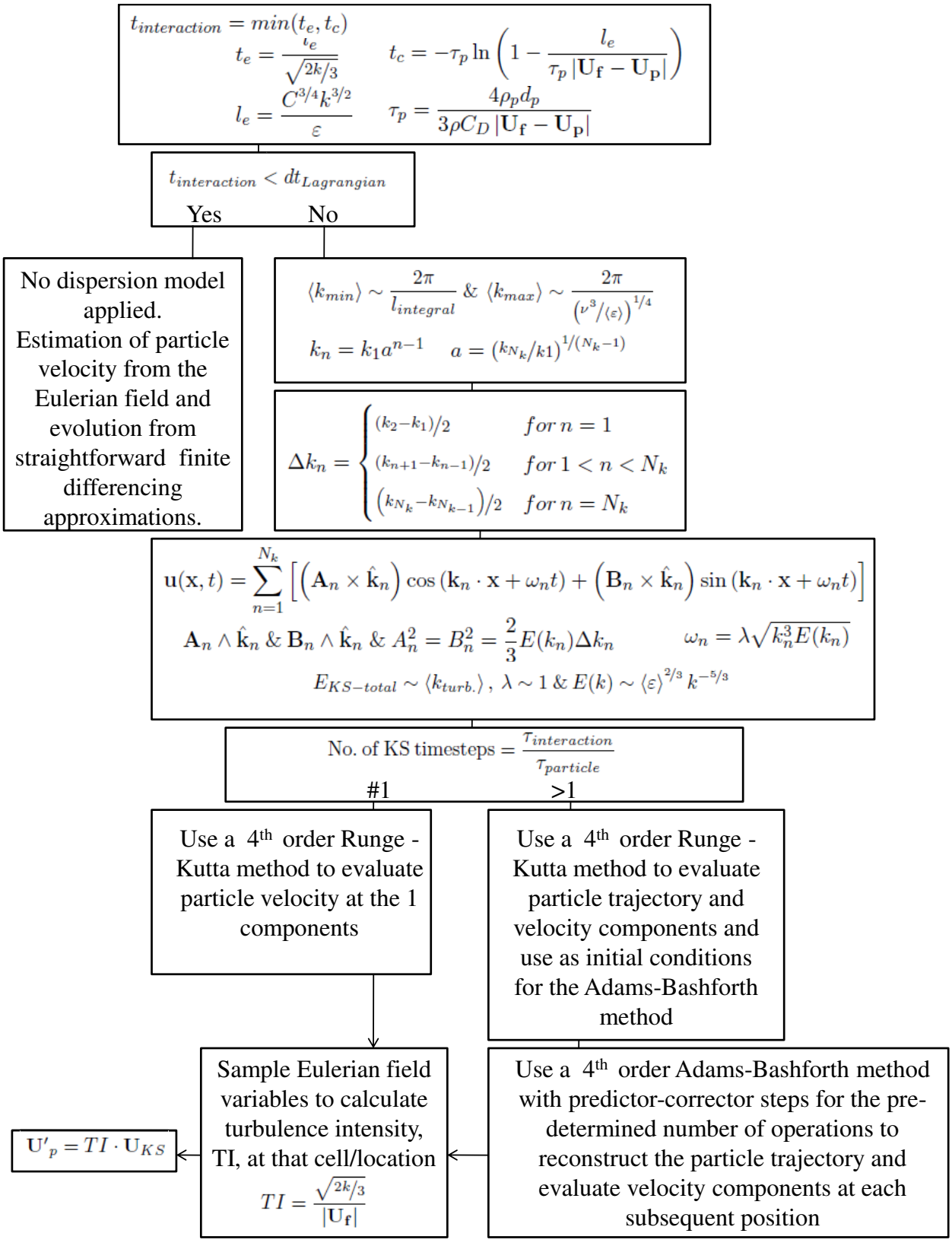

Figure 77: Flowchart for KS version A (mathematical definitions)

of the turbulent energy spectrum. Additionally, alterations include a wavespace range for the KS method individually selected for every particle based on the local Eulerian field attributes. The smallest wavenumber, k_{min} is determined from the size of the 'eddy' with which the particle has been determined to interact and the largest wavenumber, k_{max} is determined from the size of the Kolmogorov scale, estimated from the local value of the dissipation rate of turbulent kinetic energy, ε. These modifications in turn allow the model to be used on a much greater range of problems, as no prior knowledge of the flow conditions is required whilst at the same requiring significantly less user input. Flowcharts for the process are shown in Figures 78 & 79.[73]

4.3 Particle Pair Dispersion in Isotropic Turbulent Fields

The purpose of the following section is primarily to elucidate, in a qualitative sense, the differences between the proposed KS and the widely used G&I dispersion models in a simple, yet still academically interesting, flow. This is done through the presentation of representative particle trajectories in isotropic turbulent fields. In all cases, the pair of particles is released at the center of the domain and evolved through the flow field. In the following section a comparison is made, namely of how the particle pair trajectories differ when implemented as dispersion models within OpenFOAM. This exercise is useful to provide qualitative representation of the difference between the two models on a simplified computational domain, as the sudden expansion test case does not lend itself to such a purpose.

4.3.1 Kinematic Simulations implemented as a Dispersion Model - Coupling with openFOAM

The following section serves to show differences between the proposed phenomenological model, now integrated within the openFOAM environment, against the standard implementation of the G&I model for fluid elements and inertial particles in an isotropic turbulent field. Once again, the purpose is to provide a qualitative representation of how the particle trajectories differ in a simple geometry and for a limited number of particles. This is because the large number of particles and complicated geometry of the axi-symmetric sudden expansion test case make such a comparison unnecessarily complicated.

In Figures 82 & 83, comparisons are made for particle pair dispersion using the G&I model, the proposed KS model as well as trajectories calculated with the use of no dispersion model for inertial particles, $80\mu m$ in diameter with a density equal to that of water, with intra-particle release times much shorter and greater than the *Kolmogorov* time scales. Additionally, representative streamlines for the isotropic turbulent field are shown in Figure 81.

This comparison also makes use of the same FV computational domain described earlier with the details pertaining to the Eulerian phase remaining unchanged but with modifications to those of the Lagrangian phases. The Lagrangian class are now included in the original unmodified form; the G&I implementation is the standard one included within the openFOAM modeling environment; while our implementation of the KS model is included in an identical manner to

[73] The use of of the Adams-Bashforth & Runge-Kutta methods followed the approach of Malik & Vassilicos (1999). For the intended application of KS these higher order methods could probably be replaced with 'quicker' methods.

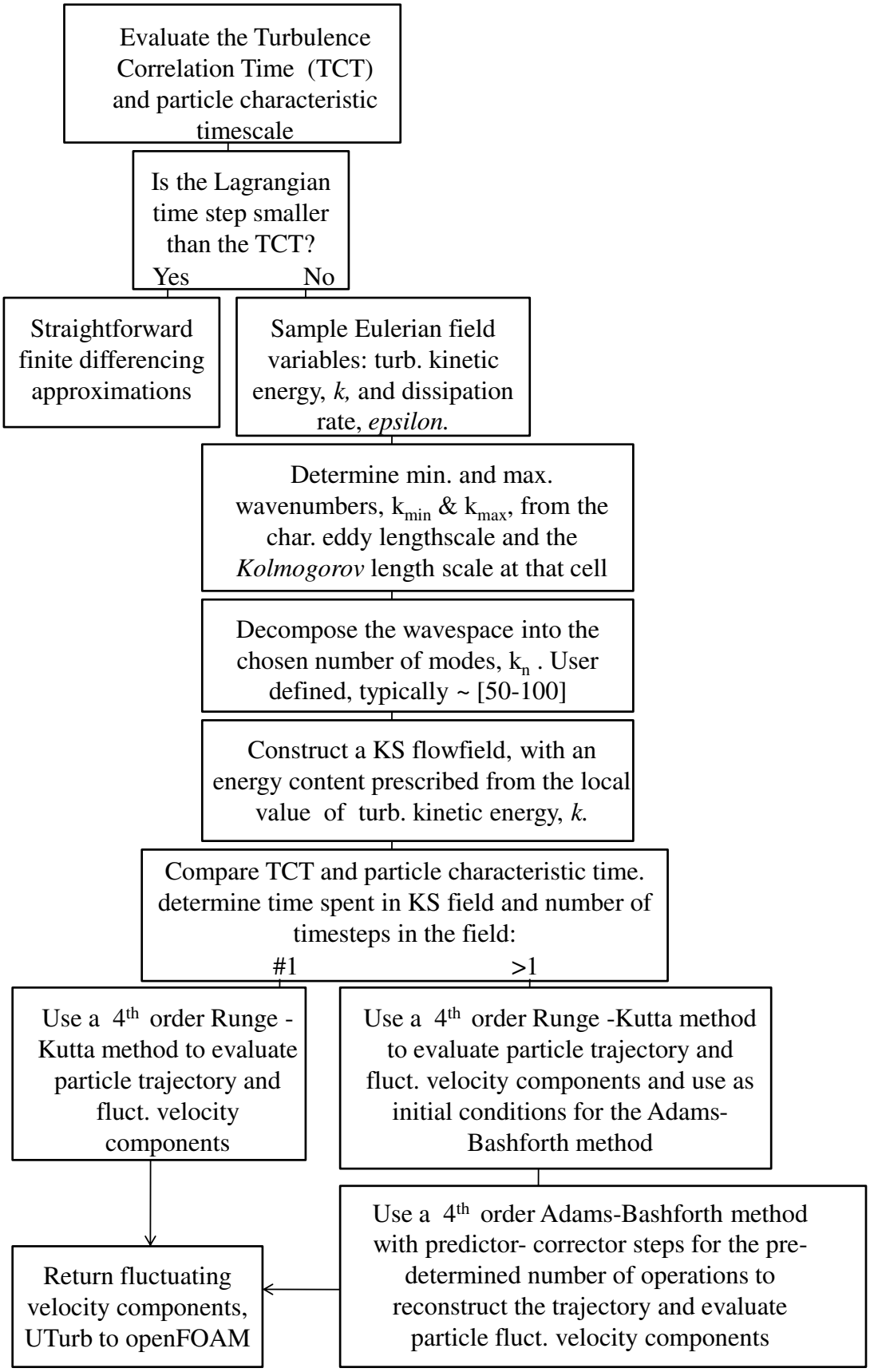

Figure 78: Flowchart for KS version B (descriptive)

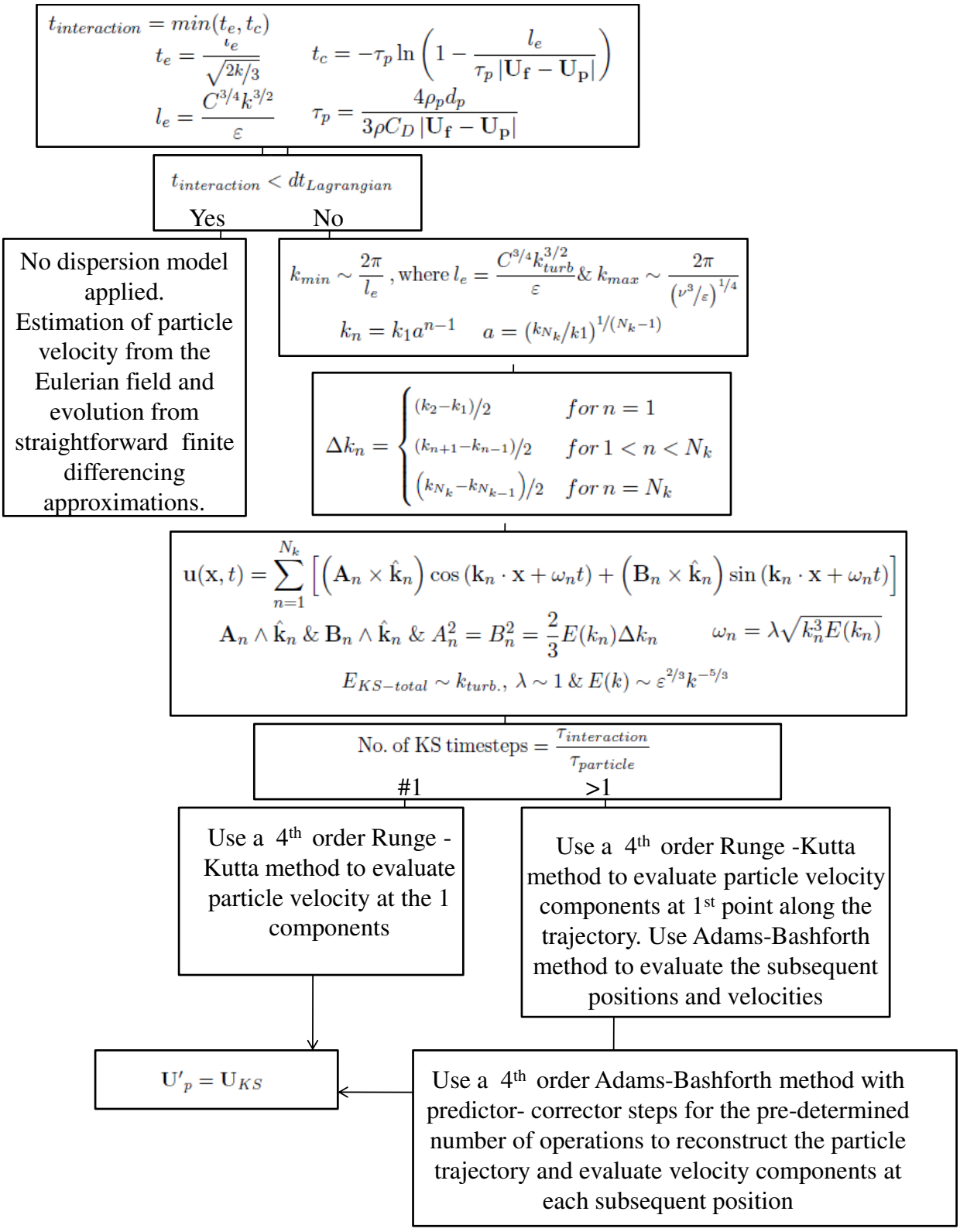

Figure 79: Flowchart for KS version B (mathematical definitions)

that described at the beginning of this chapter (KS-B) in the section regarding the integration of the KS model as a dispersion mechanism in the coupled transient incompressible Eulerian-Lagrangian solver. That is to say, both of the dispersion models are returning a fluctuating velocity component to be added to the mean velocity component prescribed from the local condition of the Eulerian phase. As the DNS domain has already been deemed inadequately resolved, the dispersion models are being used here in a more appropriate context as they attempt to model the effects of the unresolved scales on the particles. The FVM domain remains unchanged from the previous section, with periodic boundary conditions and a specific energy content of $Ea = 30\,m^2/s^2$ and on this occasion is used for all the trajectories presented for the remainder of this chapter. A series of screen-shots, shown in Figure 80, are presented for the Eulerian phases of the domains to convince the reader that, although there is an element of randomness introduced through the spectral forcing in the DNS-like solver along with the numerical errors, these are not enough to significantly change the flow field over the short period of time the Lagrangian trajectories are calculated ($5s$ of physical time are modeled). This clarification is needed since the comparison between the 'G&I', the KS and 'no-dispersion' models cannot be made simultaneously *i.e.* during the same run. Rather it is necessary to perform the simulation three times starting from exactly the same initial field and showing that, for a small enough time, the numerical errors will not result in significantly different Eulerian fields. Additionally, it may be constructive to present some representative streamlines for the isotropic turbulent field; these are shown in Figure 81.

Recalling that the Eulerian conditions within the domains remain very similar for the different dispersion models tested, any differences in particle trajectories may be attributed to the dispersion models. For the shorter intra-particle release time, Figure 82, the initial portions of the trajectories are similar, a result of the low turbulent/energetic conditions at the center of the domain. For this length of the trajectory, the TCT –evaluated at every time step– is such that none of the particles interact with the 'eddies' of the surrounding flow, rather they are being advected by the Eulerian phase. The location at which the trajectories suddenly diverge, indicates a location where the TCT was such that a dispersion model was activated, imposing on the particle a fluctuating velocity vector resulting in the departure from the *no-dispersion* trajectories. From then on, as the trajectories diverge further, the particle pair may experience significantly different Eulerian conditions resulting in either differing amounts of advection and/or interaction with 'eddies', prompting yet further generation of fluctuating velocity components to be prescribed by the dispersion models. As far as the comparison for the longer intra-particle release times are concerned, Figure 83, the conclusion is that the simulations reflect expectation; namely no correlation whatsoever between the trajectories of the particle pair, as the surrounding carrier phase has changed significantly within that time.

A few general remarks arise regarding the shape of the trajectories or, specifically the absence of sudden changes in curvature in the KS trajectories seen in the previous section. As detailed at the beginning of this chapter the integration of KS into a coupled Eulerian-Lagrangian solver required some modifications, the most important of these being the generation of a fluctuating velocity component rather than modifying the whole trajectory as that would result in violations of the conservation principles for coupled Eulerian-Lagrangian solvers. This was explained in

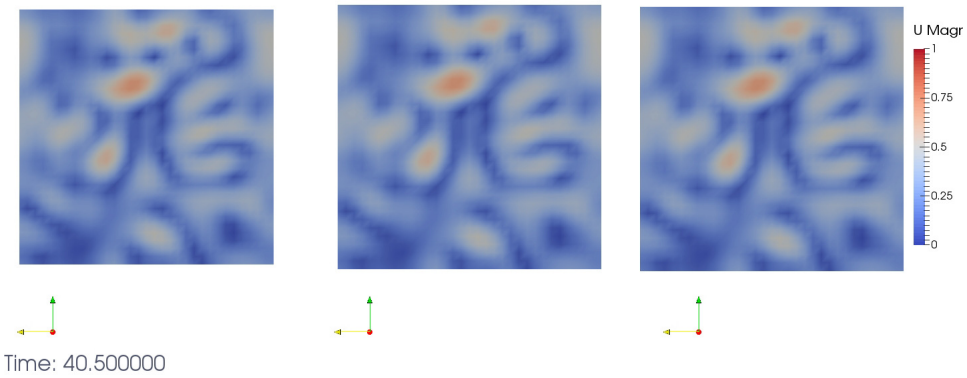

(a) at a time corresponding to just after particle injection

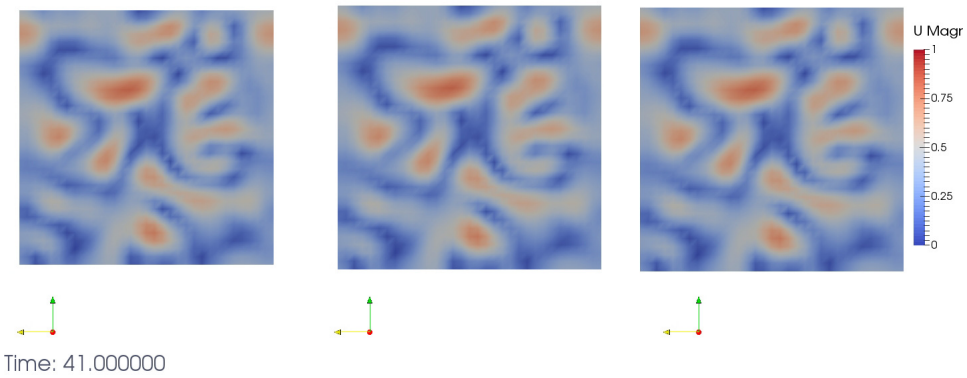

(b) after 0.5 s

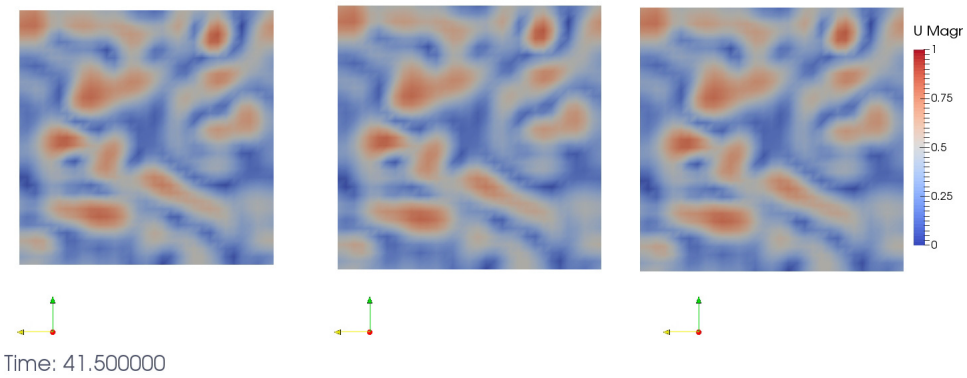

(c) after 1 s

Figure 80: From left to right the continuous domains for the G&I, KS & no-dispersion dispersion models; depicting the magnitude of velocity on the periodic boundary face, at several instants in time confirming that the 3 domains are almost identical.

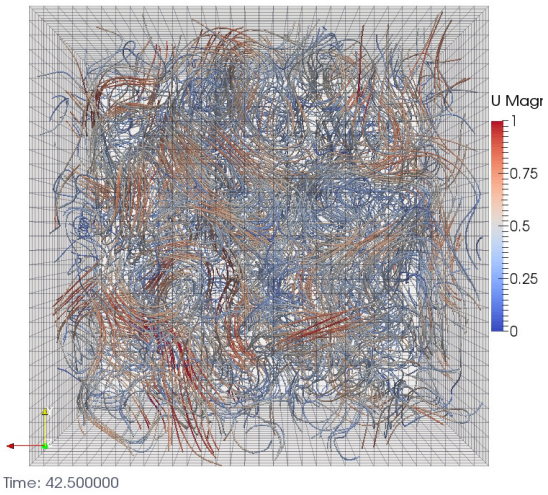

(a) Viewed from the XY-plane

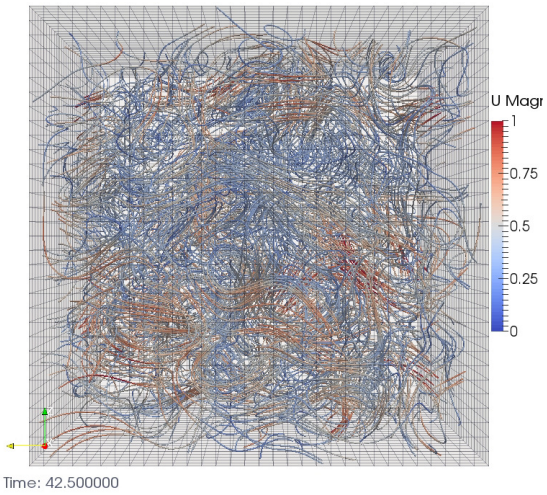

(b) Viewed from the YZ-plane

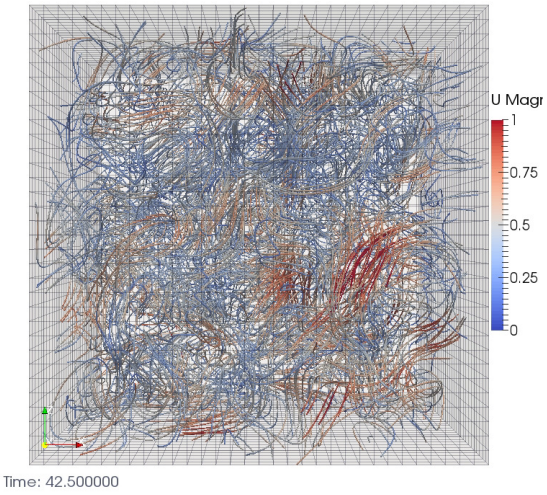

(c) View from the XZ-plane

Figure 81: Streamlines within the isotropic turbulence domain

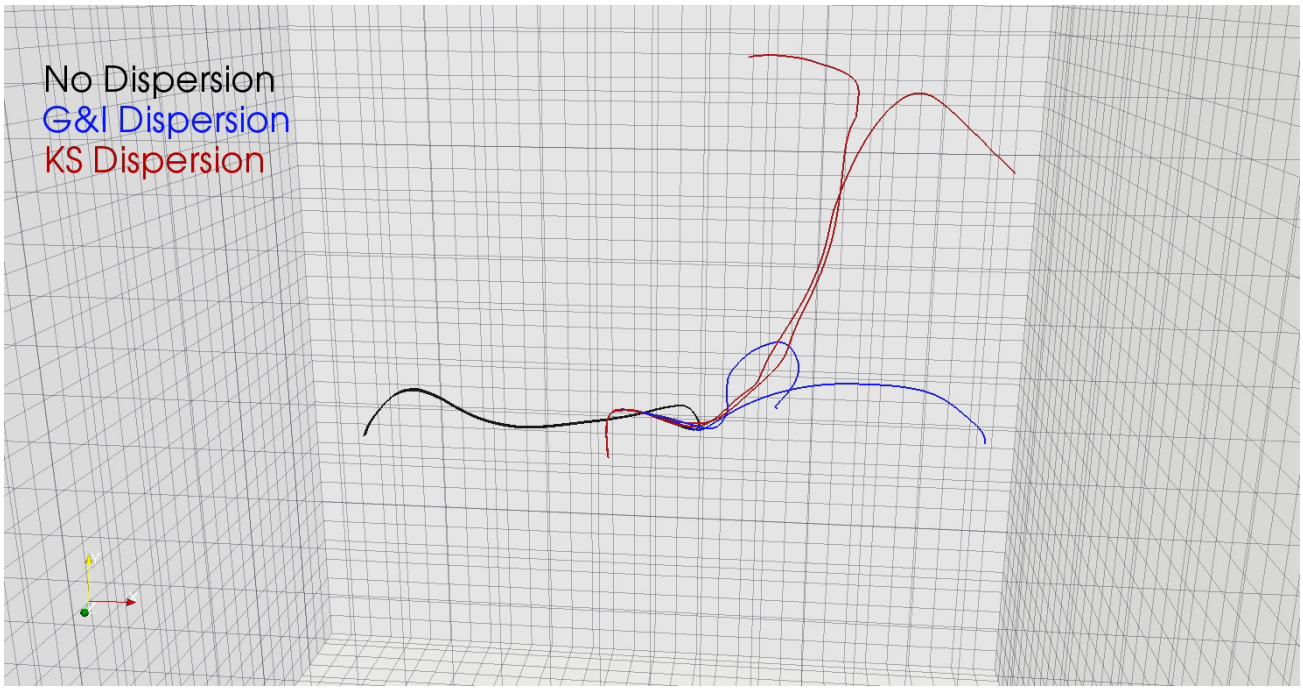

(a) Perspective view

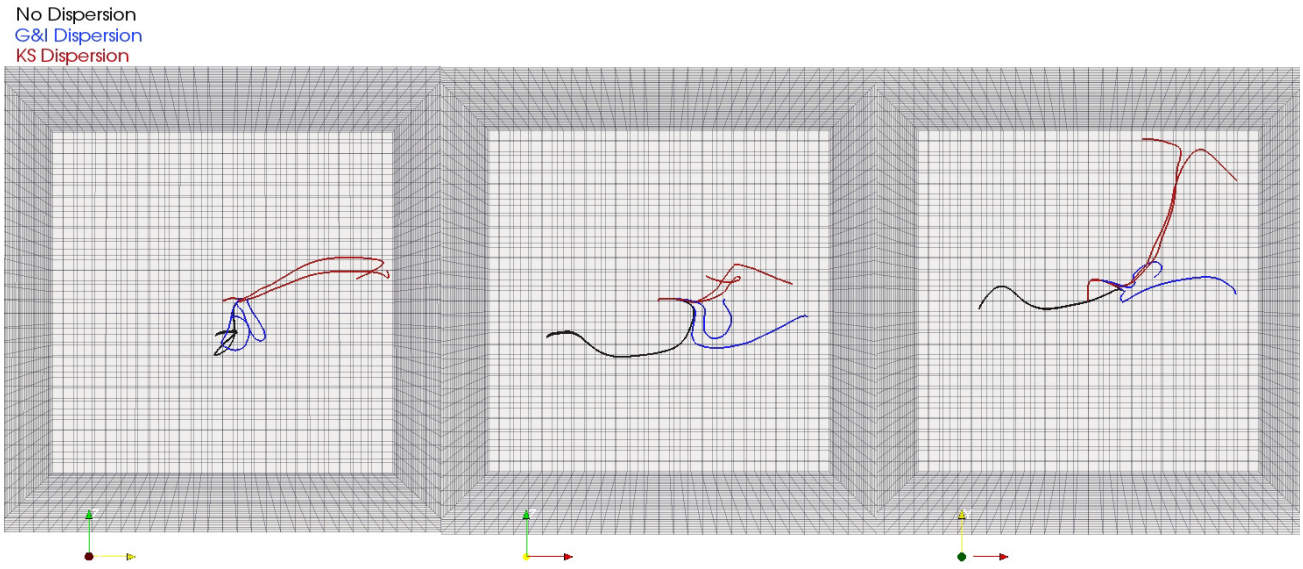

(b) From left to right; viewed from the XY, YZ & XZ planes, respectively.

Figure 82: Particle pair trajectories for $80\mu m$ diameter particles with a release time smaller than the *Kolmogorov* timescale. Black trajectories indicate the no dispersion model, red indicate the KS dispersion model and blue the G&I dispersion model particle pair respectively.

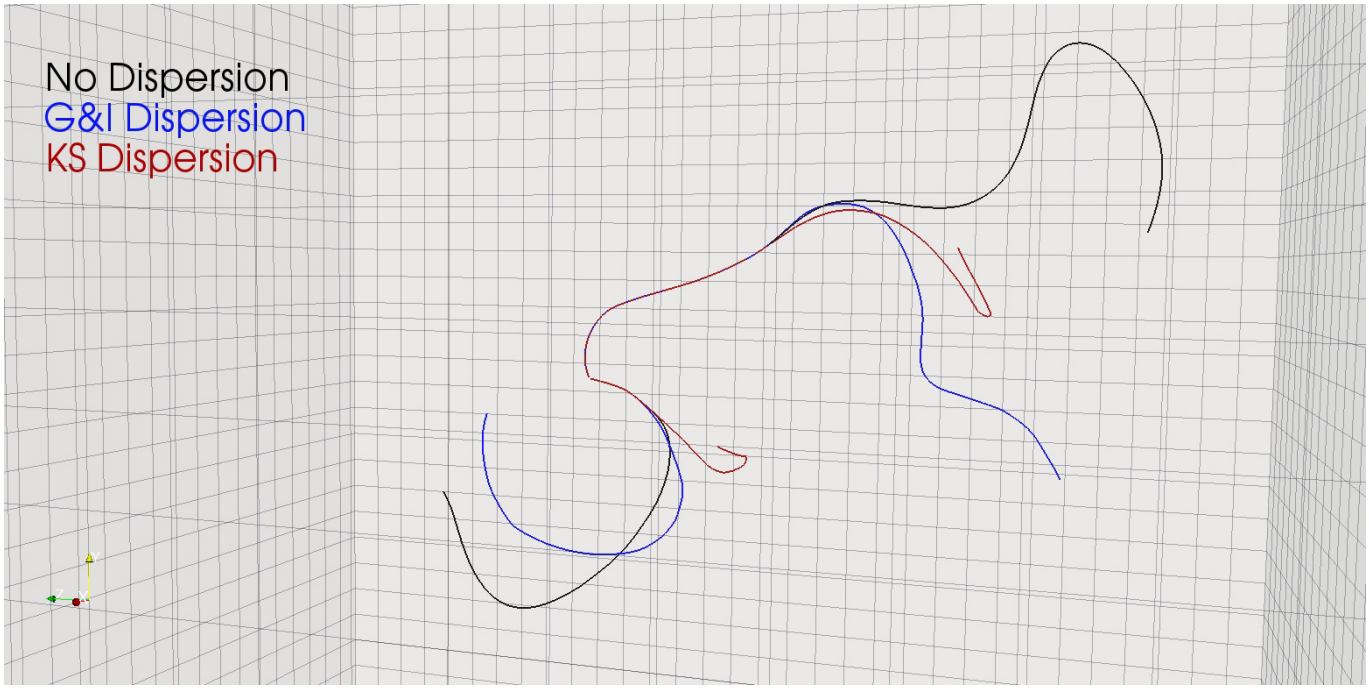

(a) Perspective view

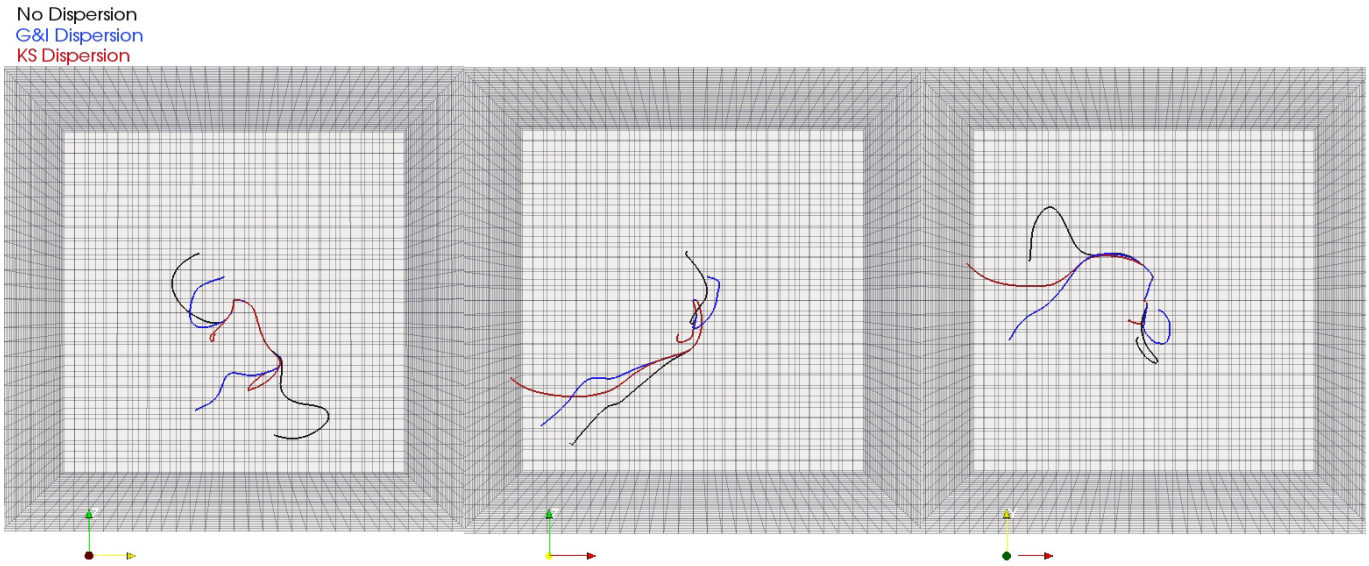

(b) From left to right; viewed from the XY, YZ & XZ planes, respectively.

Figure 83: Particle pair trajectories for $80\mu m$ diameter particles with a release time larger than the *Kolmogorov* timescale. Black trajectories indicate the no dispersion model, red indicate the KS dispersion model and blue the G&I dispersion model particle pair respectively.

detail earlier and will be shown to be well founded by the validation presented in the following chapter. Effectively, when the KS dispersion model is activated, a KS is created and the trajectories through the isotropic field are computed. However, as the (u)RANS calculations timesteps are very short, so too is the time allocated for the particle to traverse through the KS field –with only a few KS-timesteps being performed– in turn resulting in small computed KS trajectories. This minimizes the effect of having used a fluctuating component only, as the updated particle position –predicted by the KS trajectory– still lies within the same computational cell for most instances. This results in a small KS, small in terms of the trajectories computed, because this is a spectral method, there are no physical domain extents, rather the length of the trajectory determines the size of the KS. In any case the interaction of a particle with the inadequately resolved or averaaged 'eddies' of the Eulerian phase calculation, modeled by isotropic turbulent fields –whose size, range of scales and intensity are determined from the local Eulerian conditions– are accounted for through the generation of fluctuating velocity components.

4.4 Summary

A novel phenomenological dispersion model for coupled Eulerian-Lagrangian frameworks has been developed and presented in this chapter. This is based on the standard RANS solvers for modeling the large scales structures of the mean flow and then Kinematic Simulations are introduced to model the effect of the integral to dissipative ranges of the turbulent flow on the dispersion of Lagrangian particles. The interaction of a particle with an under-resolved or averaged 'eddy' is accounted for through the evolution of this particle through an isotropic turbulent field that has been created using Kinematic Simulations. The energy content and extent of scales of this field are determined from the local properties of the 'eddy' as resolved by the Eulerian calculation.

Qualitative comparisons between the proposed model and the G&I dispersion model showed differences in the underlying dispersion mechanisms as well as marked differences in particle trajectories when used as a dispersion model through identical flow-fields. In the G&I model, the particle pair separates gradually and a sudden change in particle pair separation distance occurs when the particles are eventually advected apart by the larger resolved Eulerian scales of the flow. Whereas the KS trajectories are capable of modeling the sudden separation even within the unresolved scales. This is an important point to note as the intended use of such models is primarily to 'compensate' for the lack of the averaged or unresolved scales of a flow-field and the expectation is that they should result in increased dispersion.

5 KS in sudden expansion

The test case chosen for validation of the proposed phenomenological model was the axisymmetric sudden expansion particle laden flow of Hardalupas *et al.* (1992) that investigated the dispersion of different sizes of mono dispersed particles through an axisymmetric sudden expansion for a range of air flows. What makes this particular set of experimental data interesting is the detailed measurements of both Eulerian and Lagrangian phases, for two different bead sizes, with nominal diameters of $40\mu m$ and $80\mu m$, at high Reynolds number $\left(Re \sim 10^4\right)$. In the present context it is a particularly insightful test case as past investigations of existing dispersion models in RANS frameworks have predicteds, that only a limited number of the $80\mu m$ particles enter the recirculation zone, contrary to experimental observations where a significant number of particles were observed. An additional consideration, though, is the inherent similarity of the axisymmetric sudden expansion recirculation zone to the external recirculation zones formed downstream of aviation air-blast atomizers. Such an environment necessitates a RANS approach as the computational costs of LES are still prohibitive. **Both in a qualitative and a quantitative sense the new model should predict a greater number of particles entering the recirculation zone and/or an increase in magnitude of the fluctuating velocity component without overpredicting the levels of dispersion in the remaining regions.**

The geometry has already been introduced in the previous chapter and what needs to be mentioned here is that the *k-Epsilon* closure model is chosen for reasons explained in the following section and that all other mesh details are the same as the standard mesh of the LES calculations, with the exception of the wall models employed being replaced by the corresponding RANS ones. The justification for using what may be argued is a fine mesh for a u-RANS calculation was the desire to capture the large scale oscillations of the jet as it entered the expansion chamber since its importance in particle distribution was observed and discussed earlier extensively. A fine mesh and a small timestep were necessary to achieve this.

5.1 Selection of k-Epsilon closure model

One of the weaknesses of the standard *k-Epsilon* model, and models derived directly from it, lies with the modeled equation for the dissipation rate, ε. The limitation manifests itself in what has come to be known as the plane jet - round jet anomaly, so named because while the spreading rate in planar jets is predicted reasonably well, the prediction of the spreading rate for an axisymmetric jet is much poorer[74]. This means that although the recirculation zone downstream of a plane jet is modeled accurately the same is not true for an axisymmetric round jet, where the *k-Epsilon* under-predicts the spreading rate resulting in a jet that 'fans-out' over a greater axial/longitudinal distance. Wilcox (2006) attributes this to the inferior representation of cross-diffusion in *k-Epsilon* models when compared to *k-Omega* ones. He proceeds to compare the most popular RANS models against experimental measurements for the spreading rates of round and plane jets. He confirmed that *k-Epsilon* model exhibits superior performance for

[74]The spreading rate in such contexts may be defined as the radial distance from the centreline where the velocity drops to half the value measured along the centreline.

the plane jet overall, but for the round jet although the overall shape of the variation of the spreading rate with spanwise distance from the centreline is captured correctly, it is consistently offset, predicting greater velocities. In contrast, the *k-Omega* captures the velocities near the centreline accurately its performance drops with increasing distance from the centreline. Wilcox (2006) attributes the superior performance of the *k-Omega* model to the better modeling of cross-diffusion terms in the model's closure equations. The reason this is not noticed in the plane jet for the *k-Epsilon* model is due to the fact that vortex stretching in two dimensional flow is not present, on average, and in turn the effects of cross-diffusion smaller. He does however investigate the sensitivity of *k-Omega* models to the free stream values of the closure equations for which little data is available from experimental measurements. Meanwhile, in the absence of any noticeable swirl in the present flow the benefits of a *k-SST-Omega* model should be small especially when the exaggerated prediction of turbulence levels near stagnation points and regions of large normal strain and acceleration is considered (Menter (1994)).

The dispersion model should be capable of predicting adequate Lagrangian dispersion in the recirculation zone from the chosen closure equations rather than, resulting to overprediction of the discrete phase fluctuating velocities across the domain. Furthermore, Versteeg & Malalasekera (1995) summarizing the work of Rodi (1980) and Launder *et al.* (1975) note that the *RSM* models suffer similar limitations which are exacerbated in the presence of swirling flows making them completely unsuitable for the intended industrial application before the increased computational cost is even taken into account. So the choice of appropriate closure model for the present test case is between the *k-Omega* and the *k-Epsilon* closure models. The latter was chosen for several reasons. First, it may be argued that it is the simplest of all closure models. Secondly, it is the original closure model on which the original Gosman & Ioannides (1981) model was developed and as such the ensuing comparison between the proposed KS model and the GI model should not favor one over the other. Finally, it was mentioned in Chapter 3 that the locus of the recirculation is predicted to occur at a slightly greater downstream locations which was what was observed in the previous chapter in the LES calculations as well. Thus no unfavorable advantage is given to the uRANS models over the LES calculations - in fact, rather the contrary.

5.2 Qualitative Comparisons

The following section will demonstrate the increased particle dispersion and flux of particles within the recirculation zone predicted by the KS models. This will be done through qualitative inspections of instantaneous snapshots from the calculations and evaluation of the increase in range of fluctuating velocity components predicted by the proposed model.

Figure 84 depicts the expansion tube section of the computational domain and shows equatorial plane slices for the Eulerian phase; namely the magnitude of velocity, the turbulent kinetic energy dissipation rate and the turbulent kinetic energy extracted from the coupled calculations. Figure 85 is a qualitative depiction of the difference between the particle locations predicted by LES and the two stochastic models for the smaller mass loading condition, ML1. The inhomogeneity of the LES calculation is seen on the left hand most pane, while comparing the center and the right hand most pane one can discern a slight increase in the number of particle entering the

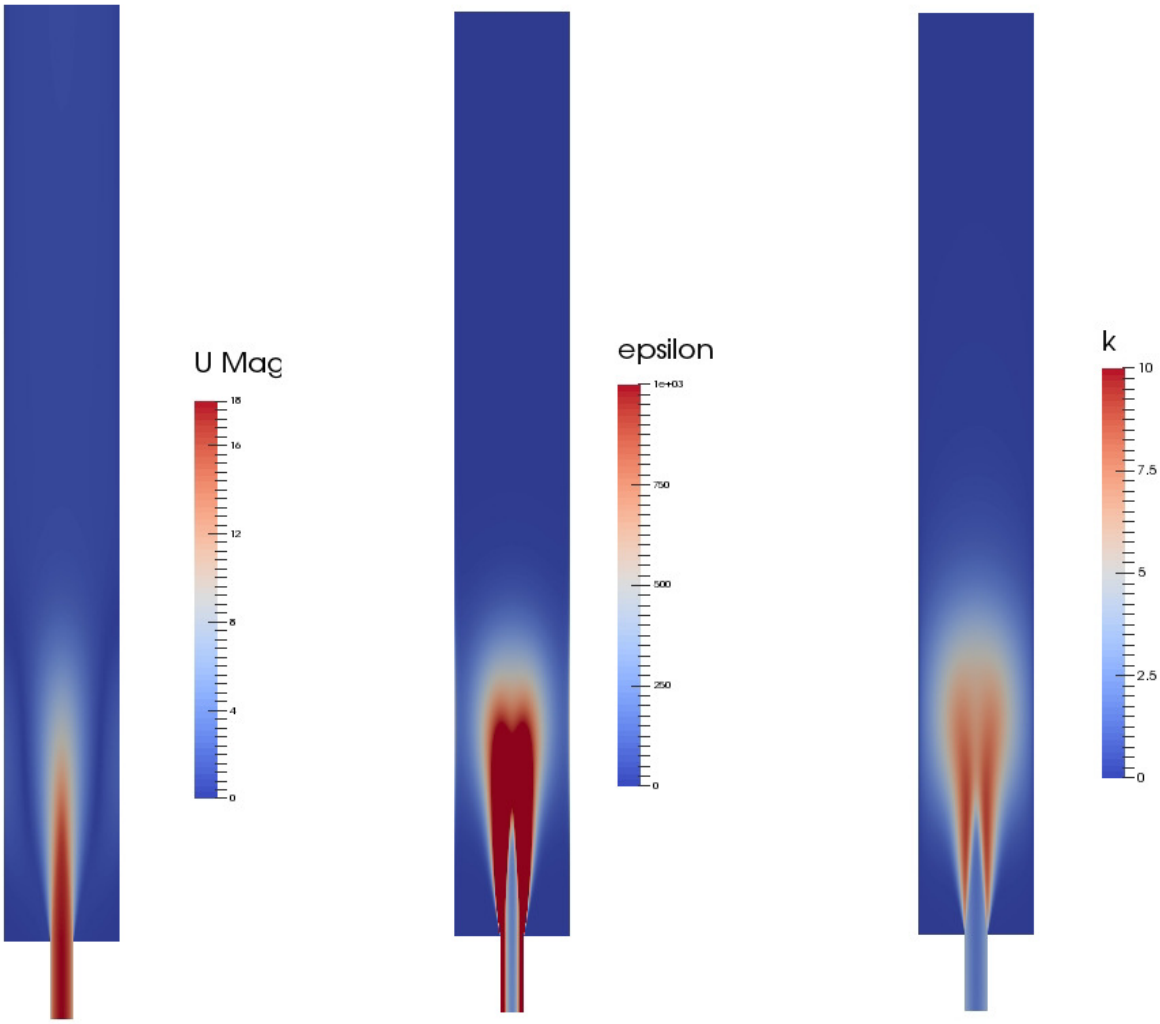

Figure 84: Slices through an equatorial plane of the RANS simulation. Visible at the bottom is the $15mm$ inlet tube and the whole domain of the expansion tube of $75mm$ diameter and $600mm$ length. Flow is from the bottom of the page to the top. Depicted from left to right; continuous phase mean velocity magnitudes colored for a range [0, $18m/s$]; dissipation rate of turbulent kinetic energy colored between [0, $1000m^2/s^3$] and turbulent kinetic energy colored between [0, $10m^2/s^2$]

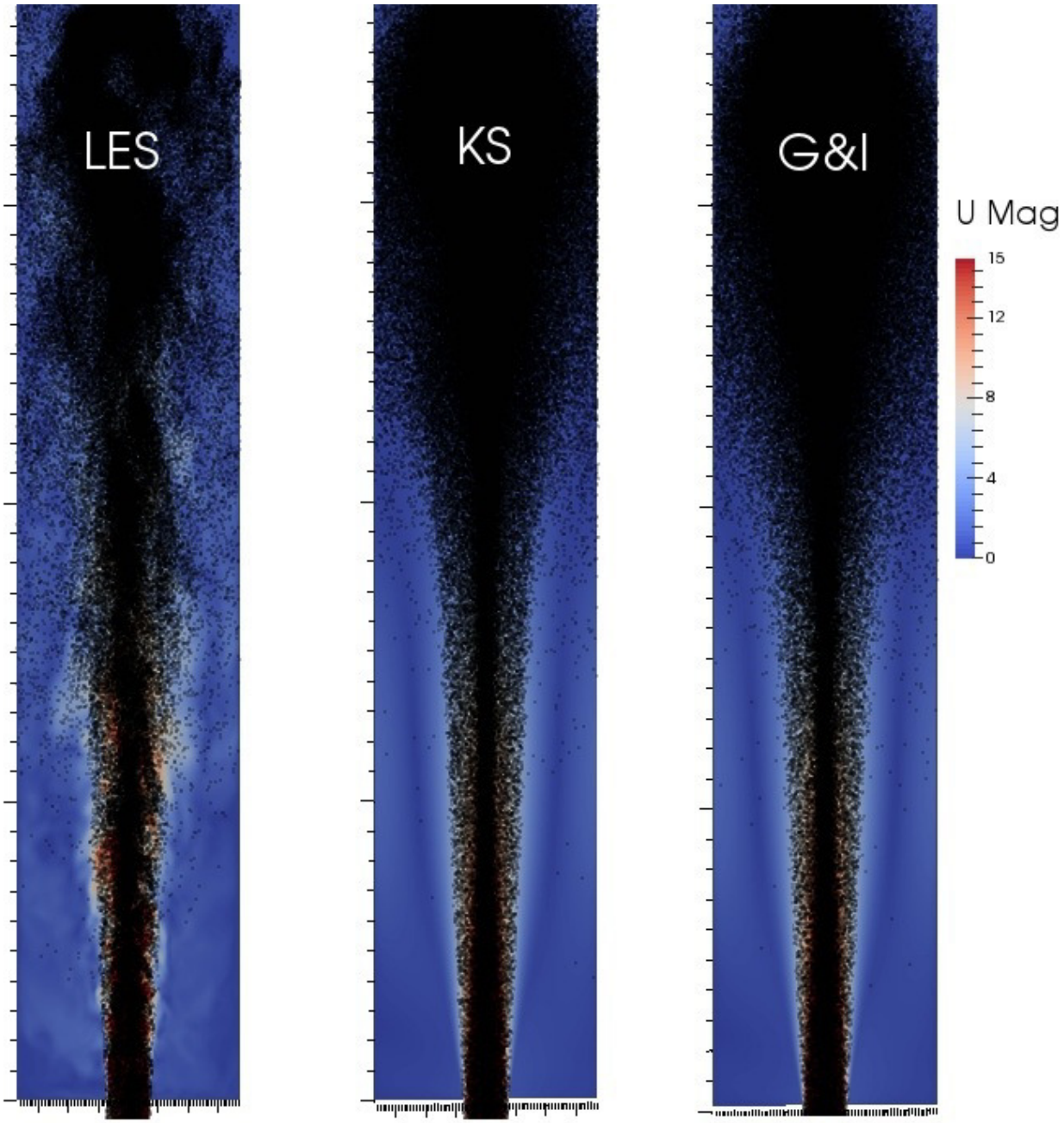

Figure 85: Comparison between LES-RANS inhomogeneity of $80\mu m$ particle spatial distributions shown on an equatorial plane through the domain colored by the continuous phase velocity magnitude $[0,\ 15m/s]$.

recirculation region, approximately half-way down the domain. The two RANS dispersion models exhibit more uniform spatial particle distributions than the LES calculations where the large scale oscillations of the jet resulted in a significant degree of inhomogeneity. These calculations used the same grid as that employed by the LES and an identical timestep ($dt = 10\mu s$). Despite the fine mesh employed and small timesteps used for the uRANS calculations, the flapping of the jet was not resolved sufficiently with the *k-Epsilon* model, with only a minute amplitude of oscillation observed near the very tip of the jet. Nevertheless, a circumferential oscillation in the flow field was observed in the region of the recirculation zone. However, this does not result in the same downstream particle spatial non-uniformity as that caused by the shedding of particles at the tip of the oscillating jet. These findings are consistent with the work of Dunham *et al.* (2009) who investigated a confined swirling-jet flow in both uRANS and LES frameworks and noticed that although uRANS was able to predict large scale vortical structures, these were not consistent with experimental measurements.

Figure 86 shows perspective views of the computational domain from a position just above the step looking downstream for the higher mass loading cases, ML2, for both the $40\mu m$ and $80\mu m$ particle size classes. In this series of screen-shots all the injected particles are plotted and the equatorial plane depicts contour of the concentration evaluated on the Eulerian field with the method described in the following section. This series of screen shots serves to show the spatial non-uniformity of the LES calculations, which is ultimately the desired goal of uRANS dispersion models. For the higher mass loading case the discrepancies appear to be smaller, but this is probably an artifact due to the sheer number of additional particles introduced which makes distinguishing such discrepancies in a qualitative sense cumbersome. An additional point that should be made is that this series of images correspond to instantaneous snapshots and once temporal averaging is performed the discrepancies, namely departures from axisymmetry, will be significantly smaller. It is exactly this instantaneous non-uniformity which needs to be captured in order to allow the combustion models to take into account temporal temperature and stoichiometry fluctuations within the domain if they are ever to predict accurate emissions.

Up until now we have been inspecting the entire domain, however it is important to focus on the recirculation zones since it is at exactly these regions where the limitations of the GI model were most pronounced, especially concerning the $80\mu m$ particle case and the very small number of particles that are observed to enter these recirculation zones. Figure 87 shows the particle dispersion as predicted by the GI and KS models in the expansion tube downstream of the step along with a representation of the locus of the recirculation zone in the continuous phase where blue colors indicate regions of flow reversal. For both models, calculations were performed from identical starting conditions and Eulerian parameters and allowed to run for the same number of iterations. The KS model predicts an increased number of particles entering into the recirculation zone and traveling upstream when compared to the particle dispersion predicted by the GI model.

To understand how this is being achieved, one's attention must be drawn to the computed particle velocities from the two models and restricted to the region of the expansion tube that corresponds to the recirculation zone. Depicted in the following series of figure, Figure 88 to 94

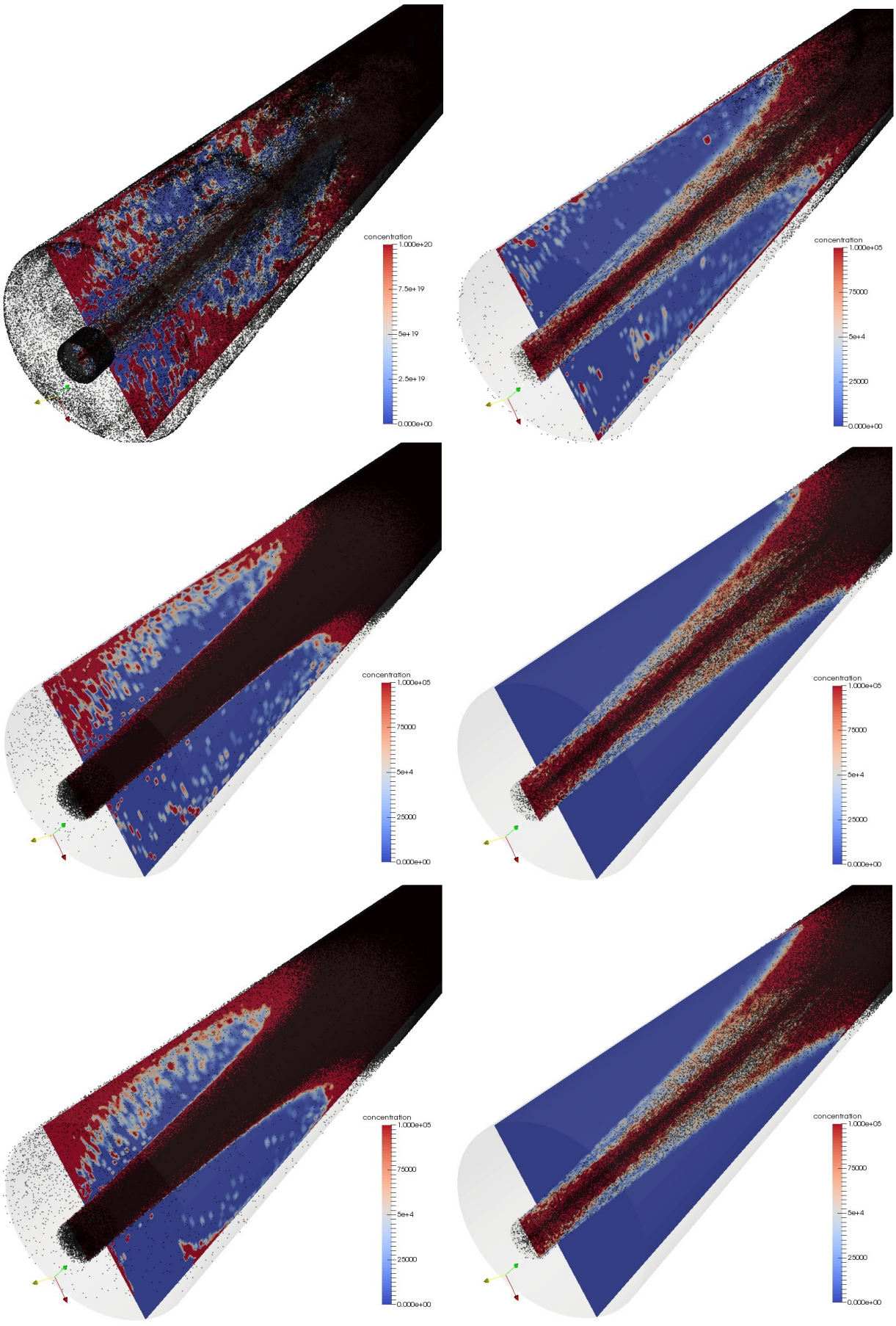

(a) $40\mu m$ (b) $80\mu m$

Figure 86: From top to bottom; LES, KS & GI. Depicting the instantaneous particle positions and the equatorial plane depicting the particle concentration before normalization.

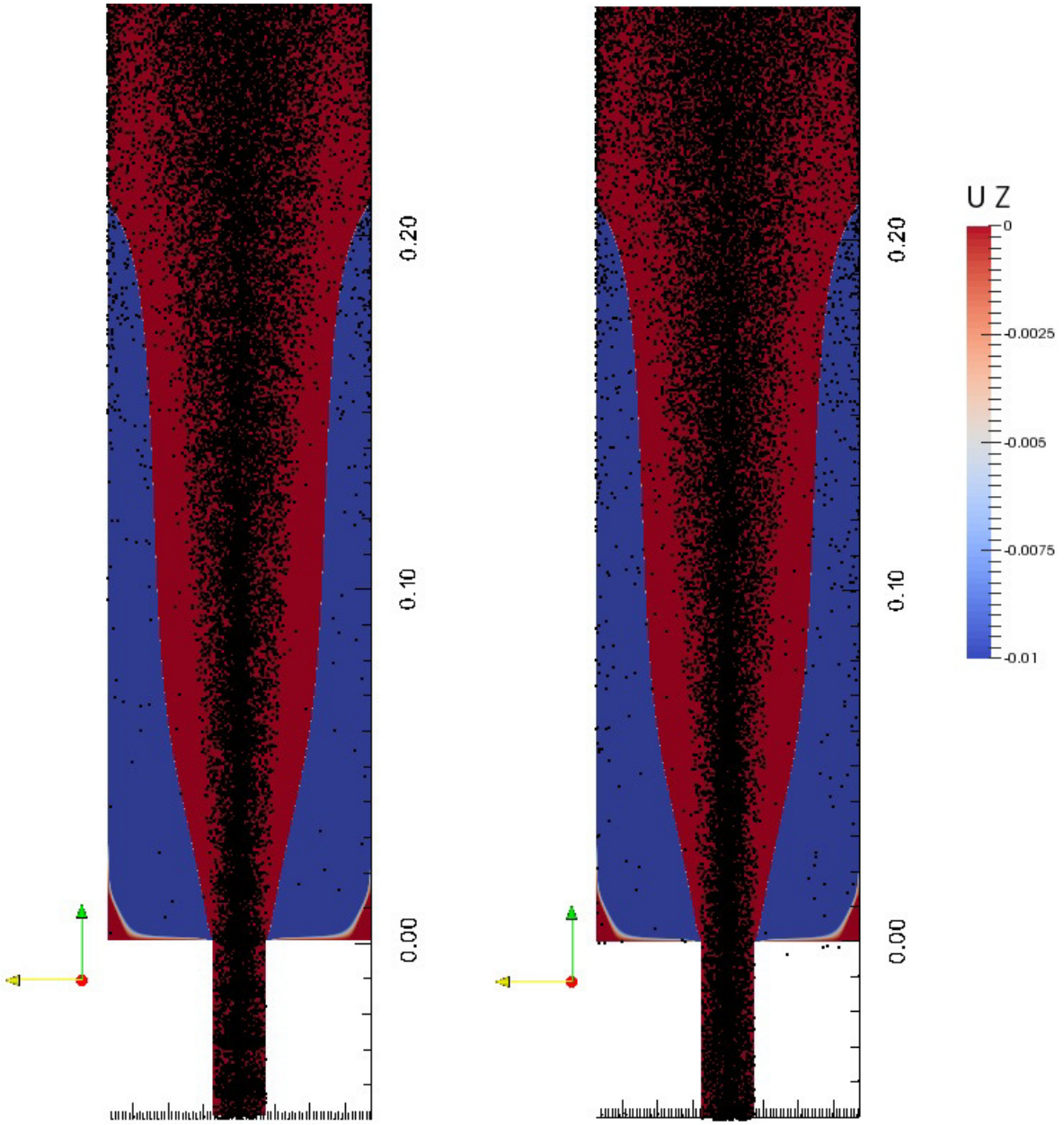

Figure 87: $80\mu m$ particles positions, collapsed onto a single azimuthal plane, depicted within the expansion tube, equatorial planes through the Eulerian domain shows the continuous phase axial velocity, blue regions indicate negative velocities and the extend of the recirculation zone. G&I on the left and KS2 on the right. (Note: The particles that appear to lie outside the domain are a result of the rendering process and are actually within the domain. The concentration has not been normalized here)

are the particle fluctuating velocities computed by the KS and the GI models. The Lagrangian domain has been clipped or reduced to the region of interest in order to make the visualization and post processing more tractable; specifically only the particles downstream of the step are shown extending to a region corresponding to half the expansion tube length (z=0.3m).

Figures 88 to 94 compare the GI and KS simulations starting with a qualitative depiction of the magnitude of the particles' fluctuating velocity components intended to show the overall increase of particle dispersion, especially past the axial location indicated by the horizontal axis. While Figures 88a to 94a have been colored by a range corresponding to the extremities of the computed velocities, the subsequent plots (Figures 88b to 94b) are colored to the same scale showing clearly the increased velocities of the KS dispersed particles. Once the particle velocities are depicted inthe latter manner, it becomes clear that the larger range of fluctuations predicted by the proposed KS model is not present throughout the Lagrangian phase rather it is restricted to the regions of high turbulent kinetic energy near the centreline and close to the step. The range of predicted velocities decreases markedly as the distance from the step increases and the particles travel downstream.

Similar comparisons are repeated for the individual fluctuating velocity components. For every one of these individual velocity component plots the presentation is repeated, coloring with two distinct scaling schemes and then is repeated but with the Lagrangian data clipped in two distinct ways; Either the Lagrangian data is clipped in solely in the axial direction, restricting the analysis to those particles close to recirculation region or it is clipped in both the axial direction and in a spanwise direction parallel to a vector normal to the plane of the page, further restricting the comparison to particles that lie on a equatorial plane. The former three dimensional Lagrangian representations serve to show circumferential non-uniformities but most importantly, to elucidate that the large fluctuating velocity components predicted by the KS model are limited to regions near the centreline while near the walls both models predict very similar ranges of near zero velocities as would be expected. The series of images depicting the particle velocities that have been restricted in both the streamwise and circumferential directions (a 2D representation of the Lagrangian phase) serve to show the increased dispersion in this region ($z \sim [0.20 - 0.26m]$) and to remove any falsehood in interpreting the qualitative data that might arise from a two dimensional representation of a three dimensional spatial distribution where it may be hard to distinguish between increased dispersion and a particle that lies near the wall but at a different circumferential direction.

The entire discussion so far has been a qualitative descripton of the way the KS model performs in this region and this information will be quantified in a following sections.

5.3 KS-model Evaluation

The evaluation of the KS model in the axisymmetric sudden expansion geometry will be done in two parts. First, attention is directed in evaluating how the particle spatial distribution is affected from use of the proposed model. Evaluation will be done by evaluating the particle concentration at several locations and comparing it to the G&I model, to LES predictions, as well as to the experimental measurements. Then, a comparison of the fluctuating velocities generated by the G&I and the proposed models will be performed.

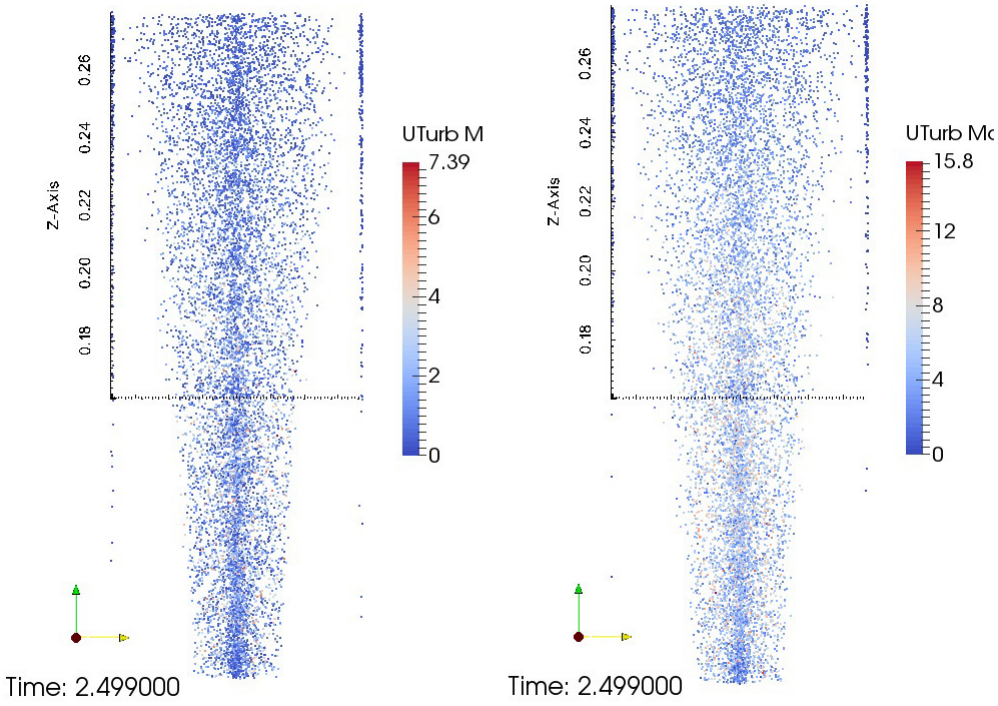

(a) Colored by respective extent of the maximum and minimum velocities

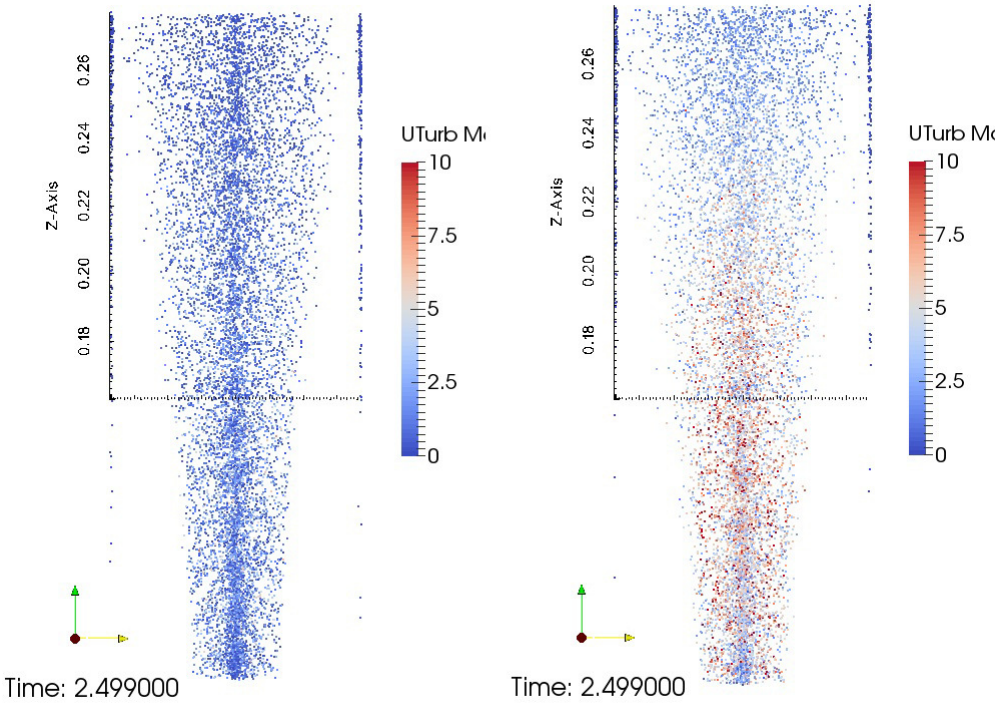

(b) Colored to a common velocty range

Figure 88: Magnitude of fluctuating velocity vector, u', for $80\mu m$ particles as calculated by the GI on the left and the KS2 models on the right. Note that the domain is restricted to show only the particles lying close to an equatorial plane.

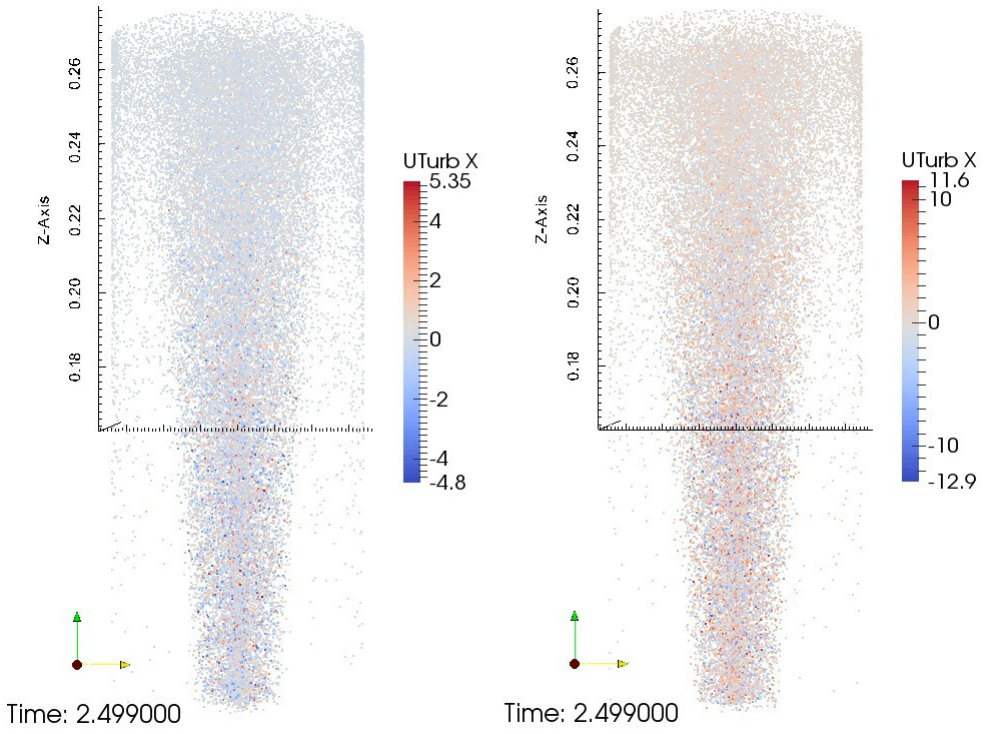

(a) Colored by respective extent of the maximum and minimum velocities

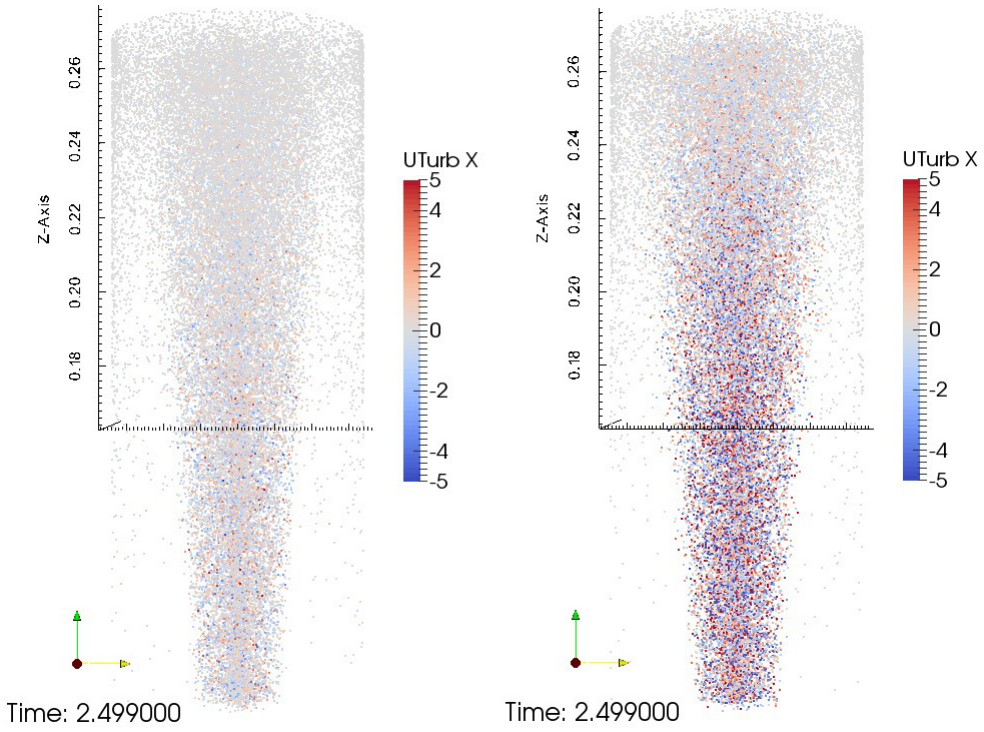

(b) Colored to a common velocity range

Figure 89: x-component of fluctuating velocity for $80\mu m$ particles as calculated by the G&I on the left and the KS2 models on the right

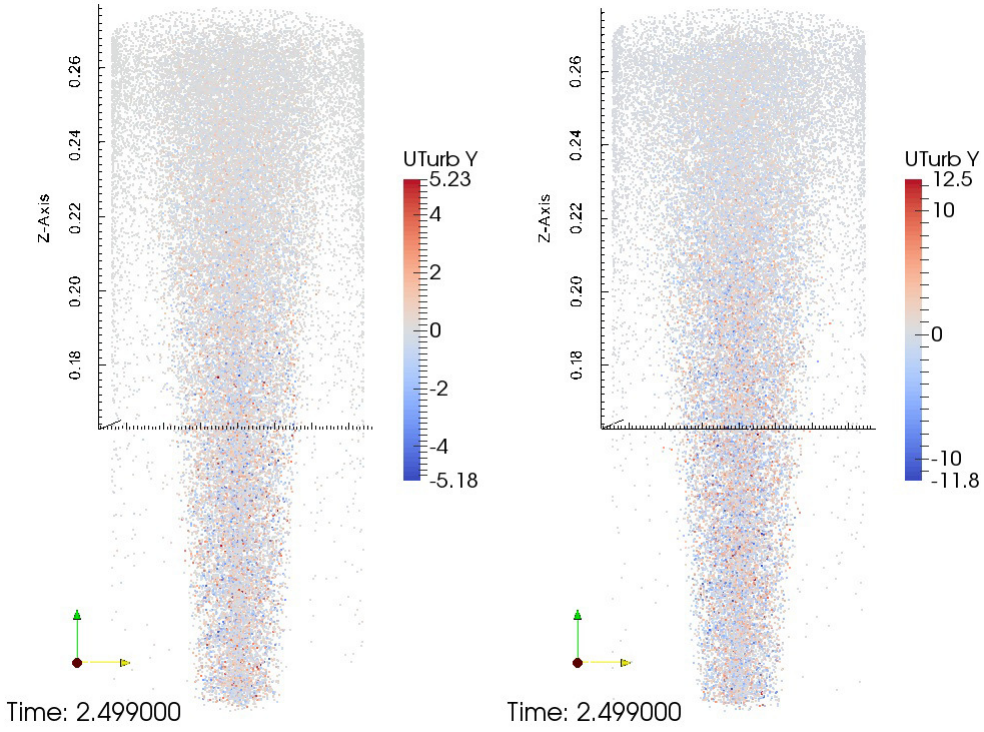

(a) Colored by respective extent of the maximum and minimum velocities

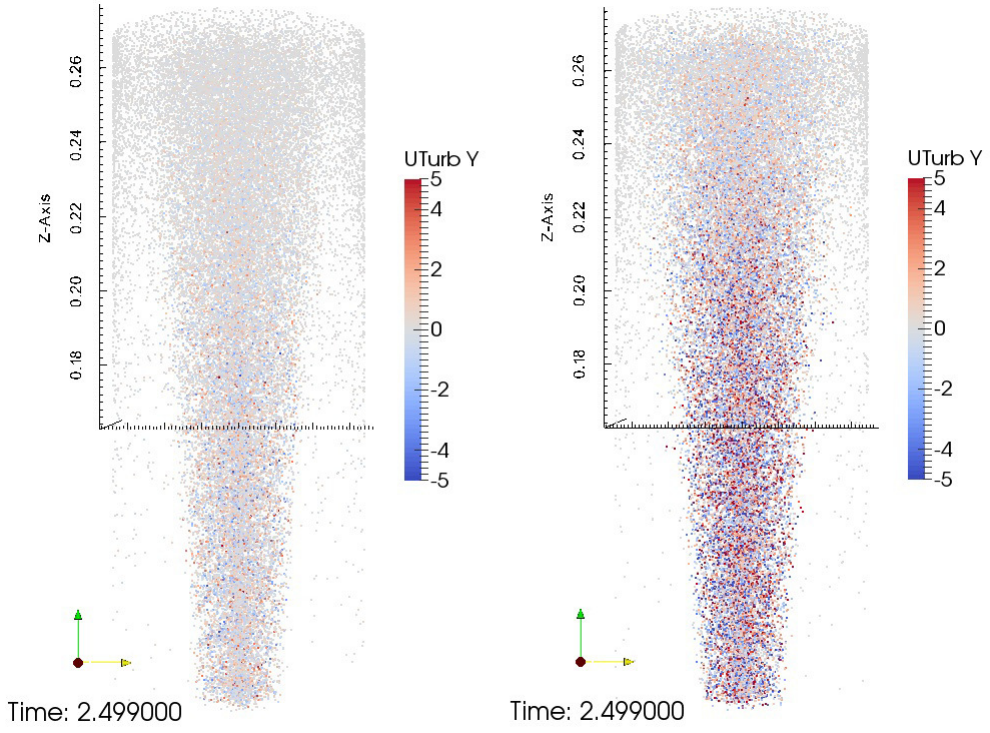

(b) Colored to a common velocity range

Figure 90: y-component of fluctuating velocity for $80\mu m$ particles as calculated by the G&I on the left and the KS2 models on the right

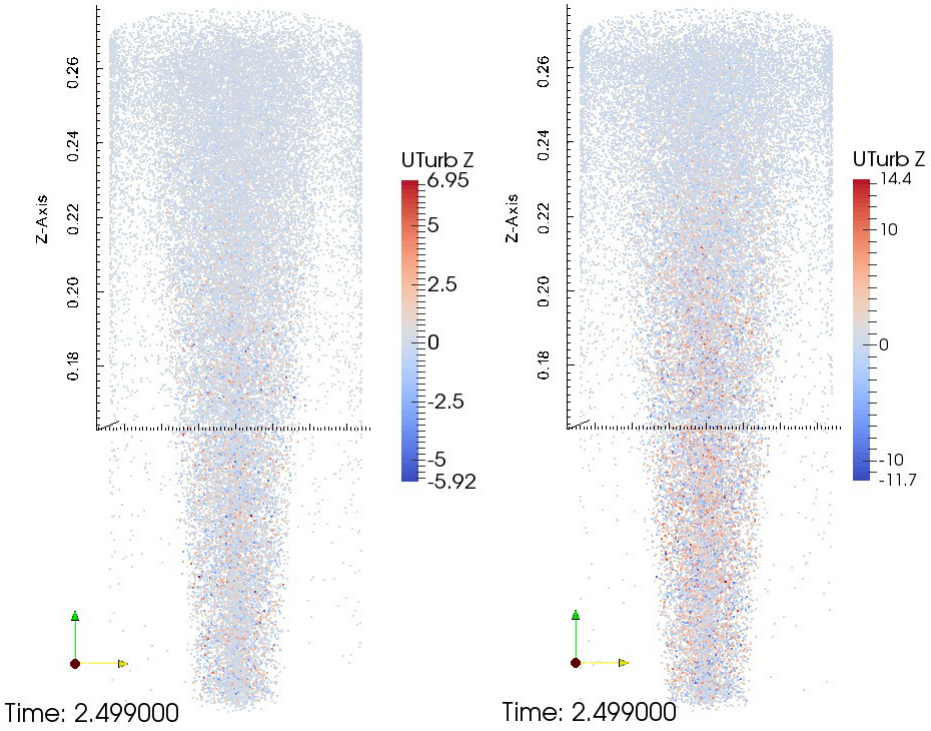

(a) Colored by respective extent of the maximum and minimum velocities

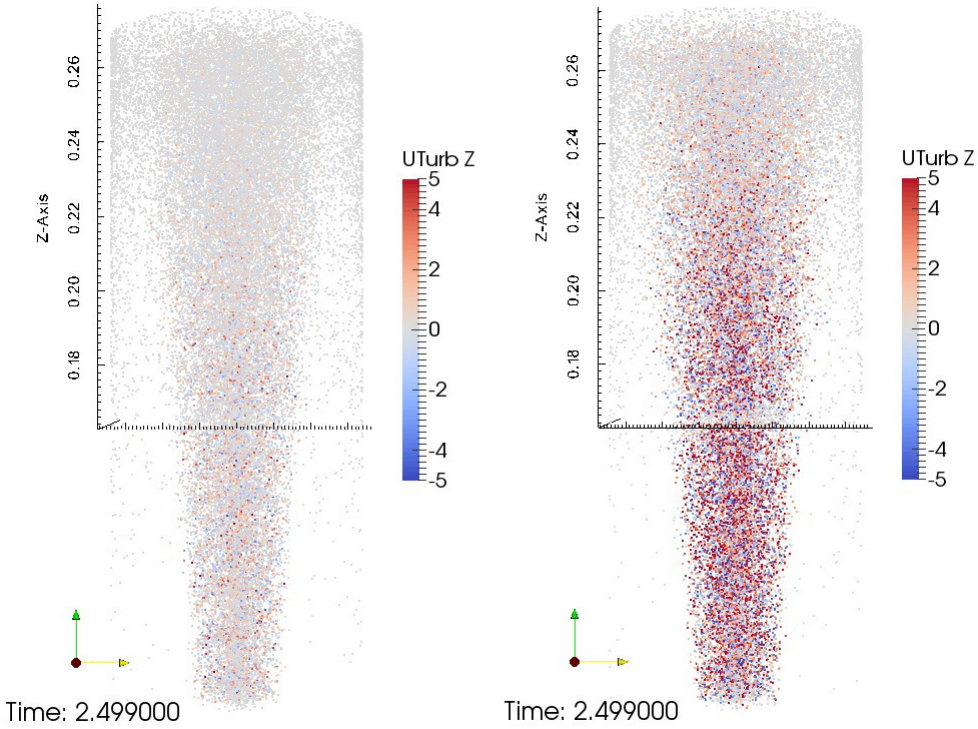

(b) Colored to a common velocity range

Figure 91: z-component of fluctuating velocity for $80\mu m$ particles as calculated by the G&I on the left and the KS2 models on the right

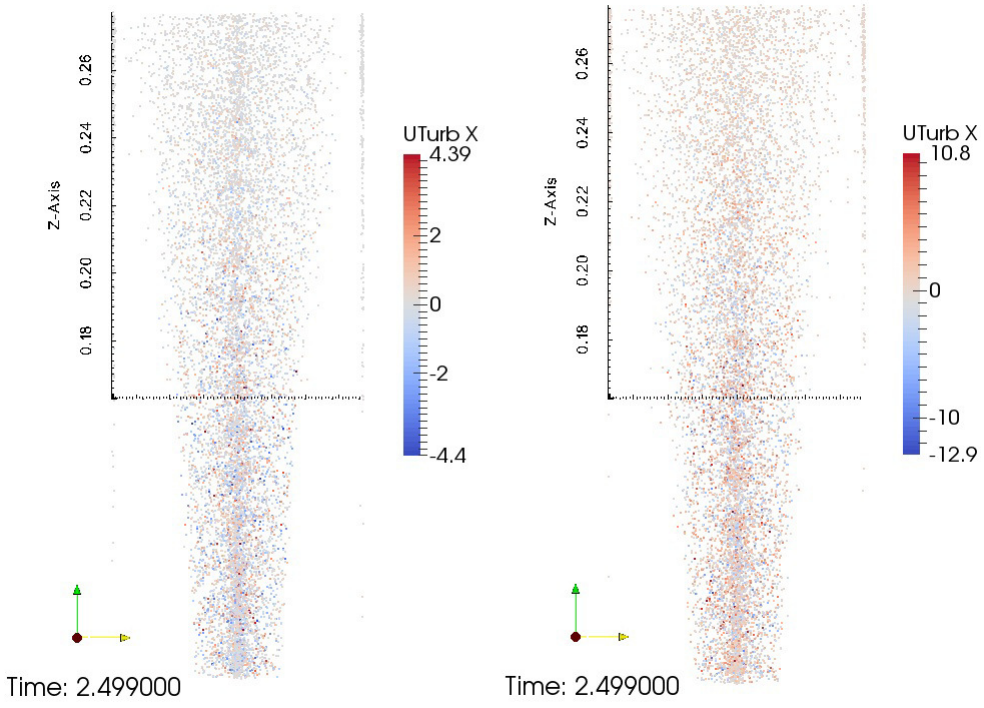

(a) Colored by respective extent of the maximum and minimum velocities

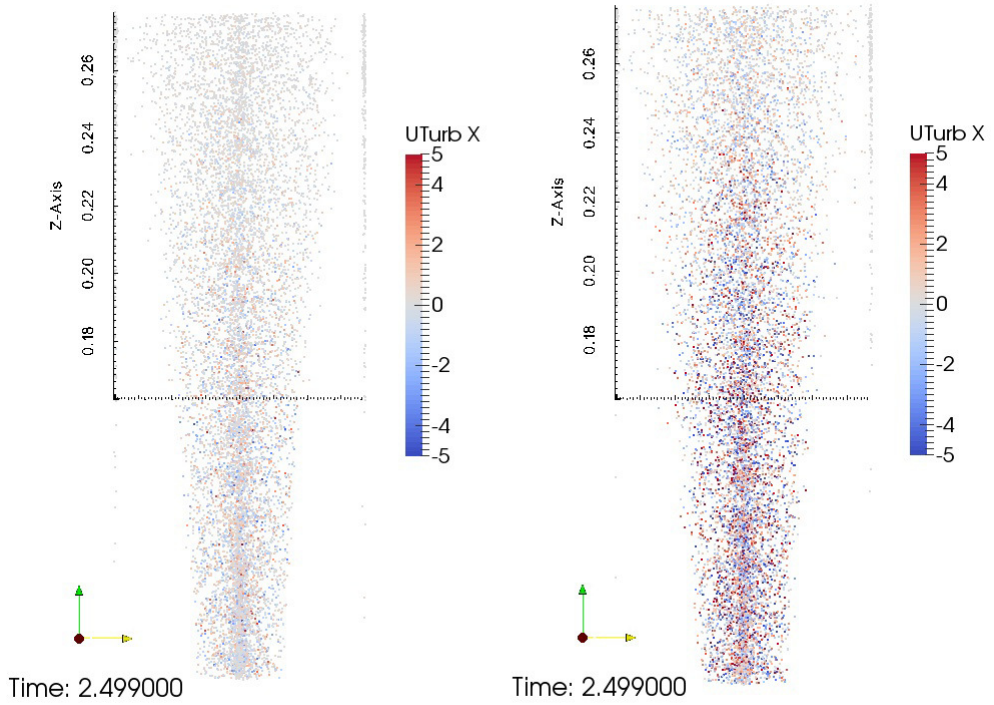

(b) Colored to a common velocity range

Figure 92: x-component of fluctuating velocity for $80\mu m$ particles as calculated by the G&I on the left and the KS2 models on the right. Note that the domain is restricted to show only the particles lying close to an equatorial plane.

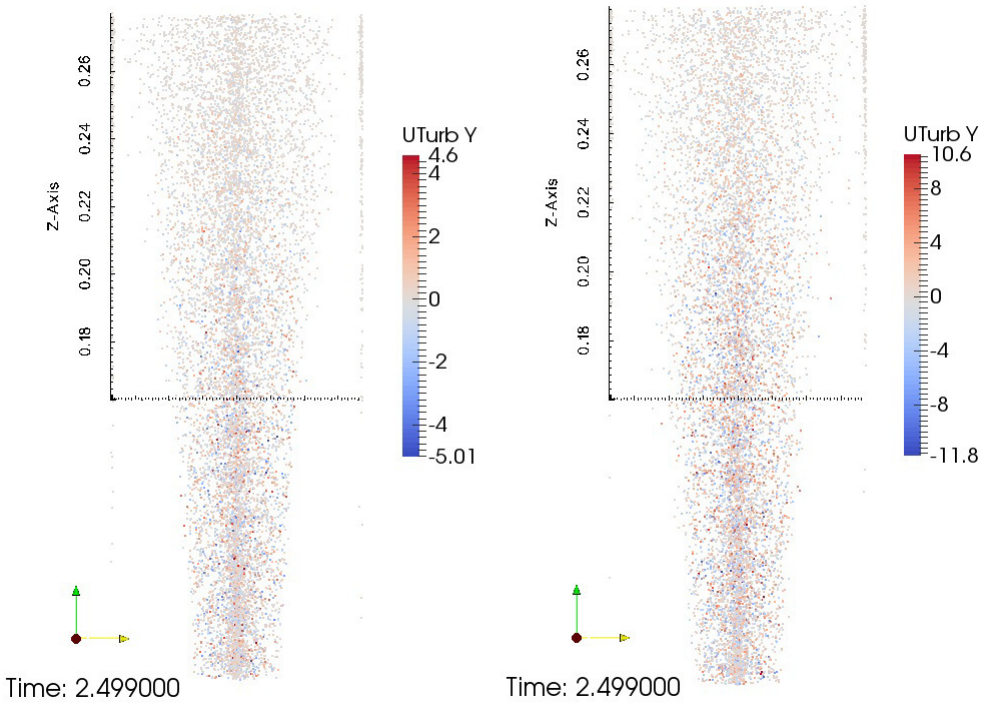

(a) Colored by respective extent of the maximum and minimum velocities

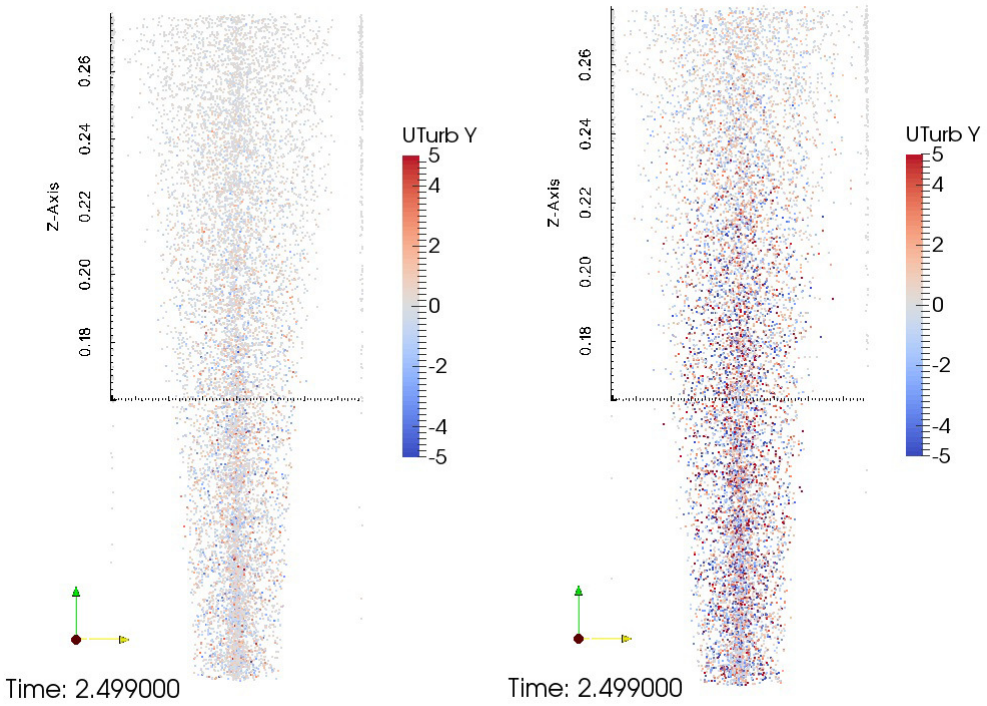

(b) Colored to a common velocty range

Figure 93: y-component of fluctuating velocity for $80\mu m$ particles as calculated by the G&I on the left and the KS2 models on the right. Note that the domain is restricted to show only the particles lying close to an equatorial plane.

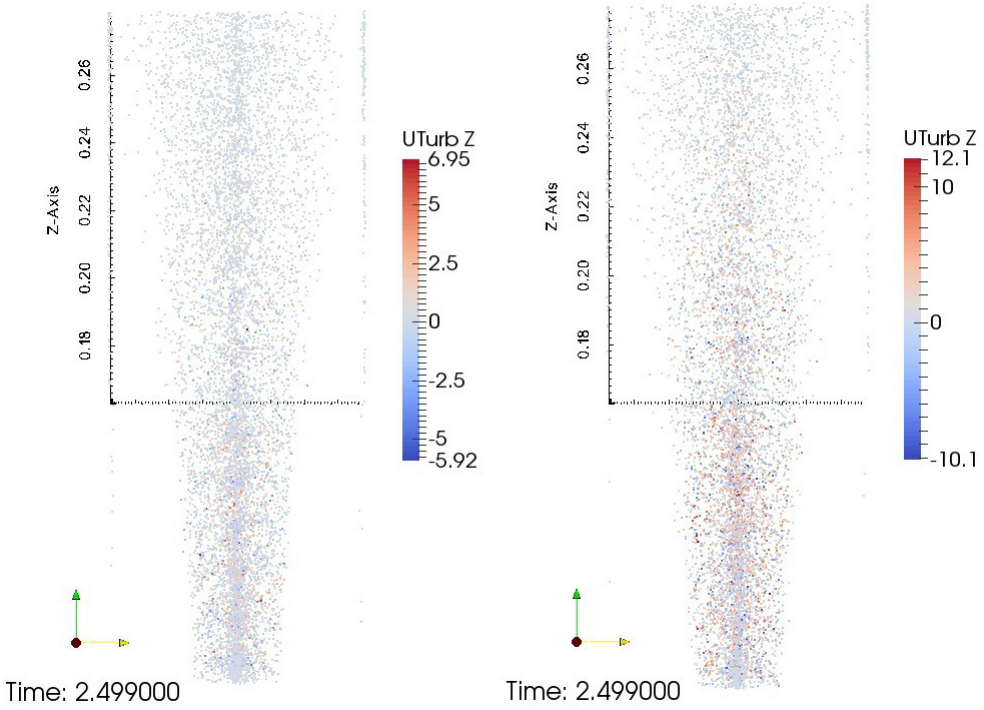

(a) Colored by respective extent of the maximum and minimum velocities

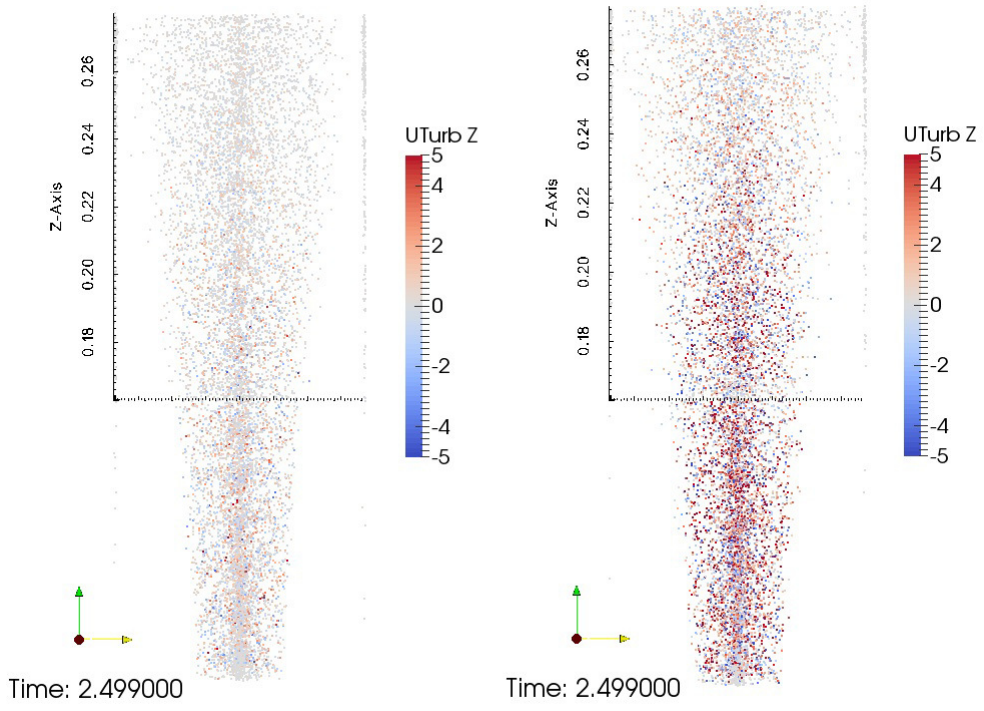

(b) Colored to a common velocty range

Figure 94: z-component of fluctuating velocity for $80\mu m$ particles as calculated by the G&I on the left and the KS2 models on the right. Note that the domain is restricted to show only the particles lying close to an equatorial plane.

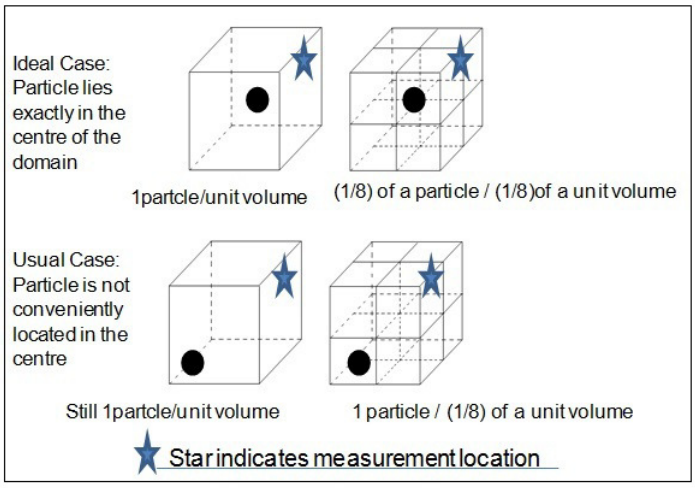

Figure 95: Schematic indicating the particle number density evaluation problem; For the two boxes on the top the number density evaluated at the measurement location will be the same, while for those at the bottom of the figure, the result will be completely different.

5.3.1 Evaluation of particle concentration

Before the quantitative comparison is performed, it is necessary to clarify how particle concentrations are evaluated for the remainder of this work. A problem arises in the standard definition of particle number density for computational meshes with varying mesh density. This may be seen in Figure 95, where a schematic is drawn indicating the issue at hand. The phenomenon is especially acute on unstructured meshes, or when mesh refinement occurs, and the measuring plane is located arbitrarily in space. It is just as much a problem in the test case, where the cell spacing is finer near the walls, since the usual method of evaluating number density of particles involves summation of the number of particles within a cell and dividing by the cell volume. The problem is exaggerated when comparing with experimental data where the measured experimental stations will rarely lie in areas corresponding to regions of uniform mesh density.

The solution adopted was to implement an analogue to the experimental approach for evaluating the concentration. The approach was developed by Hardalupas & Taylor (1989) for the measurement of particle concentration measured during Laser Doppler Velocimetry experiments near stagnation points, but can be adapted to a computational context. It involves measuring the transit time, τ_n, of every particle crossing the measurement probe and dividing by the sample time, T_S and the probe volume, V, according to:

$$C(d_i) = \frac{\left[(\sum \tau_n)_i / T_s\right]}{V\,(d_i)}$$

where the index relates to particle concentrations of different size classes.

In the present computational study, every cell becomes a "measurement probe" and the particle transit times are stored as they cross each cell[75]. Figures 96 & 97 depict the annuli

[75]Following a private communication with Braun (2014) of ANSYS, it was determined that a very similar procedure is adopted by the commercial ANSYS computational package where the residence time of every particle through every cell is stored in order to be able to evaluate the concentrations of Lagrangian particles.

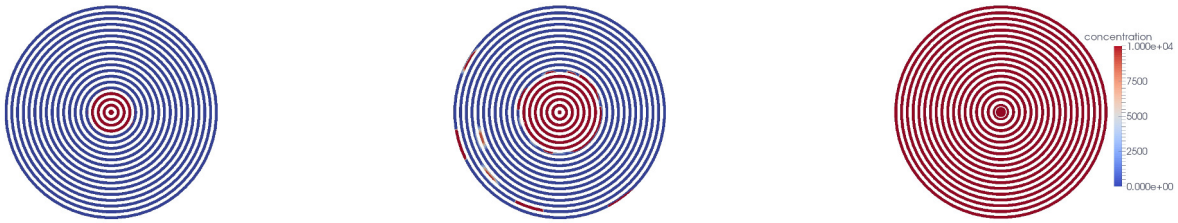

(a) at z/D=0.08 (b) at z/D=1.33 (c) at z/D=2.67

Figure 96: Sample instantaneous $40\mu m$ particle concentration representation of the concentration evaluation annuli of the domain. (Note: the concentration here has not been normalized)

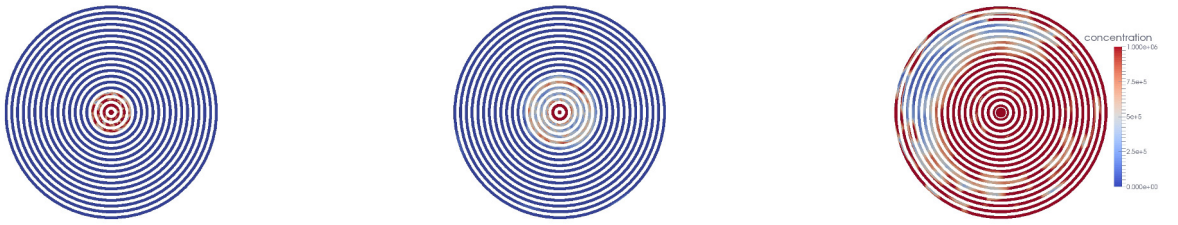

(a) at z/D=0.08 (b) at z/D=1.33 (c) at z/D=2.67

Figure 97: Sample instantaneous $80\mu m$ particle concentration representation of the concentration evaluation annuli of the domain. (Note: the concentration here has not been normalized)

used for circumferential averaging that will be presented shortly during the comparison with the experimental data. Figure 98 shows the three measurement stations downstream of the step at z/D = 0.08, 1.33 & 2.66, where the origin of the ordinate system is on the centreline at the step location. Meanwhile, Figures 99 & 100 show sections through the plane of symmetry of the domain and the evaluated instantaneous particle concentrations for both mass loading cases. The improved predictive capability of the KS is visible as the contour plots resemble the LES predictions closer; this is also true for the ML2 conditions (Figures 99b & 100b) . The cells used as "measurement probes" were averaged in the circumferential direction, which explains why in Figures 101 through 104, depicting the comparisons between measured and computed particle concentration, the latter only extends over half the extent of the abscissa.

Mass Loading Condition 1

So far only a qualitative comparison has been made. We will now show how the particle concentrations compare for the two particle size classes against the LES and experimental data. In both cases, measurements are for three spanwise locations at z/D= 0.08, 1.33 & 2.66. Figures

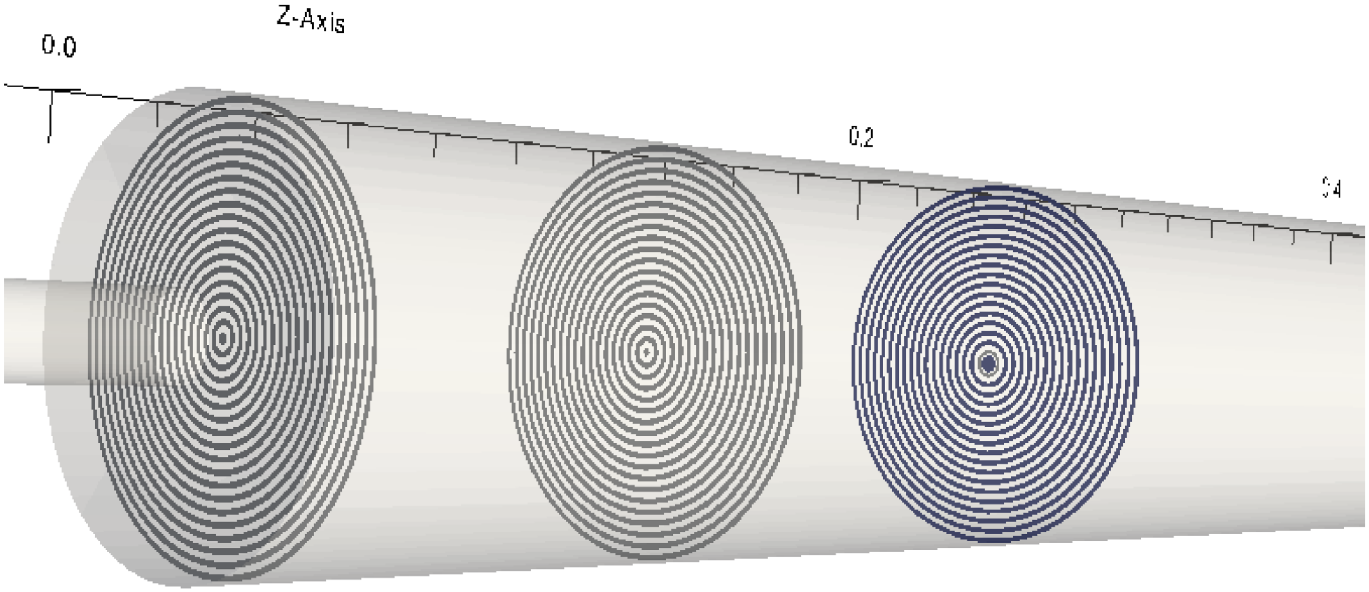

(a) Perspective view of the computational domain showing the three measurement locations at z/D=0.08, 1.33 & 2.66 from left to right with the step visible on the left

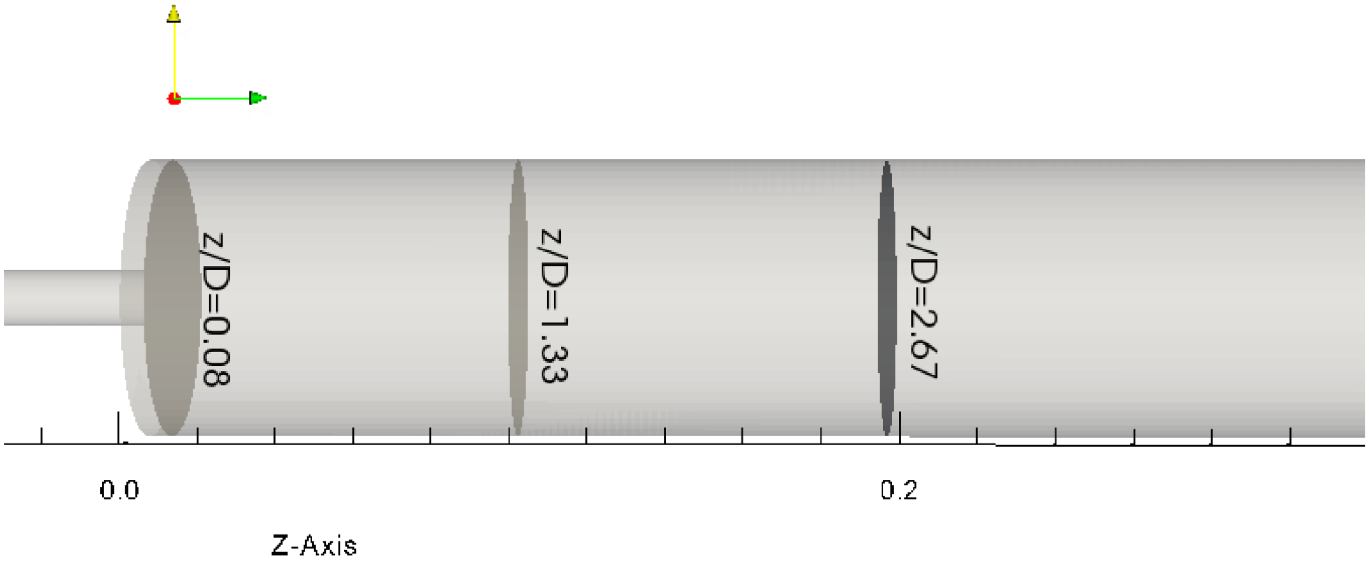

(b) Plan view of the computational domain showing the three measurement locations at z/D=0.08, 1.33 & 2.66 starting from the step

Figure 98: Schematic depiction the three spanwise stations in the pipe at z/D=0.08-1.33-2.66

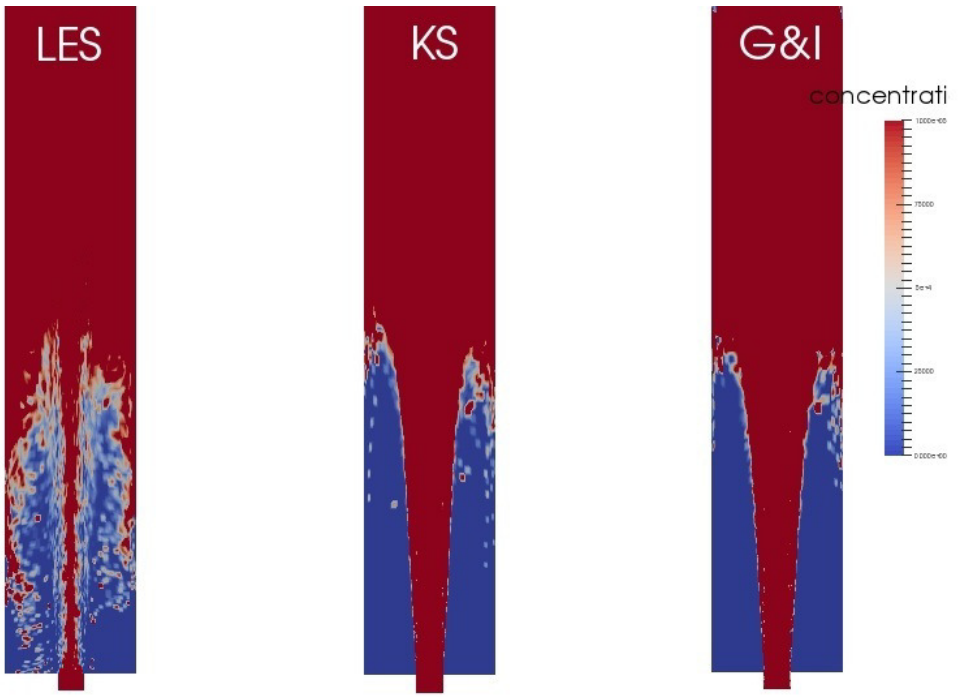

(a) ML1 - the extent of the domain has been clipped near the outlet

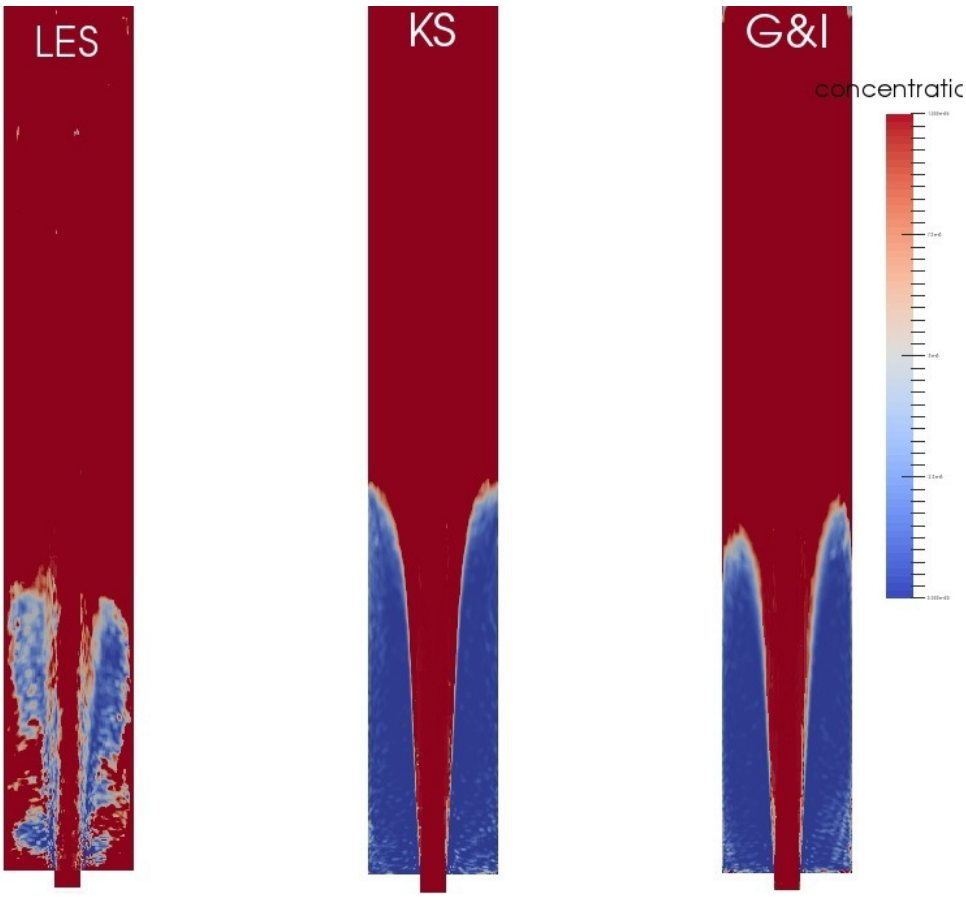

(b) ML2

Figure 99: Eulerian representation of instantaneous particle concentrations - $40\mu m$ particles, section through a plane of symmetry. Flow direction is from the bottom to the top of the page. (Note: the concentration here has not been normalized)

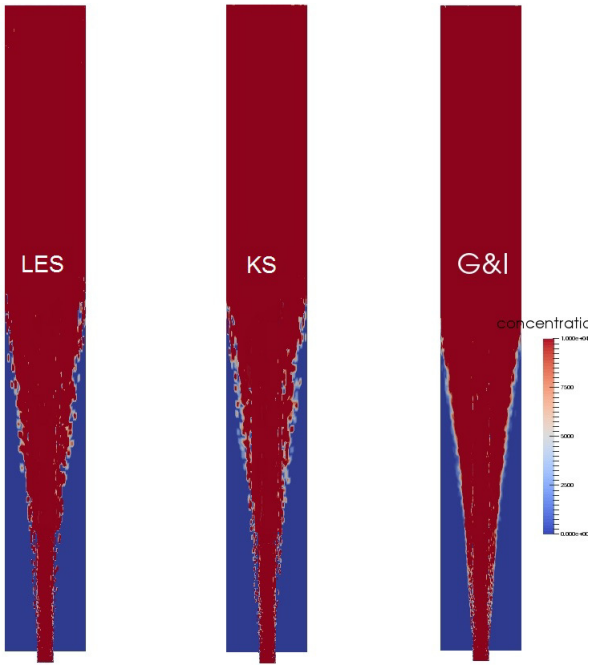

(a) ML1

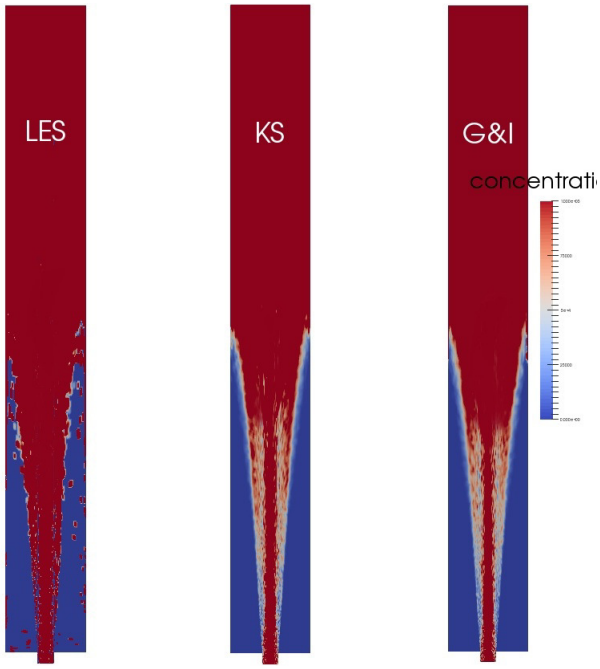

(b) ML2

Figure 100: Eulerian representation of instantaneous particle concentrations - 80μm particles, section through a plane of symmetry. Flow direction is from the bottom to the top of the page. (Note: the concentration here has not been normalized)

101 & 102, for the $40\mu m$ and $80\mu m$ particles respectively, show the good agreement between calculations and experiments for the low mass loading case, ML1, note that the ordinate is logarithmic.

The concentrations have been normalized in a similar manner to Hardalupas *et al.* (1992) from which the experimental data is taken in order to generate a dimensionless quantity. Near the centreline, we see that all three simulations slightly over predict concentration. For the two uRANS models, this can be attributed to the fact that the *k-Epsilon* model under predicts the velocity along the centreline. An under-predicted velocity would result in the particle transit time through the measurement volume being over predicted and hence resulting in a larger concentration. The effect is more pronounced for the smaller size class, where there is the compounding effect of accurate estimation of drag coefficients. These are still associated with a large degree of uncertainty due to the difficulty in obtaining accurate experimental data and the effect is more pronounced near the centreline where the velocities are higher.

In Figures 101 & 102, for the $40\mu m$ and $80\mu m$ particles repsectively, as one moves away from the centreline in the physical domain, the agreement deteriorates. This is at least partly a result of the statistical uncertainties of the calculations, since the sampling for the experimental measurements is performed over several minutes rather than a few seconds, which is the case for the calculations. Even though several flow-through times are modeled, longer values are necessary to build up statistically significant averages as the velocity field within the recirculation zone is transporting the particles upstream at a significantly smaller velocity than that of bulk velocity in the downstream direction. This explains why even the LES calculations are under predicting the concentration near the wall even more than the stochastic models as there were fewer flow through times calculated and averaged for the LES calculations.

Near the expansion tube walls (y/D=|0.5|) the experimental data show very large concentrations and this was the result of the tendency of a large percentage of particles to adhere to the expansion tube walls. As it is very hard to quantify the exact percentage that stick to the wall, the calculations do not reflect this phenomenon and all particles are modeled to rebound elastically off the wall (billiard-ball model). The effect is that far downstream of the expansion step (several inlet diameters downstream of the recirculation zone), we expect our calculations, when compared to the experimental data, to over-predict the concentration in the near wall regions but to under-predict it on the wall. Overall, the proposed model shows acceptable agreement, especially for the $80\mu m$ particle class size, with the LES and experimental data of Hardalupas *et al.* (1992), outperforming the GI based model.

Mass Loading Condition 2

Figures 103 & 104 present the comparison between the experimental data and calculations based on the dispersion models for the higher mass loading case, ML2. The agreement is improved for the higher mass loading cases and the effects of the aforementioned limitations seem to be reduced due to the larger number of particles present providing improved statistics for the comparison of the calculations. This results in smaller error bands (calculated from the standard deviation of each circumferential averaging annulus variation over time) for the measurements near the walls especially for the two measurement stations within the recirculation zone at z/D=

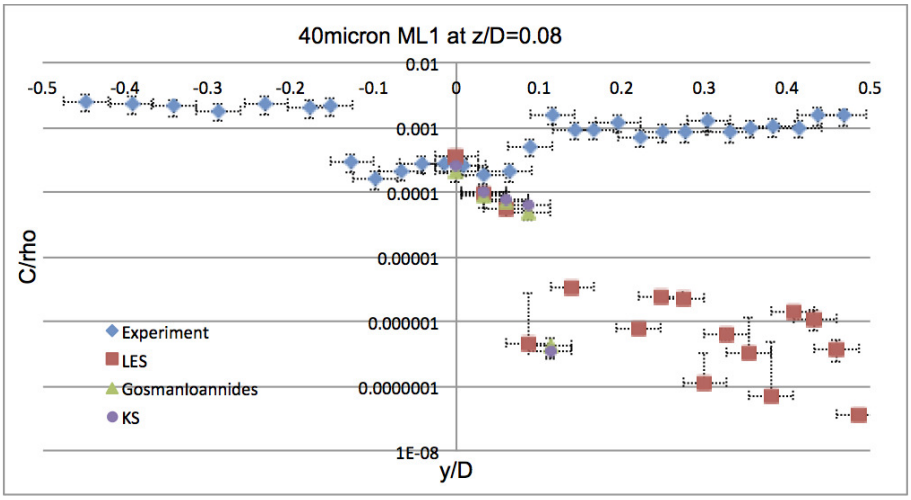

(a) at z/D=0.08

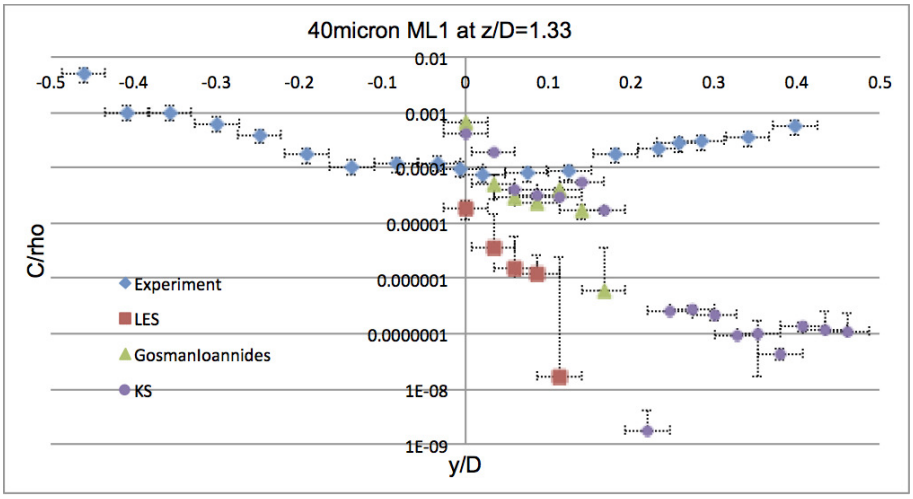

(b) at z/D=1.33

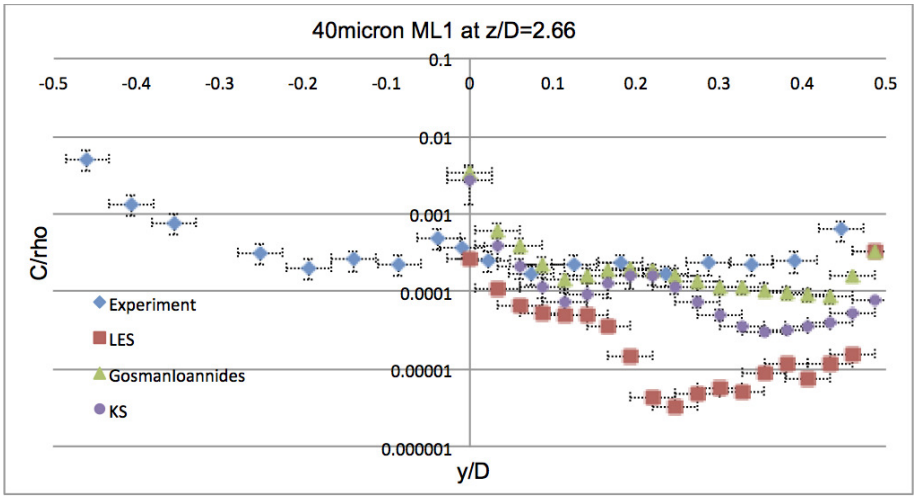

(c) at z/D=2.67

Figure 101: 40μm-ML1 condition

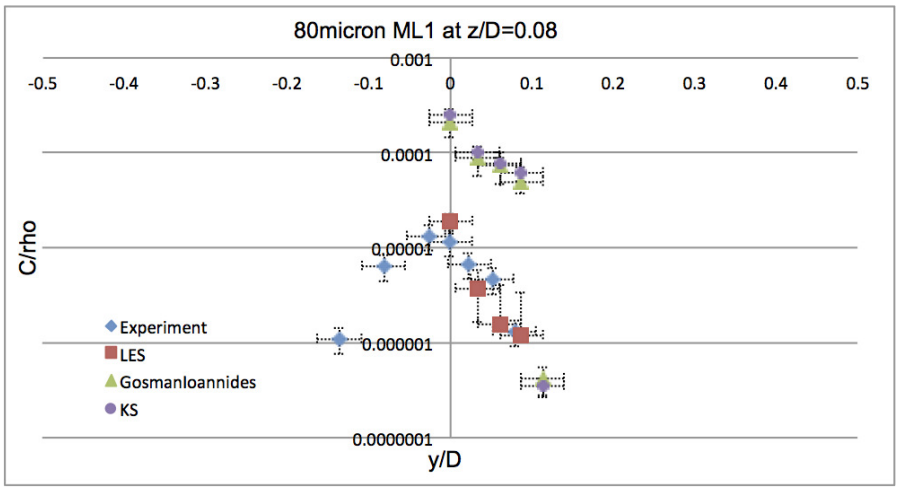

(a) at z/D=0.08

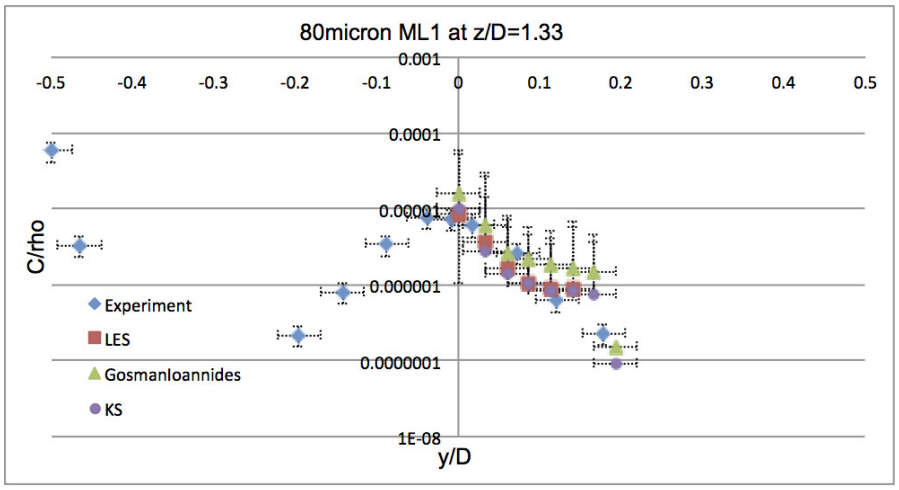

(b) at z/D=1.33

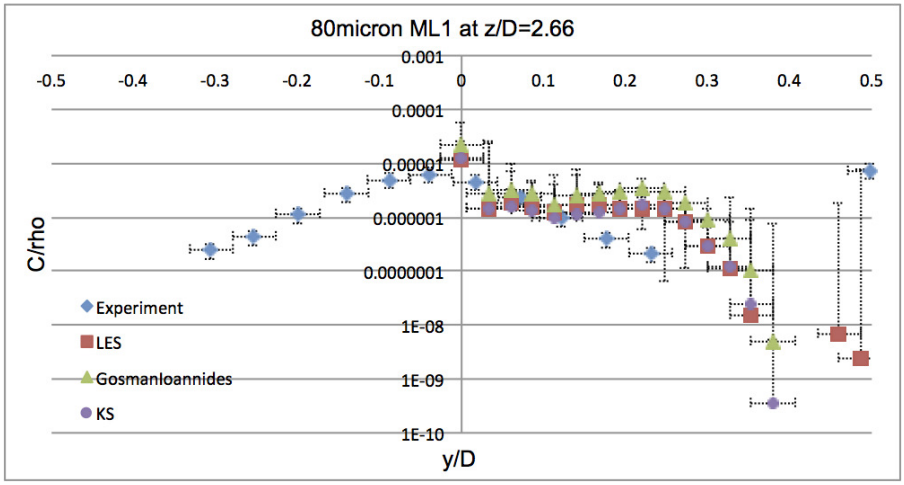

(c) at z/D=2.67

Figure 102: 80μm-ML1 condition

0.08 & 1.33.

Overall, agreement for the ML2 conditions is improved over that for the ML1 conditions, attributable to the greater number of particles in the computational domain improving the quality of the statistics. For both mass loading conditions the agreement between all the calculations and experimental measurements is improved at the farther downstream measurements stations over those close to the step. A result of the well-mixed conditions further downstream in the expansion tube and of the discrepancies between the calculated continuous and discrete phases just before entrance into the expansion tube discussed in Chapter 3. There is further small improvement at the downstream measurement stations between the LES predictions for the two particle size classes; it appears that for the limited simulation time available, the absence of clustering for the $80\mu m$ particles improves the agreement between calculations and experiments due to the greater predicted spatial uniformity. This is also true for the two RANS dispersion models where the greater spatial uniformity –compared to the LES predictions– improves the agreement with the experimental data.

5.3.2 Quantitative comparison of fluctuating velocity components

This section quantifies the information presented in the qualitative comparison presented earlier in section 5.2. The comparison is made by looking at the probability functions of the individual velocity components generated by the dispersion models for the $80\mu m$ particles for the higher mass loading case, ML2. The histograms are presented in Figures 105 to 109. Once again the study is restricted to those particles lying in the region within the recirculation zone ($z \sim [0 - 0.3m]$) in order for the individual differences to be better highlighted. Here a comparison is also made between the two distinct implementations of the KS models, KS1 & KS2 and the GI model, as up until this point only results from the KS2 model have been shown. In all cases the extent of the abscissa extends to the extremities of the range predicted by the corresponding model. Both KS1 & KS2 models predict a greater range of fluctuating velocities components than the GI model; that is to say, the variance is significantly larger for all three fluctuating velocity components. Between the KS1 and KS2 it is evident that the latter results in an even greater variance, a result of the fact that for KS1 both the energy content and the range of wavespace extent were computed from mean values and then scaled by the local value of the turbulence intensity. An important point that needs to be made relates to the shape of the distributions. In the GI model the Gaussian shape is prescribed (*i.e.* the shape is known beforehand from the construction of the model), whereas for the KS models this is a result (*i.e* a simulation outcome) and in turn a confirmation of the validity of the method's implementation.

The analysis continues by presenting combined plots for the individual fluctuating velocity components of the three individual dispersion models shown in Figure 108. The abscissa here has been restricted in order to draw attention to the slight differences in the shapes of the distributions where the smaller kurtosis of KS2 is evident.

It is worth pointing out that what appears to be a 'spike' about the mean and is more pronounced in the KS2 than in the KS1 model, is a result of having generated these statistics from all of the particles in the aforementioned region and there is a significant number of particles which either lie on the wall or do not interact with an 'eddy' and hence the fluctuating velocity

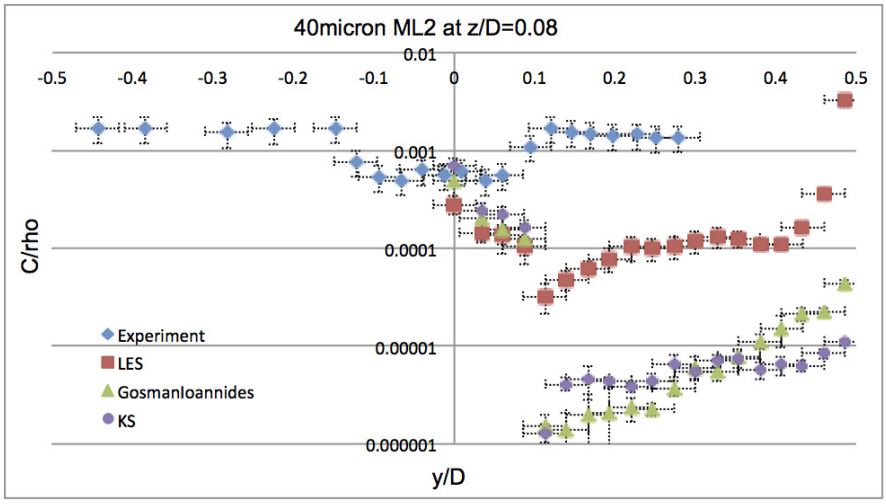

(a) at z/D=0.08

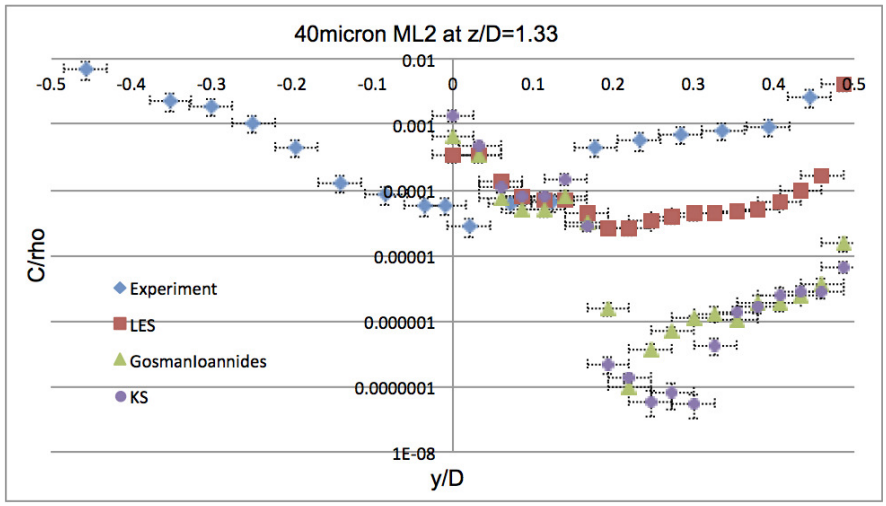

(b) at z/D=1.33

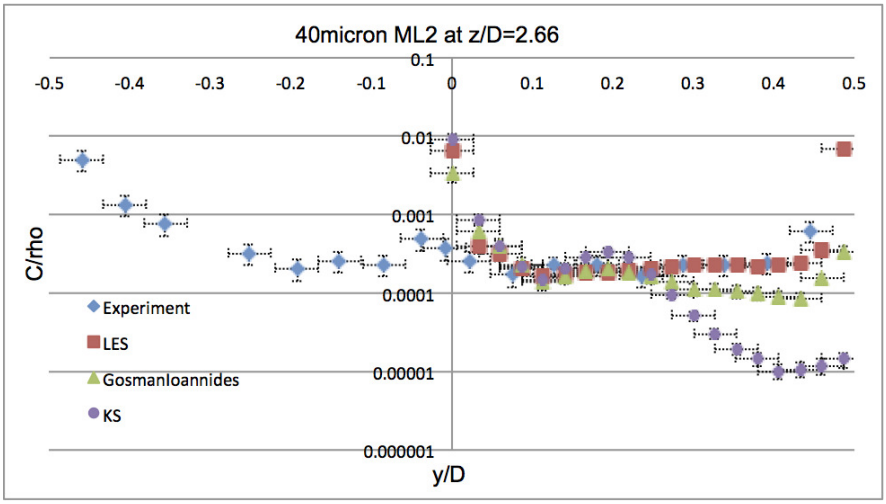

(c) at z/D=2.67

Figure 103: 40μm-ML2 condition

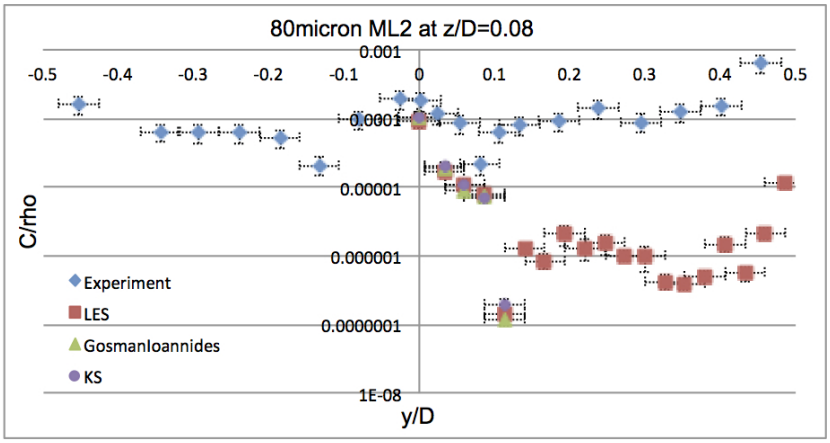

(a) at z/D=0.08

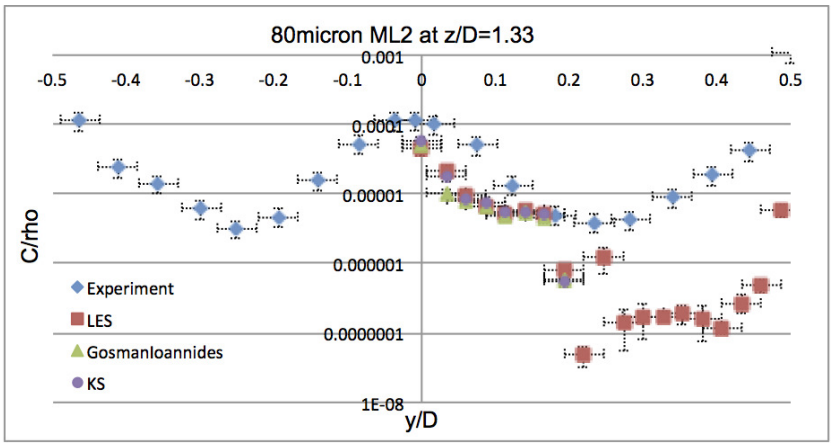

(b) at z/D=1.33

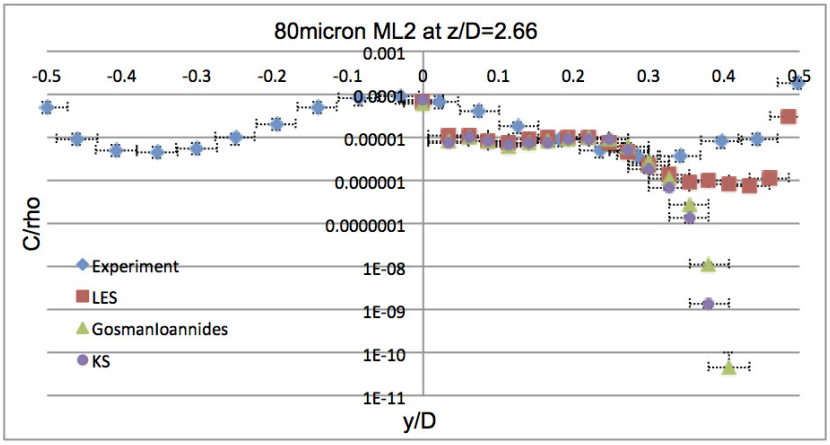

(c) at z/D=2.67

Figure 104: 80μm-ML2 condition

component prescribed is zero. This is also true of the GI model but the smaller variance and greater kurtosis means that is a less pronounced feature.

Finally, for illustrative purposes a comparison is made between the velocity components generated by the RANS and LES calculations and is presented in Figures 109. Differences in the results between the RANS models are not expected to be significant since the main contribution to the mean velocity of the particle comes from the surrounding fluid which should be very similar for all RANS cases. As far as the comparison between LES & RANS is concerned, noticeable differences are observed for the z-component of velocity only. The LES predictions exhibit a bimodal pattern, with a strong lower peak being associated with negative velocities and a comparatively (by comparison with the uRANS calculations) less pronounced peak at the far end of the positive velocity range. The first is attributed to the larger number of Lagrangian particles predicted to be within the recirculation zone of the LES calculation while the latter is attributed to the fact that the LES calculations predict a less uniform axial velocity near the centreline for the Eulerian phase due to the amount of large scale oscillations observed and greater range of modeled scales; this in turn affects the Lagrangian velocities. Both of these differences indicate that the chosen dispersion model should generate fluctuating velocities that have greater kurtosis and standard deviation than the GI modeld since both of these attributes will reduce the uniformity in the predicted velocity –especially in the axial direction– after the fluctuating components have been added to the mean velocity components. This last section has focused on demonstrating that the dispersion model presented in the thesis possessed both of these attributes and provides further support for the suitability of the KS dispersion model over the currently employed models.

5.4 Summary

To conclude, a novel phenomenological dispersion model for coupled Eulerian-Lagrangian frameworks has been developed. This is based on the standard RANS solvers for modeling the large sweeping structures of the mean flow and then Kinematic Simulations are introduced to model the effect of the inertial and dissipative ranges of the turbulent flow on the dispersion of particles calculated in a Lagrangian framework. The interaction of a particle with an inadequately resolved –whether averaged or filtered out– 'eddy', –whose size, range of scales and intensity are determined from the local Eulerian conditions– is accounted for through the generation of a fluctuating velocity component.

Initial validation was performed through comparison of the proposed model against the most commonly used dispersion model for RANS simulations, LES and experimental data. Further calculations with larger mass loadings were performed to confirm the promising initial results. Additionally, the validation process required the development of a novel approach, in the CFD context, for accurately estimating particle concentrations without relying on the evaluation of number density based on an instantaneous approach rather, adoptinga time of a 'time of flight' approach.

Quantitative and qualitative analysis has been performed and the proposed model addresses the limitations of the currently employed model. Improved agreement was noted between the proposed model and the experimental results and LES calculations, over that of the GI model, on

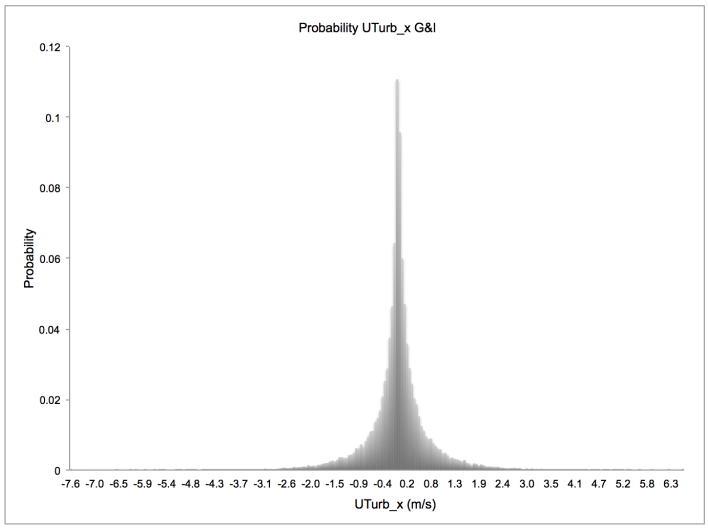

(a) G&I

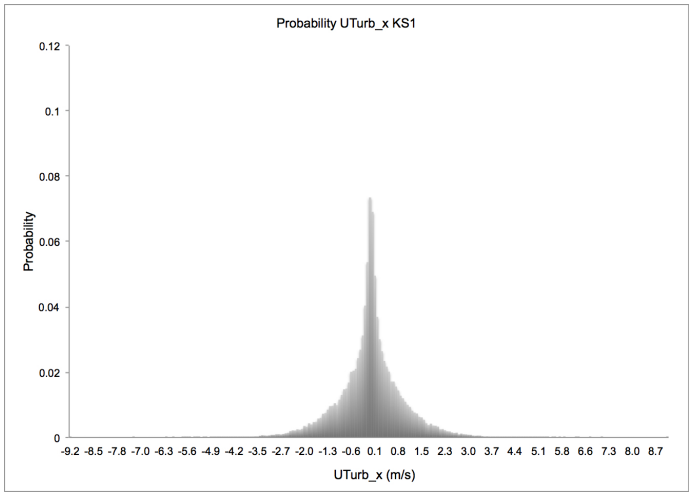

(b) KS1

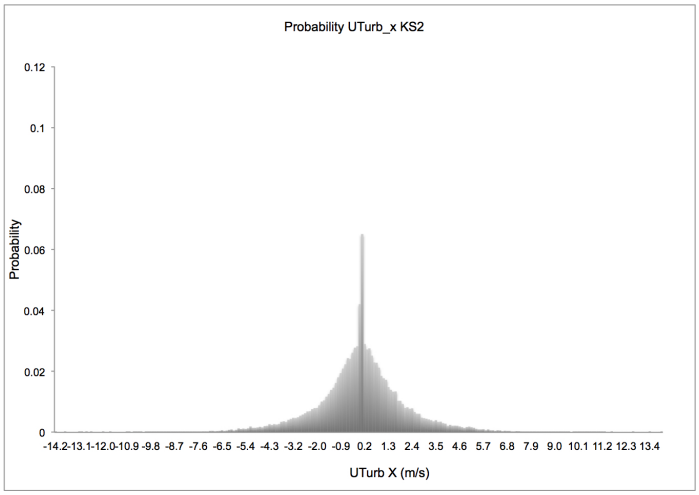

(c) KS2

Figure 105: Comparison of the probability of occurrence of the particle fluctuating velocity component, $\mathrm{UTurb_x}$, calculated from the dispersion models restricted to those particles lying within the recirculation zone.

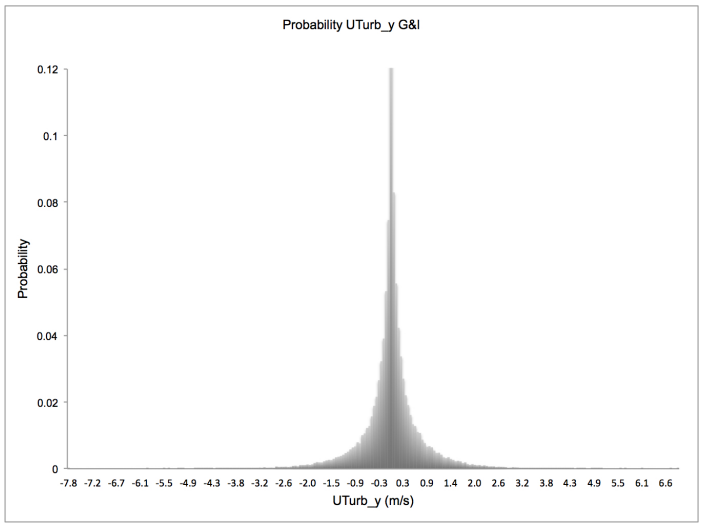

(a) G&I

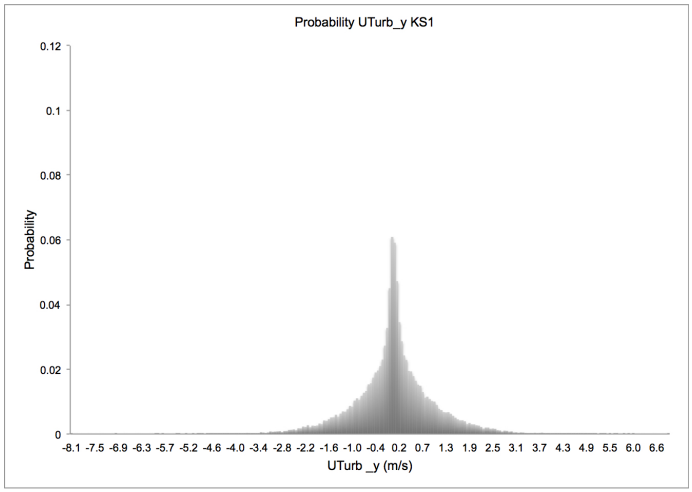

(b) KS1

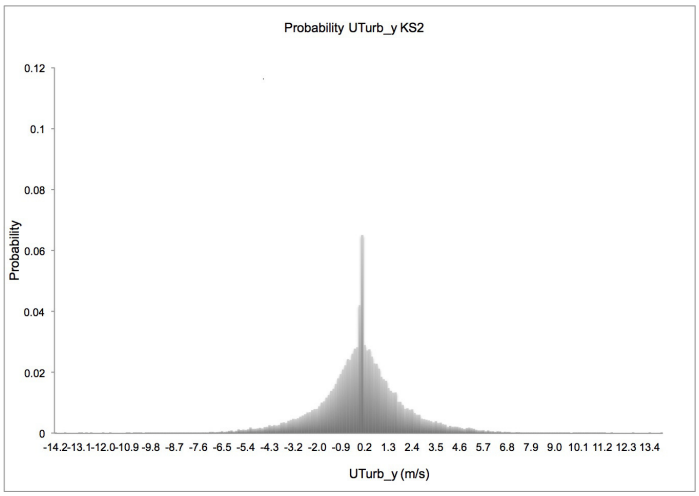

(c) KS2

Figure 106: Comparison of the probability of occurrence of the fluctuating velocity component, $UTurb_y$, calculated from the dispersion models restricted to those particles lying within the recirculation zone.

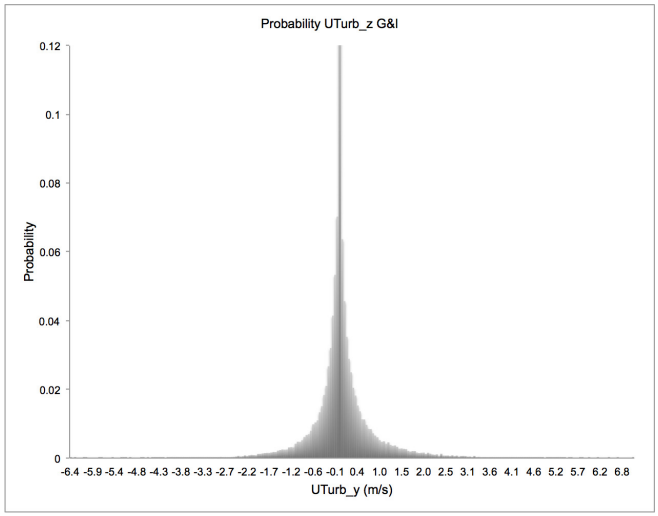

(a) G&I

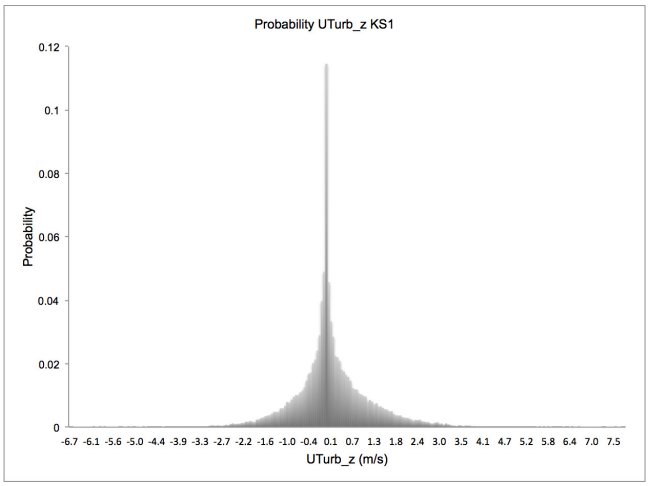

(b) KS1

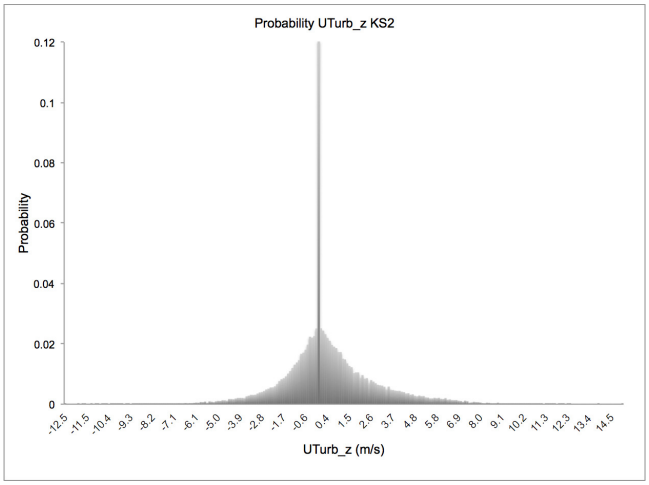

(c) KS2

Figure 107: Comparison of the probability of occurrence of the particle fluctuating velocity component, $UTurb_z$, calculated from the dispersion models restricted to those particles lying within the recirculation zone.

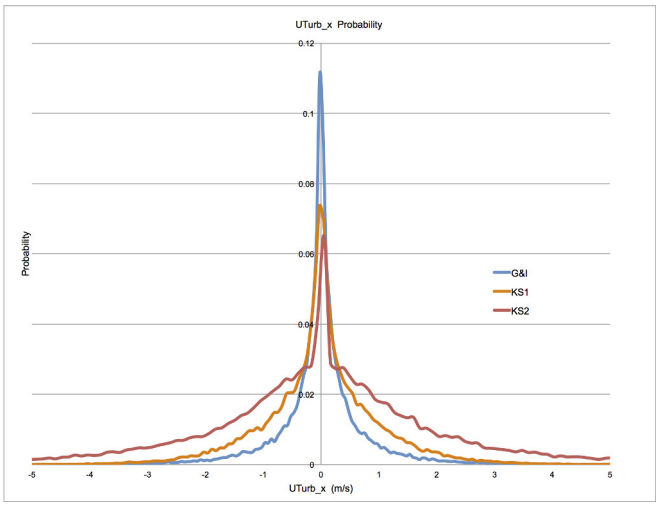

(a) $\mathrm{UTurb_x}$

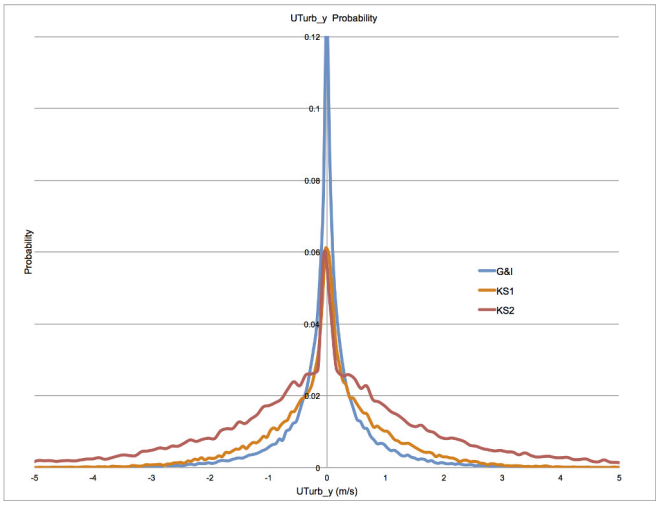

(b) $\mathrm{UTurb_y}$

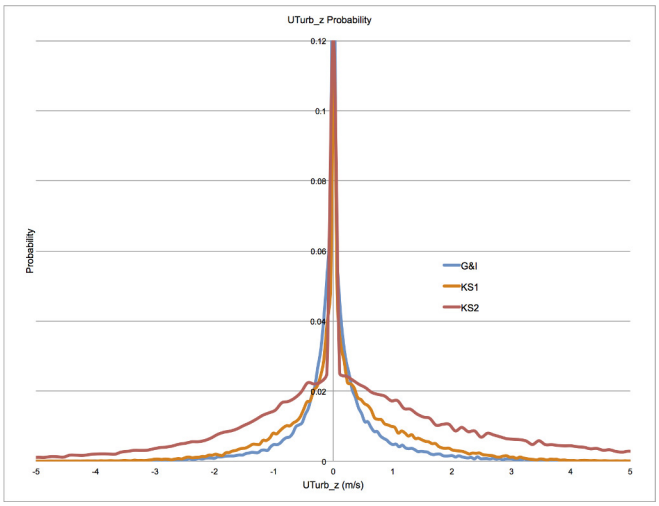

(c) $\mathrm{UTurb_z}$

Figure 108: Comparison of the probability of occurrence of the particle fluctuating velocity components, calculated from the dispersion models restricted to those particles lying within the recirculation zone.

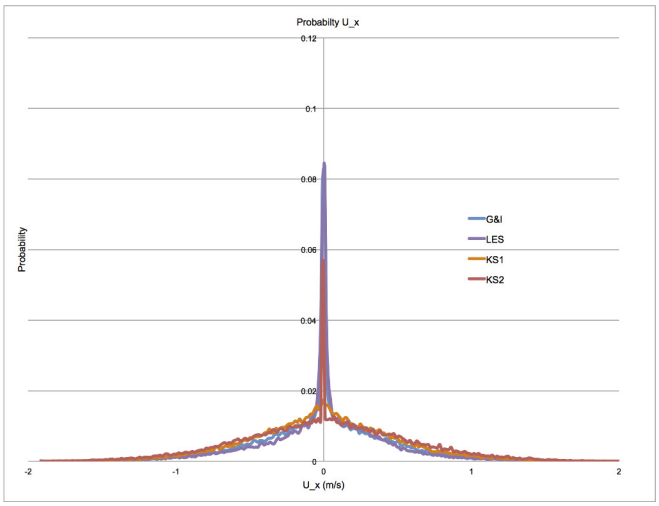

(a) U_x

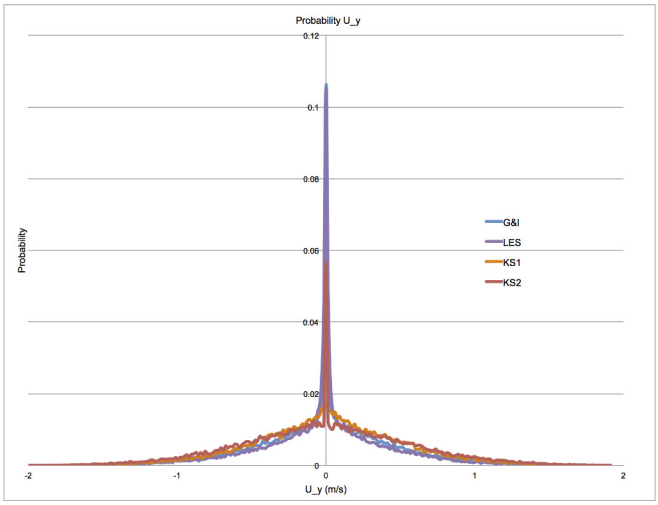

(b) U_y

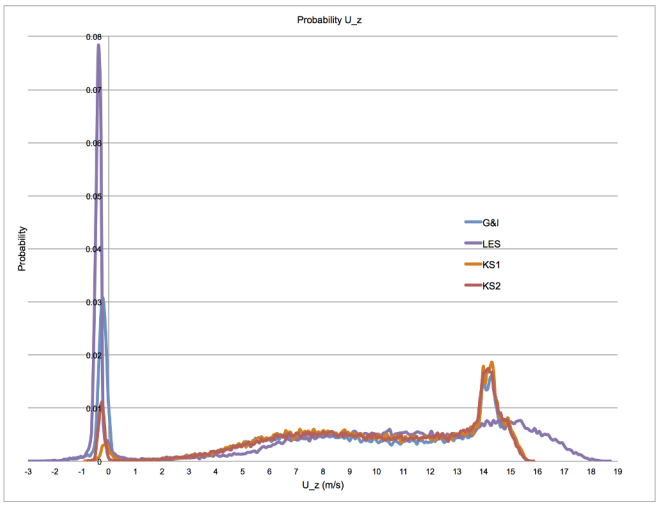

(c) U_z

Figure 109: Comparison of the probability of occurrence of the particle velocity components, calculated from the dispersion models, and restricted to those particles lying within the recirculation zone.

the axisymmetric sudden expansion test case. Subsequently, the proposed model was provided to the industrial sponsors of this work for testing on their proprietary CFD package with promising results reported for two industrial geometries (results included in Appendix C).

6 Future work & Conclusions

6.1 Summary

- The industrial and the engineering community have recognized a need for improved particle dispersion models. The completed literature review has identified that there exist computational tools to accurately describe particle dispersion and preferential concentrations. However the cost associated with such calculations remains prohibitively expensive. The implication is that there is a need within the community, especially the industrial one, for a model that is capable of producing improved particle dispersion characteristics without the costs associated with the more expensive methods. The model proposed in this thesis does not aspire to describe all the physics accurately. Rather it will introduce, in a phenomenological sense, some of the characteristics of the more costly methods in an effort to allow industrial codes to predict spatial and temporal non-uniformities of particle concentrations and more realistic dispersion properties.

- A custom, coupled Eulerian-Lagrangian solver was developed for unsteady incompressible flows since such a solver was missing from the standard distribution of openFOAM. The solver developed was capable of using a wide range of Lagrangian sub-models present within openFOAM such as collision, injection and dispersion models amongst others. It is this flexibility and adaptability available within openFOAM that was the main reason for its selection and use as a base to develop the proposed phenomenological dispersion model.

- The developed Eulerian-Lagrangian solver for the RANS and LES calculations was evaluated on the axisymmetric sudden expansion test case. The test case was introduced along with an investigation to determine the required mesh resolution. This was followed by a validation of the solver's capabilities. First, in terms of the Eulerian phase through the comparison of the calculations and the experimental data which showed acceptable agreement between the measured quantities and predicted recirculation zones; and subsequently in terms of the Lagrangian phase where good agreement was observed. The results from the calculations demonstrate the formation of instantaneous particle clusters in the flow for the $40\mu m$ particles; but not for the $80\mu m$ particles. An effort was made to identify dominant vortical structures throughout the LES calculation, using enstrophy, vorticity and the 2^{nd} invariant of the velocity gradient tensor, but this posed several difficulties primarily due to the complexity of the flow. No clear correlation was identified between the location of particle clusters and these characteristic features of the gas phase. Finally, *Voronoi* analysis was used to quantify the scale of the particle clusters which indicated that the cluster dimensions, in the cross-stream direction, could be of the order of the downstream, expansion tube radius. This is much larger than the cluster dimensions reported in the literature from DNS calculations of isotropic turbulence, which tend to link the size of the clusters to the *Kolmogorov* scale..

- A novel phenomenological dispersion model was developed for coupled Eulerian-Lagrangian frameworks. This is based on the standard RANS solvers, for modeling the large sweeping

structures of the mean flow and then Kinematic Simulations are introduced to model the effect of the inertial sub-range of the turbulent flow on the dispersion of Lagrangian particles. The interaction of a particle with an under-resolved 'eddy' is accounted for through the evolution of this particle through an isotropic turbulent field that has been created using Kinematic Simulations. The energy content and extent of scales of this field are determined from the local Eulerian properties of the under-resolved 'eddy'. Qualitative comparisons between the proposed model and the G&I dispersion model showed differences in the underlying dispersion mechanisms as well as marked differences in particle trajectories when used as a dispersion model through identical flow-fields. This may be attributed to the underlying mechanisms of each model. In the G&I model, the particle pair separates gradually and a sudden change in particle pair separation distance occurs when the particles are eventually advected apart by the larger, resolved scales of the flow. In contrast, the KS is capable of modeling the sudden separation even within the unresolved scales. This is an important point to note, as the intended use of such models is primarily for the unresolved scales of a flow-field and should result in increased overall dispersion.

- Validation of the phenomenological dispersion model was performed through comparison of the proposed model against the most commonly used dispersion model for RANS simulations, that is the G&I model, LES and experimental data. Further testing with larger mass loadings was performed to confirm the promising initial results. Additionally, the validation process required the development of a novel approach, in the CFD context, for accurately estimating particle concentrations without relying on a number density approach. Quantitative and qualitative analysis has been performed and the proposed model addresses the limitations of the currently employed model, predicting increased particle entrance within the recirculation zone. Good agreement was noted between the proposed model and the experimental results and LES calculations.

- Finally, Appendix C shows the proposed model developed within this theis provided to the industrial sponsors of this work for integration within their proprietary CFD software and tested on an industrial geometry of an aviation gas-turbine combustor currently in flight with promising initial results.

6.2 Recommendations for Future Work

- The present work has validated the use of KS within a RANS framework. The first step was to establish the validity of the method through its use as a dispersion model. Having shown that it addresses some of the limitations of the presently available models and shows good comparison with experimental results and more costly computational methods, a logical next step is to take advantage –even if it is limited to the phenomenological level– of the improved physical representation of turbulence provided by the KS method. That is, to investigate the method's ability to predict preferential concentrations on the smaller scales (those modeled by KS) within the RANS framework. The literature review has identified that the method is capable of predicting preferential concentrations and has also shown that it is capable of such predictions across a range of scales, capturing the self-similar

nature of the phenomenon. The present proposition is to take advantage of these abilities of KS and to predict preferential concentration at the smaller scales. One way of doing this would be to track the evolution of neighboring particles –say those that are separated by a distance smaller than the *Kolmogorov* scale– through the same KS field. Such an approach would might allow the RANS method some of the KS method's ability to predict clusters.

- A worthwhile pursuit would be further development and testing of the KS dispersion model within an uncoupled Eulerian-Lagrangian RANS solver where the particle position (in addition to its velocity) would be adjusted according to the KS trajectory. Such a version has been developed and tested with the solver being stable for small mass loadings. What is required, now, is the identification of a suitable test case for validation purposes. Such a version of the dispersion model would be particularly suited for modeling larger geometries, such as pollutant dispersion in environment-scale flows.

- The proposed model could be adapted for use within the LES environment. In this context the KS model would be used as an SGS model for particle dispersion in cases where the grid was relatively coarse and the *Stokes* number of the grid was small. Such modifications have already been carried out and a suitable test case is currently being sought. Additionally, it need-not be limited to the Lagrangian phase but could be adapted for use as an SGS model to improve the prediction of the mixing of scalars within the unresolved scales.

- The increased computational cost of the KS dispersion model over the G&I model was small, in the region of 10-15% as measured by both the author and the industrial partner, when implemented within their CFD package and tested on their geometries. There may be room for improvement of the code structure in order to reduce the computational overheads although this was not examined as such modifications would have increased the efforts required by the project partners during integration within their proprietary CFD code.

- An interesting development of the KS dispersion model abilities would be to investigate the potential for use in wall bounded or stratified flows, regions where the hypothesis of isotropic turbulence is not applicable. This could be achieved by prescribing separate turbulent energy spectra for the principal directions or changing the prescribed exponent of the energy spectrum.

- Finally, the LES results showed some interesting features in terms of the size of the clusters that were formed. It could be a worthwhile endeavor to investigate how these clusters are formed and for how long these persist in addition to correlating their formation and evolution with the surrounding flow structures.

6.3 Conclusions

This thesis has shown that the initial hypothesis of combining a spectral method with the standard RANS simulations for improved modeling of the dispersed phase is promising one.

Kinematic Simulations were introduced to provide a more realistic representation of turbulence with which the discrete phase interacts with, given the absence of small scale resolution in a RANS simulation. The effect of the large flow scales on the particles are modeled with RANS while Kinematic Simulations are employed for the modeling of the inertial and dissipative ranges.

The improvement observed after introducing the dispersion model in this thesis may be attributed to the fact that the prescription of the fluctuating velocity component of the continuous phase which is 'sampled' by the Lagrangian phase is no longer based on the 'one time' event drawn from a Gaussian distribution. Rather, the interaction of a particle with an under-resolved 'eddy' is accounted for by evolving the particle through an isotropic turbulent field. This field is constructed with Kinematic Simulations, a relatively non-costly computational method. The energy content and spatial extent of scales of the isotropic field are determined from the local Eulerian properties independently every time a particle meets an under-resolved 'eddy'. The evaluation of the proposed model was performed on a simple well documented test case and showed good agreement with experimental results and LES calculations.

The validation of the particle concentrations required the development of a new method for evaluating particle number density. Inspired by a experimental technique, the new method requires the evaluation of the particle residency time within each cell and removes many of the issues associated with the evaluation of concentrations on non-uniform or unstructured grids. In addition, *Voronoi* analysis was performed on the outcome of the LES calculation for the identification of particle clusters. These were found to be of the order of the expansion tube radius, much larger than *Kolmogorov* sized clusters identified in DNS calculations.

Further testing of the proposed model was performed on industrial geometries by the industrial sponsors of this work. These tests confirmed the relatively small increase in computational overhead required by the proposed method compared to the presently used dispersion model. Most important, though, was the observation of significant differences between the particle trajectories computed with the proposed model and those with a model widely used in industry. This last point is of particular significance as one of the limitations of the currently used models was the high degree of spatial uniformity in the predicted particle distribution. This was addressed by the present model both on the basic test case but also on the industrial geometry.

Having validated the proposed model's implementation as a a dispersion model it is deemed a worthwhile endeavor to further extend and investigate its capabilities, since Kinematic Simulations provide a substantially improved representation of turbulence that can reproduce clustering and the higher order statistics of the dispersed phase.

References

[1] R.J. Adrian, K.T. Christensen & Z-C. Liu, 2000, Analysis and interpretation of instantaneous turbulent velocity fields, Experiments in Fluids, Vol. 29, p. 275-290

[2] R.J. Adrian & Z-C. Liu, 2002, Observations of Vortex Packets in Direct Numerical Simulation of Fully Turbulent Channel Flow, Journal of Visualization, Vol. 5, No.1, p. 9-19

[3] V.I. Arnold, 1988, Geometrical Methods in the Theory of Ordinary Differential Equations, 2nd Ed., A series of Comprehensive Studies in Mathematics, Springer-Verlag

[4] D. Baldocchi, 1992, A Lagrangian random-walk model for simulating water vapor, CO2 and sensible heat flux densities and scalar profiles over and within a soybean canopy, Boundary Layer Meteorology, Vol. 61, p. 113-144

[5] J. Bardina, J.H. Ferziger & W.C. Reynolds, 1983, Improved turbulence models based on Large Eddy Simulation of homogeneous incompressible turbulent flows, Report No. TF-19, Thermosciences Division, Dept. of Mech. Eng., Stanford, CA, p. 1-183

[6] A.B. Basset, 1888, On the motion of a sphere in a viscous liquid, Philosophical Transactions of the Royal Society London, A, 179, p. 43-63

[7] G.K. Batchelor, 1950, The application of the similarity theory of turbulence to atmospheric diffusion, Quarterly Journal of The Royal Meteorological Society, Vol. 76, p. 133-146

[8] G.K. Batchelor, 1952, Diffusion in a field of homogeneous turbulence - The relative motion of particles, Proceedings of The Cambridge Philosophical Society, Vol. 48, No.2, p. 345-362

[9] G.K. Batchelor, 1957, Diffusion in free turbulent flows, J. Fluid Mechanics,Vol. 3, p. 67-80

[10] G. K. Batchelor & A.A. Townsend, 1956, Turbulent Diffusion, Surveys in Mechanics, The University Press, Cambridge

[11] A. Berlemont, P. Desjonqeres & G. Gouesbet, 1990, Particle Lagrangian simulations in turbulent flows, Int. J. Multiphase Flow, 16, p. 19-34

[12] L. Biferale, G. Boffetta, A. Celani, B.J. Devenish, A. Lanotte & F. Toschi, 2005, Lagrangian statistics of particle pairs in homogeneous isotropic turbulence, Physics of Fluids, Vol. 17, p. 1-16

[13] G. Birkhoff & E.H. Zarantonello, 1957, Jets, Wakes and Cavities, Applied Mathematics and Mechanics Monographs, Academic Press, New York

[14] R. B Bird, W.E. Stewart & E.N. Lightfoot, 1960, Transport Phenomena, John Wiley & Sons

[15] R.N. Bracewell, 1986, The Fourier Transform and its Applications, Revised 2nd Edition, McGraw-Hill

[16] M. Braun, 2014-September-12, Private communication, Bremen, Germany

[17] G. Boffetta, F, De Lillo & A. Gamba, 2004, Large Scale inhomogeneity of inertial particles in turbulent flows, Physics of Fluids, Vol. 16, p. 20-23

[18] M.S. Borgas & B.L. Sawford, 1994, A family of stochastic models for two-particle dispersion in isotropic homogeneous stationary turbulence, J. Fluid Mech., Vol. 279, p. 69-99

[19] J. Boussinesq, 1877, Theorie de l'ecoulement tourbillant, Mem. par.div. Sav., Paris, p. 1290-1295

[20] J. Boussinesq, 1903, Theorie Analytique de la Chaleur, L'Ecole Polytechnique de Paris

[21] R.S. Brodkey, 1967, The Phenomena of Fluid Motions, Addison-Wesley Publishing Company, Reading, MA, USA

[22] D. Burry & G. Bergeles, 1993, Dispersion of Particles in Anisotropic Turbulent Flows, Int. J. Multiphase Flow, Vol. 19, No. 4, p. 651-664

[23] L.S. Caretto, A.D. Gosman, S.V. Patankar & D.B. Spalding, 1972, Two calculation procedures for steady, three dimensional flows with recirculation., Proceedings Third International Conference on Numerical Methods in Fluid Dynamics, Paris, p. 60-68

[24] S. Chandrasekhar, 1961, Hydrodynamic and hydromagnetic stability, Dover Publications, New York

[25] C.Chicone, 1999 & 2006, Ordinary Differential Equations with Applications, 2nd Ed., Texts in Applied Mathematics, Springer

[26] E. Chronopoulos, 2005, Particle Pair Dispersion In Turbulent Flows, Thesis, University of London, Imperial College London

[27] S. Corrsin & M. S. Uberoi, 1949, Further Experiments on the Flow and Heat Transfer in a Heated Turbulent Air Jet, NACA Tech. Note No. 1865

[28] R. Courant, K. Friedrichs& H. Lewy, 1967, On the partial Differential Equations of mathematical physics, IBM J.Res.Develop, 11, p. 215-234, (Translated from R. Courant, K.O. Friedrichs & H. Lewy, 1928, Uber die partiellen Differenzigleichungen der matematishen Physik, Matematishe Annalen, 100:32)

[29] G.T. Csanady, 1963, Turbulent diffusion of heavy particles in the atmosphere. J. Atmos. Science, Vol. 20, p. 201-208

[30] L. Davidson, 2007, Using isotropic synthetic fluctuations as inlet boundary conditions for unsteady simulations, Advances and Applications in Fluid Mechanics, Vol. 1, Is. 1, p. 689-694

[31] DANTEC 2005, BSA Flow Software V4.10 - Installation & User Guide, 10th Ed., DANTEC DYNAMICS, Denmark

[32] S.M. Damian, 2013, An Extended Mixture Model for the Simultaneous Treatment of Short and Long Scale Interfaces, PhD thesis, Universidad Nacional del Litoral

[33] P.A. Davidson,Y. Kaneda, K. Moffatt & K.R. Sreenivasan, 2011, A voyage through turbulence, University Press, Cambridge

[34] S. H. Davis, 1969, On the Principle of Exchange of Stabilities, Proceedings of the Royal Society of London, Series A, Mathematical and Physical Sciences, Vol. 310, No. 1502, p. 341-358

[35] J.W. Deardorff, 1978, Closure of Second- and Third-Moment Rate Equations for Diffusion in Homogeneous Turbulence, Physics of Fluids, Vol. 21, p. 525-530

[36] J. Dombard & G. Iaccarino, 2012, Sensitivity analysis to the normal grid-resolution in a turbulent channel flow using large-eddy simulations, Center For Turbulence Research, Annual Research Briefs, Stanford, CA, p. 265-274

[37] P.A. Durbin, 1980, A random flight model of inhomogeneous turbulent dispersion, Physics of Fluids, Vol. 23, p. 2151-2153

[38] P.A. Durbin & B.A. Petterson Reif, 2001, Statistical Theory and Modeling for Turbulent Flows, John Wiley & Sons

[39] D. Dunham, A. Spencer & J.J. McGuirk, 2009, Comparison of the Performance of URANS and LES CFD methodologies for Air Swirl Fuel Injectors, ASME Journal of Engineering for Gas Turbines and Power, Vol. 131, p. 011502:1-8

[40] M. van Dyke, 1964, Perturbation Methods in Fluid Mechanics, Applied Mathematics and Mechanics, Academic Press, New York-London

[41] G. Eyink, 2012, Course Notes on Turbulence Theory II, Johns Hopkins University, available online at: http://www.ams.jhu.edu/~eyink/

[42] D.L Ermak & J.S. Nasstrom, 2000, A Lagrangian Stochastic Diffusion Method for Inhomogeneous Turbulence, Atmospheric Environment, Vol. 34, p. 1059-1068

[43] V. Eswaran & S. B. Pope, 1988, Direct numerical simulations of the turbulent mixing of a passive scalar, Physics of Fluids, Vol. 31, Is. 3, p. 506-520

[44] G. M. Faeth, 1983, Recent advances in modeling particle transport properties and dispersion in turbulent flow, Proceedings of the ASME-JSME Thermal Engineering Conference, Vol. 2, ASME, New York, p. 517–534

[45] T.E. Faber, 1995, Fluid Dynamics For Physicists, University Press, Cambridge

[46] L-S. Fan & C. Zhu, 1998, Principles of Gas-Solid Flows, Cambridge Series in Chemical Engineering, Cambridge University Press, Cambridge

[47] A. Favre, 1965, Equations des gaz turbulents compressibles, J. de Mecanique, Vol. 4, No. 3, p. 361-367

[48] J.H. Ferziger, 1977, Large Eddy Numerical Simulations of Turbulent Flows, AIAA Journal, Vol. 15, No. 9, p. 1261-1267

[49] J.H. Ferziger & M. Peric, 1997, Computational Methods for Fluid Dynamics, Springer-Verlag, Berlin

[50] J. M. Floryan & H. Rasmussen, 1989, Numerical Methods for Viscous Flows With Moving Boundaries, Applied Mechanics Reviews, Vol. 42, Is. 12, p. 323-341

[51] Fluent 6.3, Documentation, available online at: http://aerojet.engr.ucdavis.edu/fluenthelp/index.htm

[52] J.C.H Fung, J.C.R. Hunt, R.J. Perkins, A.A. Wray & D.D. Stretch, 1991, Defining the zonal structure of turbulence using the pressure and the invariants of the deformation tensor, Proceedings 3rd European Turbulence Conference, Springer, Stockholm, p. 395-404

[53] J.C.H Fung, J.C.R. Hunt, N.A. Malik & R.J. Perkins, 1992, Kinematic Simulation of homogeneous turbulence by unsteady random Fourier modes, Journal of Fluid Mechanics, Vol. 236, p. 281-318

[54] J.C.H. Fung, J.C.R. Hunt & R.J. Perkins, 2002, Diffusivities and velocity spectra of small inertial particles in turbulent-like flows, Proc. of the Royal Society London, 459, The Royal Society, p. 445-493

[55] D. Fuster, J.P. Matas, S. Marty, S. Popinet, J. Hoepffner, A. Cartellier & S. Zaleski, 2013, Instability regimes in the primary breakup region of planar coflowing sheets, Journal of Fluid Mechanics, Vol. 736, p. 150- 176

[56] A. Garcia-Olivares, J. Isern-Fontanet & E. Garcia-Ladona, 2007, Dispersion of passive tracers and finite-scale Lyapunov exponents in the Western Mediterranean Sea, Deep-Sea Research I, p. 253-268

[57] M. Germano, U. Piomelli, P. Moin & W.H. Cabot, 1991, A dynamic subgrid-scale eddy viscosity model, Physics of Fluids, Vol. 3, p. 1760-1765

[58] M. Gerritsen, 2008, Introduction to Matrix Computation - CME200, Course Reader, Stanford University

[59] D. Gueyffier, J. Li, A. Nadim, R. Scardovelli & S. Zaleski, 1999, Volume-of-Fluid Interface Tracking with Smoothed Surface Stress Methods for Three-Dimensional Flows, Journal of Computational Physics, Vol. 152, p. 423–456

[60] S. Goto & J.C. Vassilicos, 2004, Particle Pair diffusion and persistent streamline topology in two-dimensional turbulence, New Journal of Physics,Vol. 6, No. 65, p. 1-35

[61] S. Goto & J.C. Vassilicos, 2006, Self-similar clustering of inertial particles and zero-acceleration points in fully developed two-dimensional turbulence, Physics of Fluids, Vol. 18, p. 115103:1-10

[62] Y. Hardalupas & A.M.K.P. Taylor, 1989, On the measurement of particle concentration near a stagnation point, Experiments in Fluids, Vol. 8, p. 113-118

[63] Y. Hardalupas, A.M.K.P. Taylor & J.H. Whitelaw, 1992, Particle dispersion in a vertical round sudden-expansion flow, Phil. Trans. R. Soc. London, Series A, Vol. 341, p. 411-442

[64] D. Hansell, I.M. Kennedy, W. Kollman, 1992, A simulation of particle dispersion in a turbulent jet, International Journal on Multiphase Flows, Vol. 18, p. 559-576

[65] H. Hetsroni & M. Sokolov, 1971, Distribution of Mass, Velocity and Intensity of Turbulence in a Two-Phase Turbulent Jet, American Institute of Chemical Engineers, Journal, Vol. 93, p. 315-328

[66] J.O. Hinze, 1975, Turbulence, 2nd Ed., McGraw-Hill

[67] C. Hirsch, 1991, Numerical Computation of internal and external flows, John Wiley & Sons

[68] J.C.R. Hunt, 1985, Turbulent Diffusion From Sources In Complex Flows, Ann. Rev. Fluid. Mech., Vol. 17, p. 447-485

[69] G. Iaccarino, 2009, Computational Methods in Fluid Dynamics - ME469 & ME469B, Course Readers , Stanford University

[70] R. I. Issa, 1986, Solution of the implicitly discretized fluid flow equations by operator splitting. J. Computational Physics, Vol. 62, p. 40-65

[71] P. Holmes, J.L. Lumley & G. Berkooz, 1996, Turbulence Coherent Structures and Dynamical Systems and Symmetry, Cambridge Monographs on Mechanics, Cambridge University Press

[72] H. Jasak, 1996, Error analysis and estimation for the finite volume method with applications to fluid flows, PhD thesis, Imperial College, University of London

[73] J. Jimenez, 2004, The contributions of A.N. Kolmogorov to the theory of turbulence, Arbor CLXXVIII, Vol. 704, p. 589-606

[74] W.P. Jones & B.E. Launder, 1972, The prediction of laminarization with a two-equation model of turbulence, Int. J. of Heat Transfer, Vol. 15, p. 301-314

[75] W.P. Jones & B.E. Launder, 1973, The calculation of Low-Reynolds number phenomena with a two equation model for turbulence, Int. J. of Heat Transfer, Vol. 16, p. 1119-1130

[76] T. von Karman, 1930, Mechanische Aehnlichkeit und Turbulenz, Nachrichten von der Gesselschaft der Wissenschaften zu Goettingen, Mathematisch-Physikalische Klasse

[77] Y. Kimura & J.R. Herring, 1996, Diffusion in stably stratified turbulence, J. Fluid Mech., Vol. 328, p. 253- 269

[78] A.N. Kolmogorov, 1941, The local structure of turbulence in incompressible viscous fluid for very large Reynolds number, C. R. Acad. Sci. USSR, 32

[79] P. Kotelenez, 2008, Stochastic Ordinary and Stochastic Partial Differential Equations, Stochastic Modelling and Applied Probability, Springer

[80] R.H. Kraichnan, 1964, Lagrangian-History Closure Approximation for Turbulence, Physics of Fluids, Vol. 8, Is.. 4, p. 314-332

[81] R.H. Kraichnan, 1966a, Isotropic Turbulence and Inertial-Subrange Structure, Physics of Fluids, Vol. 9, Is. 9, p. 1728-1752

[82] R.H. Kraichnan, 1966b, Dispersion of Particle Pairs in Homogeneous Turbulence, Physics of Fluids, Vol. 9, Is. 10, p. 1937-1943

[83] R.H. Kraichnan, 1970, Diffusion by a random velocity field, Physics of Fluids, Vol.13, Is. 1, p. 22-31

[84] L.D. Landau & E.M. Lifshitz, 1987, Fluid Mechanics, Vol. 6 of Course on Theoretical Physics, 2nd Ed., Elsevier

[85] B.E. Launder, & D.B. Spalding, 1973, The numerical computation of turbulent flows, Computer methods in applied mechanics and engineering Vol. 3, p. 269-289

[86] B. E. Launder, G.J. Reece & D.B. Spalding, 1975, Progress in the Development of a Reynolds-stress Turbulence Closure, Journal of Fluid Mechanics, Vol. 68, Pt 3, p. 537-566

[87] J. Lawrence, 1956, Intensity Scale and Spectra of Turbulence in Mixing Region of free subsonic jet, NACA Report 1292

[88] M. Lesieur, 2008, Turbulence in fluids, 4th Ed., Vol. 40 of Fluid Mechanics and its Applications, Springer-Verlag, Berlin

[89] H.W. Liepmann & J.Laufer, 1947, Investigation of Free Turbulent Mixing , NACA Tech. Note. No. 1257

[90] D.K. Lilly, 1992, A proposed modification of the Germano subgrid scale model, Physics of Fluids, Vol. 4, Is. 3, p. 633-635

[91] F. Lucci, V.S L'vov, A. Ferrante & S. Elghobashi, 2013, Eulerian-Lagrangian bridge for the energy and dissipation spectra in isotropic turbulence, Theoretical and Computational Fluid Mech., DOI 10.1007/s00162-013-0310-5

[92] J.L. Lumley & S. Corrsin, 1959, A random walk with both Lagrangian and Eulerian statistics, Advances in Geophysics, Vol. 6, p. 179-183

[93] N.A. Malik & J.C. Vassilicos, 1999, A Lagrangian model for turbulent dispersion with turbulent-like flow structure: Comparison with direct numerical simulation for two-particle statistics, Physics of Fluids, Vol. 11, No. 6, p.1572-1580

[94] F. Mashayek & R.V.R. Pandya, 2003, Analytical description of particle/droplet-laden turbulent flows, Progress in Energy and Combustion Science, Vol. 29, p. 329-378

[95] T. Menard, S. Tanguy & A. Berlemont, 2007, Coupling level set/VOF/ghost fluid methods: Validations and application to 3D simulation of the primary break-up of a liquid jet, International Journal of Multiphase Flows, Vol. 33, p. 510–524

[96] F.R. Menter, 1993, Zonal Two Equation $k-\omega$ Turbulence Models for Aerodynamic Flows, AIAA paper 93-2906, p.1-21

[97] F.R. Menter, 1994, Two Equation Eddy-Viscosity Turbulence Models for Engineering Applications, AIAA Journal, Vol. 32, p. 1598-1605

[98] F.R. Menter, M. Kuntz & R. Langtry, 2003, Ten Years of Industrial Experience with SST Turbulence Model, Turbulence Heat & Mass Transfer, Vol. 4, Begell House, p. 1-8

[99] A.S. Monin & A.M. Yaglom, 1971, Statistical fluid Mechanics Vol. 1, Edited by J.L. Lumley, 2007 Dover Publishing Edition

[100] A.S. Monin & A.M. Yaglom, 1975, Statistical fluid Mechanics Vol. 2, Edited by J.L. Lumley, 2007 Dover Publishing Edition

[101] A. Monterfano, 2011, Boundary Conditions for LES and RANS, openFOAM Workshop July 11-12 2011, Milano, Italy

[102] A. A. Mostafa, 1992, Turbulent Diffusion of Heavy Particles in Turbulent Jets, ASME Journal on Applied Mechanics, Vol. 114, p. 667-671

[103] J. von Neumann & R. D. Richtmyer, 1950, A Method for the Numerical Calculation of Hydrodynamic Shocks. Journal of Applied Physics, Vol. 21, No. 3, p. 232-237

[104] E.A. Novikov, 1963, Method of random forces in turbulence theory, Zh. Exper. Teor. Fiz., 44, No. 6, p. 2159-2168

[105] A.M. Obukhov, 1959, Description of Turbulence in terms of Lagrangian variable, Advances in Geophysics, Vol. 6, p. 113-116

[106] H. Oertel, 2010, Prandtl-Essentials of Fluid Mechanics, 3rd Ed., Applied Mathematical Sciences, Springer, New York

[107] C.W. Oseen, 1927, Hydrodynamik, Leipzig, Akademische Verlagsgesellschaft

[108] S. Ott & J. Mann, 2000, An experimental investigation of the relative diffusion of particle pairs in three-dimensional turbulent flow, Journal of Fluid Mechanics, Vol. 422, Cambridge University Press, p. 207-223

[109] S.V. Patankar, 1980, Numerical heat transfer and fluid flow, Hemisphere Publishing Corporation

[110] G.S. Jr Patterson & S. Corrsin, 1966, Computer experiments on random walks with both Eulerian and Lagrangian statistics, Dynamics of Fluids and Plasmas, ed. S.I. Pai, New York, p. 275-307

[111] R.J. Perkins, N.A. Malik & J.C.H Fung, 1993, Cloud Dispersion Model, Advances in Turbulence IV, p. 539-545

[112] M.M. Rogers & R.D. Moser, 1992, The three dimensional evolution of a plane mixing layer: the Kelvin-Helmholtz rollup, J. Fluid Mech, Vol. 243, p.183-226

[113] I. Pesmatzoglou, 2014, A Stochastic Model for Turbulent Poly-Disperse Flows, PhD Thesis, Imperial College London

[114] U. Piomelli, 1991, Local space time averaging in the dynamic subgrid scale model, American Physical Society, Vol. 35, No. 10, p. 313-325

[115] F. Piscaglia, 2011, Development of Boundary Conditions for compressible ICE, openFOAM Workshop July 11-12 2011, Milano, Italy

[116] L. Prandtl, 1932, Zur Turbulenten Stroemung in Rohren und langs Platten, In Ergebnisse der Aerodynamischen Versuchsanstalt zu Goettingen, 4, Ludwig Prandtls Gesammelte Abhandlungen

[117] L. Prandtl, 1945, Uber Reibungsschichten bei dreidimensionalen Stroemungen, MoS RT64, Betz Festschrift, Goettingen

[118] L. Prandtl & K. Wieghardt, 1945, Uber ein neues formelsystem fur die ausgebildete turbulenz - On a new formulation for fully developed turbulence, Nachrichten der Akademie der Wissensschaften zu Goettingen, Mathematische-Physikalische Klasse, Technical Report Academy of Sciences, Goettingen, p. 6-19

[119] C.M. Rhie & W.L. Chow, 1982, A numerical study of the turbulent flow past an isolated airfoil with trailing edge separation, AIAA-82-0998, AIAA/ASME 3rd Joint Thermophysics, Fluids, Plasma and Heat Transfer Conference, St. Louis, Missouri,

[120] M. M. Ribeiro & J. H. Whitelaw, 1975, Statistical Characteristics of a Turbulent Jet, Journal of Fluid Mechanics, Vol. 70, Is. 1 , p. 1-15

[121] L. F. Richardson, 1926, Atmospheric diffusion shown on a distance-neighbour graph, Proceedings of the Royal Society London, A 110, p. 709-737

[122] W. Rodi, 1980, Turbulence Models and Their Application in Hydraulics - A State of the Art Review, IAHR, Delft, the Netherlands

[123] J.R. Sack & J. Urrutia, 1999, Handbook of Computational Geometry, Elsevier, Amsterdam

[124] P.G. Saffman, Vortex Dynamics, 1992, Cambridge University Press, from the series: Cambridge Monographs on Mechanics and Applied Mathematics

[125] R.Salmon, 1988, Ann. Review of Fluid Mechanics, Vol. 20, p. 225-256

[126] A.M. Savill, 1987, Recent Developments in Rapid-Distortion Theory, Ann. Review of Fluid Mechanics, Vol. 19, p. 531-573

[127] B. Sawford, 1983, The effect of Gaussian particle-pair distribution functions in the statistical theory of concentration fluctuations in homogeneous turbulence, Quarterly Journal of The Royal Meteorological Society, Vol. 8, p. 339–353

[128] B.L. Sawford, 1991, Lagrangian Statistical simulations of concentration mean and fluctuation fields, J. Clim. Appl. Meteorology, Vol. 24, p. 1152–1166

[129] B. Sawford, 2001, Turbulent Relative Dispersion, Annual Review Fluid Mechanics, Vol. 33, Annual Reviews, p. 289-317

[130] H. Schlichting, 1968, Boundary-Layer Theory, 6^{th} Edition, translated J. Kestin, McGraw-Hill, New York

[131] R.S. Scorer, 1978, Environmental Aerodynamics, Ellis Horwood Limited, Chichester, England

[132] S.C. Shadden, F. Lekien, J.D. Paduan, F.P. Chavez & J.E. Marsden, 2009, The correlation between surface drifters and coherent structures based on high-frequency radar data in Monterey Bay, Deep-Sea Research II, Vol. 56, p. 161-172

[133] P. Shen & P.K. Yeung, 1997, Fluid particle dispersion in homogeneous turbulent shear flow, Physics of Fluids, Vol 9, p. 3472-3484

[134] T-H. Shih, W.W. Liou, A. Shabbir, Z. Yang, & J. Zhu, 1995, New k-ϵ eddy viscosity model for high Reynolds number turbulent flows, Computers Fluids Vol. 24, No.3, p. 227-238

[135] J. Smagorinsky, 1963, General circulation experiments with the primitive equations, Monthly Weather Reviews, Vol. 91, American Meteorological Society, p. 99-164

[136] K. D. Squires & J. K. Eaton, 1991, Preferential concentration of particles by turbulence, Physics of Fluids, Vol. 3, Is. 5, p. 143-169

[137] Sir G.G. Stokes, 1850, On the effect of the internal friction of fluids on the motion of pendulums, Transactions of the Cambridge Philosphical Society, IX, p. 8-96

[138] G.R. Tabor, M.H. Baba-Ahmadi, E. de Villiers & H.G. Weller, 2004, Construction of inlet conditions for turbulent channel flow, ECCOMAS 2004 Conference Proceedings

[139] G.I. Taylor, 1921, Diffusion by continuous movements, Proceedings of the London Mathematical Society, Series 2, Vol. 20, p.196

[140] S. Tanguy & A. Berlemont, 2005, Application of Level Set method for simulations of droplet collisions, International Journal of Multiphase Flows, Vol. 31, p. 1015-1035

[141] S. Tanguy, T. Menard & A. Berlemont, 2005, Droplet collisions using Level Set method: comparisons between simulation and experiments, Computational Methods in Multiphase Flow III, A.A. Mammoli & C.A. Brebbia (*Eds.*), WIT Press, Southampton

[142] J.C. Tannehill, D.A. Anderson & R.H. Pletcher, 1997, Computational fluid mechanics and heat transfer, 2nd Ed., Taylor & Francis, Washington D.C

[143] C.M. Tchen, 1947, Mean Value and Correlation Problems Connected with the motion of small particles in turbulent field, PhD thesis, Delft University, Netherlands

[144] H. Tennekes & J.L. Lumley, 1972, A first course in turbulence, MIT press, Cambridge, MA

[145] D.J. Thompson, 1987, Criteria for the selection of stochastic models of particle trajectories in turbulent flows, Journal of Fluid Mechanics, Vol. 180, p. 529-556

[146] D.J. Thompson, 1990, A stochastic model for the motion of particle pairs in isotropic high-Reynolds-number turbulence and its application to the problem of concentration variance, Journal of Fluid Mechanics, Vol. 210, p. 113- 153

[147] G.E. Uhlenbeck & L.S. Ornstein, 1930, On the theory of Brownian Motion, Phys. Rev. 36, 823

[148] S.O. Unverdi & G. Tryggvason, 1992, A Front-Tracking Method for Viscous, Incompressible, Multi-fluid Flows, Journal of Computational Physics, Vol. 100, p. 25-37

[149] H.K. Versteeg & W. Malalasekera, 1995, An introduction to computational fluid dynamics - The finite volume method, Pearson-Prentice Hall

[150] G.A. Voth, 2000, Lagrangian Acceleration measurements in turbulence at large Reynolds numbers, PhD thesis, Cornell University

[151] E. de Villiers, 2007, The potential of Large Eddy Simulation for the modeling of wall bounded flows, PhD thesis, Imperial College, University of London

[152] M. Virant & T. Dracos, 1997, 3D PTV and its application on Lagrangian motion, Meas. Sci. Technol., Vol. 8, p. 1539-1552

[153] B. Vreman, B. Geurt & H. Kuerten, 1994, Realizability conditions for the turbulent stress tensor in large-eddy simulations, J. Fluid Mech, Vol. 278, p.351-362

[154] R.F. Warming & R.M. Beam, 1976, Upwind second order differencing schemes and applications in aerodynamic flows, AIAA Journal, Vol.14, p. 1241-1249

[155] H.G. Weller, G. Tabor, H. Jasak & C. Fureby, 1998, A tensorial approach to computational continuum mechanics using object-oriented techniques, Computers in Physics, Vol. 12, No. 6, p. 620–631

[156] D.C. Wilcox, 1988, Reassessment of the Scale-Determining Equation for Advanced Turbulence Models, AIAA, Vol. 26, No.11, p. 1299-1310

[157] D.C. Wilcox, 2006, Turbulence Modeling for CFD 3rd Ed., DCW Industries, La Canada, CA, USA

[158] P. K. Yeung, 1994, Direct numerical simulation of two-particle relative diffusion in isotropic turbulence, Physics of Fluids, Vol. 6, p.3416-3428

[159] P.K. Yeung, 2002, Lagrangian Investigations of Turbulence, Annu. Rev. Fluid. Mech., Vol. 34, p.115-142

[160] P.K. Yeung & Y. Zhou, 1998, Numerical Study of rotating turbulence with external forcing, Physics of Fluids, Vol. 10, p. 2895-2909

[161] S. Yuu, N. Yasukouchi, Y. Hirosawa & T. Jotaki, 1978, Particle Turbulent Diffusion in a dust laden round Jet, American Institute of Chemical Engineers, Journal Vol. 24, No. 3, p. 509-519

[162] M. Zedda, 2014-November-21, Private communication, Derby, Derbyshire, U.K

A Spectral Methods

Before we delve any further into the field of KS it is perhaps necessary as well as instructive to review the fundamentals of spectral methods which form the core of KS. The summary presented here is an amalgam of the chapters dedicated to this field by the classic monographs of Monin & Yaglom (1975), Tennekes & Lumley (1972) and Lumley (1970). It is not intended to be an exhaustive review of these methods as that is beyond the scope of this thesis and would require a volume to be complete, rather the aim of this section is to introduce or remind the reader of the tools and methods commonly used in order to make the following sections more approachable.

In the field of fluid dynamical turbulence the study of homogeneous -in a statistical sense- turbulence has proved invaluable in shedding light into this chaotic phenomenon. The most valuable tool available to researchers for its study is the Fourier transform. Significant insight has been gained through the investigation of two-point statistics. Of these the velocity autocorrelation is perhaps the most widely used as its Fourier transform yields the energy spectrum of the field which in turn forms the basis for the investigation of the transfer of energy amongst the turbulent scales.

If the velocity correlation is a function of a time interval, τ, the transform variable is a frequency, ω. Alternatively, if the correlation is a function of a separation vector, $\mathbf{r}$, the transform variable is a wavenumber vector, $\mathbf{k}$. It should be noted that the accuracy of the Fourier transform representing the random function depends on the frequency domain or the size of the wavenumber interval, respectively. An alternative way of viewing this is that the greater the number of uncorrelated harmonic motions of random amplitude and phase that are used in the summation the closer the random function will be approximated.

Durbin & Petterson-Reif (2001) summarize the main benefits of the use of the Fourier transform when studying turbulence; they are listed now and will be reviewed further in the following sections. These are the ease with which translational and rotational invariance is accommodated for within the Fourier transform. The fact that each random Fourier mode is not correlated with all the others and finally the simplification of the differential form of the Navier-Stokes equations into simpler algebraic relations as well as the subsequent simplification of the higher order statistics and derivatives.

The mathematical foundation for spectral methods lies in the harmonic analysis of random functions. When the latter has only one dependent variable we are dealing with a random process whereas when the order of variables increases we are dealing with random fields. The number of variables of the function in question increases the complexity of the process somewhat but the underlying mathematics remains largely unchanged. The basis is the representation of the random process through a number of Fourier series or integrals. Strictly speaking the former is used for purely periodic functions while the latter approach is applicable to functions that vanish as they approach infinity. However, for all stationary random processes[76]and for all homogeneous random fields there exists an appropriate Fourier expansion that can represent the process or field. It is exactly this representation of any random process or field by the superposition of harmonic oscillations or plane waves that we call a spectral representation. Monin & Yaglom

[76]By stationary we mean statistics exhibit temporal translational invariance that is they are independent of the time origin. However these methods can be extended to cases of non-stationarity see Lumley (1970b)

(1975) clarify that such a representation is a special case of representing a random function through the summation of a series of components of given functional form and of random and uncorrelated coefficients.

We will return at a later stage to clarify the importance of the randomness and non-correlation of the components but for now we will restrict ourselves to distinguishing between the two main types of random functions. Those defined over a finite interval, or perhaps more appropriately those of finite energy that may be represented by a series expansion of a finite set of orthogonal functions and those extending over an indefinite interval or alternatively of infinite energy that may be represented as an integral expansion of a continuous set of functions.

The spatial and temporal correlation tensors are, respectively, given by the following relations:

$$R_{ij}(\mathbf{r}) \equiv \overline{u_i(\mathbf{x},t)u_j(\mathbf{x}+\mathbf{r},t)}$$

[77] &

$$R_{ij}(\tau) \equiv \overline{u_i(\mathbf{x},t)u_j(\mathbf{x},t+\tau)}$$

Where $\mathbf{r}$ is the separation vector and τ is the time interval. Their corresponding Fourier transforms result in the following spectrum tensors:

$$\phi_{ij}(\mathbf{k}) = \frac{1}{(2\pi)^3}\iiint_{-\infty}^{\infty} e^{(-\mathrm{i}\mathbf{k}\cdot\mathbf{r})}R_{ij}(\mathbf{r})d\mathbf{r}$$

$$\phi_{ij}(\omega) = \frac{1}{2\pi}\int_{-\infty}^{\infty} e^{(-\mathrm{i}\omega\tau)}R_{ij}(\tau)d\tau$$

The inverse relationships are also true, that is, knowledge of the spectrum tensor can result directly in the correlation tensors:

$$R_{ij}(\mathbf{r}) = \iiint_{-\infty}^{\infty} e^{(\mathrm{i}\mathbf{k}\cdot\mathbf{r})}\phi_{ij}\left(\mathbf{k}\right)d\mathbf{k}$$

$$R_{ij}(\tau) = \int_{-\infty}^{\infty} e^{(\mathrm{i}\omega\tau)}\phi_{ij}(\omega)d\omega$$

Limiting the separation vector's orientation to lie parallel with one of the principal directions, *i.e.*

$$\mathbf{r} = (r,0,0)\,,(0,r,0)\,or\,(0,0,r)$$

results in the most frequently measured correlations. These are the longitudinal and transverse correlations, for parallel and perpendicular velocity components respectively. The related one dimensional spectra, $F_{11}\&F_{22}$ are known as the longitudinal and transverse spectra respectively and given by the following relationships:

[77] We have not normalized with the variances $\sqrt{\overline{u_i^2}\overline{u_j^2}}$because in tensor notation these looks like the Reynolds Stress from Reynolds averging. These are two-point correlations and there should be no confusion.

$$R_{11}(r,0,0) = \int_{-\infty}^{\infty} e^{(ikr)} F_{11}(k_1) dk_1 = \int_{-\infty}^{\infty} e^{(ikr)} \iint_{-\infty}^{\infty} \phi_{11}(\mathbf{k}) dk_2 dk_3$$

$$R_{22}(r,0,0) = \int_{-\infty}^{\infty} e^{(ikr)} F_{22}(k_1) dk_1 = \int_{-\infty}^{\infty} e^{(ikr)} \iint_{-\infty}^{\infty} \phi_{22}(\mathbf{k}) dk_2 dk_3$$

The nested double-integration implies that the integration is not calculated over the entire wave-number space but rather for a smaller slice at a given wave-number k_1 [78]. Successive measurements of the correlations of incrementally increasing wave-numbers and subsequent superposition of the resultant Fourier transforms results in the complete one dimensional energy spectrum.

At this point it should be mentioned that we have overlooked one issue that burdens all Fourier transform operations. This is known as aliasing and the problem is exasperated further in three dimensional turbulence as not only do the greater wavenumbers in the same direction contribute to the measured correlation but the wavenumbers of the other two directions contribute as well. At the higher end of the wavenumber space the problem tends to be less significant as the turbulence tends to be isotropic and the eddies in all directions are approximately equal. This is not true though for the large scales (small wavenumbers) in the inertial range. The solution is to obtain measurements of the same correlation in all possible directions. However, Tennekes & Lumley (1972) note that such a measurement would yield more information than one can physically reason.

The complexity arises because it is uncommon to be able to describe the velocity field purely in terms of the superposition of even and real function (*i.e.* cosines). Rather to accurately describe the field one must resort to the superposition of odd and even functions (*i.e.* sines and cosines). The Fourier transform of an odd function will result in a Real and an Imaginary part. Hence, the Fourier transform of a 1D odd function needs to be represented on 2-axes, the Fourier transform of a 2D odd field will require 4-axes and that of 3D field 6-axes[79]. The solution is to integrate the spectrum over spherical shells of wave-number space, that is a spectrum representing the total energy at that scalar wavenumber. The scalar radius, k is determined by calculating the modulus of the vector $\mathbf{k}$:

$$|\mathbf{k}| = \sqrt{\mathbf{k} \cdot \mathbf{k}} = \sqrt{k_i k_i}$$

Finally, in order to account for the total kinetic energy and not only for the contribution of a single velocity component, the spectra of all three velocity components must be added together.

[78] Regarding the shape of R_{22} which turns negative: The mean velocity in the transverse direction should be zero, the implication for an incompressible field is that in order to avoid net flux in one direction (or the other) through a plane, whose normal vector is aligned with the transverse direction, the correlation must turn negative eventually.

[79] Recalling that (Bracewell (1986)):

- The Fourier transform of the even part of a Real function is Real and even.
- The Fourier transform of the odd part of a Real function is Imaginary and odd.

That is we are interested in the diagonal terms, of the spectrum tensor, ϕ_{ij}:

$$\phi_{ii} = \phi_{11} + \phi_{22} + \phi_{33}$$

The resulting energy spectrum is known as the three-dimensional spectrum, given by:

$$E(k) = \frac{1}{2} \oiint \phi_{ii}(\mathbf{k}) dS(\mathbf{k})$$

Where, $dS(\mathbf{k})$, is a surface element on the wavenumber spherical shell at a radius $|\mathbf{k}|$. As the energy may be distributed in a variety of ways amongst the wavenumber components contributing to the spectrum *E(k),* does not uniquely define $\phi_{ii}(\mathbf{k})$. The relationships between the one-dimensional spectra and the three-dimensional ones are complicated bar the special case of isotropy, where they are as follows:

$$E(k) = k^3 \frac{d(\frac{1}{k}\frac{dF_{11}}{dk})}{dk} \;\&\; \frac{d\left(F_{22}(k_1)\right)}{dk_1} = -\frac{k_1}{2}\frac{d^2(F_{11}(k_1)}{dk_1^2}$$

Although the measurement and experimental apparatus for obtaining the spectra can be complicated at times, working with the Fourier transforms has two benefits of great importance for researchers investigating turbulence; the higher order statistical moments and the partial derivatives of the equations of motion once cast in Fourier space are significantly easier to solve. One should also note the tendency of the two-point correlation to rapidly approach zero as the separation vector increases, which, in turn is a consequence of the finite energy available at higher wavenumbers (observed in the energy spectrum) as the converse would constitute a violation of the energy conservation principle.

A further convenient property of the homogeneous turbulence described by Fourier transforms is that their wavenumber components are uncorrelated:

$$U_i(\mathbf{k}) U_i^*(\mathbf{k}') = 0 \; for \; \mathbf{k} \neq \mathbf{k}'$$

Given that the flow-field is a Real valued function, the complex conjugate can be freely replaced with its negative:

$$U_i(\mathbf{k}) U_i^*(-\mathbf{k}') = 0 \; for \; \mathbf{k} \neq -\mathbf{k}'$$

where, * denotes the complex conjugate quantity and $U_i(\mathbf{k})$ denotes the Fourier transform of $u_i(\mathbf{x})$ given by:

$$U_i(\mathbf{k}) = \frac{1}{(2\pi)^3} \iiint_{-\infty}^{\infty} e^{\mathrm{i}\mathbf{k}\cdot\mathbf{x}} u_i(\mathbf{x}) d\mathbf{x}$$

We will see in subsequent sections dealing with the construction of KS, that this property is especially accommodating in the synthesis of turbulent flow fields. Durbin & Petterson-Reif (2001), have an elegant derivation of this result avoiding the somewhat abstract mathematical proof usually given and it will be presented here:

$$\overline{U_i(\mathbf{k})U_i^*(\mathbf{k}')} = \overline{\frac{1}{(2\pi)^3}\iiint_{-\infty}^{\infty} e^{\mathrm{i}\mathbf{k}\cdot\mathbf{x}}u_i(\mathbf{x})d\mathbf{x}\,\frac{1}{(2\pi)^3}\iiint_{-\infty}^{\infty} e^{-\mathrm{i}\mathbf{k}'\cdot\mathbf{x}'}u_i(\mathbf{x}')d\mathbf{x}'}$$

$$= \frac{1}{(2\pi)^6}\iiint_{-\infty}^{\infty}\iiint_{-\infty}^{\infty} e^{\mathrm{i}(\mathbf{k}\cdot\mathbf{x}-\mathbf{k}'\mathbf{x}')}\overline{u_i(\mathbf{x})u_i(\mathbf{x}')}d\mathbf{x}d\mathbf{x}'$$

By rearranging the exponents we can substitute with the two-point correlation, R_{ii} since $\mathbf{r} = \mathbf{x} - \mathbf{x}'$ and in turn with the spectrum tensor, ϕ_{ii}: [80]

$$\overline{U_i(\mathbf{k})U_i^*(\mathbf{k}')} = \frac{C}{(2\pi)^6}\iiint_{-\infty}^{\infty}\iiint_{-\infty}^{\infty} e^{\mathrm{i}(\mathbf{k}-\mathbf{k}')\cdot\mathbf{x}'}e^{\mathrm{i}\mathbf{k}\cdot\mathbf{r}}R_{ii}(\mathbf{r})d\mathbf{r}d\mathbf{x}'$$

$$= \frac{C}{(2\pi)^3}\phi_{ii}\iiint_{-\infty}^{\infty} e^{\mathrm{i}(\mathbf{k}-\mathbf{k}')\cdot\mathbf{x}'}d\mathbf{x}'$$

But the term within the triple integral is the Dirac delta expressed in three dimensions: $\delta(\mathbf{k}-\mathbf{k}') = \iiint_{-\infty}^{\infty} e^{\mathrm{i}(\mathbf{k}-\mathbf{k}')\cdot\mathbf{x}'}$substituting gives the desired result, as the delta function will be zero when $\mathbf{k} \neq -\mathbf{k}'$[81]:

$$\overline{U_i(\mathbf{k})U_i^*(\mathbf{k}')} = \delta(\mathbf{k}-\mathbf{k}')\,\phi_{ii}$$

At this point the following observation should be made, although we have mentioned that the flow-field may be constructed from the summation of Fourier modes, each of these extends within $[-\infty, +\infty]$ unattenuated, whereas an eddy is a local feature or structure. Durbin & Petterson-Reif (2001), attribute this to the phenomenon of statistical scrambling of the random oscillations. The summation results in a correlation that statistically represents the eddies and provided the total energy content of the Fourier and physical system are preserved so should the overall statistics. The immediate implication of this, is that no single wavenumber should be associated with a single size eddy, that is a single wavenumber does not correspond to a wave-like disturbance. Rather, as Tennekes & Lumley (1972) point out, each eddy should be thought of as contributing not a narrow but a broad spike/peak to the energy spectrum and hence many Fourier coefficients and knowledge of the phase angle between them is required to accurately describe them. This should not come as a surprise as an eddy is far from static, instead it is constantly interacting with its neighbors exchanging energy and as it does so it must also change its shape.

In order to clarify the rationale behind the existence of a broad spike it is necessary to consider the energy cascade, that is the exchange of energy between the different scales of turbulence. As the discussion of the energy cascade is by no means a trivial issue with several monographs devoted to this subject alone, we will attempt to restrict the discussion here to the key concepts.

[80] C is an integration constant but can be related to the turbulence intensity, see Durbin & Petterson-Reif (2001)

[81] Recall that in 1D: $\int_{-\infty}^{\infty}\delta(x)dx = 1$ and in 3D:$\int\int\int_{-\infty}^{\infty}\delta(\mathbf{x})d\mathbf{x} = 1$ which may also be interpreted as $\delta(x) = \lim_{a\to 0}\frac{e^{-x^2/a^2}}{a\sqrt{\pi}}$ and $\delta(\mathbf{x}) = \delta(x)\delta(y)\delta(z) = \lim_{a\to 0}\frac{e^{-(x^2+y^2+z^2)/a^2}}{a^3\pi^{3/2}}$ respectively

The starting point for this analysis is to consider two vortex tubes aligned perpendicular to each other in a straining flow field that varies only along two of its directions, *i.e.* it is a planar strain-rate field (where the strain tensor is a 2x2 and not a 3x3 matrix). The latter requirement simplifies significantly the investigation without loss of generality while the requirements for vortex tubes rather than eddies arises from the fact that the turbulence is a three dimensional phenomenon and to draw any meaningful conclusions we should not restrict ourselves to the elementary, and perhaps flawed point of view of turbulence as two dimensional revolving structures or features. One of these vortex tubes is aligned in the direction of positive strain whilst the other lies perpendicular to the first along the direction of an equal in magnitude but negative strain. This requires that at the same time the strain tensor is diagonal, meaning that the vortex tubes are under the strain alone and there is no shear present.

The principle of conservation of angular momentum dictates that the vortex tube under positive strain increases its vorticity as it elongates thus reducing its diameter. The converse must be true for the vortex tube under negative strain which contracts in length while increasing in diameter and thus decreasing its rate of rotation. The general vorticity equation is given by:

$$\frac{d\omega_i}{dt} = \omega_j s_{ij}$$

And if the original vorticity of both tubes was, $\omega_1 = \omega_2 = \omega$ and the magnitude of strain is constant and equal to s then the equations governing the vorticity evolution for the vortex tubes for this case reduce to[82]:

$$\frac{d\omega_1}{dt} = \omega_1 s_{11} = \omega s \;\&\; \frac{d\omega_2}{dt} = \omega_2 s_{22} = -\omega s$$

and in turn:

$$\omega_1 = \omega e^{st}\,,\; \omega_2 = \omega e^{-st} \;\&\; \omega_1^2 + \omega_2^2 = 2\omega^2 \cosh 2st$$

From which it should be evident that for all but the smallest of values of st the vorticity of the tube being elongated will increase faster than the rate at which the vorticity of the other decreases. At the same time though, an increase in the vorticity, ω_1 must equate into an increase of u_2 and u_3. Similarly a decrease in the magnitude of ω_2 must correspond to a decrease of u_1 and u_3. The net effect should be an increase of u_2, a more gradual increase of u_3 and a decrease of u_1. If the energy exchange rate per unit mass is given by the following equation:

$$T = s(u_2^2 - u_1^2)$$

this quantity must be positive. Hence the eddies tend to remove energy from their surrounding field and if one starts to think of large eddies convecting smaller ones the idea of an energy cascade from the large scales to the smaller ones becomes apparent. But the question still remains as to whether only the immediately larger-sized eddy transfers some of its energy to the smaller one or is it a range of larger eddies that contribute to the energy transfer. To determine the relevant energy contributions of the large scales to the smaller ones it is necessary to estimate the contribution of the strain rate.

[82]Note that we have assumed that this is a high Re flow and are using the inviscid versions of the equations

From simple scaling arguments one can see that the strain rate of the largest scales must be of the order of u/l while that of the Taylor micro-scale should be of the order of u/λ, from which one may deduce that the strain rate increases as the length scale decreases or alternatively, the strain rate increases as the wavenumbers increase. Lumley (1970) & Tennekes & Lumley (1972) consider the contribution of progressively larger neighboring scales to arrive at the conclusion that the strain rate contribution of the immediately larger scale is equal to half of that of the next scale over which, is in turn equal to a quarter of the total contribution and so forth.

Subsequently with knowledge of the slope of the energy spectrum one can derive the corresponding energy cascade between the scales. This is calculated to be equal to two-thirds for the given wavenumber while the neighboring eddy of greater wavenumber receives one-sixth and the remaining one-sixth is distributed to the yet smaller scales. We will limit the extent of the discussion here as any further discussion is well beyond the scope of this work, suffice to say, that the debate is still ongoing as to the precise nature of the energy cascades shape and slope however there is general agreement on the concept of local isotropy, that smaller scales can respond to changes much quicker than the larger scale thus restoring equilibrium faster and in a statistical sense are isotropic.

Up until this point this short treatise on spectral methods has only dealt with the definitions and the mathematics of the methods, except for the notion of homogeneity and isotropy which permitted the introduction of invariance and hence served to reduce the complexity by removing a preferential direction, there has been no other mention of any physical characteristics of the flow field. Restricting the analysis to incompressible fields, what are often called solenoidal fields, a very interesting and useful result emerges once the continuity equation is cast in Fourier space:

$$\partial_i u_i = \nabla \cdot \mathbf{u} = 0$$

But in Fourier space the dot product of the divergence operator and the velocity vector should reduce to the dot product of the wavenumber vector with the velocity vector, $-\mathrm{i}\mathbf{k} \cdot \mathbf{u}$. This can be seen if the inverse Fourier transform of the velocity is differentiated with respect to the wavenumber:

$$\partial_i u_i = \partial_i \left(\iiint_{-\infty}^{\infty} U_i e^{-\mathbf{ik}\cdot\mathbf{x}} d\mathbf{k} \right) = \iiint_{-\infty}^{\infty} -\mathrm{i}k_i U_i e^{-\mathbf{ik}\cdot\mathbf{x}} d\mathbf{k}$$

Therefore incompressibility of the flow field results in the velocity vector's orthogonality with the wavenumber vector: $k_i U_i = 0$. This means that the amplitude of the Fourier wave must be normal to the wavenumber vector, which as Lumley (1970) points out is simply a statement that in an incompressible field the waves must be transverse and the motion must be parallel to the wave crest. Furthermore, if the function is ergodic, the spectrum is guaranteed to be a regular function and we can extend the previous result to the spectrum tensor, ϕ_{ij}, as follows: $k_i \phi_{ij} = \phi_{ij} k_j = 0$ which follows from differentiating the two point velocity correlation, R_{ij} and using the previous result:

$$\partial_{x_i}(R_{ij}) = \partial_{x_i} \overline{[u_i(\mathbf{x}) u_j(\mathbf{x}')]} = \overline{[\partial_{x_i} u_i(\mathbf{x})]\, u_j(\mathbf{x}')} = 0$$

and similarly

$$\partial_{x_j}(R_{ij}) = \partial_{x'_j}\overline{[u_i(\mathbf{x})u_j(\mathbf{x}')]} = \overline{\left[\partial_{x'_j}u_j(\mathbf{x}')\right]u_i(\mathbf{x})} = 0$$

Another interesting result that arises from the condition of isotropy is the simplification in evaluating the spectrum tensor thanks to reflectional and rotational invariance that must apply[83]. The main result is that if the field is isotropic so too must the spectrum tensor, ϕ_{ij}, and hence it is only a function of the wavenumber vector, $\mathbf{k}$, and the delta function, δ_{ij}:

$$\phi_{ij} = A\delta_{ij} + Bk_ik_j$$

where the coefficients A and B may be functions of the magnitude of the wavenumber vector. Using $\phi_{ij}k_j = 0$ it may be shown that:

$$\phi_{ij}k_j = \left[A\delta_{ij} + Bk_ik_j\right]k_j = Ak_i + Bk_i\left|\mathbf{k}\right|^2 = 0 \leftrightarrow A = -B\left|\mathbf{k}\right|^2$$

However, we know that the energy of the spectrum may be determined by integrating the trace of the spectrum tensor, ϕ_{ii} , over spherical shells of radius $|\mathbf{k}|$:

$$E(|\mathbf{k}|) = 2\pi\left|\mathbf{k}\right|^2\phi_{ii}(|\mathbf{k}|)$$

Combining these two results yields the following equation for evaluating the spectrum tensor provided the energy, $E(|\mathbf{k}|)$ has been either measured or arbitrarily specified :

$$\phi_{ij} = \frac{E(|\mathbf{k}|)}{4\pi\left|\mathbf{k}\right|^2}\left(\delta_{ij} - \frac{k_ik_j}{\left|\mathbf{k}\right|^2}\right)$$

At this point the fundamental concepts of spectral methods have been covered and we can introduce an elementary spectral method illustrated by Durbin & Petterson-Reif (2001). They describe a method by which a random field may be constructed from a sum of Fourier modes of random amplitudes and phases with the only constraint being that the amplitudes be a function of the energy of the spectrum. The starting point is an isotropic random function, $\xi(\mathbf{k})$ defined in wavenumber space. One possible choice for such a random process is given as:

$$\xi_i(\mathbf{k}) = \sqrt{3}e^{\mathrm{i}\phi_k}\frac{\overrightarrow{\eta(\mathbf{k})}}{\sqrt{dk}}$$

Where ϕ_k denotes the phase angle, distributed uniformly between $[0, 2\pi]$ and $\overrightarrow{\eta(\mathbf{k})}$ is a unit vector

[83]

- Consider the reflection in the yz-plane, homogeneity requires that the single point statistics at x and -x be the same and u should become -u:

$$\overline{u(x,y)v(x,y)} = \overline{-u(x',y)v(x,y)} = 0$$

- Similarly for the two-point statistics reflected in an xy-plane, from points *((x',y') & (x,y'))* to *((x',y) & (x,y))* :

$$\overline{u(x,y)v(x',y')} \propto (x-x')(y-y') \rightarrow \overline{u(x,y)v(x',y')} = \overline{-u(x,y')v(x',y)}$$

of random orientation independently chosen for each $\mathbf{k}$, one possible definition is as follows:

$$\overrightarrow{\eta} = \left(p, \pm\cos\theta\sqrt{1-p^2}, \pm\sin\theta\sqrt{1-p^2}\right)$$

Where $p \,\&\, \theta$ are uniformly distributed between $[-1,+1]$ & $[0,2\pi]$ respectively and are chosen randomly and independently for each $\overrightarrow{\eta(\mathbf{k})}$. Meanwhile, the requirement for independent and random orientation of each unit vector results in:

$$\overline{\eta_i \eta_j} = {}^1\!/_3 \delta_{ij}$$

While, the independence of the wavenumber vectors result in the following property, for $\mathbf{k} \neq \mathbf{k}'$:

$$\overline{\eta_i\left(\mathbf{k}\right)\eta_j\left(\mathbf{k}'\right)} = 0$$

These last properties lead to:

$$\overline{\xi_i(\mathbf{k})\xi_j(\mathbf{k}')} = \delta_{ij}\delta\left(\mathbf{k}-\mathbf{k}'\right)$$

which may be used to confirm that the proposed method does indeed result in an isotropic spectrum when evaluating the velocity correlation $\overline{U_i U_j^*}$. Finally, the condition of incompressibility, as mentioned above, requires that the velocity is orthogonal to the wavenumber vector and the proposed Fourier transform modes of the velocity field are:

$$\mathbf{U} = \mathbf{k} \wedge \overrightarrow{\xi}\sqrt{\frac{E(\kappa)}{4\pi\kappa^4}} \;\; or \;\; U_i = \varepsilon_{ijl}k_j\xi_l\sqrt{\frac{E(\kappa)}{4\pi\kappa^4}}$$

where we have also given the index notation for ease of interpretation and have used the substitution of the modulus of the wavenumber $\kappa = |\mathbf{k}|$ for the sake of clarity[84]. What remains to be confirmed is that the proposed field is truly isotropic, this will be shown through evaluation of the velocity correlation:

$$\overline{U_i(\mathbf{k})U_i^*(\mathbf{k}')} = \varepsilon_{ilm}\varepsilon_{jnp}k_l k_n \xi_m \xi_p \left(\sqrt{\frac{E(\kappa)}{4\pi\kappa^4}}\right)^2 =$$

$$= (\delta_{ij}\delta_{ln} - \delta_{in}\delta_{lj})k_l k_n \delta\left(\mathbf{k}-\mathbf{k}'\right)\frac{E(\kappa)}{4\pi\kappa^4} = \delta\left(\mathbf{k}-\mathbf{k}'\right)\frac{E(\kappa)}{4\pi\kappa^4}(\kappa^2\delta_{ij} - k_i k_j)$$

Where we have made use of the property:

$$\overline{\xi_i(\mathbf{k})\xi_j(\mathbf{k}')} = \delta_{ij}\delta\left(\mathbf{k}-\mathbf{k}'\right)$$

along with the following useful result for the product of two skew symmetric tensors:

$$\varepsilon_{ilm}\varepsilon_{jnp} = (\delta_{ij}\delta_{ln} - \delta_{in}\delta_{lj})$$

[84] $\wedge$ denotes the wedge or exterior product and ε_{ijl} a skew symmetric tensor, that is: $\varepsilon_{ijl}^T = -\varepsilon_{ijl}$

Comparing the right hand side of the equation with

$$\overline{U_i(\mathbf{k})U_i^*(\mathbf{k}')} = \delta(\mathbf{k}-\mathbf{k}')\,\phi_{ii}$$

which was derived earlier, we obtain the desired result:

$$\phi_{ij} = \frac{E(\kappa)}{4\pi\kappa^4}(\kappa^2\delta_{ij} - k_i k_j)$$

Note that this is not the only possible construction that will yield this result as will be shown in subsequent sections[85].

[85] Durbin & Petterson-Reif (2001) mention that energy spectrum may be replaced by a number of different random variables provided the chosen one maintains the same variance as $E(\kappa)$

B Time Averaging for LES

The question remains however, as to how many samples from every simulated flow are required to average over in order to produce acceptable statistics. This is especially true when extracting results from LES flows where the size of the generated data sets is massive leading to a tedious and time consuming post processing process.

To answer this question a *bootstrapping method* is employed. For the standard mesh case 30 records were extracted for the centreline and one spanwise location at $z/D = 2.67$, the location where the jet exhibits the largest amplitude of oscillations in its flapping pattern. From the 30 samples, averages were created with 25, 20, 15, 10 and 5 samples. Each average was created by randomly selecting a number of samples from the total number with replacement, *i.e.* a particular sample might be selected twice and used in the averaging process.

Figure 110 portrays all the samples for the streamwise and spanwise locations respectively while figures 111 and 112 show the mean lines generated from the bootstrapping method along with detailed views, respectively. The process of time-averaging is constructive as it allows an indication for the spread of the data and the 95% confidence intervals are also depicted here. As the distribution of the fluctuating component of the velocity is expected to be Gaussian for the Eulerian phase the standard deviation from the averaging process may be used to calculate the specified confidence interval. Examination of the last few figures indicated that there was little to gain in generating averages with more than 10 samples, as the location of the mean lines did not change significantly and the spread of the confidence band is very similar bar for the two extreme cases of 5 and 25 samples. Hence 10 samples were deemed to be sufficient for the estimate of the mean value of the various parameters. This approach is adopted for the remainder of the chapter and all of the subsequent time-averaged information presented from the calculations are generated in this manner.[86]

[86] Noting that for the coarse and fine meshes it is expected that 10 samples will result in smaller and wider confidence bands, respectively, since it is expected that the fine grid predicts larger or more extreme fluctuations than the standard grid and reciprocally for the coarse mesh.

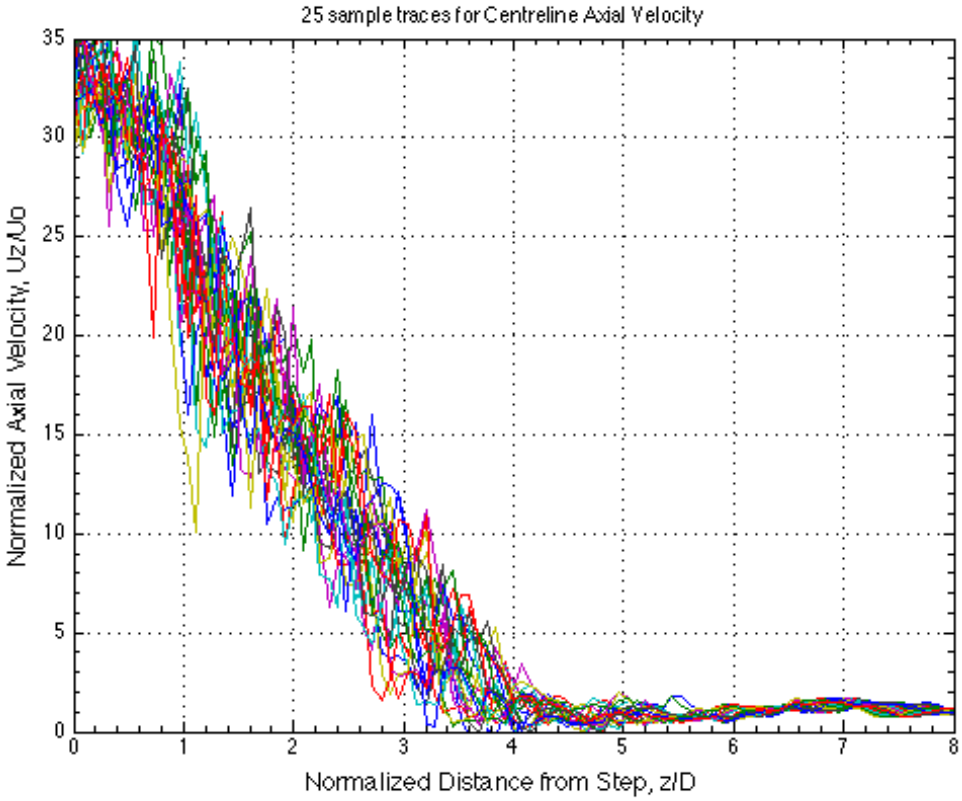

(a) Streamwise instantaneous axial velocity profiles at the centreline $y/D = 0$

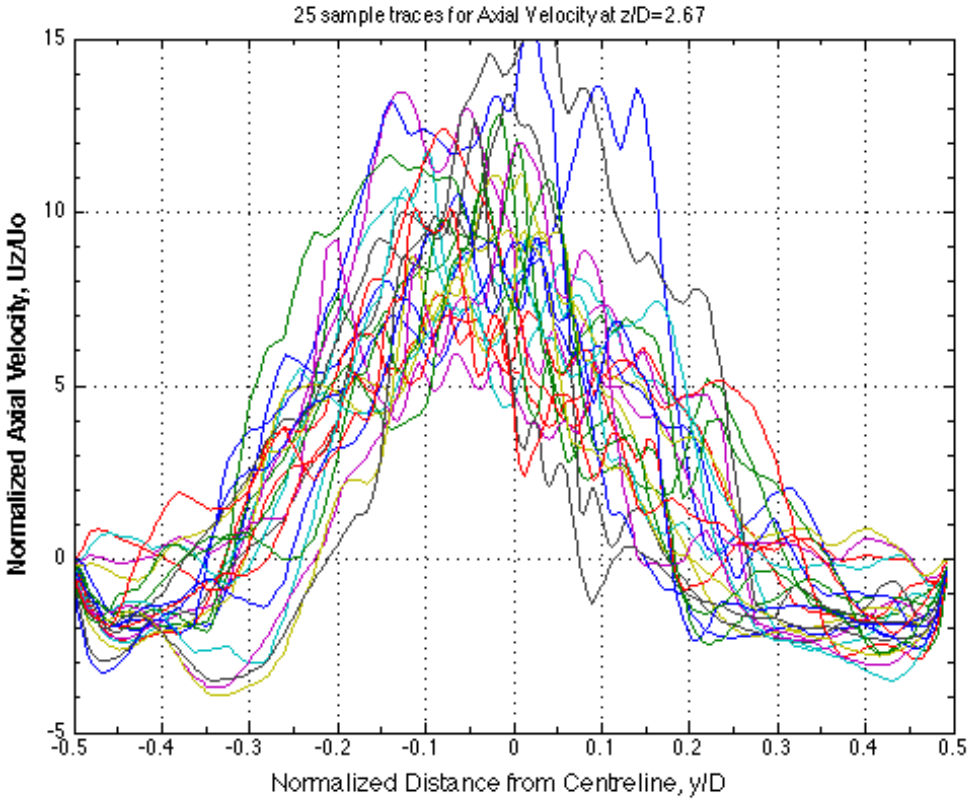

(b) Spanwise instantaneous axial velocity profiles at $z/D = 2.67$

Figure 110: Instantaneous axial velocity profiles for bootstrap method

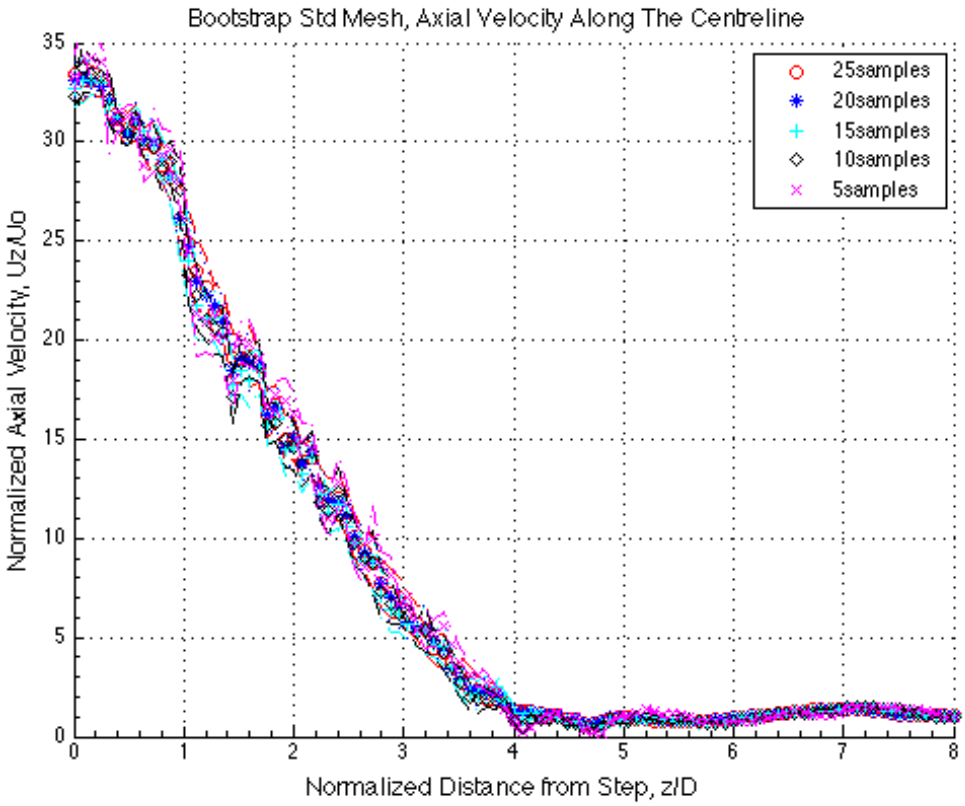

(a) Streamwise averaged axial velocity profiles at the centreline ($y/D = 0$) for various number of samples

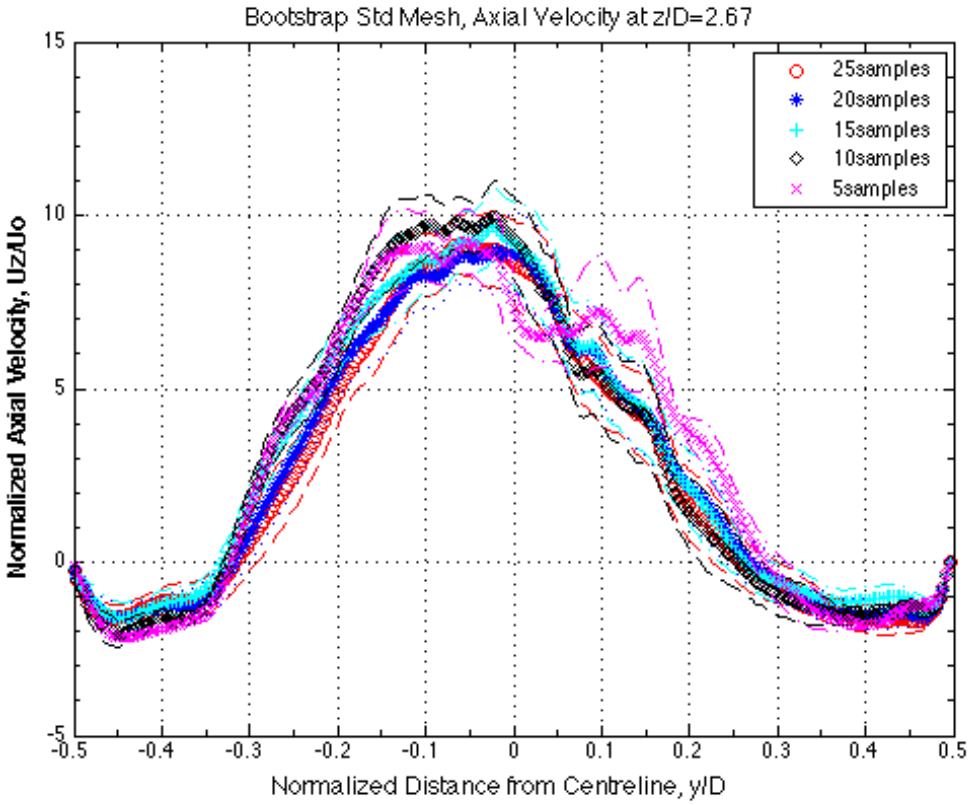

(b) Spanwise averaged axial velocity profiles at $z/D = 2.67$ for various number of samples

Figure 111: Averaged axial velocity profiles for bootstrap method using different number of samples

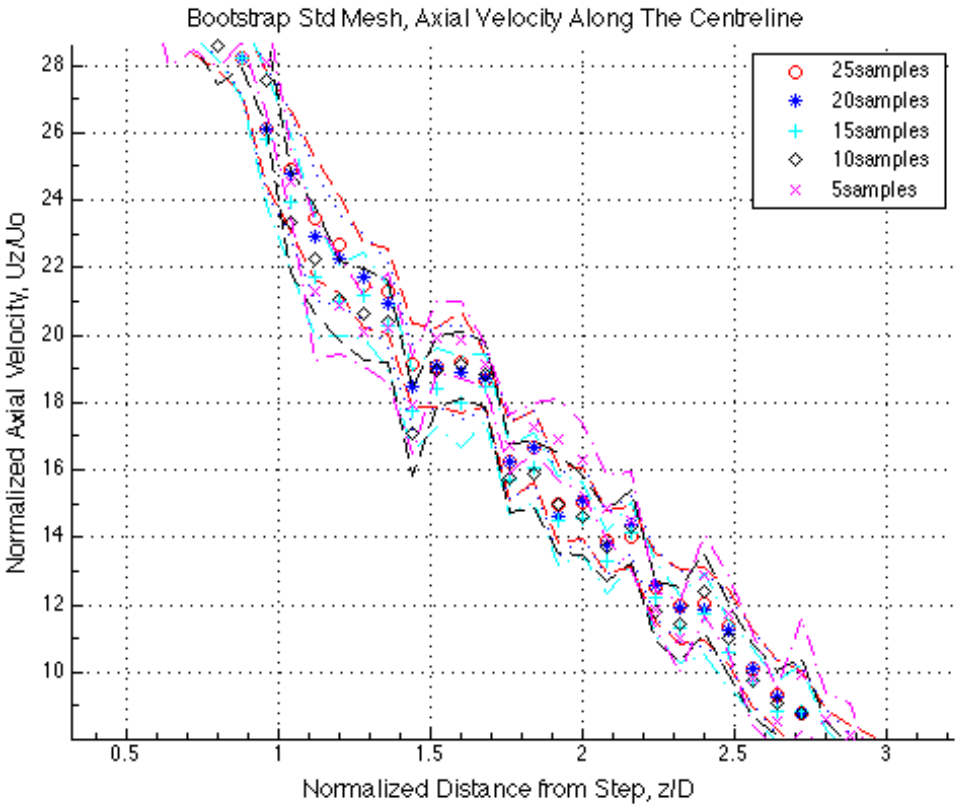

(a) Detail of streamwise averaged axial velocity profiles at the centreline ($y/D = 0$) for various number of samples

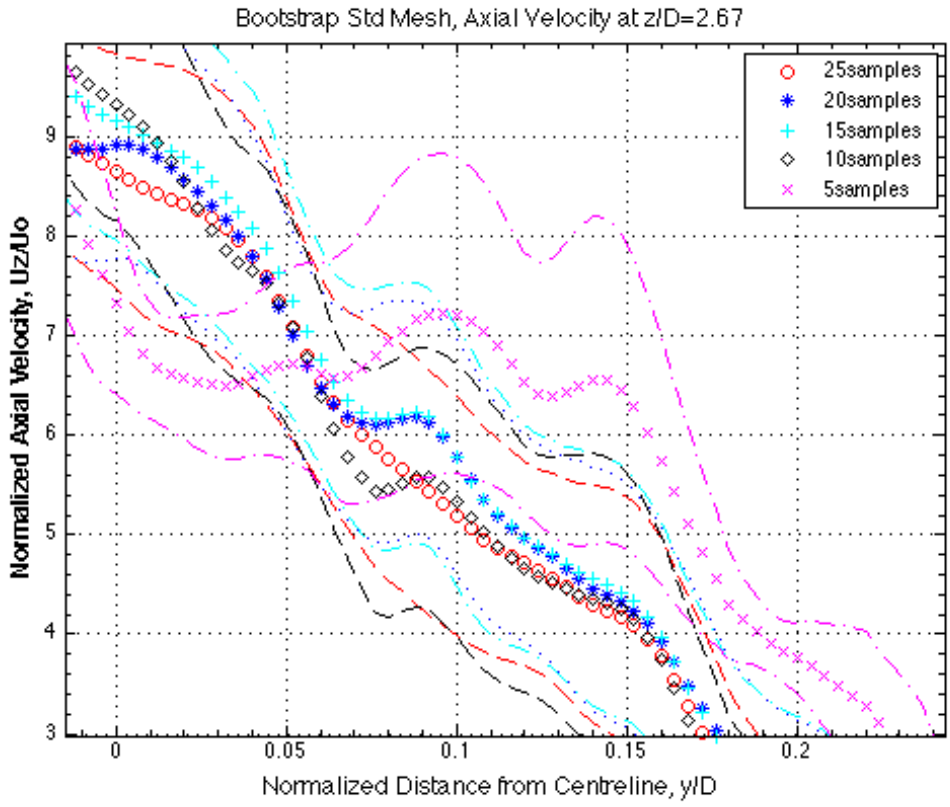

(b) Detail of spanwise averaged axial velocity profiles at $z/D = 2.67$ for various number of samples

Figure 112: Detailed view of averaged axial velocity profiles for bootstrap method using different number of samples

C Industrial Geometry

This final section describes the implementation of the KS2 dispersion model within an industrial geometry. The results presented below are from simulations performed by Drs S. Stowe and M. Zedda of Rolls Royce plc. with the KS2 model implemented within their proprietary CFD modeling software, PRECISE. Figures 113 & 114 presented below are from simulations performed on a section of one of their rich burn annular combustors currently in flight. Calculations were performed in a uRANS framework employing the k-SST-*Omega* closure model on an unstructured grid. Figure 113 shows trajectories for the fuel droplets along with the Sauter Mean Diameter represented by color in a spanwise slice, which is looking upstream from the combustor exit. What is immediately noticeable is the increased dispersion of the KS model into the external recirculation zone but more also into the inner recirculation zone when compared to the trajectories predicted by the G&I model. This is an important improvement as the experimental measurements available for the combustor indicated that the G&I dispersion model was under-predicting the droplet dispersion.

Also noteworthy, is the asymmetry in the increased dispersion observed as the model predicts greater dispersion on the top side of the combustor than the bottom. Recalling that the energy content of the modeled isotropic turbulence and the extent of its wavespace are both determined from local Eulerian quantities one may attribute the decreased dispersion to the smaller magnitude of generated velocity fluctuations. In turn, attributed to the increase in k_{min} resulting from the slightly smaller sized eddies at the smaller radial position.

This apparently small detail has an important effect on the subsequent combustion as is evident in Figure 114, where the reader's attention is drawn to in the primary combustion zone near the position of the inner recirculation zone. Furthermore, the radial asymmetry of particle dispersion also affects the secondary combustion zone downstream. The smaller predicted fluctuating velocities at the bottom have an equally important effect on the combustion rate compounding the effect observed in the simulations of the other two instances and may be explained through a reduction in overall heat transfer rate caused by the decreased velocities near the top of the combustor which result from the conservation of angular momentum of both the swirling airflow exiting the atomizer and the circumferential flow extant in the annual combustor. Unfortunately non-disclosure agreements prevent us from showing, the exact temperature range but cold regions are in the region of $600K$ and hot ones in excess of $2000K$. It is important to note that the spanwise temperature profile predicted by the KS model matches closely the values and the trends (profiles) that have been measured experimentally. Zedda (2014) noted the importance of predicting such inhomogeneity and hot spots as these will in turn allow the emissions models to predict more accurate results.

Finally, it should be noted that the model was also tested on a lean-burn annular combustor with good overall performance, equally distinct predictions between KS and GI computed trajectories and good temperature agreement with the experiment data. Unfortunately, these results may not be presented here as that particular geometry has yet to be disclosed to the public.

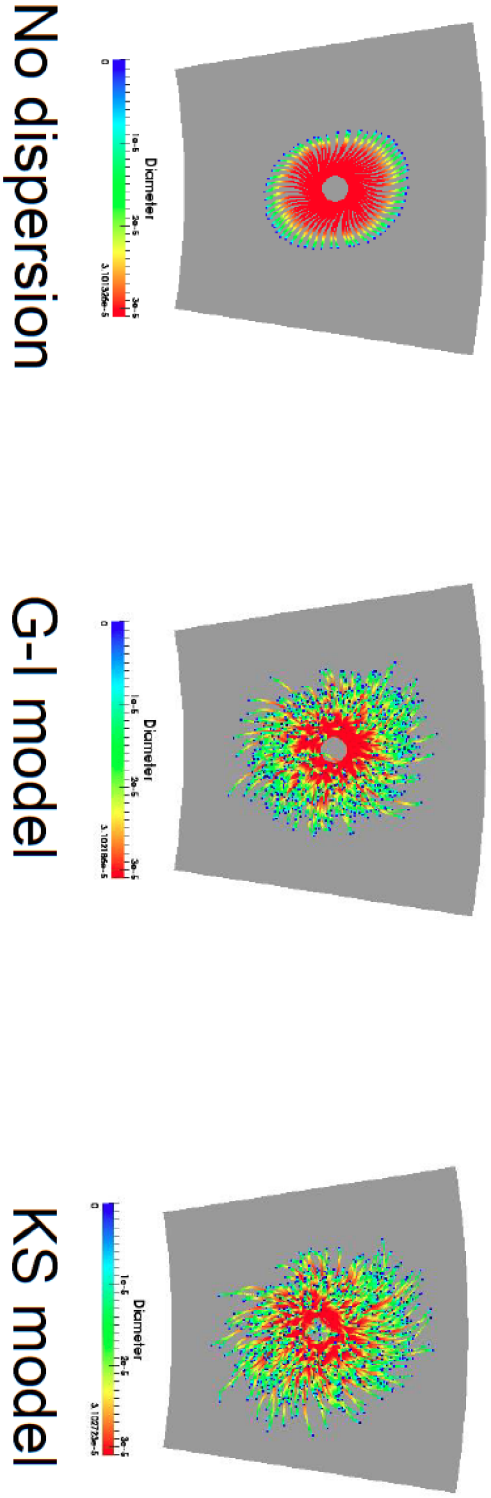

Figure 113: Particle Dispersion in the gas turbine combustor, from left to right, no dispersion model, GI dispersion model and finally the KS2 dispersion model. Coloring is by Sauter Mean Diameter

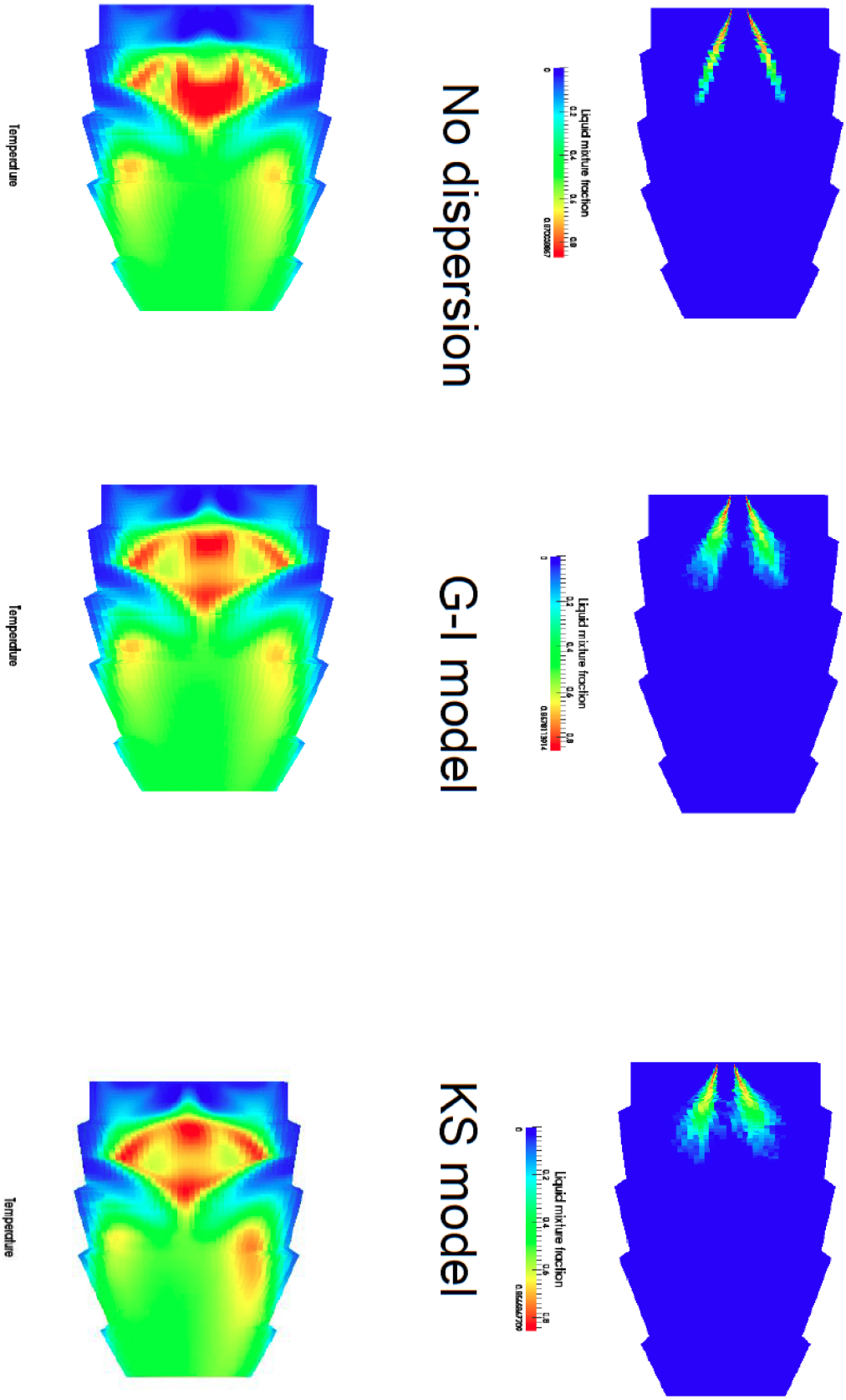

Figure 114: Liquid mixture fraction and temperature shown on the top and bottom respectively in the gas turbine combustor employing no dispersion, GI dispersion and the KS2 dispersion models from left to right respectively.